FACULTY OF ENGINEERING
AND ARCHITECTURE

Computational Fluid Dynamics Models for Patient-Specific Planning of Liver Transarterial Radioembolization

Tim Bomberna

Doctoral dissertation submitted to obtain the academic degree of
Doctor of Biomedical Engineering

Supervisors
Prof. Charlotte Debbaut, PhD* - Prof. Geert Maleux, PhD**

* Department of Electronics and Information Systems
Faculty of Engineering and Architecture, Ghent University

** Department of Imaging and Pathology & Department of Radiology
Faculty of Medicine, KU Leuven & UZ Leuven

September 2024

GHENT
UNIVERSITY

ISBN 978-94-6355-882-2
NUR 954
Wettelijk depot: D/2024/10.500/87

Members of the Examination Board

Chair

Prof. Joris Degroote, PhD, Ghent University

Other members entitled to vote

Prof. Jorge Aramburu Montenegro, PhD, Universidad de Navarra, Spain
Annelies Coene, PhD, Ghent University
Prof. Liesbet Geris, PhD, Université de Liège
Prof. Peter Vanlangenhove, PhD, Ghent University

Supervisors

Prof. Charlotte Debbaut, PhD, Ghent University
Prof. Geert Maleux, PhD, KU Leuven & UZ Leuven

To achieve great things
two things are needed:
a plan,
and not quite enough time.

L. Bernstein

Preface

Not so long ago, at a Master thesis fair, a Master student asked me if it is OK to do a Master thesis in computational fluid dynamics (CFD) even if it isn't your number one interest. He reasoned that, because I was doing a PhD in CFD, it must be *my* number one interest, *and* I must've always known that I wanted to do CFD, as if it had been my calling from birth. My answer was disappointing: no, CFD isn't my number one passion, I told him (more a means to a very noble end, but we'll come back to that throughout this book), and I hadn't always known I would want to do a PhD. What, then, sparked my interest in CFD and computational drug delivery? Which road brought me here? (He didn't end up asking me that, but I told him nonetheless.) Here is a short summary of what I said:

In 2018, in the first year of my Master in Biomedical Engineering, I took up an elective course at the Faculty of Pharmaceutical Sciences focusing on drug delivery, taught by professor Stefaan De Smedt. He taught me about using nanoparticles for targeted drug delivery, the enhanced permeation and retention effect, and the blood-brain barrier, among many other things. The topic fascinated me so much that, by the time I had to choose my own Master thesis topic, this interest led me to prof. Charlotte Debbaut, who had an active topic in the domain of targeted drug delivery (we would later re-name it to *locoregional drug delivery*, since it is probably a more apt name for the subject). Even though I was very stressed throughout and had to spend many weekends alone at Blok B, running my simulations, I thoroughly enjoyed my Master thesis research. More than CFD specifically (again, a means to an end), I thought the concept of using simulation for pre-operative planning was very cool, even though the full implications of that concept still eluded me (they probably still do). And so, when Charlotte asked me to stay on for a PhD, I was captivated. I went through the typical doubts that one has at the end of their studies, but eventually, in the summer of 2019, I decided to go for it. In September 2019, I joined the BioMMedA (although it was capitalized differently at the time) lab and started my PhD. And I guess they say, the rest is history?

Of course, a PhD cannot be completed without the help of many, many people. And so I wanted to use this preface to thank all the people involved in the scientific side of the PhD. Of course, my main thank you in this preface has to go out to my promotors, Charlotte Debbaut and Geert Maleux. Without Charlotte, it should be clear from the story above that I would not be here. She introduced me to the subject, encouraged me to stay on, gave me all the freedom in the world to explore what I felt needed to be explored, and provided feedback to every single line of scientific text that I've written in the past five years. For that, I am incredibly grateful. At the side of UZ Leuven, Geert provided me with clinical insights that steered the direction of this project, gave us crucial data that made our research so novel, and supported and provided feedback throughout the multi-year process. Of course, to Geert, I am similarly grateful.

Luckily, I had the opportunity to collaborate with many different people on this topic, something that I don't take for granted, and something I will think back on fondly in the years to come. To my Dutch colleagues of the ULTIMO project (past and present), Jan van der Hoek, Romaine Kunst, Erik Groot Jebbink, Tristan Vlogman, Kartik Jain, Tess Snoeijink, Anne van den Brekel, Frank Nijsen: I'm glad we had the pleasure to exchange thoughts on a regular basis, visit each other's labs and that we could use your very relevant experimental data to validate our models. To Unai Lertxundi, my Basque counterpart: it's a shame your internship wasn't a bit earlier in my PhD process, as I would've had more time to help you (and your interesting ideas and work would have guided my own work, for sure). To Jorge Aramburu and Raúl Anton: your enthusiasm during the meeting we had during one of my first months led me to believe that I could actually do this, for which I'm very grateful. To my colleagues at UZ Gent and UZ Leuven, Elisabeth Dhondt, Laurens Hermie, Luc Defreyne, Peter Vanlangenhove, Lawrence Bonne, Chris Verslype (and again, Geert, of course): I'm indebted to you because of all your relevant insights, your help during data transfer, and your willingness to provide me with feedback despite your busy schedules. To Jurgen Deviche: your help with the experimental set-up was not only useful but crucial. To Saskia Claessens: thank you for all your necessary help with all things administration and my on-boarding. To Natalie Van den Ende from UZ Leuven, and Hélène De Naeyer, Lieselot Burggraeve and other colleagues from HIRUZ: I could not have completed the administrative side of data transfer (and, by extension, my research) without your help. To my UGent-colleagues at TechTransfer, including but not limited to Alessandro Biondi, David Aubert and Katia Stevelinck: it was incredibly fascinating to experience the valorization side of research, so I want to specifically thank you for your relevant work. To my UGent-colleagues at IOF, Eline Soetens and Celine Vanhaverbeke: thank you for all your time and insights during my search for follow-up funding. To Klaus Bacher and Brent van der Heyden: thank you for your incredibly relevant input regarding the side of medical radiation physics (you made me realize I do not know enough about this). To Pascal Verdonck: thank you for lighting the spark in my 3rd Bachelor that eventually brought me to Biomedical Engineering. To my jury members, Jorge Aramburu, Annelies Coene, Liesbet Geris, Peter Vanlangenhove, and chair, Joris Degroote: thank you for spending your time to go through this work and for providing your insightful comments. To my fellow members of the Youngster National Committee on Biomedical Engineering, including (but not excluded to) Andrea Menichetti, Dries Hendrikx, Jonathan Dan, Virginie Otlet, and especially Alexandra Tits and Sophie Bekisz: thank you for your amazing efforts to make our National Days happen, and making me feel part of a team! Finally, to my own colleagues at BioMMedA and Medisip, who I feel each contributed to my research in their own way: Ghazal Adeli Koudehi, Amith Balasubramanya, Lise Gheysen, Mathias Peirlinck, Patrick Segers, Annette Caenen, Pieter van Mierlo, and my co-inventors Jolan Heyse and Saar Vermijs: thank you to each of you for providing pieces of the puzzle (in research, sometimes even the smallest of comments can lead to big, interesting detours). Of course, to my other colleagues, if you're looking for your name, you'll find that in the back!

Throughout the years, it was my absolute honor to be able to guide and supervise many Bachelor and Master students at both the Faculties of Engineering and Medicine as they navigated their own specific sub-topics within this broad topic. In fact, supervising them was by far my proudest work. My thank you to them is for their interest in the topic, their motivation and critical attitude, and their ability to come up with their own novel methods and insights, which steered my own research in new and exciting directions: Matthias, Heather, Marthe, Laura, Vic, Ekaterina, Danaë, Julie, Luca, Braïm, Gilles, Amaryllis, Charlotte C. and Rosario for your innovative experimental work; Thibault and Marius for your segmentation work; Rosario (again), Nathalie, Inten, Tibo, Casper, Gaël, Elien, Noah, Lucas, Charlot, Jana Z., Marthe (again), and Rune for your computational work. (Of course, the same goes for the students who did *not* work on the liver topic: Lieve, Laurens, Veerle, Jana P., Kenzo, Louise, Robbe, Elise, Kaat and Elke; you helped me broaden my horizons significantly beyond the domain of the liver.)

The work you will find below is not only the result of the thoughts I had and the person I became between 2019-2024, but also of the collaboration with all the people mentioned above, from student to professor and everything in-between; people who steered my research in both obvious and more subtle ways, giving critical remarks that led to further thinking, developing methods that I would not have developed on my own, cheering me on, inspiring me.

And so, thinking it over, I should've told that Master student: no, CFD isn't my number one passion - but working on a state-of-the-art project that, if successful, could help people around the world *and* doing that together with loads of interesting, smart people? Oh, there are worse things to be passionate about.

Table of contents

Abbreviations and symbols

The following list summarizes the most commonly used abbreviations and symbols in this dissertation.

Abbreviations

2D	Two-dimensional
3D	Three-dimensional
CFD	Computational fluid dynamics
CT	Computed tomography
PET	Positron emission tomography
SPECT	Single photon emission computer tomography
MRI	Magnetic resonance imaging
PHA	Proper hepatic artery
RHA	Right hepatic artery
LHA	Left hepatic artery
(C)PRM	(Composite) Particle Release Map
(C)PRG	(Composite) Particle Release Grid
GPR	Gaussian Process Regression
LHS	Latin hypercube sampling
SA	Sensitivity analysis
ADOE	Adaptive design of experiments
RDOE	Rigid design of experiments
PNEF	Particle non-exit fraction

Symbols

$\vec{u}$	Fluid velocity vector [m/s]
ρ	Density [kg/m^3]
$\vec{\vec{\tau}}$	Shear stress tensor [Pa]
$\vec{f}$	Fluid forces [N]

μ	Viscosity [kg/m·s]
$\dot{\gamma}$	Shear rate [s^{-1}]
μ_0	Minimum viscosity [kg/m·s]
μ_∞	Asymptomatic viscosity [kg/m·s]
τ_0	Apparent yield stress [Pa]
λ	Shear stress modifier [s^{-1}]
d_p	Particle diameter [m]
ρ_p	Particle density [$\mathrm{kg/m}^3$]
m_p	Particle mass [kg]
$\vec{F_G}$	Gravitational force [N]
$\vec{F_D}$	Drag force [N]
C_D	Drag coefficient
$\vec{u_p}$	Particle velocity vector [m/s]
Re_p	Particle Reynolds number
$\vec{F_P}$	Pressure gradient force [N]
$\vec{F_V}$	Virtual mass force [N]
C_V	Virtual mass coefficient
Q_b	Branch flow [ml/min]
$Q_{h,b}$	Healthy contribution of the branch flow [ml/min]
$Q_{t,b}$	Tumor contribution of the branch flow [ml/min]
V_s	Segmental volume [ml]
Q_s	Segmental flow [ml/min]
k_h	Healthy perfusion parameter [1/min]
k_c	Tumor perfusion parameter [1/min]
BF_b	Branching factor
Q_t	Tumor flow [ml/min]
V_t	Tumor volume [ml]
TPP	Tumor perfusion percentage [%]
$(T)CF_x$	(Truncated) cell fraction for outlet x [%]
FF	Flow fraction to outlet x [%]
$(T)EF_x$	(Truncated) exit fraction for oulet x [%]
IPS	Index of Particle Spread [%]
UIPS	Uniformity Index of Particle Spread [%]
N_{plane}	Plane grid cells
N_{particle}	Particle grid cells
U	Grid cell particle percentage for uniform particle distribution [%]
p_{ij}	Grid cell particle percentage [%]
tIPS	Time-dependent Index of Particle Spread [%]
WIPS	Particle-Weighted Index of Particle Spread [%]
N_{burst}	Number of particle grid cells during a specific injection burst

P_b	Number of particles present in a specific injection burst
N_i	Fraction of particles exiting outlet i [%]
$PEP_{b,i}$	Particle exit percentage in outlet i of batch b [%]
TF_i	Tumor flow percentage in outlet i [%]
TD_b	Tumor dose of batch b [%]
$D_{b,i}$	Difference in particle exit percentage for a simulation of batch b compared to the baseline batch for outlet i [%]
D_{ave}	Average difference in particle exit percentage compared to the baseline batch over all outlets [%]
D_{max}	Maximum difference in particle exit percentage compared to the baseline batch over all outlets [%]
D_{dose}	Difference in tumor dose compared to baseline batch [%]
$\Delta PEP_{b,i}$	Minimum-maximum range in particle exit percentage for a specific outlet i in simulation batch b [%]
$\Delta\Delta PEP_i$	Similarity in sensitivities for outlet i [%]
ΔTD	Minimum-maximum range in tumor dose [%]
$k(x_i, x_j)$	Gaussian Process Regression model kernel for input points x_i and x_j
S_i	First-order sensitivity index of parameter i [-]
ST_i	Total-order sensitivity index of parameter i [-]
$V[Y]$	Variance of output parameter Y
N_{init}	Initial number of samples for initialization of the ADOE
B	Number of bins considered in the ADOE
e	Error of the surrogate model [%]
$x_{nominal}$	Nominal value for a certain input parameter
x_{sample}	Sampled value of an input parameter
γ	Tumor coverage [%]
τ	Tortuosity [-]
$L_{centerline}$	Sum of the Euclidian distances between each successive point of the centerline [m]
$L_{rectilinear}$	Euclidian distance between start and end of the centerline [m]
κ	Curvature [1/mm]
C	Vascular cost [-]

Graphical Abstract

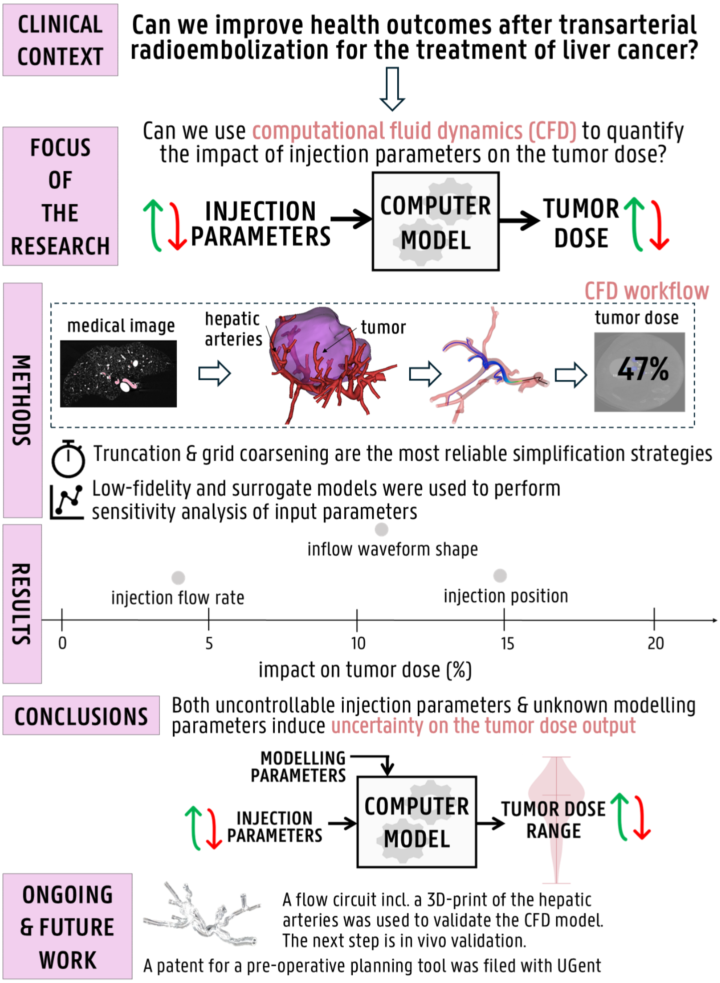

Can we improve health outcomes after transarterial radioembolization for the treatment of liver cancer?

Can we use computational fluid dynamics (CFD) to quantify the impact of injection parameters on the tumor dose?

Truncation & grid coarsening are the most reliable simplification strategies

Low-fidelity and surrogate models were used to perform sensitivity analysis of input parameters

Both uncontrollable injection parameters & unknown modelling parameters induce uncertainty on the tumor dose output

A flow circuit incl. a 3D-print of the hepatic arteries was used to validate the CFD model. The next step is in vivo validation.

A patent for a pre-operative planning tool was filed with UGent

Figure 1: Graphical abstract.

Summary

Transarterial therapies, such as transarterial radioembolization (TARE) and chemoembolization (TACE) are the preferred methods of treatment at the unresectable intermediate stage of hepatocellular carcinoma (HCC), the most common form of primary liver cancer. During these catheter-directed therapies, microspheres are injected superficially or selectively in the hepatic arteries with the goal of locally embolizing the tumor tissue, which is mainly fed arterially. However, the treatment outcomes (mean survival times) of TARE and TACE are highly heterogeneous, with many patient-specific aspects, such as commonly varying hepatic arterial anatomies and tumor size(s) and location(s), complicating treatment execution. Additionally, both computational, experimental and clinical studies have shown that several clinical injection parameters (e.g. injection location, injection flow rate, catheter type), which typically vary in clinical practice, can have a large impact on the downstream microsphere distribution.

In this PhD thesis, we aim to develop and use computer models to quantify the impact of injection parameters on the microsphere distribution, and develop a pre-operative planning framework to improve health outcomes of transarterial therapies.

Part I: Clinical Rationale and State-of-the-Art in Modeling of Transarterial Therapies consists of **Chapters 1, 2 and 3**. **Chapter 1** serves as a short introduction. In **Chapter 2**, the clinical background of transarterial therapies and the clinical rationale of this dissertation is discussed. Importantly, we identify the current challenges of transarterial therapies. Next to variable health outcomes and governing uncertainties regarding the impact of specific injection parameters (as discussed above), there is also a lack of reliable, non-invasive pre-treatment planning tools. Current pre-treatment methods to assess the suitability of these injection conditions are lacking in

either reliability or repeatability. When a pre-treatment injection of low-dose radioactive particles is done, this has several disadvantages: (1) it is an invasive procedure, (2) it is not always fully reliable because injection conditions (such as microsphere properties and injection location) can still change between pre-treatment and the actual treatment, and (3) it does not allow to extensively finetune various injection parameters. Ideally, we would be able to assess the suitability of current injection conditions repeatably, non-invasively and reliably. As such, we define the governing clinical questions informing this PhD dissertation as: (1) Can we reliably predict the tumor dose before the procedure? and (2) Can we decrease variable outcomes in TARE and TACE by pre-operative optimization?

The clinical questions inspire the more specific sub-goals of this dissertation, where we aim to use computer models to predict the tumor dose and pre-operatively, non-invasively and reliably assess the suitability of specific injection conditions. **Chapter 3** begins with an overview of different model types that are used in the state-of-the-art in the context of transarterial therapies, from complex fluid-structure interaction models to computational fluid dynamics (CFD) models to lumped 0D models. Currently, mostly CFD has been used, and multiple CFD studies have already given insight into the impact of clinical injection parameters: cross-sectional injection position, axial injection position, catheter direction, catheter type, injection flow rate and microsphere type, albeit that these studies have some limitations. Specifically, most of the early CFD analyses were carried out in simplified, planar geometries. While the focus has shifted to CFD analysis of patient-specific geometries, which are much more realistic, they are also computationally more complex, and may require simplification of the computational approach. Additionally, CFD models also behave differently than real-world systems, which is crucial when evaluating reliability of the these models. Typically, three important principles determine model reliability: (1) verification, (2) validation, and (3) uncertainty quantification (VVUQ). In vitro validation, which allows bench testing, has only been performed on simplified, planar geometries. In vivo validation has also been very limited. Additionally, uncertainty quantification and global sensitivity analysis of a wide range of clinical and numerical parameters has also been lacking in this domain, with only variations of 2 parameters at the same time being considered so far in 1 patient-specific geometry. Again here, computational cost is an important limiting factor.

Considering the above, we aim to address these limitations of the state-of-the-art in this PhD dissertation by developing (i) effective strategies to reliably cut down computational cost of patient-specific 3D CFD simulations (focus of Part II), (ii) uncertainty quantification techniques of numerical and clinical parameters in patient-specific geometries (focus of Part III), (iii) validation techniques in patient-specific geometries (focus of Part IV), and (iv) a computational framework for pre-operative planning, considering (but not limited to) the tumor dose as calculated with CFD (focus of Part V).

Part II: Simplification Strategies for CFD Modeling of Transarterial Therapies consists of **Chapters 4, 5 and 6**. The aim is to develop and evaluate reliable simplification strategies for our CFD models of transarterial therapies to reduce the computational cost. In **Chapter 4**, the hybrid particle-flow model as the result of a novel truncation algorithm for the downstream vessels is introduced. The original patient-specific hepatic arterial geometry (Geometry 1, 48 outlets) was moderately and severely truncated at two different levels, resulting in two additional arterial trees: Geometry 2 (38 outlets) and Geometry 3 (17 outlets). In each geometry, 1 planar injection and 3 catheter injections were simulated, with the injection location superficially in the proper hepatic artery (PHA) (before the first bifurcation). For the truncated geometries, it was assumed that, downstream of the truncated outlets, particles distributed proportionally to the blood flow (hybrid particle-flow model). For the planar injections, the median difference in outlet-specific particle distribution between Geometry 1 and 2 was 0.0442% and 0.211% between Geometry 1 and 3, clearly indicating the impact of truncation. Studying the 3 catheter injections, the maximum (of all 3 injections) median difference in particle distribution between Geometry 1 and 2 was 0.0647% and 0.240% between Geometry 1 and 3, again showing the impact of truncation. However, with these limited differences, the results indicated that the hepatic arterial tree can be reliably severely truncated. Interestingly, using just flow distribution as a surrogate for particle distribution in the entire tree was considerably less accurate than using the hybrid model, with reported maximal outlet-specific differences of ∼6% (which were significantly higher than the maxima for the catheter injections (∼3.5%) and for the planar injection (∼2%)).

In **Chapter 5**, the hybrid particle-flow model with the same levels of moderate and severe truncation is verified for selective injection in the right and left hepatic arteries, after the first bifurcation. Upstream truncation is also investigated, with truncation lengths of 20-

80 mm before the catheter tip. Severe truncation gave maximum differences in particle distribution of ∼4-11% and ∼8-9% for down- and upstream truncation, respectively. For moderate truncation, these differences were only ∼1-1.5% and ∼0.5-2%, indicating that severe truncation is much less reliable here than for superficial injection. Additionally, in each simulation, particle cross-sectional spread was quantified for 5-6 axial planes from the catheter tip to the outlets. Considering all particles, spread increased downstream of the tip to 80-90% of the cross-section. However, spread was found to be much lower at specific time points, indicating high time-dependency. Interestingly, these time-dependent spread measures could show where differences might arise between flow and particle modeling, and if particle-flow alignment could be improved in the future.

From these two chapters, we conclude that combining domain truncation with hybrid particle-flow modeling is an effective method to reduce computational complexity, but that moderate truncation is more reliable than severe truncation (especially for selective injection).

Next, in **Chapter 6**, we identify five simplification strategies: severe truncation, and additionally, steady flow modeling, moderate and severe grid coarsening, and reducing the number of flow cycles. We evaluated whether they can be used to (1) accurately predict the CFD output (i.e. the particle distribution, as before, and the tumor dose) and (2) estimate the sensitivity of the output towards a specific injection parameter (injection flow rate). For both accuracy and sensitivity purposes, grid coarsening was shown to be the most reliable simplification strategy, allowing to predict the tumor dose with only a maximal deviation of 1.4%, and a similar sensitivity (deviation of 0.7%). The steady strategy performed the worst, with a maximal deviation in the tumor dose of 20% and a difference in sensitivity of 10%. Additionally, coarsening the grid decreased the computational time by roughly 45%.

From **Chapters 4, 5 and 6**, we conclude that moderate truncation of the downstream vessels (in combination with the hybrid particle-flow model) is the most reliable strategy when the focus is on accurately predicting the tumor dose. If the focus is on quantifying sensitivity towards a specific input parameter, grid coarsening is also a viable option, allowing to significantly reduce the computational time. However, to allow uncertainty quantification and global sensitivity analysis (which often require hundreds or thousands of simulations), we require new strategies to even further reduce computational cost. This is the focus of Part III.

Part III: Uncertainty Quantification of Clinical and Numerical Parameters consists of **Chapters 7 and 8**. The goal is to quantify the uncertainty on the tumor dose prediction due to unknown catheter tip position and unknown boundary conditions. In **Chapter 7**, we quantified the uncertainty of the tumor dose towards the uncontrollable but important parameter of catheter tip location. To cheaply repeat similar simulations, we used a simplified CFD model, where a catheter injection was mimicked by simulating a planar injection and calculating which release positions within the axial cross-section led to tumor deposition (low fidelity CFD modeling approach). By then sampling 50 random catheter release positions across the axial cross-section, the tumor dose range resulting from an unknown (or uncontrollable) catheter tip position was calculated, showing a variation of ∼15%. While this novel low fidelity approach allowed uncertainty quantification in the tumor dose, the strategy of simplifying the CFD model by a planar injection is limited in applicability, stressing the need for more broad simplification strategies.

Hence, in **Chapter 8**, we build a surrogate Gaussian process regression (GPR) model trained on a minimal number of 3D CFD simulations of drug transport to easily perform uncertainty quantification and sensitivity analysis. As an example case, we determined the sensitivity of the tumor dose towards the inflow waveform shape, extracting three shape parameters from our input waveform (peak systolic flow rate, heart rate, systolic duration ratio) and defined our 3D input space by varying them within 75%-125% of their nominal values. To cheaply fit our GPR, we developed an adaptive design of experiments (ADOE) algorithm, which initially used 100 Latin hypercube sampled points in 3D input space to define the initial design of experiments (DOE). Based on this DOE, we fit a GPR, and used this to determine the sensitivity indices for each parameter with Sobol's variance-based method. Next, in each of 27 equivolume bins which divide our 3D input space, we determined the most uncertain predictions of the current GPR, computed their true values using CFD, and added these points to the DOE. We continued to add batches of 27 points to the DOE until the Sobol indices stabilized. We tested our ADOE algorithm on the exemplary Ishigami function and showed that we could reliably obtain Sobol's indices with an absolute error <0.1 (which was enough for our purposes). Finally, applying the ADOE to our waveform, we found that the first-order sensitivity indices were 0.0550, 0.0191 and 0.407 for the peak systolic flow rate, heart rate, and the systolic duration parameters, respectively, based on 181 CFD simulations (initial DOE of 100 simulations). This showed that we can reduce uncertainty on the tumor dose prediction most by accurately measuring the duration of systole. Hence, the ADOE allows reliable sensitivity analysis with a relatively limited number of complex model evaluations. In the future, we can use this to identify the highest-impact numerical input parameters to diagnose our model, and find the most important clinical parameters for pre-operative optimization.

Next to uncertainty quantification, the final important principle of VVUQ is validation. **Part IV: Validation** consists of **Chapter 9**, where we focus on in vitro validation. The aim is to illustrate the feasibility of patient-specific in vitro validation, which is a significant advancement over the generalized, planar geometries used in literature. In **Chapter 9**, an in vitro set-up was built by means of an experimental flow circuit in which a 3D-print of a patient-specific hepatic arterial geometry was mounted. Water flowed down from an elevated reservoir through the 3D-print, to polyvinyl chloride (PVC) connecting tubes with tunable resistances leading into 10 collecting reservoirs. The outflows to each reservoir were set manually by iteratively adapting the resistances at the PVC tubes until all outflows matched the computational boundary conditions ($< 5\%$ error margin). Non-radioactive SIR-Spheres were injected and the distribution over the 10 reservoirs was calculated by filtering the reservoir particle-water mix and measuring the particle weight. The high similarity between experimental and theoretical flow distribution (0.407% difference per reservoir on average) showed that the implementation of the outlet BCs through tuning of the resistances was successful. Moreover, the average difference for a reservoir between numerical and experimental particle distribution was 2.73% (min: 0.394% - max: 6.47%) and 2.97% (min: 1.21% - max: 6.17%) for the 2 performed injections. This in vitro validation set-up confirmed that flow distribution was far from a perfect surrogate for the particle distribution. While we showed the possibility of using a patient-specific hepatic arterial geometry and implement patient-inspired BCs in an in vitro set-up, we conclude that the current set-up should still be improved by developing among others more robust particle measurement methods.

Finally, we introduce a framework for the pre-operative planning tool, considering what we learnt before regarding uncertainty on the tumor dose prediction. **Part V: Valorization** consists of **Chapter 10**. In **Chapter 10**, we showcase a pre-treatment planning framework which not only considered the tumor dose range, but also considered the trade-off between the target specificity (higher for selective injection) and vascular accessibility (typically more difficult for selective injection). As a patient-specific case study, we identified four relevant injection locations to compare using the proposed framework: superficially (in the PHA), selectively in the right hepatic artery (RHA) and left hepatic artery (LHA), and super-selectively in the RHA, which perfuses most of the tumor tissue. A tumor coverage of 100% was only reached for superficial PHA injection. Regarding accessibility, even for the most distal injection locations (selective LHA injection and super-selective RHA injection), the diameter was still >4 mm and not considered a limiting factor. Selective injection in the LHA had the lowest accessibility, with high tortuosity and curvature values due to the bend after the first bifurcation. Regarding the tumor dose ranges for all scenarios, the minima were relatively constant (i.e. within the range 25.7%-38.6%), but the maxima varied significantly between 50.5%-81.9%, with the maximum reached for super-selective RHA injection. Combining all decision criteria in our framework, selective RHA injection seemed most optimal, with high tumor coverage (69.6%), a similar median tumor dose compared to other scenarios (48.7%) and high accessibility.

To conclude, in **Part VI: Conclusions**, which consists of **Chapter 11**, limitations of the computational approach, such as the modeling of the catheter as thin-walled and the catheter fluid as blood, are first discussed. Next, we identify key results. These include (1) the introduction of the hybrid particle-flow model as a reliable simplification strategy for accuracy purposes, (2) grid coarsening as the optimal strategy for simplification for sensitivity purposes, (3) converting tumor dose values into tumor dose ranges given uncertain clinical parameters such as catheter tip position, (4) showing that specific surrogate models can help reduce computational complexity of performing sensitivity analysis, (5) using a patient-specific in vitro flow circuit to highlight important differences between flow and particle distribution, and (6) developing a multi-objective pre-operative framework, which maximizes tumor dose under specific constraints, such as limited vascular access. Next, future work building on our results is suggested. Aside from verifying the current results for more patient-specific geometries, we suggest focusing more on in vivo validation using SPECT- and PET-CT scans, using the current in vitro validation methods mainly for bench testing novel catheter types, expanding current uncertainty quantification techniques to wider ranges of parameters, and using our novel spread measures to investigate whether novel catheter types can promote particle-flow alignment. Finally, we advise the future steps that will likely need to be undertaken to bring these CFD simulations to clinical practice. We suggest simulating to health end-points (such as the radioactive dose delivered to the tumor, which can be measured with in vivo imaging), quantifying inter-subject variability to determine under which circumstances patient-specific geometries need to be used, and using deep learning or other surrogate models to advance towards (near-) real-time predictions.

As a final note of this dissertation, we remark that studies in this field have focused on two methods for improving health outcomes of transarterial therapies: (1) through optimizing injection conditions and then tightly controlling these peri-operatively (*school of control*), or (2) through promoting mixing of the microspheres with the blood to lessen the impact of these injection conditions (*school of mixing*). This dissertation considers that while we cannot know which strategy will prove optimal in the future, both strategies have merit, and could be combined: since tight control of all injection parameters might not be possible, the consideration of uncertain tumor dose ranges (as in this dissertation) could become crucial, and is probably the most relevant development in this work. However, if these uncertainty ranges become too large, the novel spread measures we developed can help identify whether promoting particle-flow mixing is a viable strategy to lessen the impact of these injection conditions (and hence, the size of the uncertainty range). This combination strategy can be named as a novel, third method for improving health outcomes of transarterial therapies: (3) because full control of injection conditions is likely impossible, we are forced to consider the governing uncertainties on the tumor dose prediction (uncertainty quantification), and use novel solutions, such as novel catheter types, to decrease the uncertainty ranges as much as possible (uncertainty mitigation). This third approach can be named the *school of uncertainty quantification and mitigation*). In that sense, our pre-operative workflow to optimize injection conditions under governing uncertainties might be a good starting point for future endeavors.

Samenvatting

Transarteriële therapieën, zoals transarteriële radio-embolisatie (TARE) en chemo-embolisatie (TACE) zijn de voorkeursbehandelingen tijdens het niet-resectabele, intermediaire stadium van hepatocellulair carcinoom (HCC), de meest voorkomende vorm van primaire leverkanker. Tijdens deze kathetergestuurde transarteriële therapieën worden microsferen oppervlakkig of selectief in de leverslagaders geïnjecteerd met als doel het tumorweefsel, dat voornamelijk arterieel wordt gevoed, lokaal te emboliseren. De behandelingsresultaten (gemiddelde overlevingstijd) van TARE en TACE zijn echter zeer heterogeen, met veel patiënt-specifieke aspecten, zoals de slagaderanatomie van de lever en de grootte en locatie(s) van de tumor(en), die de procedure complex maken. Daarnaast hebben zowel computationele, experimentele als klinische studies aangetoond dat klinische injectieparameters (bv. injectielocatie, injectiesnelheid, kathetertype), die sterk kunnen variëren in klinische praktijk, een grote invloed hebben op de verdeling van microsferen in de slagaderboom.

In dit proefschrift willen we computermodellen ontwikkelen en gebruiken om de invloed van injectieparameters op de microsfeerdistributie te kwantificeren en een preoperatieve planningstool ontwikkelen om de gezondheidsresultaten van transarteriële therapieën te verbeteren.

Deel I: Klinische rationale en meest relevante ontwikkelingen in het modelleren van transarteriële therapieën bestaat uit **Hoofdstukken 1, 2 en 3**. **Hoofdstuk 1** dient als korte introductie. In **Hoofdstuk 2** wordt de klinische achtergrond van transarteriële therapieën en de klinische rationale van dit proefschrift besproken. Belangrijk is dat we de huidige uitdagingen van transarteriële therapieën duiden. Naast variabele gezondheidsuitkomsten en heersende onzekerheden over de invloed van specifieke injectieparameters (zoals hierboven besproken), is er ook een gebrek aan betrouwbare, niet-invasieve methoden voor het plannen van de behandeling. De huidige TARE-voorbehandeling om de geschiktheid van injectiecondities te beoordelen is niet helemaal betrouwbaar of herhaalbaar. Wanneer tijdens deze voorbehandeling een injectie van laag gedoseerde radioactieve microsferen wordt gedaan, heeft dit verschillende nadelen: (1) het is een invasieve procedure, (2) het is niet altijd volledig betrouwbaar omdat de injectieparameters (zoals microsfeertype en injectielocatie) nog kunnen veranderen tussen de voorbehandeling en de daadwerkelijke behandeling, en (3) het laat niet toe om verschillende injectieparameters uitgebreid te optimaliseren. Idealiter zouden we de geschiktheid van de huidige injectieparameters herhaalbaar, niet-invasief en betrouwbaar kunnen beoordelen. Als zodanig definiëren we de klinische rationale die ten grondslag ligt aan dit proefschrift als volgt: (1) Kunnen we de tumordosis vóór de procedure betrouwbaar voorspellen? en (2) Kunnen we variabele uitkomsten in TARE en TACE verminderen door preoperatieve optimalisatie?

De klinische vragen inspireren de meer specifieke subdoelen van dit proefschrift, waarbij we computermodellen willen gebruiken om de tumordosis te voorspellen en preoperatief, niet-invasief en betrouwbaar de geschiktheid van specifieke injectiecondities te beoordelen. **Hoofdstuk 3** begint met een overzicht van verschillende modeltypen die worden gebruikt in de context van transarteriële therapieën, van complexe vloeistof-structuur interactiemodellen via computationele vloeistofdynamica (CFD) tot 0D-modellen. Momenteel wordt vooral CFD gebruikt en hebben meerdere CFD-studies al inzicht gegeven in de invloed van klinische injectieparameters, zoals injectiepositie (in het vlak), axiale injectiepositie, katheterrichting, kathetertype, injectiesnelheid en microsfeertype. Deze studies hebben echter hun beperkingen. Zo werden de eerste CFD-analyses vooral uitgevoerd in vereenvoudigde, vlakke geometrieën. Hoewel de aandacht is verschoven naar CFD-analyse van patiënt-specifieke geometrieën, die veel realistischer zijn, zijn ze rekenkundig ook complexer en moet de computationele aanpak mogelijk worden vereenvoudigd. Daarnaast gedragen CFD-modellen zich ook anders dan systemen in de fysieke wereld, wat van cruciaal belang is bij het beoordelen van de betrouwbaarheid van deze modellen. Typisch bepalen drie belangrijke principes de betrouwbaarheid van een computermodel: (1) verificatie, (2) validatie en (3) onzekerheidsanalyse (VVUQ). Op vlak van validatie is in vitro validatie alleen uitgevoerd op vereenvoudigde, vlakke geometrieën. Daarnaast is in vivo validatie is ook zeer beperkt in de literatuur. Bovendien ontbrak het in dit domein ook aan onzekerheidsen gevoeligheidsanalyse van een breed scala aan klinische en numerieke parameters. Tot nu toe werden slechts variaties van 2 parameters tegelijkertijd beschouwd in 1 patiënt-specifieke geometrie. Ook hier is de computationele kost van een computermodel een belangrijke beperkende factor.

Met het oog op het bovenstaande willen we in dit proefschrift deze beperkingen in de huidige stand van zaken aanpakken door (1) effectieve strategieën te ontwikkelen om de computationele kosten van patiënt-specifieke 3D CFD simulaties betrouwbaar te verlagen (focus van Deel II), (2) technieken voor onzekerheidsanalyse van numerieke en klinische parameters in patiënt-specifieke geometrieën te ontwikkelen (focus van Deel III), (3) validatietechnieken in patiënt-specifieke geometrieën te ontwikkelen (focus van Deel IV), en (4) een workflow te ontwikkelen voor pre-operatieve optimalisatie van de uitvoering van transarteriële therapieën, rekening houdend met (maar niet beperkt tot) de tumordosis zoals berekend met CFD (focus van Deel V).

Deel II: Vereenvoudigingsstrategieën voor CFD-modellen van transarteriële therapieën bestaat uit **Hoofdstukken 4, 5 en 6**. Het doel is om betrouwbare vereenvoudigingsstrategieën te ontwikkelen en te evalueren voor onze CFD-modellen van transarteriële therapieën om zo de totale rekenkost te verlagen. In **Hoofdstuk 4** wordt het hybride microsfeer-stromingsmodel geïntroduceerd als het resultaat van een nieuw truncatie-algoritme voor de stroomafwaartse vaten. De oorspronkelijke patiënt-specifieke arteriële geometrie van de lever (Geometrie 1, met 48 uitlaten) werd op matig en ernstig niveau getrunceerd, wat resulteerde in twee extra arteriële vaatbomen: Geometrie 2 (38 uitlaten) en Geometrie 3 (17 uitlaten). In elke geometrie werden 1 planaire injectie en 3 katheterinjecties gesimuleerd, met de axiale injectielocatie in de arteria hepatica propria (PHA) (voor de eerste bifurcatie). Voor de getrunceerde geometrieën werd aangenomen dat de microsferen zich stroomafwaarts van de getrunceerde uitlaten evenredig met de bloedstroom verspreidden (hybride microsfeer-stromingsmodel). Voor de vlakke injecties was het mediane verschil in uitlaat-specifieke microsfeerverdeling tussen Geometrie 1 en 2 0,0442% en 0,211% tussen Geometrie 1 en 3, wat duidelijk de invloed van truncatie aangeeft. Bij bestudering van de 3 katheterinjecties was het maximale (van alle 3 injecties) mediane verschil in microsfeerverdeling tussen Geometrie 1 en 2 0,0647% en 0,240% tussen Geometrie 1 en 3, wat opnieuw de invloed van trunceren aantoont. Met deze beperkte verschillen gaven de resultaten echter aan dat de arteriële boom in de lever tot op ernstig niveau kan worden getrunceerd. Interessant genoeg was het gebruik van alleen de stromingsdistributie als surrogaatmodel voor de microsfeerverdeling in de gehele arteriële vaatboom aanzienlijk minder nauwkeurig dan het gebruik van het hybride model, met maximale uitstroom-specifieke verschillen van 6% (die aanzienlijk hoger waren dan de maxima voor de katheterinjecties (3,5%) en voor de planaire injectie (2%)).

In **Hoofdstuk 5** wordt het hybride microsfeer-stromingsmodel met dezelfde niveaus van matige en ernstige truncatie geverifieerd voor selectieve injectie in de rechter- en linkertakken van de arteria hepatica propria (na de eerste bifurcatie). Stroomopwaartse truncatie wordt ook onderzocht, met truncatielengtes van 20-80 mm voor de katheterpunt. Ernstige truncatie gaf maximale verschillen in microsfeerverdeling van 4-11% en 8-9% voor respectievelijk stroomafwaarts en stroomopwaarts trunceren. Voor matige truncatie waren deze verschillen slechts 1-1,5% en 0,5-2%, wat aangeeft dat ernstige truncatie bij selectievere injectie veel minder betrouwbaar is dan bij oppervlakkige injectie. Bovendien werd in elke simulatie de verspreiding van de microsferen in de doorsnede gekwantificeerd voor 5-6 doorsneden tussen de katheterpunt en de uitlaten. Rekening houdend met alle microsferen nam de spreiding stroomafwaarts van de katheterpunt toe tot 80-90% van de volledige doorsnede. De verspreiding bleek echter veel lager te zijn op specifieke tijdstippen, wat duidt op een hoge tijdsafhankelijkheid van de verspreiding. Interessant is dat deze tijdsafhankelijke spreidingsmaten kunnen laten zien waar verschillen kunnen ontstaan tussen de bloedstroming en de microsferenverdeling, en of de overeenkomst tussen stromings- en microsferenverdeling in de toekomst kan verbeterd worden.

Uit deze twee hoofdstukken concluderen we dat het combineren van truncatie met het hybride microsfeer-stromingsmodel een effectieve methode is om de complexiteit van de modelleringsaanpak te verminderen, maar dat gematigde truncatie betrouwbaarder is dan ernstige truncatie (vooral voor selectieve injectie).

Vervolgens identificeren we in **Hoofdstuk 6** 5 vereenvoudigingsstrategieën: ernstige truncatie, aangevuld met modellering van constante stroming, matige en ernstige vereenvoudiging van het numerieke raster, en vermindering van het aantal stromingscycli. We evalueren of deze strategieën kunnen worden gebruikt om (1) de CFD-resultaten nauwkeurig te voorspellen (de microsfeerverdeling, zoals voorheen, en de tumordosis) en (2) de gevoeligheid van die resultaten tegenover een specifieke injectieparameter (injectiedebiet) te schatten. Voor zowel nauwkeurigheid als gevoeligheid bleek rastervereenvoudiging de meest betrouwbare vereenvoudigingsstrategie te zijn, die het mogelijk maakte de tumordosis te voorspellen met slechts een maximale afwijking van 1,4% en een vergelijkbare gevoeligheid (afwijking van 0,7%). De strategie die gebruik maakte van constante stroming presteerde het slechtst, met een maximale afwijking in de tumordosis van 20% en een verschil in gevoeligheid van 10%. Bovendien verminderde het vereenvoudigen van het raster de rekentijd met ongeveer 45%.

Uit **Hoofdstukken 4, 5 en 6** concluderen we dat gematigde truncatie van de stroomafwaartse vaten (in combinatie met het hybride microsfeer-stromingsmodel) de meest betrouwbare strategie is als de nadruk ligt op nauwkeurigheid. Als de focus ligt op gevoeligheid, dan is rastervereenvoudiging ook een acceptabele optie waarmee de rekentijd aanzienlijk verkort kan worden. Maar om onzekerheidskwantificatie en globale gevoeligheidsanalyse mogelijk te maken (waarvoor vaak honderden of duizenden simulaties nodig zijn), hebben we nieuwe strategieën nodig om de rekenkosten nog verder te verlagen. Dit is de focus van Deel III.

Deel III: Onzekerheidsanalyse van klinische en numerieke parameters bestaat uit **Hoofdstukken 7 en 8**. Het doel van dit deel is om de onzekerheid te kwantificeren op de voorspelling van de tumordosis als gevolg van onbekende positie van de katheterpunt en onbekende randvoorwaarden. In **Hoofdstuk 7** kwantificeerden we de onzekerheid op de tumordosis veroorzaakt door de oncontroleerbare locatie van de katheterpunt in het vlak. Om soortgelijke simulaties goedkoop te kunnen herhalen, gebruikten we een vereenvoudigd CFD-model, waarbij een katheterinjectie werd nagebootst door een vlakke injectie te simuleren en te berekenen welke afgifteposities binnen de axiale doorsnede leidden naar de tumor (lage fidelity-aanpak). Door vervolgens 100 willekeurige posities voor de katheterpunt in de axiale doorsnede na te bootsen, werd het tumordosisbereik als gevolg van een onbekende (of oncontroleerbare) positie van de katheterpunt berekend, met een totale variatie van 15%. Hoewel deze nieuwe lage fidelity-aanpak het mogelijk maakte om de onzekerheid in de tumordosis te kwantificeren, is de strategie om het CFD-model te vereenvoudigen door een vlakke injectie slechts beperkt toepasbaar, en moeten we op zoek naar een breder toepasbare vereenvoudigingsstrategieën.

Daarom bouwen we in **Hoofdstuk 8** een surrogaat Gaussiaans proces regressiemodel (GPR) dat is gefit op een minimaal aantal 3D CFD simulaties van microsfeertransport om eenvoudige onzekerheids- en gevoeligheidsanalyses uit te voeren. Als voorbeeldcasus bepaalden we de gevoeligheid van de tumordosis tegenover de vorm van de stroomsnelheidsgolf aan de inlaat van de arteria hepatica propria. We definieerden onze 3D-inputruimte door drie vormparameters uit onze stroomsnelheidsgolf te extraheren (systolische piekdebiet, hartslag, systolische duur) en deze 3 parameters te variëren binnen 75-125% van de nominale waarden. Om ons surrogaatmodel goedkoop te kunnen fitten, ontwikkelden we een algoritme dat werkt met een adaptieve statistische onderzoeksplanning (ADOE). Aanvankelijk werden 100 punten in de 3D inputruimte bepaald door de initiële statistische onderzoeksplanning (DOE) te definiëren aan de hand van Latin hypercube sampling. Op basis van deze DOE gebruikten we de huidige GPR om de gevoeligheidsindices van elke input parameter in te schatten met de variantie-gebaseerde methode van Sobol. Vervolgens bepaalden we in elk van de 27 equivolume bins die onze 3D inputruimte verdelen, de meest onzekere voorspellingen van de huidige GPR, berekenden we hun werkelijke waarden met CFD en voegden we deze punten toe aan de DOE. We gingen door met het toevoegen van reeksen van 27 punten aan de DOE totdat de Sobol-indices gestabiliseerd waren. We testten ons ADOE-algoritme op de voorbeeldfunctie van Ishigami en toonden aan dat we betrouwbaar Sobol-indices kunnen verkrijgen met een absolute fout <0,1 (wat voldoende was voor onze doeleinden). Tot slot, bij het toepassen van ADOE op onze stroomsnelheidsgolf, vonden we de eerste-orde gevoeligheidsindices na 181 CFD simulaties (initiële DOE van 100): 0,0550 voor het systolisch debiet, 0,0191 voor de hartslag, en 0,407 voor de systolische duur. Dit toonde aan dat we de onzekerheid op de voorspelling van de tumordosis het meest kunnen verminderen door de duur van de systole nauwkeurig te meten. De ADOE maakt dus een betrouwbare gevoeligheidsanalyse mogelijk met een relatief beperkt aantal complexe modelevaluaties, die we kunnen gebruiken om de numerieke inputparameters met de grootste impact te identificeren om ons model te diagnosticeren. We kunnen ze ook gebruiken om de belangrijkste klinische parameters voor pre-operatieve optimalisatie te identificeren.

Naast onzekerheidsanalyse is validatie het laatste, belangrijke principe van VVUQ. **Deel IV: Validatie** bestaat uit **Hoofdstuk 9**, waar we focussen op in vitro validatie. Het doel is om de haalbaarheid van patiënt-specifieke in vitro validatie te illustreren, wat een aanzienlijke vooruitgang is ten opzichte van de algemene, vlakke geometrieën die in de literatuur worden gebruikt. In **Hoofdstuk 9** werd een in vitro opstelling gebouwd door middel van een experimenteel stromingscircuit waarin een 3D-print van een patiënt-specifieke arteriële levergeometrie werd gemonteerd. Water stroomde van een verhoogd reservoir door de 3D-print naar beneden, naar verbindingsbuizen van polyvinylchloride (PVC) met instelbare weerstanden die naar 10 verzamelreservoirs leidden. De uitstroom naar elk reservoir werd handmatig ingesteld door iteratief de weerstanden ter hoogte van de PVC-buizen aan te passen totdat alle uitstromen overeenkwamen met de randvoorwaarden opgelegd in het computermodel ($< 5\%$ foutmarge). Niet-radioactieve SIR-sferen werden geïnjecteerd en de verdeling over de 10 reservoirs werd berekend door het microsfeer-watermengsel van het reservoir te filteren en het toegevoegd gewicht van de microsferen te meten. De grote overeenkomst tussen de experimentele en theoretische stroomverdeling (gemiddeld 0,407% verschil per reservoir) toonde aan dat de implementatie van de uitlaatstromen door het afstemmen van de weerstanden succesvol was. Bovendien was het gemiddelde verschil voor een reservoir tussen de numerieke en experimentele microsfeerverdeling 2,73% (minimum: 0,394% - maximum: 6,47%) en 2,97% (minimum: 1,21% - maximum: 6,17%) voor de 2 uitgevoerde injecties. Deze in vitro validatieopstelling bevestigde dat de stromingsverdeling verre van een perfecte surrogaat was voor de microsfeerverdeling. Terwijl we in dit hoofdstuk de mogelijkheid illustreerden om een in vitro opstelling te ontwikkelen met een patiënt-specifieke arteriële geometrie en patiënt-geïnspireerde randvoorwaarden, concluderen we dat de huidige opstelling nog verbeterd zal moeten worden door o.a. robuustere meetmethoden voor de microsfeerverdeling te ontwikkelen.

Ten laatste introduceren we een workflow voor de pre-operatieve planningstool, rekening houdend met de eerder geïllustreerde onzekerheid op de voorspelling van de tumordosis. **Deel V: Valorisatie** bestaat uit **Hoofdstuk 10**. In **Hoofdstuk 10** ontwikkelden we een workflow voor het plannen van de behandeling dat niet alleen rekening hield met het tumordosisbereik, maar ook met de afweging tussen doelspecificiteit (hoger voor selectieve injectie) en vasculaire toegankelijkheid (doorgaans moeilijker voor selectieve injectie). In een patiënt-specifieke casus identificeerden we vier relevante injectielocaties om te vergelijken met behulp van de workflow:

oppervlakkig in de arteria hepatica propria (in de PHA), selectief in de rechtertak van de PHA (RHA), selectief in de linkertak van de PHA (LHA), en superselectief in de RHA, die het grootste deel van het tumorweefsel doorbloedt. Een tumorbedekking van 100% werd alleen bereikt bij injectie van PHA aan de oppervlakte. Wat toegankelijkheid betreft, was zelfs voor de meest distale injectielocaties (selectieve LHA-injectie en superselectieve RHA-injectie) de diameter nog steeds >4 mm en werd deze dus niet als beperkende factor beschouwd. Selectieve injectie in de LHA had de laagste toegankelijkheid, met hoge tortuositeit en kromming vanwege de bocht na de eerste bifurcatie. Wat betreft de tumordosisbereiken voor alle scenario's waren de minima relatief constant (d.w.z. binnen het bereik van 25,7-38,6%), maar de maxima varieerden aanzienlijk tussen 50,5-81,9%, waarbij het maximum werd bereikt voor superselectieve injectie in RHA. Door alle beslissingscriteria in onze workflow te combineren, leek selectieve RHA-injectie het meest optimaal, met een hoge tumordekking (69,6%), een vergelijkbare mediane tumordosis vergeleken met andere scenario's (48,7%) en een hoge toegankelijkheid.

Tot slot, in **Deel VI: Conclusies**, dat bestaat uit **Hoofdstuk 11**, worden limitaties van de computationele aanpak, zoals de modellering van de katheter als dunwandig en de kathetervloeistof als bloed, eerst besproken. Vervolgens herhalen we de belangrijkste resultaten. Deze omvatten (1) de introductie van het hybride microsfeerstromingsmodel als een betrouwbare vereenvoudigingsstrategie voor nauwkeurigheidsdoeleinden, (2) het identificeren van rastervereenvoudiging als de optimale strategie voor vereenvoudiging voor gevoeligheidsdoeleinden, (3) het omzetten van tumordosiswaarden in tumordosisbereiken gegeven onzekere klinische parameters, zoals de positie van de katheterpunt, (4) het aantonen dat specifieke surrogaatmodellen kunnen helpen bij het verminderen van de computationele complexiteit van het uitvoeren van gevoeligheidsanalyses, (5) gebruik van een patiënt-specifiek in vitro stromingscircuit om belangrijke verschillen tussen stroming en microsfeerdistributie te kwantificeren, en (6) het ontwikkelen van een multi-objectief preoperatieve workflow, dat de tumordosis maximaliseert onder specifieke beperkingen, zoals beperkte vasculaire toegang. Vervolgens wordt toekomstig werk voorgesteld dat voortbouwt op onze resultaten. Naast het verifiëren van de huidige resultaten voor meer patiënt-specifieke geometrieën, stellen we voor om ons meer te richten op in vivo validatie met behulp van SPECT- en PET-CT-scans, de huidige in vitro validatiemethoden voornamelijk te gebruiken voor het testen van nieuwe kathetertypen, de huidige technieken voor het kwantificeren van onzekerheden uit te breiden naar een grotere en meer diverse verzameling parameters, en onze nieuwe spreidingsmaten te gebruiken om te onderzoeken of nieuwe kathetertypen de overeenkomst tussen microsfeer- en stromingsverdeling kunnen bevorderen. Tot slot geven we advies over de toekomstige stappen die waarschijnlijk genomen moeten worden om deze CFD-simulaties naar klinische toepassing te brengen. We stellen voor om te simuleren tot op gezondheidseindepunten (zoals de radioactieve dosis geleverd aan de tumor, die kan worden gemeten met in vivo beeldvorming), de variabiliteit tussen personen te kwantificeren om te bepalen onder welke omstandigheden patiënt-specifieke geometrieën moeten worden gebruikt, en deep learning of andere surrogaatmodellen te gebruiken om (bijna) real-time voorspellingen mogelijk te maken.

Als laatste nota van dit proefschrift merken we op dat studies op dit gebied zich hebben gericht op twee methoden om de gezondheidsuitkomsten van transarteriële therapieën te verbeteren: (1) door de injectiecondities te optimaliseren en deze vervolgens peri-operatief streng te controleren (*school van controle*), of (2) door vermenging van de microsferen met het bloed te bevorderen om de impact van deze injectiecondities te verminderen (*school van menging*). In dit proefschrift wordt gesteld dat, hoewel we niet kunnen weten welke strategie in de toekomst optimaal zal blijken te zijn, beide strategieën voordelen hebben en gecombineerd zouden kunnen worden: aangezien strenge controle van alle injectieparameters wellicht technisch niet mogelijk is, zou het rekening houden met onzekere tumordosisbereiken (zoals in dit proefschrift) cruciaal kunnen worden. Dit is waarschijnlijk de meest relevante ontwikkeling in dit werk. Als deze onzekerheidsbereiken echter te groot worden, kunnen de nieuwe spreidingsmaten die we hebben ontwikkeld, helpen identificeren of het bevorderen van afstemming tussen microsfeer- en stromingsverdeling een realistische strategie is om de grote impact van deze injectiecondities (en dus de grootte van het onzekerheidsbereik) te verminderen. We benoemen deze combinatiestrategie als een nieuwe, derde methode om gezondheidsuitkomsten te verbeteren: (3) wegens gebrek aan total controle van injectiecondities, trachten we zoveel mogelijk de heersende onzekerheden in kaart te brengen (onzekerheidsanalyse), en kunnen we bijvoorbeeld nieuwe kathetertypes gebruiken om de grootte van onzekerheden te beperken (onzekerheidsvermindering). Deze nieuwe, derde aanpak kunnen we benoemen als de (*school van* *onzekerheidsanalyse en -vermindering*). In die zin kan onze preoperatieve workflow voor het optimaliseren van injectiecondities onder heersende onzekerheden een goed uitgangspunt zijn voor toekomstige inspanningen.

Chapter 1

Introduction

1.1 Clinical rationale

Hepatocellular carcinoma, the most common form of primary liver cancer, is one of highest-mortality cancers worldwide with an expected incidence of over 1 million people by 2030 [1, 2]. At its intermediate stage, transarterial therapies such as transarterial radioembolization (TARE) and transarterial chemoembolization (TACE) are typically considered as the primary choices of treatment [3]. During TARE, a microcatheter is inserted via the femoral artery and advanced retrogradely to the hepatic arteries perfusing both the healthy liver parenchyma and the tumor(s) [4]. There, radioactive microparticles are infused to selectively embolize the tumor tissue. Usually, a low-dose pre-treatment injection is done to assess the intra- and extrahepatic radioactivity spread, and the suitability of the current injection conditions [5].

However, TARE is associated with a high variability in execution, and highly fluctuating clinical outcomes [6, 7]. For example, the impact of variable clinical parameters (such as catheter type, microcatheter position, microcatheter tip orientation, etc.) on the tumor dose is poorly understood. Additionally, these parameters can still vary between the treatment and the pre-treatment used to assess tumor dose efficacy, which makes pre-treatment a unreliable tumor dose predictor [8]. Furthermore, aside from axial injection location, the current pre-treatment method does not allow to extensively tune other impactful injection parameters to patient-specific conditions. Hence, we want to investigate the possibility of using computational fluid dynamics (CFD) simulations as a virtual pre-treatment mock-up of the treatment, which would offer a completely noninvasive solution and allow extensive iterative finetuning of clinical parameters before the actual physical intervention, with the ultimate goal of maximizing the tumor dose and minimizing the spread of radioactivity to the surrounding healthy tissue.

1.2 STATE-OF-THE-ART AND OBJECTIVES

Numerical models are being increasingly used in healthcare for medical device design and pre-treatment planning. Importantly, they can be used to elucidate the impact of clinical injection parameters on the treatment outcome for both TACE and TARE [9]. Multiple computational fluid dynamics (CFD) studies have focused on this, showing among others the high impact of axial and cross-sectional injection location, injection flow rate and catheter type [10–14].

In the past, these CFD studies have mainly focused on parameter analysis in simplified geometries [12–14]. While the focus has shifted to more realistic patient-specific geometries [10, 11, 15], these geometries make the computational approach more complex. This decreases the feasibility of using these CFD analyses in daily clinical practice. Hence, reliable simplification strategies for these patient-specific 3D CFD models are needed. Additionally, global uncertainty quantification and sensitivity analysis for a wide range of input parameters has also not been performed for CFD models of TARE. This is especially relevant, as both uncertain or controllable clinical parameters (e.g. cross-sectional catheter tip position) and uncertain numerical parameters (e.g. boundary conditions) will introduce uncertainty on the output (e.g. tumor dose). However, uncertainty quantification and sensitivity analysis typically require a high number of simulations, which even further stresses the need to devise reliable simplification strategies.

Furthermore, patient-specific in vivo validation of a wide range of patients is currently lacking [16], and will be needed to translate these models to clinical practice. Additionally, experimental in vitro studies have focused on replicating CFD results in simplified geometries, but not in patient-specific geometries [13, 17]. While in vitro validation might be a powerful investigative tool, these methods have not been translated yet to a patient-specific setting.

Finally, while Kleinstreuer et al. [12] already suggested to use CFD simulation based on medical images in a pre-operative tool, they did not yet develop a specific design for this tool. Importantly, tumor dose is not the only parameter to consider in such a tool, since vascular accessibility of the tumor-feeding arteries might also be a limiting factor. Additionally, some clinical parameters might not be entirely controllable, which might introduce uncertainty on the predicted output. Hence, there is currently a lack of a specific workflow for a therapy planning tool that considers both dose maximization, cost minimization and output uncertainty.

Based on the state-of-the-art as explained above, this PhD dissertation will focus on:

- the development of patient-specific 3D CFD models of transarterial drug delivery,
- the implementation of reliable simplification strategies to accurately predict tumor dose,
- quantifying the uncertainty introduced by, and sensitivity towards, both clinical and numerical model parameters,
- the development of patient-specific validation techniques, and
- a workflow for the pre-operative planning tool.

1.3 Structure

The structure of this PhD dissertation is divided in six major parts:

- **Part I - Clinical Rationale and State-of-the-Art in Modeling of Transarterial Therapies**. Part I explains the clinical context of the dissertation, showing how hepatocellular carcinoma is one of the highest-mortality cancers worldwide, but that transarterial therapies used at its intermediate stage suffer from variable outcomes and an unclear impact of injection conditions. Furthermore, the role of modeling in healthcare and therapy planning is explained, outlining how a virtual pretreatment planning tool could help to quantify the impact of clinical injection parameters on the treatment outcome, and optimize the treatment outcome accordingly. An overview of the current models (mostly computational fluid dynamics models) already used to study transarterial therapies is given. The state-of-the-art of CFD models will lead to the motivation of the thesis objectives.

- **Part II - Simplification Strategies for CFD Modeling of Transarterial Therapies**: In Part II, effective strategies to reduce the computational cost of patient-specific 3D CFD models are discussed. First, this is done by developing and verifying the hybrid particle-flow model, which reduces the size of the hepatic arterial tree but still aims to predict intrasegmental particle distribution. This hybrid model will be verified for both realistic superficial and selective injection scenarios. Additionally, more simplification strategies, such as coarsening of the grid and reducing the number of flow cycles, are evaluated, as well as the possibility of more severe simplification when the focus is on uncertainty quantification and sensitivity rather than accuracy.

- **Part III - Uncertainty Quantification of Clinical and Numerical Parameters**: Part III will show how we can use patient-specific 3D CFD models and the simplification strategies from Part II to quantify the uncertainty on the tumor dose caused by uncertain input parameters. First, a low fidelity modeling approach will be used to quantify the uncertainty on the tumor dose induced by an uncertain cross-sectional injection position. Second, a surrogate Gaussian Process Regression model will be used to quantify the sensitivity of the model towards specific shape parameters of the input waveform.

- **Part IV - Validation**: Part IV illustrates the development of a patient-specific in vitro validation technique, where a 3D-print of a patient-specific hepatic arterial geometry is integrated in a flow circuit. This set-up is used to underline the difference between flow and particle distribution, and paves the way towards future validation efforts.

- **Part V - Valorization**: Part V illustrates how CFD simulations can be integrated into a pretreatment planning workflow for TARE, considering the uncertainty on the tumor dose prediction, as well as quantifying vascular accessibility of specific injection locations.

- **Part VI - Conclusions**: Part VI overviews the key results of this dissertation, and discusses avenues for future work. Finally, we situate the current work in the state-of-the-art, showing how the work builds an important bridge between concurrent strategies for transarterial treatment optimization.

1.4 LIST OF PEER-REVIEWED PUBLICATIONS

Accepted and published papers as first author

- T. Bomberna, G. Adeli Koudehi, C. Claerebout, C. Verslype, G. Maleux, and C. Debbaut. Transarterial drug delivery for liver cancer: numerical simulations and experimental validation of particle distribution in patient-specific livers. Expert Opinion on Drug Delivery, 2021, doi:10.1080/17425247.2021.1853702 [18].
- T. Bomberna, S. Vermijs, M. Lejoly, C. Verslype, L. Bonne, G. Maleux and C. Debbaut. A hybrid particle-flow CFD modeling approach in truncated hepatic arterial trees for liver radioembolization: a patient-specific case study. Frontiers in Bioengineering and Biotechnology, 2022, doi:10.3389/fbioe.2022.914979 [19].
- T. Bomberna, S. Vermijs, L. Bonne, C. Verslype, G. Maleux, C. Debbaut, Spatiotemporal Analysis of Particle Spread To Assess The Hybrid Particle-Flow CFD Model of Radioembolization of HCC Tumors. IEEE Transactions on Biomedical Engineering, 2023, doi: 10.1109/TBME.2023.3331085 [20].
- T. Bomberna, G. Maleux, and C. Debbaut. Simplification strategies for patient-specific CFD models of drug transport during liver radioembolization. Computers in Biology and Medicine, 2024, doi: 10.1016/j.compbiomed.2024.108732 [21].
- T. Bomberna, G. Maleux, and C. Debbaut. Adaptive Design of Experiments to Fit Surrogate Gaussian Process Regression Models Allows Fast Sensitivity Analysis of the Input Waveform for Patient-Specific 3D CFD Models of Liver Radioembolization. Computer Methods and Programs in Biomedicine, 2024, doi: 10.1016/j.cmpb.2024.108234 [22].

Published book chapters as first author

- C. Debbaut and T. Bomberna, Numerical modelling in support of locoregional drug delivery during transarterial therapies for liver cancer, in Modelling of mass transport processes in biological media, S. Becker, A. Kuznetsov, G. Pontrelli, D. Zhao, and F. de Monte, Eds. Elsevier, 2022 [23] (shared first).

Accepted and published papers as co-author

- I. P. Dimov, C. Tous, N. Li, M. Barat, T. Bomberna, C. Debbaut, N. Jin, G. Moran, A. Tang and G. Soulez. Assessment of hepatic arterial hemodynamics with 4D flow MRI: in vitro analysis of motion and spatial resolution related error and in vivo feasibility study in 20 volunteers. European Radiology, 2022, doi: 10.1007/s00330-022-08890-5 [24].

I

Clinical Rationale and State-of-the-Art in Modeling of Transarterial Therapies

Chapters

CHAPTER 2

Clinical Rationale

In this chapter, the clinical rationale for this PhD dissertation is motivated. First, a brief overview is given of the liver function and liver anatomy, with a special focus on the functional segmental anatomy of the liver and the anatomy of the hepatic arterial vasculature, due to their high relevancy in this dissertation. Second, the epidemiology, risk factors and prevention, diagnosis and treatment options of hepatocellular carcinoma (HCC), the most common form of primary liver cancer, is discussed. Third, we zoom in on transarterial chemo- and radioembolization procedures, which are typically the treatments of choice at the intermediate, unresectable stage of HCC. We discuss their methods of action, but also the current challenges with transarterial drug delivery, which will lead us to the clinical rationale and motivation for this dissertation.

This chapter is partly based on the book chapter *Numerical modelling in support of locoregional drug delivery during transarterial therapies for liver cancer* from the book *Modelling of mass transport processes in biological media* (C. Debbaut and T. Bomberna, Elsevier, 2022) [23] and the Master thesis dissertation *Targeted drug delivery for liver cancer: modelling the impact of cancer burden on the particle distribution in a patient-specific cirrhotic liver* (T. Bomberna, UGent, 2019) [25].

2.1 LIVER FUNCTION AND ANATOMY

The liver is the largest organ in the body and makes up around 2.5% of the body weight [26]. Crucially, the liver carries out important bodily functions such as maintaining homeostasis, detoxification, glucose synthesis and storage, hormone metabolism, support of the immune system, etc. [27]. In this section, a short overview of the healthy liver microanatomy, macroanatomy and vascular supply is given. Special attention is spent on the hepatic arterial anatomy due to its relevance in this dissertation.

2.1.1 Vascular Supply

The liver has a double afferent blood supply: the hepatic artery carries high-pressure, oxygen-rich arterial blood to the liver, while the portal vein carries low-pressure nutrient-rich venous blood to the liver [28, 29]. Normally, blood flow to the liver is about 20-25% of the cardiac output (1–2 L/min) [29, 30]. In healthy liver parenchyma, roughly 25% of the blood supply comes from the hepatic arteries, while the remainder comes from the portal vein [31]. In cirrhotic livers, distinct changes in the microvasculature result in portal hypertension, reducing flow through the portal vein [28, 32]. However, with decreased portal venous flow, the hepatic arterial blood flow can act as a buffer and increase, which is known as the hepatic arterial buffer response [28, 33]. Blood drains from the liver via the efferent hepatic veins to the inferior vena cava [34].

Crucially, while healthy liver parenchyma has a double afferent blood supply, liver tumors are mostly fed with arterial blood. This allows selective targeting of liver tumors by injecting embolizing material in the arterial feeders of the tumor, whilst still allowing perfusion of the healthy parenchyma via the portal vein [35].

2.1.2 Microanatomy

The hepatocytes carry out most of the liver functions and make up most of the parenchymal volume [27, 36]. These hepatocytes are arranged in liver lobules, which are small functional units organized around the central hepatic veins [37]. As is shown in Figure 2.1, blood enters via branches of both the portal vein and hepatic arteries at the corners of each lobule, flows through the lobule via the sinusoids and is then drained from the liver via the central hepatic veins [38].

2.1.3 Segmental Anatomy

Anatomically, the liver consists of four lobes: two main lobes (the right and left lobe), and two additional lobes (the caudate lobe, re-

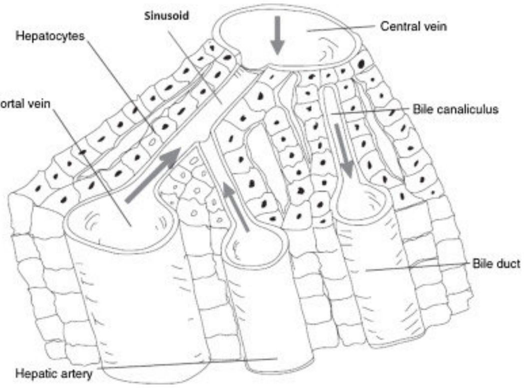

Figure 2.1: Blood from the portal vein and hepatic arteries mixes in the sinusoids, flowing to and draining in the central vein. From [39].

ferred to as Segment I below, and the quadrate lobe, referred to as Segment IV below) [40]. In the early 80s, Couinaud developed a functional division system which divides the liver into eight hepatic segments [41]. As can be seen in the schematic in Figure 2.2, the left lobe is divided in a medial section (which consists of Segment IV) and a lateral section (Segments II and III). The right lobe is divided in an anterior section (Segments V and VIII) and a posterior section (Segments VI and VII) [42]. Segment I is an independent segment.

Bismuth [43] reiterated the relevance of specific vascular structures (the hepatic veins and portal vein bifurcation) to help identify the eight hepatic segments, as illustrated in Figure 2.3. The middle hepatic vein (indicated with a red line in Figure 2.3) divides the liver into its right and left lobes. The right hepatic vein (indicated with a green line in Figure 2.3) is considered as the division line between the anterior (Segments V, VIII) and posterior (Segments VI, VII) sections. The division of the left lobe into the lateral (Segments II, III) and medial (Segment IV) sections can be made by drawing a line (indicated in blue in Figure 2.3) from the confluence of the left hepatic vein and the middle hepatic vein at the inferior vena cava (abbreviated as IVC in Figure 2.3) to the falciform ligament (indicated in panels 5 and 6 of Figure 2.3). Furthermore, the plane passing through the portal vein bifurcation is used as the reference plane in the axial direction; segments located above the portal vein bifurcation are the superior Segments II, VII and VIII (and IV), while segments lying below the portal vein bifurcation are the inferior Segments III, V and VI (and IV).

While useful, Couinaud's classification system is not always adhered to. In the past four decades, a leap in imaging and other tech-

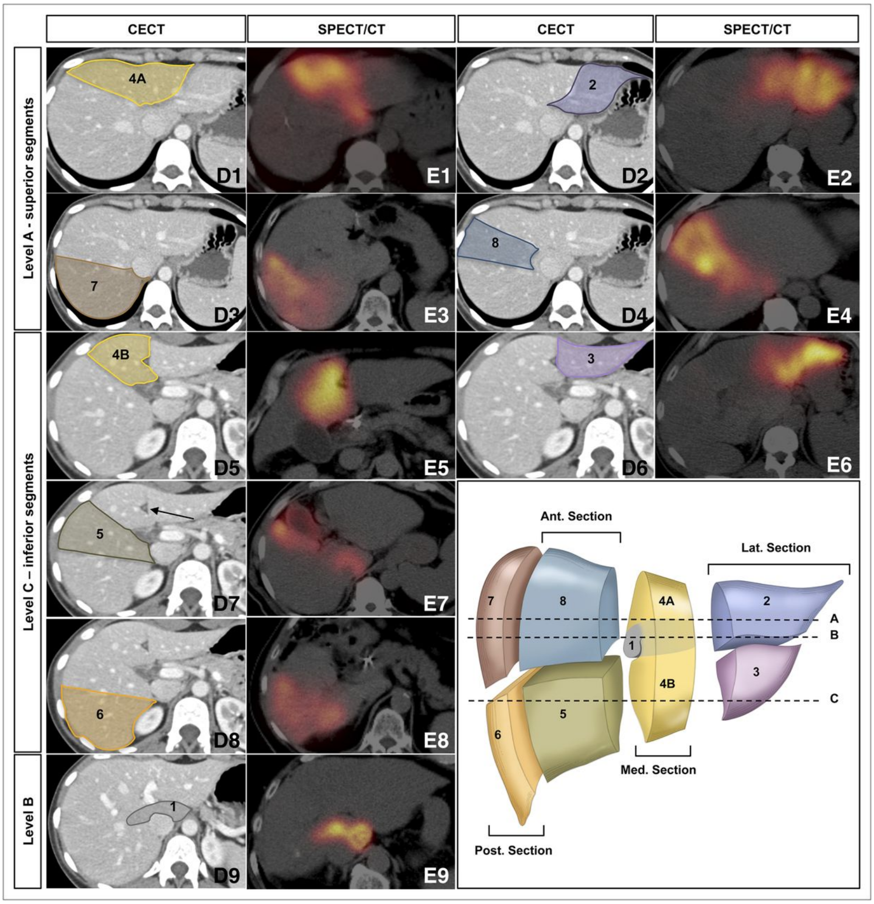

Figure 2.2: Segmental anatomy of the liver, with all 8 segments indicated on contrast-enhanced CT and SPECT-CT for 3 axial planes. A 3D reconstruction of the 8 hepatic segments and the location of the 3 axial planes is also given. From [42].

nological developments have lead to easier visualization of, easier access to, and easier interpretation of patient-specific anatomies, as well as increasingly changing patient populations that are being investigated and operated on (e.g. patients with more advanced disease) [44]. Unsurprisingly, this has led to increased findings of apparent inconsistencies and discrepancies with Couinaud's classification of the eight hepatic segments [45]. Of course, anatomic variability exists, but not all discrepancies can be explained this way [46]. Notably, Fasel et al. [46] found that on average 20 downstream portal vein vascular territories exist, instead of Couinaud's 8. Depending on the observer, these territories can be grouped in 8 or more segments [46] [47]. Hence, next to anatomic variability between patients, there is

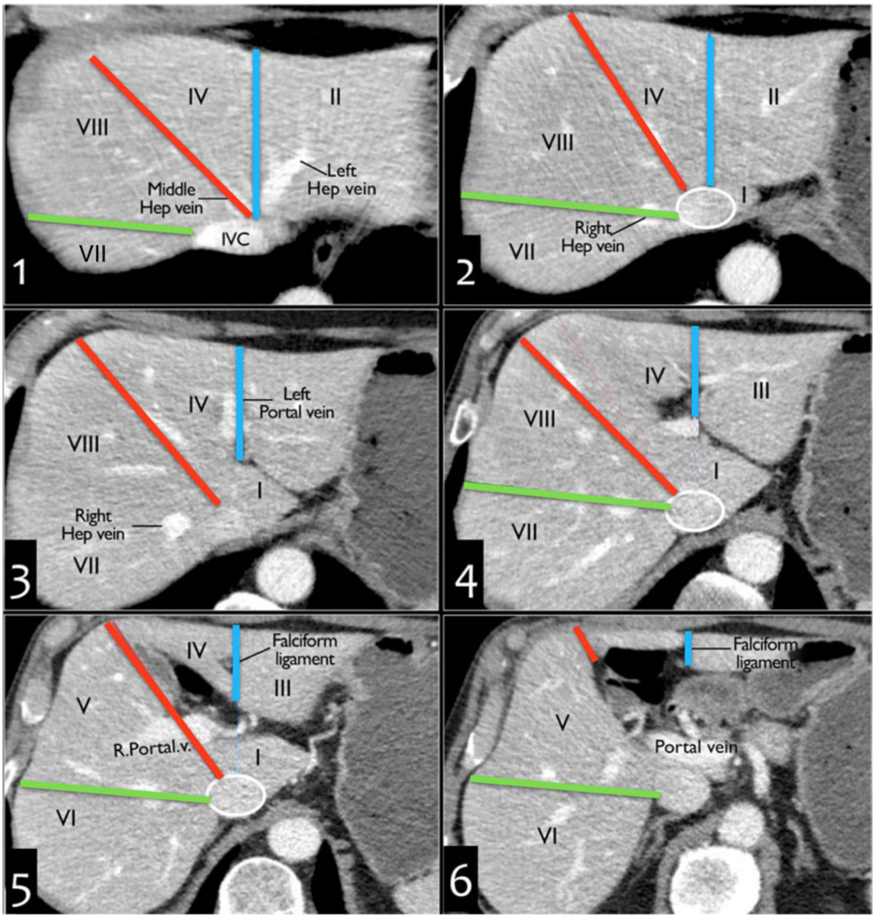

Figure 2.3: The middle hepatic vein (red line) divides the liver into the right and left lobe. The right hepatic vein (green line) divides the right lobe in its anterior and posterior section; the connection between the confluence of the inferior vena cava (IVC) and the left hepatic vein and the falciform ligament (blue line) divides the left lobe in its medial and lateral sections. From radiologyassistant.nl.

also an observer-dependent effect that does not necessarily contradict Couinaud's original classification, but indicates that Couinaud's system might be a general interpretation of a more complex reality [46].

2.1.4 Hepatic Arterial Anatomy

Knowledge of the normal hepatic arterial anatomy and its most common variants is important for transcatheter hepatic intervention, such as transarterial embolization. Hence, Michels [48] developed a classification system based on 200 cadavers, resulting in 10 types of hepatic arterial anatomies [49], that still serves as the standard [29]. The normal type (I), which occurs in approximately 55-75% of cases, consists of the common hepatic artery (CHA) branching off into the right and left hepatic artery (RHA, LHA), which perfuse the right and left lobe of the liver, respectively [29, 50]. As can be seen in a simplified visualization of the Michels Type I standard anatomy in Figure 2.4, the CHA itself originates from the celiac trunk (CT), which is a short vessel arising from the aorta. After the gastroduodenal artery (GDA) splits off from the CHA, the CHA is denoted as the proper hepatic artery (PHA), from which both the RHA and LHA emerge (in Michels Type I) [49]. Notably, in Type II and other variants of the Michels classification, the RHA and LHA can also emerge from other origins (not the PHA or CHA), such as the aorta or the superior mesenteric artery (SMA, which branches off the aorta), as either substitute or accessory vessels [31].

Inside the liver, the LHA and RHA branch into segmental arteries perfusing each hepatic segment. Typically, there also intercommunicating arcades present which still connect the LHA and RHA after the PHA bifurcation [42]. According to conventional vascularization, the LHA divides into the Segmental II artery and the Segmental III artery. In the right lobe, the RHA splits into a posterior and anterior branch. The posterior branch splits into a superior branch perfusing Segment VII and an inferior branch perfusing Segment VI, while the anterior branch splits into the superior branch perfusing Segment VIII, and an inferior branch perfusing Segment V (see Figure 2.2 for an indication of the location of the segments). As mentioned before, vascularization is subject to many anatomical variations occurring between patients [49]. Additionally, for the two additional lobes, Segment IV can be arterially fed from both the LHA or directly from the PHA. Segment I, also known as the caudate lobe, is an independent segment, and can be independently perfused by the RHA, LHA or both [49]. Even though the Michels classification is the most widely

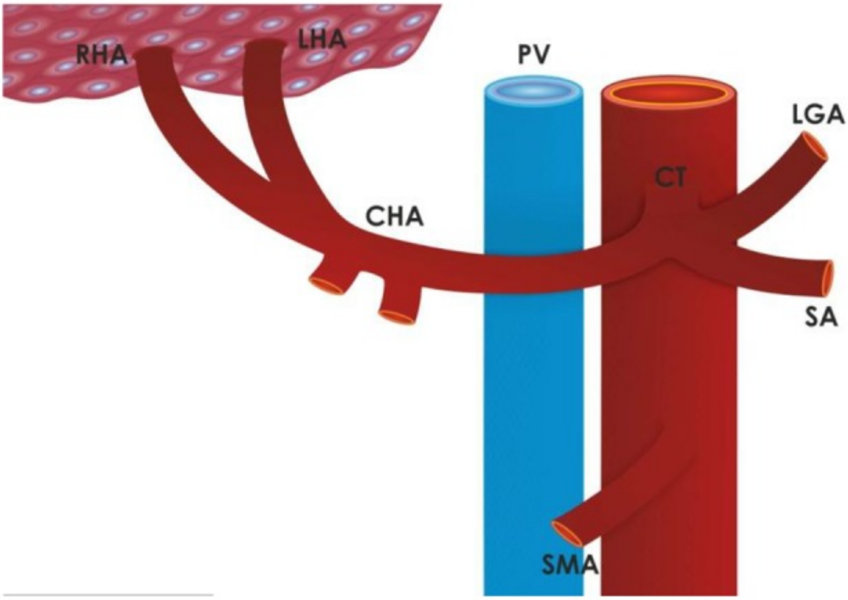

Figure 2.4: In the most standard hepatic arterial anatomy (Michels Type I), the common hepatic artery (CHA) emerges from the celiac artery or celiac trunk (CT). After the gastroduodenal artery splits off from the CHA (not indicated in the figure), the right hepatic artery (RHA) and left hepatic artery (LHA) emerge, perfusing the liver. The portal vein (PV) is also visible; the other vessels are less important here. From [50].

used, there are limitations, such as hepatic arteries showing varying courses or originating from rarer origins. For example, Chung et al. [51] reported aberrant right or left hepatic arteries (not included by Michels) in 15-16% of patients in a large cohort that underwent chemoembolization.

2.2 Liver Cancer

Global cancer incidence is expected to double by 2035, putting strain on healthcare systems and healthcare financing worldwide, and increasing the need for efficient and effective cancer care pathways [52]. HCC is the most common form of primary liver cancer and it is one of the leading causes of cancer-related deaths worldwide [2]. The World Health Organization estimates that by 2030, over 1 million people will die of liver cancer each year [1]. Alarmingly, HCC is also the fastest rising cause of cancer-related mortality [1].

2.2.1 Epidemiology of HCC

HCC occurs more in men than in women with a ratio that typically varies between 2 and 4 among populations [53]. As can be seen in Figure 2.5, in countries such as Vietnam, South Korea, Singapore, Portugal, Spain and France the ratio is remarkably high (even as high as 5 in Portugal) while, in countries such as Colombia, Mexico and Chile this ratio is much lower (well below 2, even as low as 1.1 in Colombia and Mexico). This discrepancy between genders is not well understood and may be attributed to several factors, such as hormones, epigenetics, immune response and sex-specific exposure to risk factors (e.g. smoking and excessive alcohol intake).

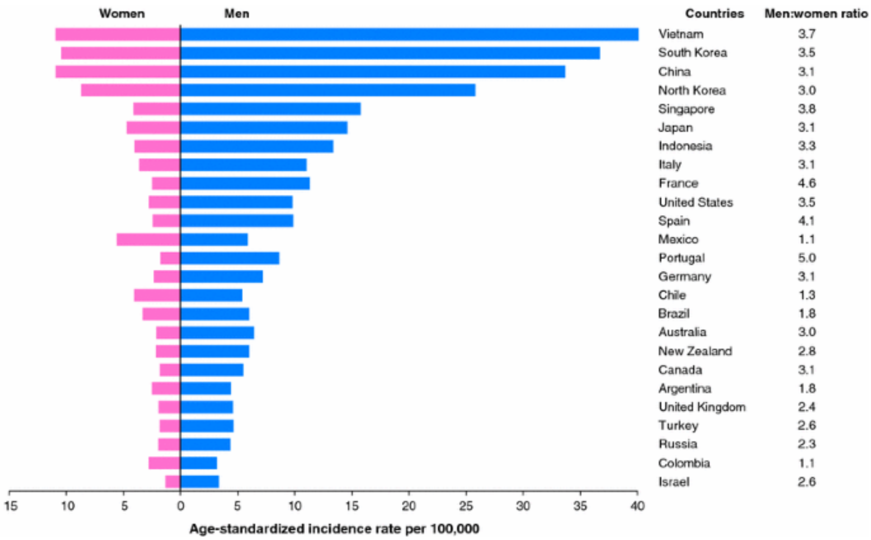

Figure 2.5: Age-adjusted incidence rate of HCC per 100,000 persons in 2012. Clearly, the incidence rate is much higher in men, and the men:woman incidence ratio fluctuates significantly between countries. From [1].

Figure 2.6 displays the worldwide age-adjusted incidence rates of liver cancer. There is a distinct geographical pattern visible [54]. Countries with the highest incidence are located in East and South-East Asia (e.g. China, South Korea, etc.) and Western and Central Africa (e.g. Senegal, Gambia, etc.) [55]. The incidence for China is notably high, while the incidence in Canada or Northern Europe is particularly low [2]. The geographic pattern displayed in Figure 2.6 matches the distribution of infection with the Hepatitis B Virus (HBV) and Hepatitis C Virus (HCV) around the world. A strong link exists between HCC and HBV and HCV infections since HCC regularly develops from the cirrhotic liver, which, in itself, can develop from hepatitis infection [1] (as discussed more in detail in Section 2.2.2).

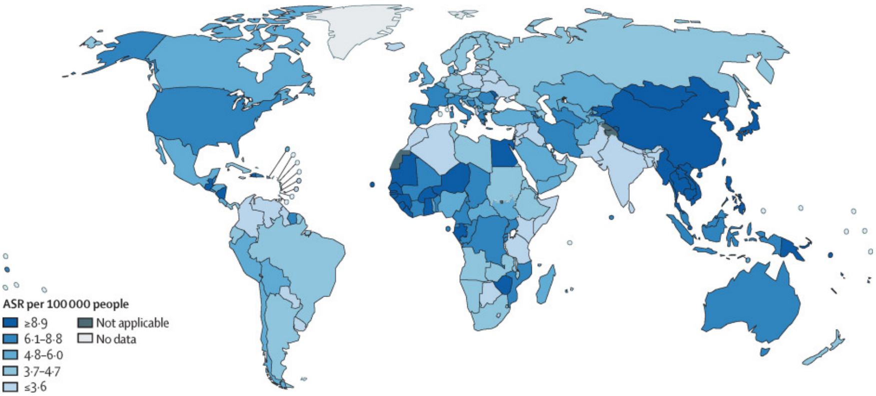

Figure 2.6: Age-standardized incidence rates for liver cancer per 100,000 persons in 2020. Incidence in (South-) East Asia and Western and Central Africa is high, while in Northern Europe, Canada and Oceania, it is particularly low. From [54].

2.2.2 Risk Factors and Prevention of HCC

The main risk factors associated with the onset of HCC are HBV infection, HCV infection, excessive alcohol intake, and non-alcoholic fatty liver disease (NAFLD) [56]. Factors such as HBV and HCV infection are expected to decrease because of widely promoted vaccination programs. However, incidence by the mycotoxin aflatoxin B1, a food carcinogenic found more often under warm and humid conditions [57], is expected to increase because of climate change [53]. In 80-90% of the cases, HCC develops from liver cirrhosis [1, 58]. Cirrhosis in itself can be caused by hepatitis infection, smoking, excessive alcohol abuse, etc. and then progress onward to HCC [2]. Prevention measures vary for each risk factor, as discussed below.

Although HBV infection accounts for about 50% of all reported HCC cases and steps have been made towards treating HBV infection as the global burden that it represents, full control over the infection is still unimaginable [3]. To that end, measures need to be implemented in all corners of society. On the one hand, the goal must be to increase global health and halt the virus from spreading. This can be done, for example, by the overall improvement of sanitation and living conditions and educating people about the risks of HBV. On the other hand, integration of the HBV vaccine into the global routine immunization program is necessary. Additionally, effective antiviral agents need to be introduced to treat HBV patients who are already in the chronic stage of the disease [59].

For HCV, infection is mainly caused by intravenous drug use and sexual transmission. Blood transfusion was a significant problem in the past, but this risk has been reduced by the introduction of anti-HCV testing in blood samples [60].

Chronic alcoholic liver disease (ALD) is, of all the risk factors mentioned in this section, probably the one that benefits most from public awareness programs. Especially in the Western world, excessive alcohol intake is a growing problem [60]. An accompanying issue is that patients who develop HCC from ALD are often diagnosed relatively late, because they are often unaware of the risks associated with high alcohol consumption (while patients with hepatitis infection tend to be diagnosed earlier on). The more the disease has progressed at the stage of diagnosis, the less likely chance of survival becomes [61].

For non-alcoholic fatty liver disease (NAFLD), obesity and diabetes are key influencing factors in the development into HCC. Therefore, physical exercise, strict diets and weight loss (surgery) are important prevention measures in these specific cases. Chemopreventive drugs are aimed at decreasing obesity-related inflammation and insulin resistance, but these are still under research [61].

2.2.3 Diagnosis of HCC

Clinical presentation for HCC varies from asymptomatic patients to patients displaying symptoms such as jaundice, weight loss, palpable mass, diarrhea, hepatic encephalopathy (impairment of consciousness), ascites, pain in the right upper quadrant [62]. Early diagnosis is important to increase survival chances. A guideline for the steps that need to be taken in order to timely and properly diagnose HCC is given in Figure 2.7 [63].

At a certain minimal size, lesions are generally hard to assess, particularly if they are less than 1 cm. For these small lesions, surveillance by ultrasound every three or six months is recommended to check whether the lesion is stable or enlarging [63, 64].

For lesions larger than 1 cm, the first attempt at a diagnosis is made with non-invasive imaging. The European Association for the Study of the Liver (EASL) guidelines indicate that the specificity of a positive diagnosis by imaging is lower in non-cirrhotic patients, because alternative diagnoses than hepatocellular carcinoma are seen

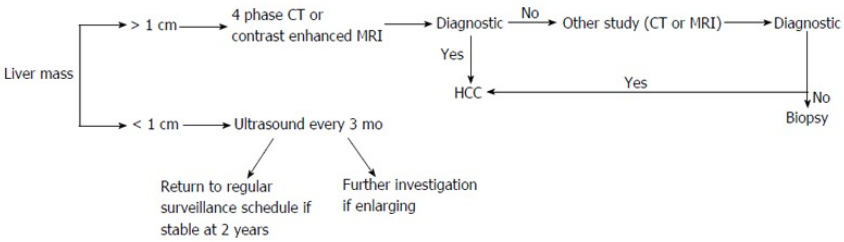

Figure 2.7: Diagnostic algorithm for HCC. For small lesions, regular ultrasound is recommended. For larger lesions, non-invasive imaging (CT, MRI) are typically used, and if they are not sufficient, an invasive biopsy can be considered. From [63].

more commonly [65]. Hence, in non-cirrhotic patients, a histological confirmation of the pathology is needed (see below). As for non-invasive imaging in cirrhotic patients, the two imaging modalities that are mostly used to diagnose HCC are four-phase CT contrast (unenhanced, arterial, venous and delayed phase) or dynamic contrast enhanced MRI [63, 65]. Since tumors are mainly fed by the arterial system, the presence of a tumor can be identified on each of these modalities by bright spots in the arterial phase, followed by washout of contrast in the delayed or venous phase. A typical example of a contrast MRI that confirms the presence of such a tumor is given in Figure 2.8 [66]. The advantages and disadvantages of these two modalities are well-known: while MRI provides the better contrast, it also more expensive and prone to artefacts than CT. Which modality is used for the first round of diagnosis, is up to the clinician. In the cases where one of these imaging modalities does not provide enough information for diagnosis, the other modality (CT/MRI) can be used.

If atypical features for the cancer are found, or if the CT/MRI studies give discordant findings, then an invasive liver biopsy must be performed to make a final diagnosis [63]. If the biopsy returns negative, then regular surveillance is opted to check any changes in the cancer. If the biopsy returns positive, then a fitting treatment based on the specific case must be considered.

2.2.4 Treatment Options for HCC

One of the most important factors in treating HCC is evaluating to what stage the cancer has developed. To this end, the Barcelona Clinical Liver Cancer (BCLC) staging system has been introduced, to quantify the prognosis of the disease and adapt the treatment

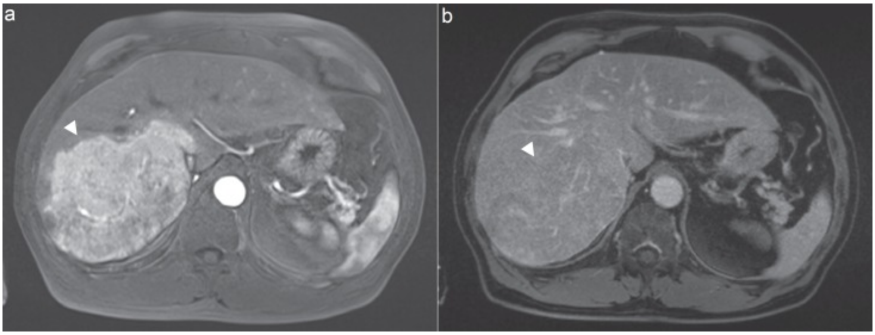

Figure 2.8: Example of a contrast MRI at the (a) arterial phase, where the arrow clearly indicates a bright zone, and (b) the venous phase, when most of the contrast has been washed out. From [66].

accordingly [3]. As is clear from Figure 2.9, the BCLC staging system is divided in four subcategories, ranked A to D according to severity of the condition.

Very early-stage HCC is difficult to diagnose since it is presented by only a single nodule with a diameter less than 2 cm. Early-stage HCC is characterized by a larger nodule or 3 smaller nodules, with each less than 3 cm in diameter. For patients with a single nodule, the preferred treatment is surgical resection. However, it is important to consider the functional capacity of the remaining liver volume after the procedure. If patients with cirrhosis are presented with no portal hypertension and normal bilirubin levels, then this is a good predictor for sufficient hepatic reserve and resection presents itself as a valid option. Although survival rates are generally high here, recurrence rates are also significant since the tumor mass was surgically removed but the underlying chronic condition was not addressed. If resection is not an option, transplantation may be opted. The downsides of transplantation are well-known: along with a need for immunosuppressive therapy, there is organ scarcity and generally very long waiting lists. If transplantation is not possible, then radio-frequency ablation may be considered. In the rarer non-cirrhotic cases, patients usually have a well-preserved liver function and and a lower risk of re-occurrence than patients with cirrhosis. Therefore, in these cases, transplantation is often not necessary and either ablation or resection is preferred [3, 66].

The intermedium stage (B) of HCC, which is characterized by large or multifocal lesions, transarterial therapies, such as transarterial chemoembolization (TACE) and transarterial radioembolization (TARE) are a valid option. For these transarterial therapies,

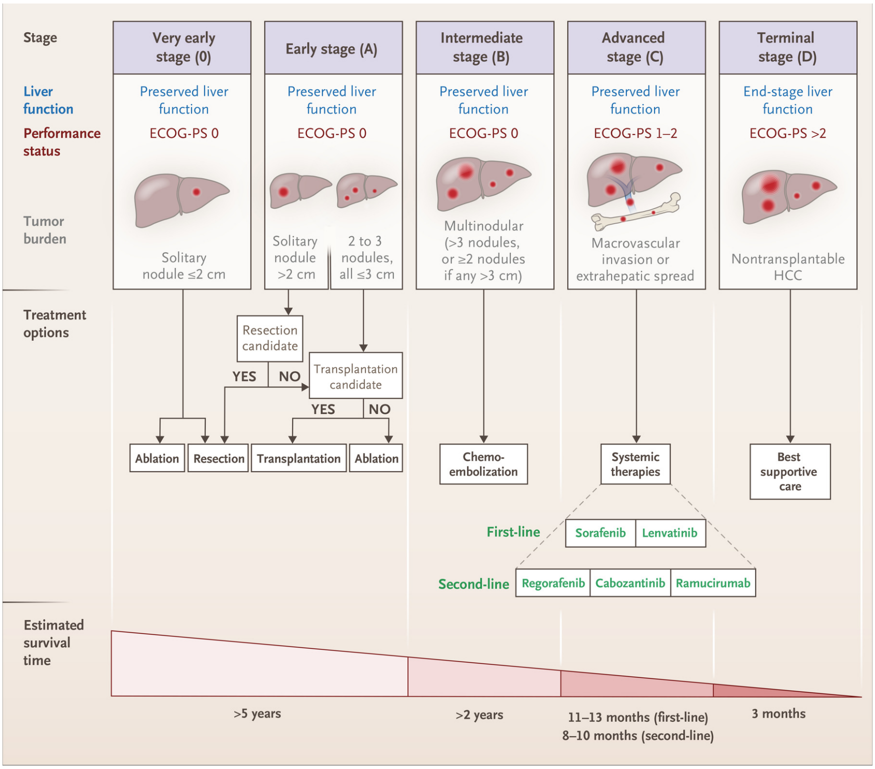

Figure 2.9: Clinical algorithm based on the BCLC algorithm. At the (very) early stage, ablation, resection and transplantation are considered. At the intermediate stage, transarterial chemoembolization or radioembolization are valid options (radioembolization not shown in the figure). At the advanced stage, mostly systemic therapies are viable. From [67].

catheters are retrogradely advanced via the femoral artery towards the hepatic arterial bed, where microspheres are locally injected to selectively embolize tumor tissue (see Figures 2.10 and 2.11 for illustrations of the principle). In the case of TACE, these microspheres damage the tumor tissue through a combined chemotherapeutic and embolic effect. In the case of of TARE (not shown in Figure 2.9, but can be considered at the same stage as chemoembolization), the microspheres are typically smaller in diameter, and tumor tissue is damaged mainly through the spread of radioactivity [4].

Advanced stage HCC (C) presents itself with extrahepatic spread and vascular invasion and is usually treated with administration of the oral chemotherapeutic drug sorafenib. As of recently, advancements have been made in discovering new systemic therapies that improve on or parallel the efficacy of sorafenib. Lenvatinib was approved by the FDA as front-line therapy alongside sorafenib in 2018.

Regorafenib and other systemic drugs been approved as a suitable second-line treatment [67]. TACE may also be considered in this scenario, but this must evaluated on a patient-specific basis [3, 66].

For patients with end-stage HCC (D), none of the therapies mentioned above work. The one-year survival rate is below 10% [3, 66]. Considering the above, it is important to re-iterate that early diagnosis is key, and that properly mapping the progression of the disease is also essential to explore the patient's options and increase their chances for survival.

2.3 TRANSARTERIAL CHEMO- AND RADIOEMBOLIZATION

For the remainder of the dissertation, we will focus on transarterial therapies (TARE, TACE) typically considered at the intermediate stage of HCC. During transarterial drug delivery, drug particles are not injected intravenously, but in the feeding arteries of the organ of interest. This makes transarterial treatments stand out from typical chemotherapeutic cancer treatments, because drug particles flow directly to the organ (locoregional drug delivery), instead of passing through the whole circulatory system. However, while this already minimizes the possible scope of side-effects, it is still possible that drug particles flow from the feeding arteries of the organ to healthy tissue within or surrounding the organ, instead of the tumor mass within the organ. Therefore, for both TACE and TARE, minimizing (or, preferably, eliminating) the delivery of drugs to the surrounding healthy parenchyma is of crucial importance to obtain optimal treatment outcomes.

2.3.1 Chemoembolization

The idea behind chemoembolization is to simultaneously occlude the feeding arteries of the tumor with an embolizing agent and inject a chemotherapeutic drug. This process is visualized in Figure 2.10. The vascular occlusion should increase the dwell time and concentration of the chemotherapeutic drug in the embolized tumor tissue [68, 69]. There are two distinct ways to deliver these two particles. Either the chemotherapeutic agent (e.g. doxorubicin, typically emulsified with Lipiodol (Guerbet, France)) and the embolizing microsphere (e.g. polyvinyl alcohol microspheres) are administered separately (conventional TACE, or cTACE), or these two agents are combined in a particle that holds the two together [70]. This latter method is known as DEB-TACE (DEB stands for drug-eluting beads). These drug-eluting beads consist of polymeric microspheres in which typically a solution of doxorubicin is injected. As the beads occlude the feeding arteries of the tumor, doxorubicin is slowly released and diffuses radially in the embolized tissue, its concentration gradually decreasing with distance [71]. Comparison between these two methods shows similar to better results for DEB-TACE than for conventional TACE [72]. The main take-away is that tumor necrosis occurs because of the combined pharmacological effect of the two agents: both the chemotherapeutic drug as the embolizing agent add to the overall therapeutic response. Different commercial microsphere carriers are available, but this is discussed more in detail in 2.4.1.4.

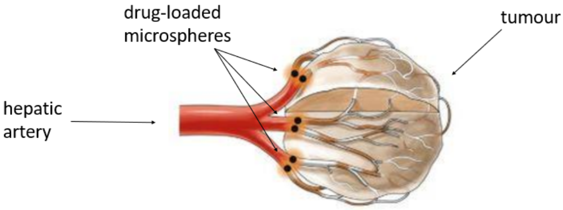

Figure 2.10: Principle of chemoembolization, where drug-loaded microspheres are injected in the hepatic artery to selectively embolize and chemotherapeutically damage the tumor. Adapted from [4].

2.3.2 Radioembolization

The principle of TARE is both deceptively similar and dissimilar to TACE. The two processes are alike in the way that they both require catheterization and injection of embolic particles in the feeding arteries of the tumor. However, they differ in the way the tumor tissue in damaged: in TARE, the embolic effect is much less important. Instead, the main pathway by which the tumor mass is fatally damaged, is by a very local delivery of radiation (see Figure 2.11). Yttrium-90 (or a different type of radiotracer) embedded in small microspheres, is injected in the hepatic arteries and emits a high-intensity, short-lived beta-radiation. These beta-particles cause damage by ionizing water molecules and creating free radicals that destroy DNA molecules. For this damage to be maximal, blood flow and adequate perfusion of this area is desired, which makes for a huge difference with TACE, where perfusion is halted and ischemia occurs [73]. As mentioned above, the different microsphere types which are commercially available are discussed in 2.4.1.4.

The procedure of TARE is relatively complicated since extra cautionary steps are required because of the small size of the

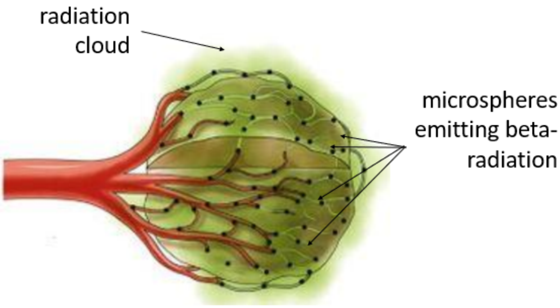

Figure 2.11: Principle of radioembolization, where radioactive microspheres are injected in the hepatic artery to selectively irradiate the tumor tissue. Adapted from [4].

microspheres, which may lead to extrahepatic radiation spread to the lungs. These pre-treatment steps include angiography, therapy simulation with Technetium-99m macro-aggregated (Tc-99m-MAA) particles, and dose calculations. First, the pre-treatment angiography should help to assess the patient-specific vasculature of the tumor. Locating and identifying the feeding arteries of the tumor in this step is crucial: if one of the feeding arteries is missed, this artery will not be targeted and the procedure will be incomplete. In some cases, vessels like the GDA are pre-emptively embolized to prevent flow of microspheres (and, by extent, radiation) in these areas [74, 75]. Second, to quantify both the intra- and unwanted extrahepatic spread of radioactivity, a pre-treatment scout scan is performed to determine among others the lung shunt fraction (which must be below 20 percent at all times) [5]. This screening is done by labeling macro-aggregated albumin (MAA) particles with Technetium-99m (Tc-99m) and injecting them in the hepatic artery (as explained above, vessels leading to extrahepatic tissue (e.g. the GDA) are embolized, or the catheter tip is placed beyond their origin). Then, the lung shunt fraction is determined by measuring lung dose. Only if the patient passes this first test, it can be assured that radiation to the lungs will be minimal, and treatment can proceed. Finally, the amount of activity that must be administered to reach the desired dose in the tumor, all while taking into account that dose limit for healthy liver tissue is about 40-50 Gy. The preferred dosimetric approach is patient-specific and makes use of information obtained from SPECT-CT scans after Tc-99m-MAA injection. An example of a SPECT/CT fusion image is given in

Figure 2.12. To calculate the optimal dose, the partition model can be used (see 2.4.3.1). In the partition model, the healthy liver tissue, tumor mass and lungs are considered as compartments (the masses of each compartment can be calculated using CT scans) and the fractional uptake of activity in each compartment can be determined using the Tc-99m SPECT scans from before. If such personalized approach is not available, the administration activity can also be calculated using generalized, empirical formulas as prescribed by the manufacturers, but this approach is considerably less accurate (e.g. body surface are method, see 2.4.3.1).

The overall success of the treatment depends on the execution and integration of all of these steps [73, 74]. After the treatment, the treatment response is typically assessed using PET/CT scans [5].

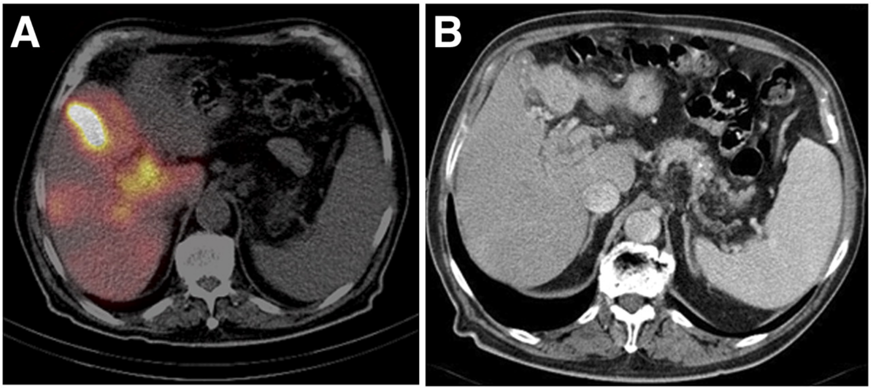

Figure 2.12: (a) SPECT/CT image showing bright hotspots with Tc-99m-MAA deposition (b) Triple-phase CT. From [75].

Possible complications of TARE include gastrointestinal complications (due to non-target radiation) [76, 77]. With regards to side-effects, the post-embolization syndrome is much less common in TARE because the endpoint of injection is not total flow obstruction, contrary to TACE [78]. However, TARE procedures are complicated by the possible delivery of higher-than-acceptable radioactive doses to the surrounding healthy parenchyma and the lungs [79].

In the past, several studies have claimed no superiority of TACE over TARE, or vice versa [78], which has been shown via several randomized controlled trials [80, 81]. However, a recent UGent-UZ Gent study showed superior survival for TARE compared to DEB-TACE in patients with early or intermediate HCC [82]. These discrepant findings might be due to the fact that TARE is a highly technical procedure, as outlined above, or due to poor patient selection [7].

2.4 CURRENT CHALLENGES WITH TRANSARTERIAL THERAPIES

Despite their wide clinical use, transarterial therapies such as TARE and TACE are not perfect. In the current section, we identify three current challenges hindering TARE: variable clinical outcomes, an unclear impact of variable injection parameters, and issues with pre-treatment or peri-treatment optimization.

2.4.1 Uncertainty Regarding Injection Parameters

Clinically, the execution of these transarterial therapies depends on the implementation of a wide range of injection parameters, which may significantly impact the near-tip hemodynamics, the downstream microsphere distribution, and the treatment outcome, and hence, lead to variable outcomes. Below, we discuss the impact of several of these injection parameters (catheter type, microsphere type, injection flow rate and injection location) as identified by experimental and clinical studies.

2.4.1.1 Injection Location

The injection location is typically determined by two coordinates: the axial position of the catheter tip along the artery, and the position of the catheter tip within the artery cross-section (for a given axial location).

For the axial injection location, Jiang et al. [8] compared segmental activity for the pre-treatment injection of Tc-99m-MAA microparticles and post-treatment SPECT imaging of Yttrium-90 radiotracers and found that 24 of the 31 discrepancies could be explained by a slight shift in catheter position. Additionally, Aramburu et al. [83] investigated the impact of axial injection location for the balloon-occluding microcatheter (BOMC), placing the BOMC tip at different axial locations in a planar phantom with water as the circulating fluid. Importantly, the phantom also contained collateral arteries, which connected different segmental arteries (both tumor-feeding and non-tumor-feeding segmental arteries). After injecting dye, they noted some catheter positions led to ineffective occlusion because of the collaterality, while others more were successful.

To study the impact of the cross-sectional injection location, Richards et al. [84] injected propylene microspheres (diameter: 106-125 µm, density: 900-1100 kg/m^3) in a steady water flow in a simplified planar branching geometry. They used an injection tube to perform targeted injections at the level of the inlet. With their injection method, they concluded a strong positive correlation

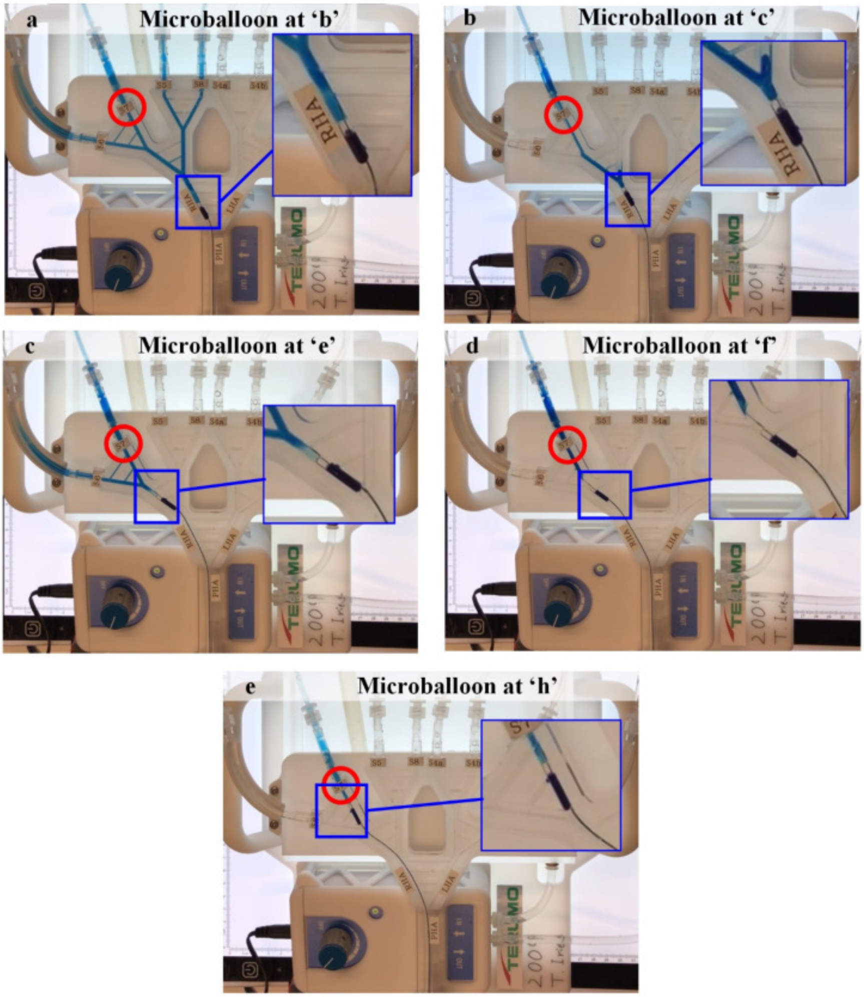

Figure 2.13: Advancing the axial position of the balloon-occluding microcatheter (indicated with the blue box) towards the tumor-bearing segments (in red) leads to a distinctly different dye distribution. From [83].

between cross-sectional injection location and outlet particle distribution.

2.4.1.2 Catheter Type

With regard to injection devices, several commercial catheter types exist. The most common type is the standard end-hole microcatheter (SMC), which is offered by several companies: the Progreat Microcatheter by Terumo Interventional Systems (Japan) [85], the DraKon Microcatheter by Guerbet (France) [86], the Direxion Microcatheter by Boston Scientific (United States) [87], etc. Typically, transarterial therapies carried out using the SMC are seen as flow-directed therapies, meaning that they rely on tumor-directed flow to carry microspheres downstream to the target tissue [88].

Next to the SMC, alternate catheter types have been developed and used for liver-related transarterial embolization procedures, which can alter the flow and pressure in the downstream compartment [88]. Importantly, progressive embolization of tumor tissue can increase the resistance (pressure) at the downstream tumor site and eventually lead to flow reversal. This can direct the microspheres back towards the vascular compartments upstream of the catheter tip and cause non-target embolization. In order to address the potential risk of backwards flow of embolic microparticles (reflux), several anti-reflux designs were conceptually developed and commercialized.

First, the anti-reflux catheter (ARC) as developed by Trisalus Life Sciences (formerly known as Surefire Medical Inc., United States) contains a flexible funnel-shaped tip, which can be expanded or contracted dynamically to vary the degree of obstruction of the artery [89, 90].

Second, for the balloon-occluding catheter (BOMC), an occluding balloon is mounted on the catheter wire before the catheter tip, enabling a complete obstruction of the blood flow through the artery in a static manner [88]. Commercially available examples are the Occlusafe Temporary Occlusion Balloon Catheter (Terumo, Japan) [85] and Sniper Balloon Microcatheter (Embolx, United States)) [91].

Blocking the backwards passage of embolic particles by means of the expanded ARC or the fully-occluding BOMC can prevent, or at least decrease, the risk of upstream non-target embolization. However, the upstream and downstream vascular compartments are not fully disconnected, as collateral connections typically still exist between the two compartments (such as the hepatoenteric and extrahepatic arteries) [88]. Hence, as the blood flow in these connections is oriented away from the hepatic artery, this may lead to non-target microsphere flow. Luckily, these therapies are not purely flow-driven anymore. It has been shown that a significant decrease in the arterial pressure in the vascular compartment downstream of the catheter tip is obtained due to the pressure drop over the ARC and BOMC [88, 90]. Due to this pressure drop, blood flowing to the downstream vascular connections (e.g. these hepatoenteric or extrahepatic arteries) may reverse towards the lower-pressure hepatic artery, washing out particles towards the tumor site and decreasing the chance of non-target downstream embolization. The nature of this effect is ambiguous because progressive embolization can again lead to higher vascular resistance and pressures at the tumor site; this in turn can direct embolic microparticles towards the non-target compartments that are downstream of the catheter tip and increase the chance of non-target downstream embolization. Therefore, blood pressure changes resulting from tip expansion or balloon inflation should be monitored, and the procedure should preferably be halted when flow stasis or reversal occurs [88]. Nonetheless, the ARC and BOMC can play crucial roles in decreasing both upstream as downstream non-target embolization.

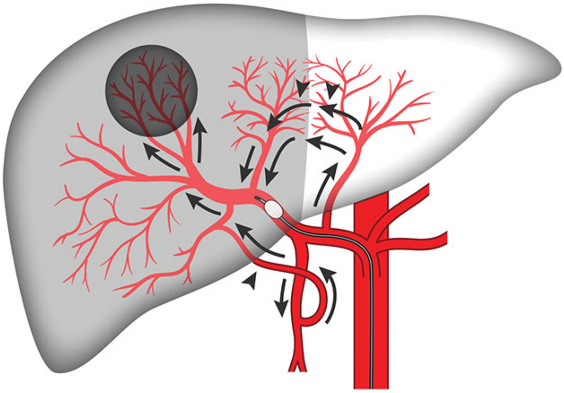

Figure 2.14: After expansion of the balloon, the pressure drop in the vascular compartment can reverse hepatofugal flow into hepatopetal flow [88].

2.4.1.3 Injection Flow Rate

Caine et al. [92] injected dye-containing saline solution in a silicone vascular phantom with constant flow rates of 5-30 mL/min into pulsating blood-mimicking flow with a viscosity of 4 cP. They found that there was a higher agreement between injection solution distribution and overall BMF distribution in the phantom for higher injection flow rates, with the ratio between the two fluid distributions approached more or less one for flow rates higher than 10 mL/min. Increasing the volume percentage of more viscous contrast agent in the injectate saline fluid necessitated the increase of the injection flow rate to reach a similar injectate and BMF fluid distribution, showing the impact of not only injection flow rate but also injection fluid properties.

2.4.1.4 Microsphere Type

The characteristics of microparticles typically used for TARE and TACE treatment differ significantly. Microsphere-based TACE allows for the release of the chemotherapeutic agent (initially attached to the embolization particles) in a controlled and sustained manner that focuses the delivery towards the tumor tissue in order to prevent the widespread toxicity associated with systemic chemotherapy. A wide range of TACE microspheres is commercially available, varying in size (reported range: 70-900 µm): e.g. HepaSphere (Merit Medical, United States) [93], Oncozene or Embozene TANDEM (CeloNova BioSciences Inc., USA), LifePearl (Terumo European Interventional Systems, Belgium) [85], etc. [94]. The range of commercially available diameters for TACE microspheres varies between 70-900 µm [94, 95], although the choice of microspheres depends on the institution, operator, patient-specific conditions, etc [94]. It has been shown that smaller microspheres (< 100 µm) lead to more distal penetration and more effective embolization in animals, emphasizing the impact of microsphere characteristics on the treatment outcome [94].

Currently, different microsphere types (with different sizes, densities) and different radionuclides (with different penetration depths, half-lifes) are availble to use for TARE. For the Y-90 radionuclide, two microsphere types are commercially available: the SIR-Spheres (Sirtex Medical, Australia) [96], which are resin-based (diameter range: 20-60 µm), and TheraSpheres (Boston Scientific, USA) [97], which are made of glass (diameter range: 20-30 µm) [42]. The SIR-Spheres are much lighter than the TheraSpheres (density of 1600 kg/m^3, compared to 3600 kg/m^3), but also have a considerably lower radioactivity per sphere (50 becquerel (Bq) compared to 2500 Bq), thus requiring a higher dose of SIR-Spheres for a similar therapeutic effect. Both types of microspheres are loaded with the beta-emitter Yttrium-90 (Y-90) [74].

An important note to make here is that two different microparticle types are typically used to treat patients with TARE: one type for the pre-treatment scout scans (i.e. Tc-99m-MAA, diameter range: 30-90 µm), followed by the actual treatment using SIR- or TheraSpheres (or other micospheres) [42]. Knowing that there are differences in microparticle characteristics (i.e. microparticle size, density) between both particle types, this may not be the ideal set-up, as the use of Tc-99m-MAA particles may result in a different particle distribution compared with the actual treatment microspheres. Hence, the scout scans may possibly lead to inaccurate predictions of the treatment microsphere activity.

Recently, QuiremSpheres (manufactured by Quirem Medical BV, The Netherlands) [85], embedded with Holmium-166 (Ho-166), have emerged as an interesting alternative to standard TARE microspheres. Ho-166 is both radioactive and slightly paramagnetic. This magnetic property allows the spheres to be visualized using magnetic resonance imaging (MRI), which offers the added advantage of being usable for both pre-treatment scout scans and actual treatments. The diameter range of QuiremSpheres is 15-60 µm, their density is 1400 kg/m^3, and the activity per microsphere lies between 67 and 400 Bq (i.e. slightly higher than SIR-Spheres, but significantly lower than TheraSpheres) [98]. Herein, the added value is that QuiremSpheres can be used both for the pre-treatment scout dose and the actual treatment, minimizing previous discrepancies in microparticle characteristics between treatment and pre-treatment [99].

2.4.2 Variable Outcomes

Importantly, the reported mean survival time after TACE ranges from 3.4 to 31 months (median of 14 months) in prospective studies [100]. For TARE, survival times typically vary between 7-27 months [6]. With regards to the varying clinical success for TARE, it has been shown that high tumor uptake of radiating microspheres is instrumental to a positive survival advantage [101]. The considerable variation in survival times could be partly explained by the lack of procedure standardization, and the fact that TARE is a highly technical procedure that is preferably executed in experienced medical centers [7]. This underlines how positive clinical response depends on proper execution of the treatment. However, it is currently unclear to which extent the above-mentioned heterogeneity and uncertainties in treatment execution (as discussed in 2.4.1) impact the microparticle flow, downstream distribution and, by extent, the treatment response.

2.4.3 Issues with Pre-Treatment or Peri-Treatment Optimization

Due to highly patient-specific nature of each TARE or TACE case (patient-specific tumor size and location, patient-specific hepatic arterial geometry, etc.) [49], it is currently difficult to know the optimal implementation of each injection parameter a priori. As shown by experimental and clinical evidence, these injection parameters can impact the treatment outcome, and TARE and TACE both suffer from varying, suboptimal outcomes. However, medical images do not show how the injected embolizing agents will distribute downstream of the catheter tip, whether an alternative injection location might offer a better outcome, etc. Hence, a pre-treatment assessment of the effectiveness of the proposed injection conditions, and whether these conditions can be improved, is useful. Several types of pre-treatment assessments already exist, as listed below, although they are imperfect.

2.4.3.1 Pre-Treatment Dosimetry

As already explained, a pre-treatment injection of low-dose (i.e. non-therapeutic) radioactive Tc-99m-MAA microparticles to mimic Y-90 microparticle distribution is already routinely done for TARE. Several methods are available to calculate the optimal injection activity based on the Tc-99m-MAA microparticle distribution. As can be used for SIR-Spheres, the body surface area method calculates the administration activity based on the patient's height and weight, as well as the volumes of cancerous and non-cancerous liver tissue [79, 102]. Alternatively, the partition model estimates the dose in three compartments (healthy liver, tumor and lungs) based on the liver mass, tumor mass, the lung shunt fraction and simulated activities in each compartment [79, 103]. These simple methods do not consider that microspheres might not distribute uniformly within one compartment, or that compartments themselves are not heterogeneous pieces of tissue. Hence, computationally more expensive voxel-based methods consider tissue heterogeneity by dividing the volume of interest in small voxels, where different properties can then be derived from medical images and prescribed to each voxel, to better represent the heterogeneous composition of the volume of interest. Then, based on the simulated radioactivity in each voxel, the 3D dose distribution can be determined [104]. An example of a commercially available voxel-based dosimetry method is MIM SurePlan Liver Y90 (collaboration between MIM Software Inc. and Sirtex Medical) [105].

In this context of pre-treatment dosimetry, it is also important to consider that the use of Tc-99m-MAA microparticles to simulate Y-90 microparticle distribution is already imperfect. This is because the properties of these microparticles differ from the ones actually used for treatment [106]. Additionally, the choice of injection location also often changes in-between pre-treatment and treatment itself, thereby not really offering a reliable assessment of the therapeutic suitability of the current injection location. For example, Jiang et al. [8] compared segmental activity for the pre-treatment injection of Tc-99m-MAA microparticles and post-treatment SPECT imaging of Yttrium-90 radiotracers and found significant differences in 31 out of 81 treatments. This makes pre-treatment far from optimal because the implementation of injection parameters should be as similar as possible between pre-treatment and treatment. Finally, this pre-treatment injection does not enable the interventional radiologist to compare many injection parameters against each other, since this method still requires physical intervention (i.e. injection of low-dose radioactive particles, medical imaging, etc.), which can be harmful for the patient.

2.4.3.2 Peri-Operative Imaging Guidance

Peri-operative imaging guidance can be of use (such as the syngo Embolization Guidance tool, Siemens Healthineers, Germany) [107]). This tool helps treatment planning at the bedside by automatically detecting the tumor feeding vessels and hence, selecting the optimal catheter tip placement. However, such tools do not consider flow-related phenomena, such as the impact of the catheter tip cross-sectional location or catheter type on near-tip hemodynamics and particle distribution, and do not allow to compare different injection scenarios.

To consider flow-related phenomena, contrast agent can be injected peri-operatively to assess whether current injection conditions lead to optimal tumor coverage. If enough contrast fluid flows to the tumor tissue, the current injection location is deemed suitable. Additionally, contrast agent has the advantage of being easily visualizable, while microspheres are not. Of course, the reliability of this assessment is hindered by the fact that the dynamics and mass transport of contrast fluid are not the same as that of small microspheres. For example, injection of embolizing microspheres can lead to progressive embolization of the downstream microvessels, which leads to an increased vascular resistance. This can cause alterations in the downstream flow distribution to the segments [108] and increased resistance to microsphere injection, which is not the case for contrast agent. However, contrast agent can be harmful [109], which makes this type of peri-treatment optimization even more invasive.

Summarizing the above, various pre-treatment methods already exist, but all lack in flexible, reliable, non-invasive comparison of injection conditions, and do not allow reliable optimization of treatment parameters.

2.5 CLINICAL QUESTIONS

Based on the current variable clinical success of transarterial therapies, high patient-specificity, a lack of standardization in procedure execution, the many variable injection parameters which can impact the treatment outcome, and a lack of a reliable pre-treatment assessment which allows to noninvasively compare different injection scenarios and select the optimal injection conditions, we define the current clinical questions for this dissertation as:

- **Question 1**: Can we reliably predict the tumor dose before the procedure, and, use this prediction to adapt treatment parameters where necessary?
- **Question 2**: Can we decrease variable outcomes in TARE and TACE by optimizing the clinical injection parameters preoperatively, given a reliable prediction of treatment outcome?

These clinical questions will help define the specific objectives of this PhD dissertation with regards to the use of computer modeling to improve treatment planning of these transarterial therapies, as will be explained in Chapter 3.

Chapter 3

State-of-the-art in, and Challenges with, Modeling of Transarterial Therapies

During the past years, in silico medicine – which entails the use of computer modeling for improving the understanding, prevention and treatment of diseases among others – has grown as a popular alternative to in vivo and in vitro experimental techniques, partly due to the continuing increase in computational power at decreasing cost [110] and the growing availability of patient-specific data. When properly developed and used, in silico medicine can prove to be a powerful tool in the advent of personalized medicine. First, we will discuss how in silico modeling - in general - can aid in therapy planning of transarterial therapies. Second, we will give a brief overview of which types of in silico models exist and have already been applied to transarterial therapies. Third, we will show which insights regarding the impact of injection conditions on the microsphere distribution have already been gained by the use of these models. Finally, we will discuss what is lacking in the state-of-the-art of these models, based on which we will define the goals of this PhD dissertation.

This chapter is partly based on the book chapter *Numerical modelling in support of locoregional drug delivery during transarterial therapies for liver cancer* from the book *Modelling of mass transport processes in biological media* (C. Debbaut and T. Bomberna, Elsevier,

2022) [23] and the Master thesis dissertation *Targeted drug delivery for liver cancer: modelling the impact of cancer burden on the particle distribution in a patient-specific cirrhotic liver* (T. Bomberna, UGent, 2019) [25].

3.1 The Added Value of In Silico Modeling for Planning of Transarterial Therapies

It was already stated that the implementation of TACE and TARE can vary widely in clinical practice [111]. Injection parameters (such as catheter type and the injection's location, velocity, and timing) are chosen depending on the clinician's preferences and experience, as there is currently no clear-cut procedure standardization available, while their exact impact on the treatment outcome is currently still unclear [10, 12, 112] and likely to be patient-specific. Hence, numerical modeling may help to elucidate the impact that these clinical parameters have on the particle distribution and treatment outcome, and distinguish high-impact parameters from low-impact parameters on a patient-specific basis. Interestingly, numerical models are completely noninvasive, as they are virtual tools that allow endless finetuning of injection conditions. Eventually, these models might be used to inform clinicians on the most optimal implementation of these clinical parameters for each patient and increase the target-specificity of the treatment. To this end, Kleinstreuer et al. have devised a 'computational medical management program' (CMMP) to help achieve optimal locoregional drug delivery [9].

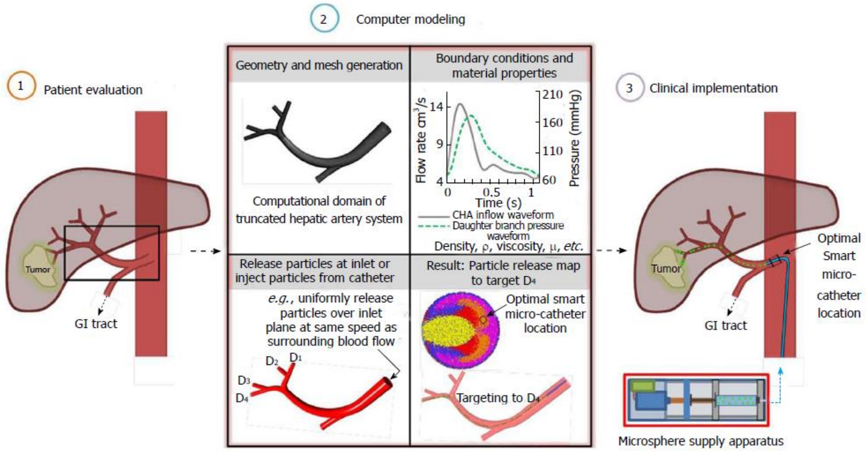

Figure 3.1: The Computational Medical Management Program, envisioning a patient-specific workflow from medical image to treatment advice [9].

The CMMP entails 3 steps: (i) acquiring patient-specific data and reconstructing patient-specific anatomies, (ii) simulating the therapy in a virtual environment and determining the ideal injection conditions, and (iii) implementing the proposed conditions in the treatment to improve patient-specific outcomes [9]. At the moment, the focus in this field of study has mainly been on steps (i) and (ii), narrowing the use of these computational models to assessing the impact of certain clinical parameters on the downstream particle distribution in a number of generalized, patient-inspired or patient-specific geometries. There has been less focus on delineating the precise role that numerical modeling can play in patient-specific outcome optimization. Additionally, there are also disadvantages to computer modeling, such as computational cost, and the severe need for proper validation of these models before they can be implemented in clinical practice.

In the context of computer modeling, there is an important tradeoff between computational complexity and accuracy. More complex models may result in a higher accuracy, but may come at a computational cost that is prohibitive for clinical use on a regular basis. In contrast, while simpler models come at a much lower computational cost, they may not capture the complex blood flow and particle behavior to its full extent with sufficient accuracy. In this regard, several key choices need to be made regarding: the overall complexity of the numerical model, the identification of the modeling parameters that are important, and the parameters that can safely be neglected. These choices may lead to discrepancies in modeling approaches and even in results and interpretation. Below, we will give a brief overview of different modeling types from complex to less complex, and indicate how they have been used to provide insights into transarterial therapies.

3.2 DIFFERENT TYPES OF IN SILICO MODELS

Several types of computer models exist, both for modeling of microsphere infusion in the hepatic arteries and the much broader field of computer modeling in medicine. Here, we distinguish (from higher to lower complexity) between fluid-structure interaction (FSI), computational fluid dynamics (CFD), and reduced-order models (i.e. 0D-models). While the crux of this work focuses on CFD, the overview below will also offer a hint of what FSI and reduced-order models have to offer in the context of hepatic arterial microsphere infusion.

3.2.1 Fluid-Structure Interaction

Starting with the most complex multiphysics models for TACE and TARE, FSI models are characterized by the simultaneous modeling of (blood) flow and/or microsphere transport, and (arterial) wall movement, modeling how the arteries contract and dilate according to the heart cycle. To inspect the impact of modeling deformable walls on the particle distribution in a simple geometry, Kleinstreuer and Childress [113] investigated how each of the 5 outlets of their deformable geometry could be targeted by placing the catheter tip in a specific spatial zone at a pre-defined axial injection location. They generated these spatial targeting zones for 10 intervals during the cardiac pulse. As a more time-efficient alternative to their computationally expensive deformable model, Childress and Kleinstreuer [113] proposed using several rigid wall geometries, where the dimensions of these rigid geometries were either extracted from the diastolic phase of the cardiac cycle, or time-averaged over the full cycle. The spatial injection zones were compared for the rigid and flexible cases, and used to inspect whether the rigid cases could predict the spatial injection zones of the deformable geometry. They noted that the best match between the deformable and the rigid wall models was found during diastole – most likely due to the absence of significant changes in the physical geometry during this phase. Compared over the whole cardiac cycle, the time-averaged geometry provided the best match with the deformable model. While differences between rigid and flexible models were still significant, they could be minimized with the selection of the best-fit rigid model (in this case, the time-averaged geometry), with a notable cost decrease of rigid over deformable models of 1:7 [113]. At present, this case study is the only example of using FSI to model transarterial drug delivery. Hence, it should be emphasized that the current conclusions only stand for the simplified geometry that was studied here.

3.2.2 Computational fluid dynamics

Scaling down complexity to pure computational fluid dynamics (CFD) applications, the walls are typically modeled as rigid, and the underlying mathematical equations (e.g. conservation of mass and momentum, see Chapter 4) focus solely on resolving fluid flow. Because they are computationally less complex than FSI, mostly these models have been used in TARE modeling. An overview of how these models have been used so far to quantify the impact of clinical parameters on the particle distribution is given in Section 3.3. Importantly, CFD simulations can be carried out in 3D, 2D or

1D geometries, providing information on the spatial distribution of hemodynamic parameters such as velocity (or flow rate) and pressure throughout the vessel network. Of course, as the number of spatial dimensions decrease, the complexity of the numerical problem decreases, but the representation also becomes less physiological. In Section 3.3, we will discuss how 3D CFD models have led to specific insights for TARE (skipping over 2D and 1D models due to a lack of relevant examples). Below, we discuss how 0D modeling approaches work and have been used to study TARE.

3.2.3 0D models

Simplifying further to zero-dimensional models, the only remaining dimension is time. For example, Debbaut et al. [114] introduced a zero-dimensional (0D) model of blood flow through a healthy human liver cast. In this model, which was based on transmission line theory, each blood vessel generation was represented by one tuned Π-filter. As a result, the three hepatic vascular trees (hepatic arteries, portal veins and hepatic veins) were each represented by a series of these Π-filters. The 0D model was used to determine flow and pressure distributions throughout the liver, and to estimate the hemodynamic impact of hypothermic machine perfusion for liver transplantation. An adaptation of this electrical model was applied to rat livers, and was then used to study the flow distribution among different liver lobes in order to investigate the impact of partial hepatectomy procedures.

Within the context of transarterial liver embolization therapies, Aramburu et al. [83, 115] posited a 0D-modeling approach using an electrical representation of an idealized HA geometry to model blood flow from the PHA to the segmental arteries. This was done by modeling the branching network as nodes interconnected by resistances, the upstream vasculature as a pressure source and the downstream vasculature as a pressure source in series with a resistance. They noted that the 0D-model could be used to assess the redistribution of blood flow, which can occur after microparticle injection using a balloon-occluding microcatheter. Despite offering no information on local flow and particle behavior, these 0D models significantly reduce the overall modeling complexity and allow fast estimations of flow (re)distributions.

Of course, hybrid modeling approaches also exist. For example, 0D Windkessel elements can be used to model the downstream vasculature and subsequently implemented as boundary conditions for 3D

CFD simulations. In Section 3.3 below, we will discuss the insights into the impact of clinical parameters that have been gained by using CFD.

3.3 INJECTION PARAMETER ANALYSIS USING CFD

3D CFD models of TARE can be interpreted as a multiphase problem, where both a continuous fluid phase (blood) and an interspersed discrete phase (microspheres) traverse the hepatic arterial domain. The mathematical background of this multiphase model, as well as the degree of coupling between both phases, are explained in Chapter 4. Here, we focus on the use of these models to elucidate the impact of injection parameters such as catheter type, microsphere type, injection flow rate and injection position. This will give us an insight into the state-of-the-art of these CFD models, and what these models are currently lacking, which will inform the objectives of this dissertation.

3.3.1 Cross-Sectional Injection Position

In 2010, Kennedy et al. [13] were the first to model particle trajectories in a representative hepatic arterial system with five outlets (see geometry in Figure 3.2) and noted that the branches through which particles exited were highly dependent on the release position within the injection plane. Hence, the injection plane could be divided in sub-sections, where injection in each sub-section lead to particles exiting through a specific outlet (Particle Release Map (PRM), as shown in Figure 3.2). Since the PRM clearly showed distinct injection regions for each of the five exit branches, they concluded that particles could be steered to particular exit branches if the release position of the catheter tip could be accurately controlled. (However, accurately controlling the tip in vivo is not a trivial problem, as we will discuss later in this dissertation, in Chapter 7 among others).

While the study by Kennedy et al. [13] was conducted under steady flow conditions, Basciano et al. [14] modeled particle transport in the same geometry, but using a realistic pulsatile flow rate waveform. They derived PRMs for the accelerating zone of their cardiac waveform and noted that the organized regions present for the steady-flow simulations were still present for their transient simulations. In 2012, Kleinstreuer et al. [12] modeled particle release at peak systole for the same waveform in the same geometry, and confirmed the distinct particle release regions present for each exit branch.

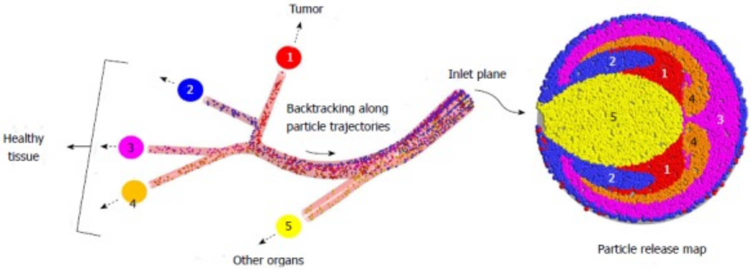

Figure 3.2: The Particle Release Map is a visualization of the axial injection plane, dividing the plane in colored cross-sectional sections. Each section is associated with an outlet of the geometry, showing how calculations predict that injection in a specific section will lead to particles exiting through the specific outlet associated with the spatial injection zone. From [13].

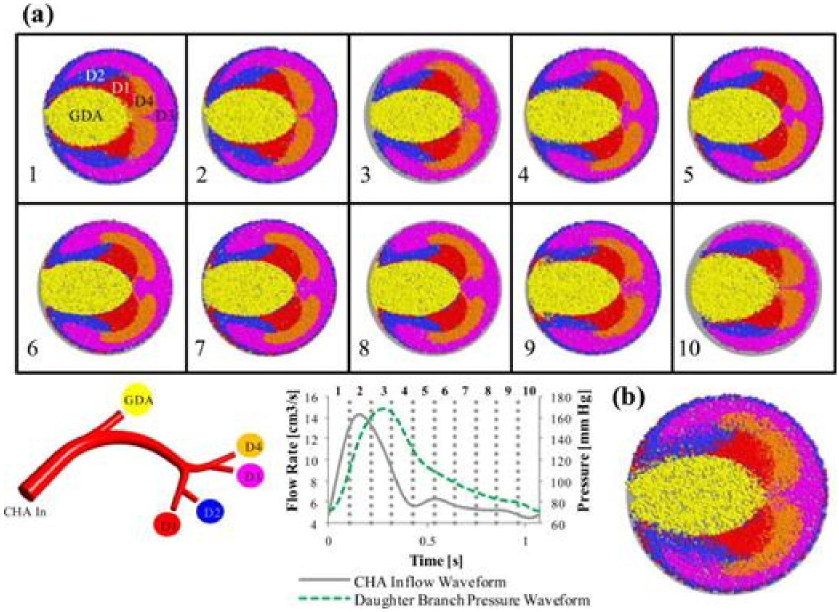

Figure 3.3: (A) PRM variations over 10 intervals throughout the pulse for a generalized 5-outlet geometry. Qualitatively, variations are limited. (B) Overlaying of the 10 PRMs leads to the Composite Particle Release Map. From [116].

However, these findings only confirm the appearance of well-ordered injection regions for a small section of the full cardiac pulse. Therefore, Childress et al. [116] computed PRMs at ten injection intervals throughout the cardiac pulse in two simple geometries to study the variation between intervals. Then, they combined these ten PRMs in a single Composite Particle Release Map (CPRM). For their first, 5-outlet geometry (Figure 3.3), there was only limited overlap between the targeting zones for the different exit branches at different injection intervals. Hence, it was theoretically possible to target one exit branch throughout the entirety of the cardiac pulse without unwanted particle delivery in one of the other exit branches. For their second, 3-outlet geometry (Figure 3.4), the variation between the PRMs at different injection timings was much higher, which caused more overlap between the different targeting zones in the CPRM. Thus, no clear targeting zones appeared for each outlet during continuous particle injection throughout the cardiac cycle. The above illustrates again the high impact of the choice of geometry on these results.

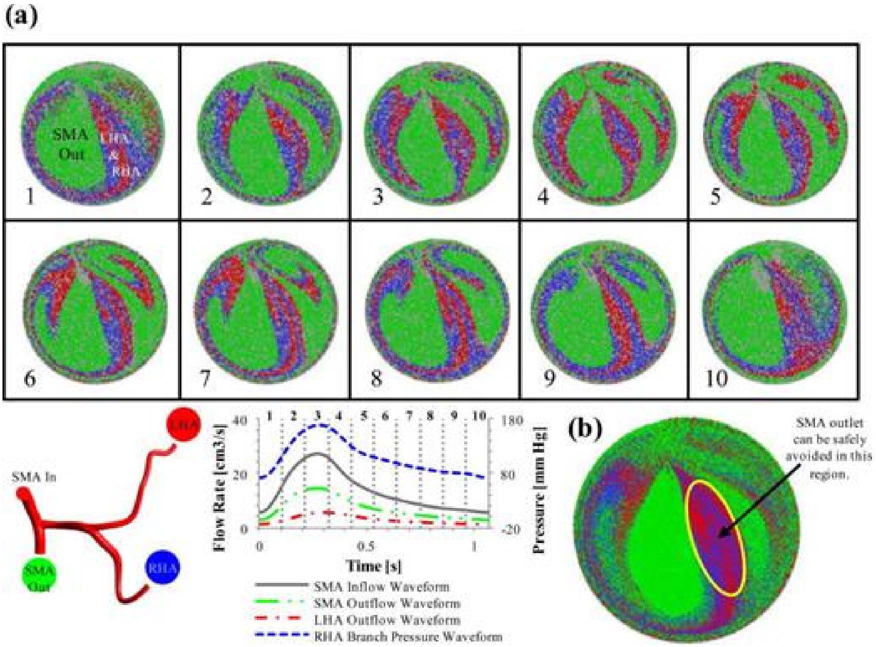

Figure 3.4: (A) PRM variations over 10 intervals throughout the pulse for a generalized 3-outlet geometry. Qualitatively, variations are limited. (B) Overlaying of the 10 PRMs leads to the Composite Particle Release Map. From [116].

Of course, the impact of release position on particle delivery is highly geometry-dependent, and that the results of a study in one patient-specific case should not simply be generalized. Moreover, PRMs had not been computed yet for patient-specific geometries. Additionally, the validation of these PRMs has also been extremely limited. The only work to validate the precise impact of injection location on particle distribution was done by Richards et al. [84] in 2012 for a simplified planar geometry. Validation of the PRMs for the patient-specific complex 3D geometries has not been done yet, and is likely to be technically challenging.

3.3.2 Axial Injection Position

In an extension to studies that examined the influence of cross-sectional injection location, several authors have investigated the impact of the axial injection location on particle distribution. Since the axial injection location is much easier to control in vivo than cross-sectional locations, the possible impact of this parameter on particle distribution is very relevant for clinical optimization and tumor targeting. In 2016, Aramburu et al. [10] modeled injection from two axial positions (at the inlet of their geometry, and near the first bifurcation) for a standard microcatheter (SMC) (see Figure 3.7). Comparing particle release from the inlet via the SMC to particle release near the bifurcation via the SMC, the maximum difference in segmental particle distribution was obtained for Segment VIII (19.68%). In a different study but in the same geometry, Aramburu et al. [106] noted that injecting via the SMC near the bifurcation resulted in a deposition of all particles in the right lobe. However, retracting the SMC by only 5 mm further away from the bifurcation resulted in particle deposition in the left lobe as well; this illustrates the high impact of small variations in axial catheter position on the particle distribution. It was also shown that a 5 mm-shift in axial catheter position mattered less for the injection position at the inlet, as the local flow field likely varied less from point-to-point for this straight, tubular part of the geometry.

These results imply that axial injection position is an important parameter to optimize, but that the precise impact of axial catheter position can fluctuate from one axial location to another, and that zones near bifurcations are likely to be more prone to high fluctuations in particle distribution due to small shifts in axial catheter position.

3.3.3 Catheter Direction

Aramburu et al. [15] remarked that while the impact of cross-sectional injection positions had been previously studied, no attention had been given to the microcatheter distal direction, while this is a clinical parameter that can differ even for the same cross-sectional injection position. They studied six distinctly different microcatheter directions (Figure 3.5), and observed that even for the same cross-sectional injection location, significant differences occurred in the segmental particle distribution for different microcatheter directions. For example, for a microcatheter originating from the top center of the vessel (North, 'N', position) and a tip located near the bottom center of the vessel (denoted as South, 'S', position in Figure 3.5), the particle exit fraction for Segment VI was 31.72% (N-S position in Figure 3.5). For a microcatheter originating in the 'E' (East) position and with a tip in the S position (note that, technically, the cross-sectional injection location is the same), the particle exit fraction for Segment VI was 12.57%. These findings are crucial, and highlight that looking only at the cross-sectional location is in fact a simplification of reality. To conclude, microcatheter distal direction seems to play an important role in (sub)segmental particle distribution, and its effect is currently under-reported in literature.

3.3.4 Catheter Type

Because of the high impact of the cross-sectional injection position, Kleinstreuer et al. [9] proposed in 2014 to use an anchored catheter to stabilize the position of the catheter tip within the bloodstream and control particle delivery location. The smart microcatheter, as shown in Figure 3.6, consisted of a reservoir containing the microspheres mixed with the injection fluid, a supply line to the microcatheter, and an actuator controlling the cross-sectional position of the microcatheter tip. The design was conceptualized and patented, but not yet developed or commercialized. Importantly, Kleinstreuer et al. [9] also found a considerable impact of catheter presence on the local flow field, which underlines the importance of explicitly modeling the catheter in CFD simulations.

In their patient-specific geometry (see Figure 3.7), Aramburu et al. [10] compared two catheter types, the SMC and ARC (see 2.4.1.2). The ARC contained an extendable, funnel-shaped tip (see Figure 3.7b), which altered the near-tip hemodynamics (reducing flow velocity inside the catheter and accelerating the bloodstream around the catheter), and caused recirculation regions after the catheter tip. They also observed that, for the SMC, particles entered the hepatic arteries in a laminar way, while, for the ARC, particles spread out showing a more complex flow behavior (i.e. still laminar, but with

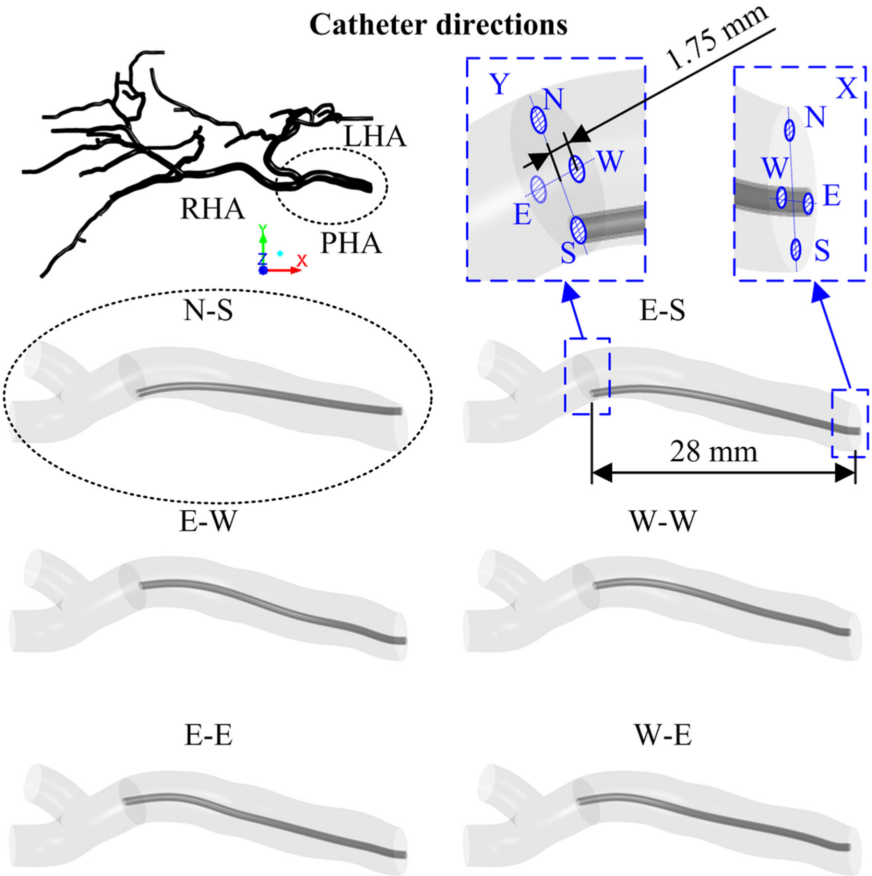

Figure 3.5: Different microcatheter directions: from points N, S, E, or W at section X to N, S, E, or W at section Y, where section Y is the injection plane. There are 28 mm between sections X and Y, and 1.75 mm between the positions N, S, E, and W and the lumen center. From [15].

large vortices appearing after the catheter tip). For SMC injection at the inlet, >30% of particles entered the left lobe, while for ARC injection near the inlet, <2% entered the left lobe. However, due to the axial extension of the ARC, it is difficult to compare particle distribution resulting from SMC and ARC injections, since the axial injection location for the two catheter types is not strictly the same (see Figure 3.7b). Near the bifurcation, all particles entered the right lobe regardless of catheter type. Seeking to clarify this phenomenon, Aramburu et al. (2016a) observed that the expanded funnel of the ARC physically extended into the RHA, explaining why particles only deposited in the right lobe (see Figure 3.7b). In the SMC, the injection velocity was high enough to give particles the necessary mo-

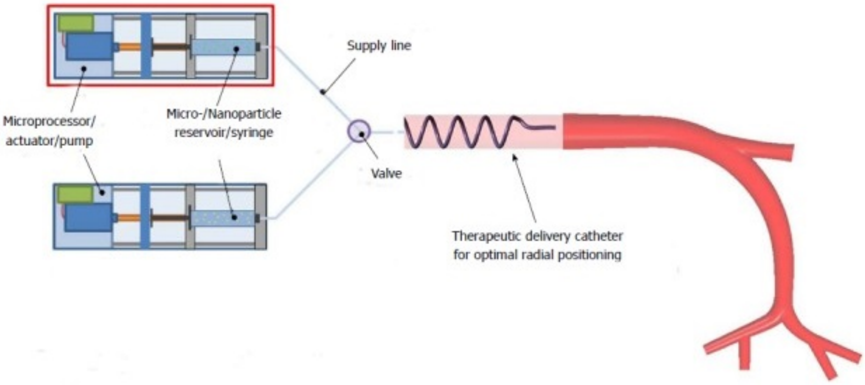

Figure 3.6: The Smart Microcatheter, containing an actuator to control the optimal cross-sectional position, which can be identified from CFD simulations. Adapted from [9].

mentum to cross blood flow streamlines and deposit directly into the RHA.

In 2017, Aramburu et al. [11] also studied a third catheter type, the angled-tip microcatheter (ATM, see Figure 3.8A) (Boston Scientific, USA) in the same patient-specific geometry, which is simply an extension of the SMC with a tip that is able to be oriented in different directions. Four different orientations (upward (U), downward (D), leftward (L), rightward (R)) were tested. The authors found that the particles did not necessarily travel towards the branch at which the tip was pointing. They attributed this result to the complex, intricate particle pathlines that result from helical flow phenomena that were present in this arterial vasculature. Additionally, the authors found considerable differences were found in segmental particle distribution due to tip orientation: e.g. 12% extra particles entered the left lobe due to the downward orientation of the catheter tip, compared to the upward tip orientation. However, for their specific clinical application, the impact was rather low, because the majority of particles entered the cancerous right lobe anyway (see Figure 3.8B for the cancer scenario under study), underling the highly patient-specific nature of their results.

In 2019, Aramburu et al. [117] modeled deployment of a balloon-occluding microcatheter at two axial injection locations in a patient-specific hepatic arterial geometry. They used a 0D model to assess the distribution of blood flow after balloon occlusion, and then used a 3D CFD model to assess the arterial hemodynamics given the current flow distribution. Importantly, the impact of the balloon catheter

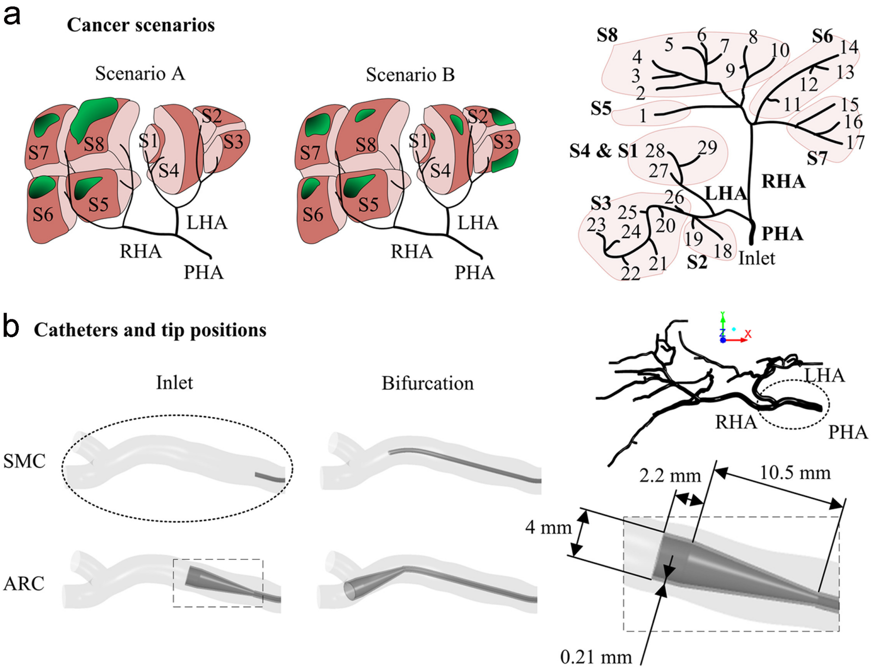

Figure 3.7: (a) 2D sketch of structure of the patient-specific hepatic artery (cancer scenarios indicated, tumors show in green) with the inlet and 29 outlets, as well as the segment that each outlet irrigates. (b) Location of the two catheter types: the standard microcatheter (SMC) and antireflux catheter (ARC). The outer diameter of the expandable tip (4 mm), thickness (0.21 mm), funnel-shaped length (10.5 mm) and cylinder-shaped length (2.2 mm) are specified. From [10].

was very large, with both flow (re)distribution compared to a no-occlusion case, and complex streamlines occurring after the tip for each injection site.

These important results highlight that there are many different commercially available designs for microcatheters, which each differ in how much they vary from the standard design (i.e. the angled-tip microcatheter is more similar to the standard microcatheter than the balloon-occlusion catheter) and that CFD simulations are useful to help determine their impact on local blood flow and downstream distribution, albeit in a patient-specific way.

3.3.5 Injection Flow Rate

In 2014, Kleinstreuer et al. [12] tested five different catheter injection volumetric flow rates in their simplified geometry (see Figure 3.9). These resulted in injection velocities ranging from 1% to 1000% of

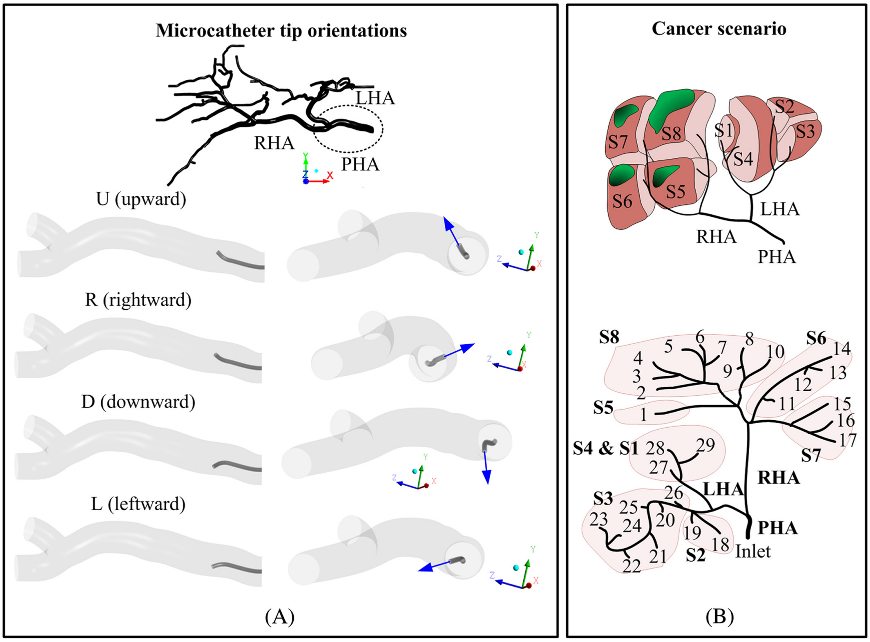

Figure 3.8: (A) The angled-tip microcatheter is embedded in the proper hepatic artery of a patient-specific geometry. The designcontains a tip that can be oriented in four different directions (upward, rightward, downward, leftward), which significantly impacts the downstream particle distribution. (B) 2D sketch of the patient-specific geometry, with the cancer scenario under study (tumors restricted to the right lobe). From [11].

the arterial blood velocity (which was assumed uniform at the inlet). At the lowest injection velocity, particles were injected at a cross-sectional position that allowed them to follow the bloodstream along the bifurcation, avoiding exiting through the GDA outlet (located opposite the injection plane), and exiting instead through the four daughter vessels (located downstream of the bifurcation). However, as is clear in Figure 3.9, by increasing injection flow rate, more and more particles exited through the GDA outlet opposite the injection plane, as higher inertial forces enabled the particles to cross fluid streamlines and carry on straightforward paths towards the GDA outlet. Kleinstreuer et al. [12] also remarked that, for lower injection flow rates, more particles tended to get stuck in the domain, or get caught in recirculation regions near the catheter tip.

Aramburu et al. [106] came to a similar conclusion in a different study in 2016, noting that the discrepancy between particle and flow distribution throughout the arterial geometry was higher when the ratio between microsphere velocity and the blood flow velocity was

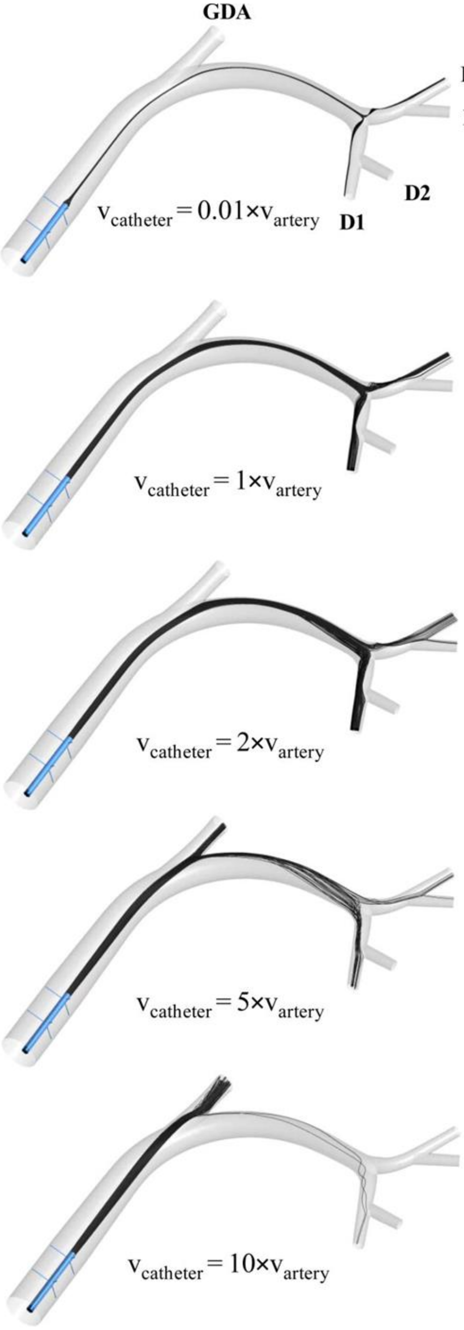

Figure 3.9: Clearly, increasing the injection velocity increases the ability of the microspheres to cross fluid streamlines, for particle inertia effects to dominate, and impact the microsphere distribution. From [12].

higher. In another study, Aramburu et al. [15] observed that, for ratios of microcatheter average velocity to arterial average velocity well above 2, particles had sufficient inertia to cross fluid flow streamlines. Notably, this regime was only valid for the diastolic phase of the input cardiac waveform of their patient-specific case, because of the higher relative difference between catheter and arterial flow rate.

Interestingly, Aramburu et al. [11] also compared the spatial distribution of particles for different injection flow rates (resulting from a microcatheter oriented in the upwards direction), and concluded that for the higher injection flow rate (18.5 mL/min compared to 5 mL/min) in their patient-specific geometry, particles traveled in a more spread-out manner in the lumen cross-section, and closer to the artery wall (due to tip orientation). This can be seen in Figure 3.10, where the first column of each Section (A-C) represents the higher flow rate.

Summarizing the above, catheter injection flow rate has shown to play a role in both the spatial distribution of particles inside the vessel lumen, and the degree to which particle distribution mimics flow distribution.

3.3.6 Microsphere Type

In 2010, Basciano et al. [14] were the first to study the particle trajectories of different commercially available microparticles, namely SIR-Spheres (diameter: normal distribution of 32 ± 10 µm, density: 1600 kg/m^3) and TheraSpheres (diameter: normal distribution of 25 ± 10 µm, density: 3600 kg/m^3). Visually, the effect on the microparticle trajectories is difficult to see (see Figure 3.11), and Basciano et al. [14] noted that most SIR- and TheraSpheres show similar behavior. However, they observed that the different particle characteristics had a larger impact on the particle trajectories in the decelerating phase of the cardiac pulse (when less inertial effects were present) than during the accelerating phase (when the impact of particle diameter was shown to be almost negligible). This can be seen in Figure 3.12, where the average particle distributions bars for the decelerating phase show a (slightly) larger difference than for the acceleration phase. Furthermore, the gravitational force also had a larger impact on the TheraSpheres than on the SIR-Spheres (mainly due to the larger density of the TheraSpheres). However, the effect of microsphere type is clearly of a order of magnitude smaller than the injection timing (comparing differences between the accelerating, peak and decelerating phases in Figure 3.12) and the cross-sectional injection

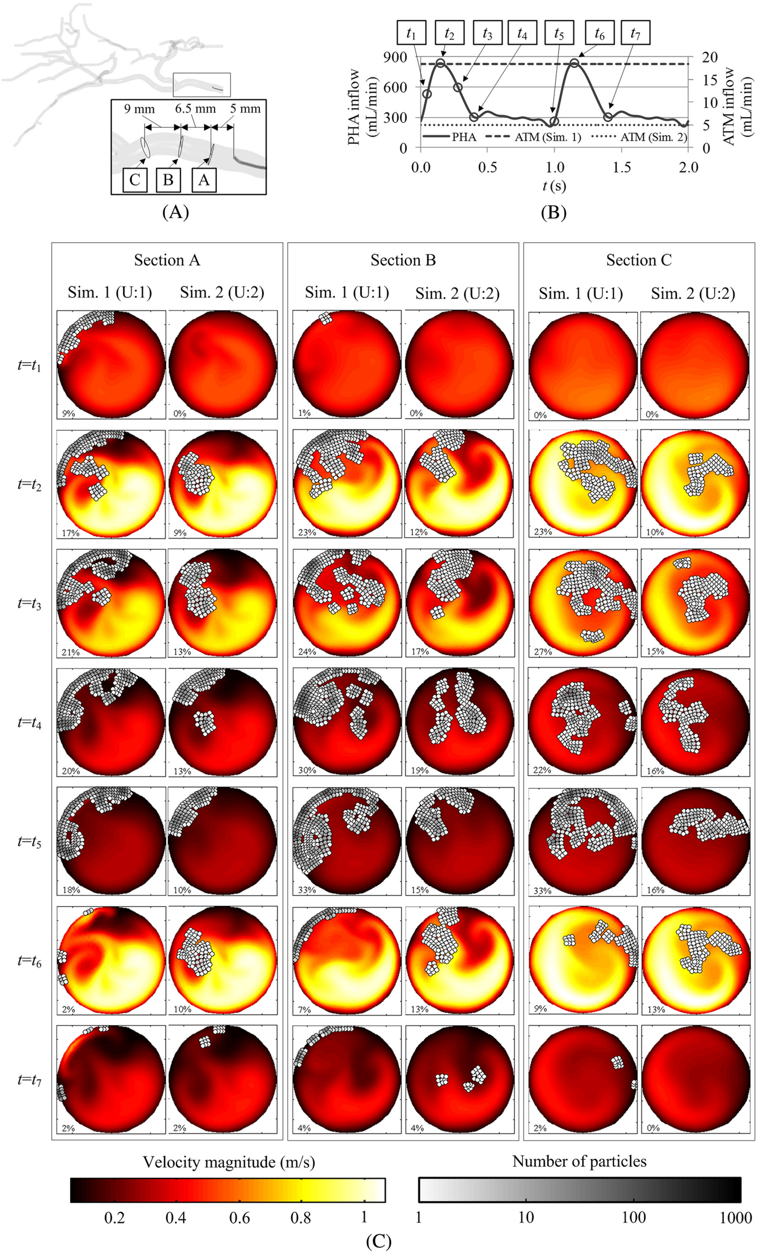

Figure 3.10: Comparing microsphere spread across the cross-section for three axial sections (A, B, C), seven timepoints (t_1 to t_7) and two injection flow rates ('1': 18.5 mL/min, '2': 5 mL/min). The percentages of particle spread are also denoted in the bottom left corner of each cell. For the same tip orientation (U, upwards) particles were almost always more spread out across the cross-section for the higher flow rate (1: 18.5 mL/min) than for the lower flow rate (2: 5 mL/min). From [11].

position (for example, from Figure 3.12, selective targeting of daughter vessel 2 and 3 seems possible using the current position under study).

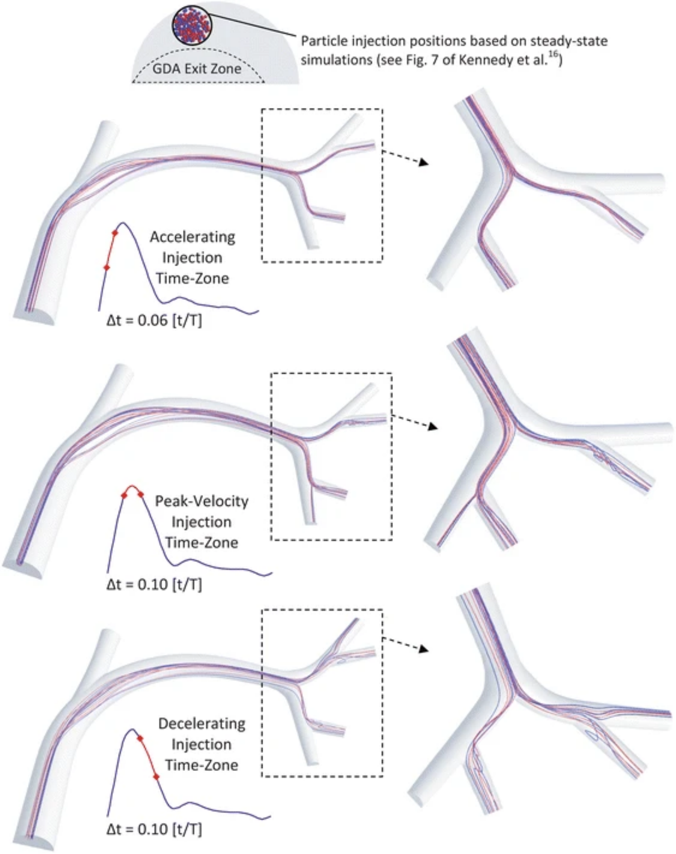

Figure 3.11: SIR-Sphere trajectories (in red) compared to Thera-Sphere trajectories (in blue). While it is visually difficult to see the impact of microsphere type on the trajectories, Basciano et al. (2010) noted the larger effect of the gravitational force on the heavier TheraSpheres. From [14].

In 2016, Aramburu et al. [106] also investigated the impact of microparticle type on the segment-to-segment particle distribution in their patient-specific geometry (see geometry in Figure 3.8A)). The two particle types modeled were SIR-Spheres, with a single diameter of 32 µm and a density of 1600 kg/m^3; and 99m-Tc-MAA microparticles, with a diameter of 15 µm and a density of 1100 kg/m^3. Aramburu et al. (2017a) noted that a skimming effect could occur in branches of considerable length, in which the larger particles tend to travel more centripetally (favoring main branches) and the smaller particles tend to travel more peripherally (favoring side branches).

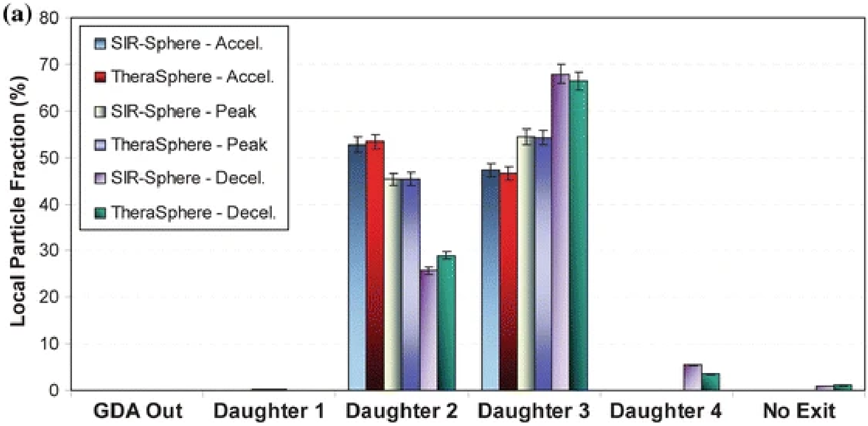

Figure 3.12: Comparing SIR-Sphere particle distributions to TheraSphere particle distributions. Clearly, both the timing of the injection (accelerating vs decelerating phase) and the selection of the spatial injection zone impact the particle distributions significantly. Particle properties also impact the distributions, but to a lesser degree. Adapted from [14].

They also noted that this effect could be negligible when the particles had to pass only a limited number of bifurcations to reach their intended destination (i.e. if total branch length was not considerably high). Therefore, Aramburu et al. [106] concluded that particle density and diameter were not critical parameters in terms of segmental particle distribution when comparing SIR-Spheres and 99m-Tc-MAA microparticles. Notably, they only studied particle distribution up to the segmental level, so this work did not consider the influence of potential intrasegmental events.

3.4 CURRENT CHALLENGES

While computer models of varying complexity (e.g. 0D, 3D) have been used to elucidate the impact of injection parameters using TARE, as explained in Section 3.3, significant steps still need to be made to make these computer models more realistic, prove their credibility for predicting patient-specific health outcomes, and to integrate them in a pre-treatment optimization tool. These challenges with the current state of research are discussed below, and will inform the thesis objectives as outlined in Section 3.5.

3.4.1 Feasibility of Patient-Specific Computational Modeling

As shown, 3D CFD models can be used effectively to quantify the impact of relevant clinical injection parameters on the treatment outcome. Since hepatic branching arterial networks are typically very complex and heterogeneous, running CFD analyses in multiple patient-specific hepatic arterial geometries is crucial. However, as more complex geometries and a wider range of clinical parameters are considered for sensitivity analyses on a patient-specific basis, the computational cost of these simulations will increase significantly, leading to high costs, high energy expenditure, and making these workflows generally unfeasible to be integrated into clinical practice. Therefore, strategies need to be devised to decrease computational cost, and make sensitivity analyses for patient-specific cases feasible.

3.4.2 Validation

Notably, CFD models (like all models) behave differently when compared to real-world systems, because some inputs cannot be measured accurately or because of assumptions that are made during model construction [118]. Therefore, steps need to be made to assess and improve model reliability.

Three important principles determine model reliability: (1) verification, (2) validation, and (3) uncertainty quantification (VVUQ) [119, 120]. Verification entails assessing whether a computational model solves the underlying mathematical problem correctly [120] (for CFD specifically, this relates to the selection of an appropriate grid size, reliable solution convergence criteria, etc.). To check whether the computational model uses the correct physics, validation is used to compare the numerical results to real-world experimental (in vitro, in vivo, ex vivo, etc.) results [120]. These experimental results can be generated in a controlled lab setting (in vitro), based on patient data (in vivo), or computed on tissue in an external environment (i.e. not the body) (ex vivo).

Preliminary in vivo validation has been carried out to show that CFD can be used to predict the segmental particle distribution [16] or tumor radioactive dose [121]. However, due to the limited number of patients on which this was tested in each study (3 or less), it is not clear whether their accuracy is high enough for clinical practice, whether the results are easily replicated, and how high the uncertainty is on the computed output. Hence, more extensive in vivo validation in a larger patient cohort is definitely needed. To our knowledge, ex vivo validation is very limited in this domain. However, it can be useful, as it is a much more realistic setting than in vitro models, and more easily controllable than in vivo experiments. Additionally, in vitro validation has only been carried out in simplified, planar geometries (as already explained in Section 2.4.1) up to the start of this PhD, which severely limits their interpretability. Hence, transferring in vitro validation to a patient-specific setting is a crucial step to make these models more usable.

3.4.3 Uncertainty Quantification

Uncertainty quantification relates to uncertainties in input parameters and how they translate into output uncertainties [120]. This can not only be done for clinical injection parameters, but also for numerical input parameters, such as boundary conditions. This is especially important when dealing with inputs that are variable and/or difficult to measure precisely. For example, it is well-known that boundary conditions in CFD introduce uncertainty because they are typically unknown. However, for this application specifically, the clinical parameter source of uncertainty, is also not be underestimated. Even if a specific clinical parameter is predicted by CFD to be very impactful, and we can determine their optimal value for a given patient-specific setting, it might not be possible to control this parameter at one specific, optimized value throughout the procedure. The clearest example is that of the catheter tip position, where we might use CFD simulation to determine the optimal catheter tip position to target the tumor (as done in Section 3.3.1), but it might be technically very difficult (or impossible) to control the catheter tip position throughout the procedure, and so variations in the catheter tip position will introduce uncertainty on the tumor dose. Hence, uncertainty quantification of both numerical input parameters and clinical injection parameters is necessary. However, uncertainty quantification typically requires a higher number of simulations, which is only feasible of the computational cost of a single simulation is limited. This is currently not the case, and severely limits the applicability of patient-specific CFD modeling for transarterial drug delivery.

3.4.4 Model Design

There is still a large gap between using computational models for investigative purposes (such as discussed in Section 3.3) and using computational models in clinical tools for preoperative optimization. In that regard, the CMMP as described by Kleinstreuer et al. [9] is still a very broad workflow, indicating conceptually how medical images may be converted into computer models which predict particle distribution. However, the possibilities of computer modeling and simulation are plentiful. To be used in the real world, the model design should be specific and detailed, with clarity on which inputs are used, which mathematical model is used, and which outputs are predicted (within a specific credibility level) [122]. Importantly, the clear definition of inputs and outputs is also needed to enable uncertainty quantification and validation, as stated above.

Alternatively to Kleinstreuer et al. [9], Roncali et al. [123] proposed a more concrete model design (CFDose), where they derived the radioactivity spread over the liver tissue for a specific patient based on medical images and simulation. While CFDose is already a much more specific model design, it is not yet a concrete model design for preoperative TARE optimization. For example, it (1) lacks crucial information that limits TARE procedures in the clinic, such as the vascular accessibility of suggested catheter tip locations, (2) does not perform uncertainty quantification on the output, or (3) does not consider that some injection parameters (e.g. cross-sectional tip position) are difficult to control in vivo. Hence, there is a need for specific model design that can be applied to pre-operatively optimize TARE procedures and considers all of the crucial aspects mentioned above.

3.5 Thesis Objectives

Summarizing the considerations above: while the CMMP was proposed as a general workflow for pretreatment optimization [9], both the patient-specific nature of these 3D CFD simulations, and the need for a high number of simulations to quantify both numerical and clinical uncertainty require more specific, feasible strategies to implement CFD in pretreatment planning, as well as patient-specific validation strategies.

Hence, the state-of-the-art of CFD studies at the start of this PhD lack (i) effective strategies to reliably cut down computational cost of patient-specific 3D CFD simulations, (ii) uncertainty quantification of numerical and clinical parameters in patient-specific geometries, (iii) validation techniques in patient-specific geometries, and (iv) a computational framework for treatment planning.

Based on these remaining challenges, we further specify the objective of this dissertation in different goals:

- **Goal 1: Simplification**: Implementing effective strategies for reliable reduction of the computational cost of our patient-specific 3D CFD models and verifying their reliability for particle distribution and tumor dose predictions. This will be the focus of Part II.

- **Goal 2: Uncertainty Quantification**: Using these simplification strategies to reduce the computational cost of our simulations enough to allow patient-specific uncertainty quantification of tumor dose due to uncertain clinical parameters, and perform sensitivity analysis of uncertain numerical input parameters. This will be the focus of Part III.
- **Goal 3: Patient-Specific In Vitro Validation**: Extension of the current in vitro validation methods in literature to realistic patient-specific hepatic arterial networks. This will be the focus of Part IV.
- **Goal 4: Model Design for Valorization**: Development of a feasible computational framework for TARE planning which considers both parameter sensitivity analysis and optimization, as well as other relevant parameters for treatment optimization, such as vascular accessibility or the uncertainty introduced by uncontrollable parameters. This will be the focus of Part V.

II

Simplification Strategies for CFD Modeling of Transarterial Therapies

Chapters

apud me omnia fiunt
Mathematicè in Natura
(to me,
everything in nature
becomes mathematical)

R. Descartes

CHAPTER 4

The Hybrid Model in Truncated Hepatic Arterial Trees

POSITIONING OF THE CHAPTER

Patient-specific 3D CFD simulations of intra-arterial blood flow and drug transport are typically computationally very costly. In the following Chapters 4, 5 and 6, we focus on techniques to cut down computational cost while still allowing to reliably predict the downstream microsphere distribution. Chapter 4 introduces a truncation algorithm to reduce the size of the physical geometry, which is verified for both planar and superficial catheter particle injection. Chapter 5 verifies the truncation technique for selective catheter injection of particles. Chapter 6 evaluates grid coarsening, reduction of the number of flow cycles, steady flow modeling as alternative simplification techniques. By the end of Chapter 6, we aim to have a clear view of which simplification techniques are reliable (and significantly cut down computational cost), and which techniques are not advised.

This chapter is based on the publication *A Hybrid Particle-Flow CFD Modeling Approach in Truncated Hepatic Arterial Trees for Liver Radioembolization: A Patient-Specific Case Study* (T. Bomberna et al., Frontiers in Bioengineering and Biotechnology, 2022) [19].

4.1 INTRODUCTION

With regards to clinical application, computational complexity of patient-specific 3D CFD simulations may hinder integration in clinical practice, since large computational times may negatively impact the potential of technology transfer to the clinical setting. Lower computational times are also necessary for uncertainty quantification and sensitivity analyses, which typically require a high number of model evaluations. Additionally, a clear and uniform workflow for these CFD simulations—including standards for the definition of hepatic arterial geometries, and inlet and outlet boundary conditions, which currently vary between computational approaches—is still lacking. Hence, this study aims to reduce the computational cost of these CFD approaches, while outlining a clear methodology to define the hepatic arterial geometry.

The main goal is to evaluate whether the particle distribution in a complex patient-specific geometry can be estimated by modeling the particle distribution in a truncated, simplified geometry, and assuming that the particles downstream of the truncated outlets distribute themselves proportional to the blood flow. This hybrid particle-flow model should significantly reduce the complexity of the computational approach, compared to explicit particle modeling in the full arterial geometry. Additionally, the fitness of the flow distribution (i.e., no explicit particle modeling) as a surrogate for particle distribution will also be evaluated.

Previously, Lertxundi et al. [124] introduced a segment-based truncation algorithm to simplify patient-specific arterial geometries, comparing truncated versions of 3 patient-specific geometries (with 1 catheter tip location for 2 geometries and 2 catheter tip locations for the other geometry). In their truncation strategy, branches perfusing the same segment downstream of the tip were grouped, and segments upstream of the tip were grouped. However, the main limit of this truncation strategy is that it only quantifies the particle distribution for the segments downstream of the catheter tip, and does not offer any information on intrasegmental particle distribution, which might still be of interest.

Here, the alternative pruning algorithm presented here goes beyond the state-of-the-art by using the hybrid particle-flow modeling assumption and a novel tumor region growing model. The hybrid particle-flow model might allow to estimate intrasegmental particle distribution, even if the intrasegmental branches are not included in the hepatic arterial geometry. Additionally, the region growing model can also inform outlet boundary conditions and identify the major arterial feeders of the tumor.

During this study, the hybrid particle-flow model for truncated hepatic arterial geometries will be evaluated for one planar injection (where particles are released over the entire vessel cross-section) and three catheter injections (where particles are only released from the catheter tip) for one patient-specific case.

4.2 METHODS

In Section 4.2.1, we discuss the simulations used in this study to evaluate the suitability of the hybrid particle-flow model in truncated arterial geometries. Details regarding the reconstruction and discretization of the full-complexity hepatic arterial geometry and the truncation algorithm are presented in Section 4.2.2. Next, the general mathematical background behind both multiphase models for blood and microsphere transport as well as inlet and outlet boundary conditions used throughout this dissertation are explained in Section 4.3. The specifics of the hybrid particle-flow model are discussed there as well. Finally, several metrics are introduced which will help compare the hybrid particle-flow model against the particle distribution in the full-complexity geometry in Section 4.3.3.

4.2.1 Study Design

In Table 4.1, an overview of the numerical simulations in this study are presented. In summary, this study considers the same set of simulations for a full-complexity hepatic arterial geometry (Geometry 1) and two arterial geometries with different levels of truncation (Geometry 2 & 3; see Section 4.2.2.2): one planar injection at a specified axial location (Sim. 1–3 in Table 4.1), and three catheter injections at specific cross-sectional tip locations in this plane (Sim. 4–12 in Table 4.1).

4.2.2 Geometry Development and Discretization

4.2.2.1 Baseline Geometry and Tissue-Perfusion Modeling

As approved by the Ethical Committee of the University Hospitals Leuven (UZ Leuven, Belgium), a patient-specific CT-image dataset of the hepatic arterial vasculature of an HCC patient was obtained by scanning the patient with a conebeam CT scanner (Philips Medical Systems, Netherlands) while intra-arterially injecting contrast agent

Table 4.1: Study design giving an overview of all simulations and their corresponding geometry, injection type and axial and cross-sectional tip location.

Simulation	Geometry	Injection	Tip location
1	Geometry 1	Planar	Axial Location 1
2	Geometry 2	Planar	Axial Location 1
3	Geometry 3	Planar	Axial Location 1
4	Geometry 1	Catheter	Inlet: Tip Location 1
5	Geometry 2	Catheter	Inlet: Tip Location 1
6	Geometry 3	Catheter	Inlet: Tip Location 1
7	Geometry 1	Catheter	Inlet: Tip Location 2
8	Geometry 2	Catheter	Inlet: Tip Location 2
9	Geometry 3	Catheter	Inlet: Tip Location 2
10	Geometry 1	Catheter	Inlet: Tip Location 3
11	Geometry 2	Catheter	Inlet: Tip Location 3
12	Geometry 3	Catheter	Inlet: Tip Location 3

into the left and right branches of the PHA. The hepatic arteries were segmented in Mimics (Materialise, Belgium) based on the contrast difference between the arterial and venous trees in the arterial phase. A large tumor nodule (estimated volume: 310 ml) was identified. 3D reconstructions of the tumor mass and the hepatic arterial tree (with 1 inlet at the PHA level and 48 outlets) can be found in Figure 4.1A.

For CFD purposes, the division of the hepatic artery outlets into tumor-perfusing outlets and healthy tissue-perfusing outlets is crucial in order to know which vessels should be targeted for the envisioned treatment. Therefore, the tumor perfusion percentage (TPP) of each outlet was determined as the percentage of the tumor volume perfused by each outlet (e.g., 0% for solely healthy tissue-perfusing outlets). To calculate the TPP of the 48 outlets, an in-house developed region growing model was used ([125]). First, the centerlines of the hepatic arterial trees were determined using the open-source Vascular Modelling Toolkit (vmtk.org). For each artery outlet segment, the centerline points between the final bifurcation and the outlet surface were labelled as seed points. Second, the hepatic arteries and tumor mass were included in a voxelated bounding box, consisting of $100 \times 100 \times 100$ cubic voxels (with a $\approx 1.2 \cdot 10^{-3}$ m edge length). During region growing, voxels were added in the six orthogonal directions starting from the seed points for each segment, until all voxels within the tumor were assigned to one of the outlets. Region growing occurred simultaneously for all branches. As a result, each arterial branch was associated with a certain perfusion zone of the tumor (and, by extension, a certain perfused volume of tumor tissue). Finally, the tumor volume perfused by each outlet was divided by the total tumor volume, giving the TPP.

In Figure 4.1B, the tumoral mass is divided in regions to show how the different segmental arteries contribute to tumor perfusion according to the tumor region growing model. Generally, the liver can be divided in eight segments according to Couinaud's classification criteria ([41]). For the color code in Figure 4.1B, the liver is anatomically divided into five sections based on these segments: the caudate lobe (Segment 1, in yellow), the left lateral section (Segments 2 and 3, in purple), the medial section (Segment 4, in orange), the right anterior section (Segments 5 and 8, in green), and the right posterior section (Segments 6 and 7, in blue). For the TPPs in Figure 4.1B, the segmental arteries are colored according to the same color code, but the annotations for Segments 5 and 8 are split because of the considerable difference in tumor perfusion (2.64% vs. 55.6%; the Segment 5 artery clearly points away from the tumor, while the Segment 8 artery points towards the tumor).

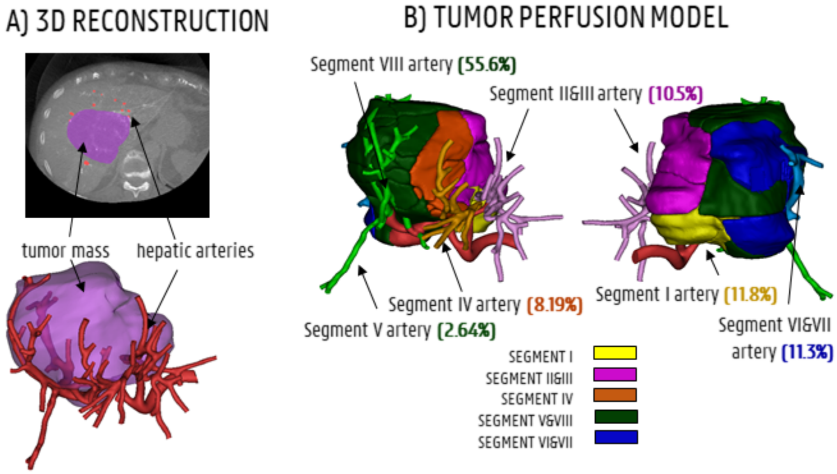

Figure 4.1: (A) CT-slice and 3D reconstruction showing the tumor mass (purple) and hepatic arteries (red). (B) The tumor perfusion model shows to which degree the segmental arteries I, II and III, IV, V and VIII, and VI and VII contribute to tumor perfusion (TPPs in %).

4.2.2.2 Truncation Algorithm

The baseline hepatic arterial tree was imported into ANSYS SpaceClaim (Ansys, United States) and manually reconstructed to generate a solid model. During the truncation process (see below), the arterial tree was pruned at three different levels, generating three solid arterial tree models with varying degrees of complexity. The full-complexity hepatic arterial tree was denoted as Geometry 1 (48 outlets, no pruning, shown in Figure 4.1A, with schematic illustration in Figure 4.2A). The diameters of these 48 outlets are given in Table 4.2 (estimations were made using the Fit Centerline and Best Fit Diameter tools in Mimics (Materialise, Belgium)). The truncation process is explained in detail below.

First, distal bifurcations containing outlets with TPPs ≤1% (orange branches in Figure 4.2A) were pruned. If the total TPP of the bifurcations containing one or more of these orange outlets was >1%, the resulting outlet (i.e., after pruning) was denoted as *tumor* (green dotted ellipses in Figure 4.2A); otherwise, the resulting outlet was denoted as *healthy* (red dotted ellipses in Figure 4.2A). Outlets which where impossible to prune due to the lack of cutting space (i.e., when bifurcation points were located so close to each other that a proper cut could not be made) were preserved (e.g., branches 2 and 3 in Figure 4.2A,B). In total, the total number of outlets was reduced from 48 to 38 outlets in this step. After pruning, some outlets were located so close to the preceding bifurcation (<5 mm distance on the centerline) that fluid flow into these pruned outlets would not be properly developed. Therefore, these outlets were artificially extruded to a total length of 20 mm (e.g., branches 22 and 25 in Figure 4.2B). Hence, the first part of the truncation process resulted in the second solid model, denoted as Geometry 2 (38 outlets, schematic in Figure 4.2B). The numbering of the resulting outlets after pruning was done according to the lowest number of the group of outlets that were pruned (i.e., if outlets 22, 23 and 24 were pruned into a single outlet, the resulting outlet was given the number 22). In the next step of the truncation process, bifurcations containing outlets which perfused the same tissue type (either healthy or tumor) were pruned (green and red circles in Figure 4.2B); bifurcations which contained both were not simplified (e.g., the bifurcation consisting of branches 37–38 and 39–46 in Figure 4.2B). The few remaining outlets with TPP <1% (orange branches in Figure 4.2B) were pruned according to the same methodology as before: if the total bifurcation to which the outlet belonged had a TPP>1%, the resulting outlet was considered *tumor* (e.g., the case for branches 30–31, which were pruned and resulted in outlet 29 in Figure 4.2D); if the TPP<1%, it was considered *healthy*. Similarly, pruned outlets that were too short (<5 mm on the centerline) were extended to a total length of 20mm (e.g., branch 6 and 44 in Figure 4.2D). The second step of the truncation process resulted in the third and final solid model, denoted as Geometry 3 (17 outlets, Figure 4.2C). In Geometry 3, the remaining branches with TPPs $\leq$1% - which could not be pruned in steps one or two - are considered *tumor* if the tumor flow contribution in that branch is >50% of the total flow through that branch (considering that each of these branches perfuses both the tumor and a fraction of the healthy tissue), and considered as *healthy* if the tumor flow contribution is <50%. A detailed explanation of how the healthy and tumor flow contributions were determined is outlined in Section 4.3.2.2. As a result, 8 out of 17 branches in Geometry 3 (i.e., branches 1, 3, 4, 5, 20, 29, 39, and 44) are considered as *tumor* (green branches in Figure 4.2D); these are the main arterial feeders that feed 98% of the tumor tissue. Additionally, in these feeders, the tumor flow contribution ranges from 48 to 94% of the total flow through the feeders.

In Figure 4.2E, three 2D-views of the 3D models of the hepatic arteries of Geometry 3 are shown, indicating the relative position of the main arterial feeders to the tumor mass. It can be seen that the main arterial feeders are either pointing towards the tumor mass, or are located inside the tumor mass. Importantly, the truncation algorithm did not allow for truncation of the two most proximal bifurcation levels in the arterial tree, since it is assumed that these bifurcations could play an important role in downstream particle distribution.

4.2.2.3 Catheter Modeling

The truncation process resulted in three arterial geometries of differing complexity, with the number of outlets varying from 17 (Geometry 3) to 48 (Geometry 1). For each geometry, the inlet was extruded by 80 mm in SpaceClaim (Ansys, United States). This was done to account for the entrance length (estimated as ~80 mm) so that a computationally straightforward, uniform velocity could be applied at the extruded inlet, and a physiological parabolic-like velocity profile would develop before the “true” inlet of the geometry. Next, four versions of the solid model of each geometry were made: three with catheters embedded in the lumen of the PHA at different cross-sectional positions (see Figure 4.3B), and one without a catheter (see Figure 4.3A). The catheter was modeled as a thin-walled, straight tube, with a total length of 80 mm and a representative inner diameter of 0.7 mm. In total, 12 solid models were made, totaling 3 planar injections in Geometries 1–3 (Sim. 1–3 in Table 4.1) and 9 catheter injections in Geometries 1–3 (Sim. 4–12).

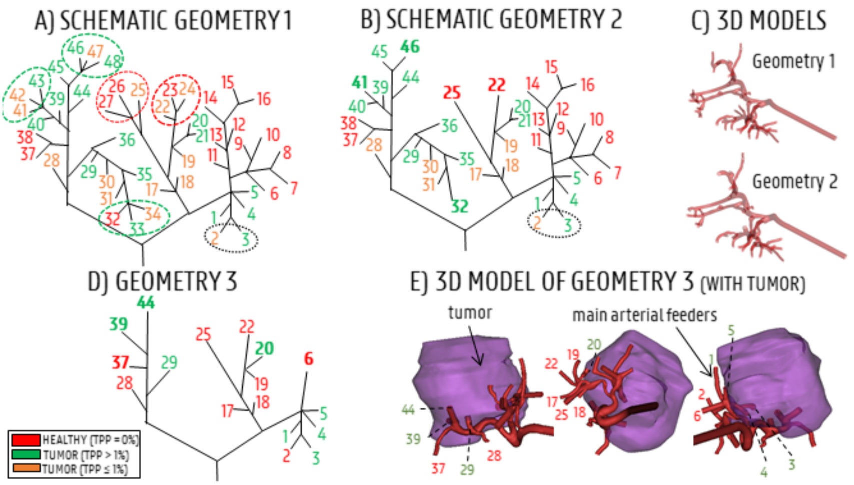

Figure 4.2: (A) Schematic of Geometry 1. Red branches indicate healthy branches (TPP = 0%), orange branches indicate branches that perfuse a small fraction of the tumor (TPP≤1%), green branches indicate branches that perfuse a significant portion of tumor tissue (TPP>1%). Ellipses indicate which branches of Geometry 1 were pruned. (B) Schematic of Geometry 2; bold indices indicate where arteries were pruned. (C) 3D reconstructions of Geometries 1 and 2. (D) Schematic of Geometry 3, with the main arterial feeders denoted in green and the healthy-perfusing branches denoted in red. (E) 3D model of Geometry 3 (3 views), showing the relative position of the 17 outlets with respect to the tumor mass.

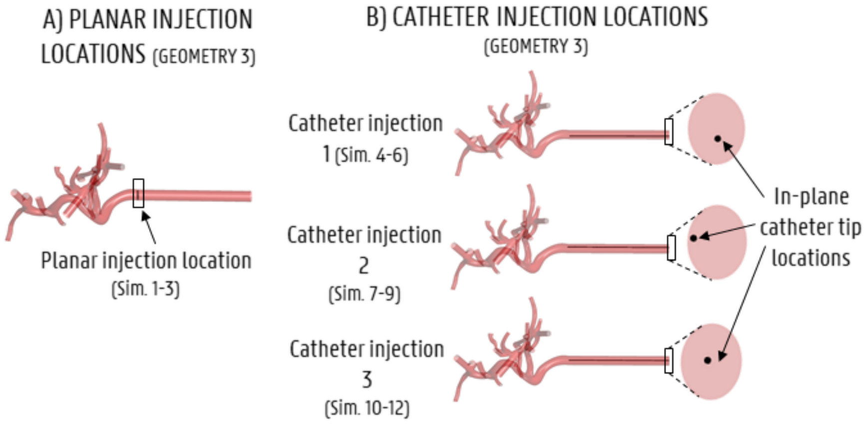

Figure 4.3: Particle injection locations for all simulations (shown here for Geometry 3). (A) Axial injection location for the planar injection, (B) axial and in-plane catheter tip locations for the 3 catheter injections.

Table 4.2: Overview of the sizes and flow fractions for the 48 outlets of Geometry 1.

Outlet	**Diameter (mm)**	**Flow fraction (%)**
1	3.58	4.07
2	3.23	0.79
3	4.94	4.37
4	4.12	3.45
5	3.39	2.99
6	3.31	0.69
7	3.05	0.62
8	3.08	0.62
9	3.35	0.62
10	3.33	0.62
11	3.6	0.34
12	3.22	0.11
13	3.36	0.11
14	3.26	0.11
15	3.10	1.24
16	2.77	1.24
17	3.25	3.66
18	3.20	1.80
19	3.35	0.33
20	4.08	3.05
21	3.26	0.84
22	3.26	0.23
23	2.29	0.11
24	3.34	0.12
25	3.11	0.50
26	3.48	0.22
27	3.01	0.22
28	3.32	3.63
29	3.40	2.60
30	2.76	1.33
31	3.01	0.26
32	3.02	0.07
33	2.74	0.77
34	2.94	0.07
35	3.35	0.97
36	4.41	8.94
37	3.73	0.82
38	2.85	0.82
39	3.33	13.32
40	2.75	6.03
41	3.25	3.39
42	3.08	2.99
43	2.92	6.00
44	3.69	2.59
45	3.55	3.95
46	3.01	4.32
47	3.81	0.59
48	2.54	3.47

4.2.2.4 Geometry Discretization

The twelve solid models were imported into ANSYS Fluent Meshing (Ansys, United States). For all geometries, the minimum and maximum size of the surface mesh elements were set as $8 \cdot 10^{-6}$ m and $3.5 \cdot 10^{-4}$ m, respectively, with a growth rate of 1.2. For the solid models without catheters embedded in the lumen, the size of the tetrahedral volume elements of the arterial body was set to $3 \cdot 10^{-4}$ m (which was determined through mesh sensitivity studies). Three layers of prism elements were enabled near the walls to better capture the near-wall fluid behavior, with a growth rate of 1.2. This resulted in meshes of $6.68 \cdot 10^6$, $6.19 \cdot 10^6$, and $3.97 \cdot 10^6$ elements for Geometry 1, 2 and 3, respectively (Sim. 1–3). For the solid models with catheters, the arterial body sizing was kept the same, while the tetrahedral element body sizing of the catheter was set at $7 \cdot 10^{-5}$ m (determined through mesh sensitivity studies). The surface mesh of the catheter inlet was sized at $3 \cdot 10^{-5}$ m. Three inflation layers of prism elements near the arterial and catheter walls were also enabled. For Geometry 1, the three catheter models resulted in meshes of $9.74 \cdot 10^6$, $9.59 \cdot 10^6$, and $9.73 \cdot 10^6$ elements (Sim. 4, 7, 10, respectively). For Geometry 2, the three meshes consisted of $9.08 \cdot 10^6$, $8.94 \cdot 10^6$ and $10.3 \cdot 10^6$ elements (Sim. 5, 8, 11, respectively); for Geometry 3, the three meshes contained $6.45 \cdot 10^6$, $6.32 \cdot 10^6$ and $6.45 \cdot 10^6$ elements (Sim. 6, 9, 12). Next, the twelve meshes were imported into Fluent (Ansys, United States) to model the flow and microparticle behavior.

4.3 NUMERICAL MODEL

4.3.1 Multiphysics Flow and Microparticle Model

To model the flow and microparticle distribution in the hepatic arterial geometries, a multiphase approach was employed which considers both the continuous phase (blood) and the discrete phase (microparticles). The governing equations of conservation of mass and momentum are given in Equation 4.1 (where $\vec{u}$ [m/s] is the velocity vector) and 4.2 (where ρ [kg/m^3] is the density of the fluid, $\vec{\vec{\tau}}$ [Pa] is the shear stress tensor, and $\vec{f}$ [N] are the forces acting on the fluid), respectively:

$$\vec{\nabla} \cdot \vec{u} = 0 \tag{4.1}$$

$$\rho(\frac{\partial \vec{u}}{\partial t} + (\vec{u} \cdot \vec{\nabla})\vec{u}) = -\nabla p + \vec{\nabla} \cdot \vec{\vec{\tau}} + \vec{f} \tag{4.2}$$

Blood is modeled as an incompressible, shear-thinning fluid with a density of 1060 kg/m^3. Generally, as shown in Equation 4.3, shear stress tensor ($\vec{\vec{\tau}}$ [Pa]) depends on the blood velocity and apparent blood viscosity ($\mu(\dot{\gamma})$ [Pa·s]), which depends on the shear rate ($\dot{\gamma}$ [s^{-1}]). The viscosity of blood is modeled with a simplified Quemada model [126], which considers that viscosity depends on the hematocrit value and shear rate. In these equations, μ [Pa·s] is the dynamic viscosity of the fluid, $\dot{\gamma}$ [s^{-1}] is the shear rate, μ_0 is the minimum viscosity, μ_∞ is the asymptotic viscosity, τ_0 [Pa] is the apparent yield stress and λ [s^{-1}] is the shear stress modifier. These parameters take the following values adapted from literature: $\mu_0 = 0.00309$ Pa·s, $\mu_\infty = 0.002654$ Pa·s, $\tau_0 = 0.004360$ Pa, and $\lambda = 0.02181$ s^{-1}. According to the simplified Quemada model, viscosity decreases with increasing shear rate, but is assumed equal to μ_0 for higher shear rates for the sake of computational simplicity, as can be seen in Equation 4.4. The shear rate can be calculated according to Equation 4.5.

$$\vec{\vec{\tau}} = \mu(\dot{\gamma})[\triangledown\vec{u} + (\triangledown\vec{u})^T] \tag{4.3}$$

$$\mu(\dot{\gamma}) = max\{\mu_0, (\sqrt{\mu_\infty} + \frac{\sqrt{\tau_0}}{\sqrt{\lambda} + \sqrt{\dot{\gamma}}})^2\} \tag{4.4}$$

$$\dot{\gamma} = \sqrt{\triangledown\vec{u}[\triangledown\vec{u} + (\triangledown\vec{u})^T]} \tag{4.5}$$

Microparticles are modeled as inert spheres with a diameter (d_p) of $40 \cdot 10^{-6}$ m and a density (ρ_p) of 1600 kg/m^3, similar to SIR-Spheres. The microparticle trajectories throughout the hepatic arterial geometries can be calculated by integrating the force balance (which equals the product of particle mass (m_p [kg]) and particle acceleration ($\frac{d\vec{u_p}}{dt}$ [m/s^2])), as given by Newton's second law in Equation 4.6, twice.

$$m_p\frac{d\vec{u_p}}{dt} = \vec{F_D} + \vec{F_G} + \vec{F_P} + \vec{F_V} \tag{4.6}$$

where the following forces acting on the microparticles are considered: the gravitational force, $\vec{F_G}$ (Equation 4.7; where $\vec{g}$ [m/s^2] is the gravitational vector); the drag force, $\vec{F_D}$ (Equation 4.8, where C_D is drag coefficient, $\vec{u_p}$ [m/s] is the particle velocity vector, and Re_p is the particle Reynolds number calculated according to Equation 4.9);

the pressure gradient force, $\vec{F_P}$ (Equation 4.10); and the virtual mass force, $\vec{F_V}$ (Equation 4.11, where C_V is the virtual mass coefficient).

$$\vec{F_G} = m_p\vec{g}\frac{(\rho_p - \rho)}{\rho_p} \tag{4.7}$$

$$\vec{F_D} = m_p\frac{18\mu}{\rho_p d_p^2}\frac{C_D Re_p}{24}(\vec{u} - \vec{u_p}) \tag{4.8}$$

$$Re_p = \frac{\rho d_p \mid \vec{u_p} - \vec{u} \mid}{\mu} \tag{4.9}$$

$$\vec{F_P} = m_p\frac{\rho}{\rho_p}(\vec{u_p} \cdot \vec{\nabla})\vec{u}) \tag{4.10}$$

$$\vec{F_V} = C_V m_p\frac{\rho}{\rho_p}((\vec{u_p} \cdot \vec{\nabla})\vec{u} - \frac{d\vec{u_p}}{dt}) \tag{4.11}$$

4.3.2 Boundary Conditions

4.3.2.1 Inlet Boundary Conditions

For the inlet boundary conditions, a spatially uniform velocity profile was imposed, while the original geometry inlet was extruded by 80 mm to account for the entrance length needed to let a more physiological flow profile develop. At the extruded inlet, a pulsatile waveform with a period of 0.8 s and a minimum/mean/max inflow velocity of 0.041/0.121/0.260 m/s was prescribed (see Figure 4.4). The waveform was derived from an in-house 1D model of the arterial circulation in humans ([127]) and scaled so that the average inflow equaled the inflow as determined by the outlet boundary conditions (see below).

Particles were injected every 0.01 s throughout the third cycle (allowing two prior cycles for flow development). For the planar injections (Sim. 1–3), particles were injected over the entirety of the axial injection plane (see Figure 4.3A). For the three catheter injections (Sim. 4–12), particles were injected (together with blood) at the start of the catheter at the hepatic arterial inlet corresponding to three different cross-sectional catheter tip locations (see Figure 4.3B). The particle injection velocity was set at 0.12 m/s (which corresponds with the mean blood flow velocity around the catheter tip), leading to a catheter flow rate of 2.77 ml/min.

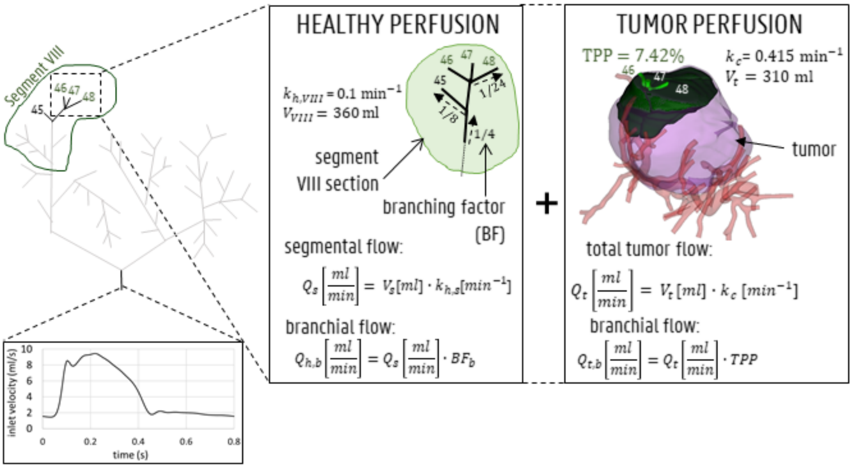

Figure 4.4: Inlet flow curve displayed for 1 representative cardiac cycle of 0.8 s. For the outlet boundary condition methodology, both healthy and tumoral flow contributions (which is 0 for outlets perfusing 0% of the tumor mass) are calculated for each outlet (shown here for outlets 46, 47, 48 in segment VIII).

4.3.2.2 Outlet Boundary Conditions

Since the tumoral mass was mainly peripherally vascularized, it was considered likely that the arterial feeders of the tumor also, partly, perfused the surrounding healthy parenchyma. Therefore, the outflow of each outlet (denoted here as b) of Geometry 1, Q_b [ml/min], was considered as the summation of two flow terms: the healthy flow contribution, $Q_{h,b}$ [ml/min], and the tumoral flow contribution, $Q_{t,b}$ [ml/min]. The healthy flow contribution for each outlet b of Geometry 1, $Q_{h,b}$, was determined according to the methodology devised by Aramburu et al. [128]. First, the volumes of each of the eight hepatic segments, V_s [ml], were set by scaling the literature-based segmental volumes to match the total liver volume of this patient-specific case (which was estimated as 1,357 ml in Mimics). Second, the total segmental arterial flow perfusing each segment s, Q_s [ml/min], was defined as:

$$Q_s = V_s \cdot k_h \tag{4.12}$$

where k_h [1/min] is the healthy perfusion parameter, which equals 0.100 1/min (considered the same for all segments and determined by Aramburu et al. [128]). Third, the total segmental flow was divided over the different outlets perfusing one segment. From the CT-scans and the 3D model, it was derived which of the 48 outlets of Geometry 1 perfused which hepatic segment. Assuming that, within a segment, the flow split occurs symmetrically along each bi- or trifurcation, the healthy flow contribution of one arterial outlet, $Q_{h,b}$, could be determined from the segmental flow, Q_s by considering the intrasegmental branching fraction BF_b(i.e., 1/2 for the first bifurcation, 1/4 for the second bifurcation, etc.).

$$Q_{h,b} = Q_s \cdot BF_b \tag{4.13}$$

Concurrently, the tumoral flow contribution for outlet b, $Q_{t,b}$ [ml/min], can be directly determined from the TPP of the region growing model. Similar to the methodology above, the total tumoral flow, Q_t [ml/min] , can be calculated from the perfusion parameter for cancerous tissue, k_c [1/min], and the tumoral volume, V_t [ml]:

$$Q_t = V_t \cdot k_c \tag{4.14}$$

Aramburu et al. previously theorized that, since the metabolic demand of tumor tissue is typically higher than that of healthy tissue, this should be reflected in the perfusion parameter, k. Here, k_c was set equal to 0.415 1/min, over four times higher than the healthy perfusion parameter, k_h (as previously estimated by Aramburu et al. [128]). Next, since the TPP reflects the fraction of tumoral volume that was perfused by one outlet, multiplying the TPP [%] with the total tumoral flow, Q_t, gives the tumoral flow contribution of each branch.

$$Q_{t,b} = Q_t \cdot TPP \tag{4.15}$$

Finally, as explained before, the total outflow in branch b is the summation of the healthy and tumoral flow (which equals zero for healthy-perfusing branches) terms:

$$Q_b = Q_{h,b} + Q_{t,b} \tag{4.16}$$

The outflow boundary condition methodology is also shown in Figure 4.4 (for outlets 46, 47 and 48). In Table 4.2, the flow fractions (calculated according to the methodology outlined above) are given for each outlet in Geometry 1. Once Q_b is determined for all outlets of Geometry 1, the total inflow through the inlet (through the principle of mass conservation) is also fixed. The healthy inflow contribution was 136 ml/min, while the tumoral inflow contribution was 129 ml/min, giving a total hepatic arterial inflow of 264 ml/min. This value was used to appropriately scale the inflow waveform, which was determined previously from the 1D model. The 1D inlet velocity waveform for 1 cardiac cycle is also shown in Figure 4.4. At the walls, the "no-slip" boundary condition was employed for the fluid phase. For the microparticles, the tangential and normal wall restitution coefficients were set to 1.

4.3.2.3 Solver Settings

For pressure-velocity coupling, the SIMPLE algorithm was used; for spatial discretization, the gradient least-squares cell-based scheme was used; for pressure and momentum the second-order and second-order upwind schemes were used, respectively. The under-relaxation factors were kept at default (0.3 for pressure, 0.7 for momentum, 1 for density and body forces). The solution was initialized using a hybrid initialization scheme of 10 iterations. The time step size was varied between $0.5 \cdot 10^{-3}$ s (for the acceleration and decelerating part of the cycle) and $1 \cdot 10^{-3}$ s (for the flatter parts of the cycle). The maximum number of iterations specified for each time step was 50. Absolute globally scaled residuals lower than $1 \cdot 10^{-5}$ were attained during every time step. Importantly, the particle distribution is sensitive to the total computational time: the more flow cycles are run, the more particles will exit the domain. To decide on the limit between convergence of the particle exit fractions and unnecessary computational time, additional flow cycles were run until <1.5% of the total injected particles exited in the latest cycle (leading to a range of simulations running for 9–14 cycles).

4.3.3 Post-Processing

4.3.3.1 Particle Grid Methodology

Particle Release Maps (PRMs) are typically used to visualize the impact of the cross-sectional injection location (for a given axial plane) on particle fate for a specific injection timing. Combining PRMs of multiple injection timings to visualize the impact of the cross-sectional injection location on particle fate throughout the cardiac cycle yields the Composite Particle Release Maps (CPRMs, as introduced by Childress et al. [116] for simplified arterial geometries). Previously, Childress and Kleinstreuer [129] also plotted PRMs against background reference grids to calculate the number of matching subsections between different PRMs (again for simplified geometries).

Here, we use uniform reference grids to systematically replot the PRMs and call this the Particle Grid methodology, allowing to compute Particle Release Grids (PRGs) and Composite Particle Release Grids (CPRGs). The added value of the Particle Grid methodology is that comparing PRMs for different axial planes is difficult, because the density of the plane points may vary between different injections, which may result in unequal comparisons. This is not the case for PRGs, due to the use of the reference grid. In our Particle Grid methodology for patient-specific arterial geometries, CPRGs are generated in three succinct steps: 1) generation of Particle Release Maps (PRMs), spatially encoding these PRMs into Particle Release Grids (PRGs) by uniform resampling inside a two-dimensional plane, and 3) combining information of different PRGs, generated at different injection timings, into one CPRG representing the full cardiac cycle.

First, Particle Release Maps (PRMs) are generated as color-coded visualizations of the axial injection plane at a specific injection timing, showing through which outlet a particle, injected at a specific cross-sectional location, exits (see Figure 4.5A for an example). As defined in Figure 4.5B, injection positions leading to particles exiting through one of the main arterial feeders of the tumor are annotated in green ("tumor"); injection positions leading to particles exiting through one of the healthy-perfusing branches are annotated in red ("healthy"); and injection positions leading to particles getting stuck and not exiting the domain are annotated in black ("no exit"). Next, Particle Release Grids (PRGs) are generated by plotting PRMs on a two-dimensional reference grid of equally-sized cells with a spacing of $1 \cdot 10^{-4}$ m (Figure 4.5C). For each grid cell, only particle injection positions within the cell limits are considered: if all injected particles within that cell exit through tumor-perfusing branches, the cell value is denoted as "tumor" (colored in green); if all injected particles exit through healthy-perfusing branches, the cell value is denoted as "healthy" (red); if all injected particles remain stuck in the domain, then the cell value is defined as "no exit" (black); if some injected particles exit through tumor-perfusing branches and others through healthy-perfusing branches (or not exiting at all), the cell value is denoted as "spatially uncertain" (gray); if no particles were injected, the grid cell is denoted as "no value" (white) (Figure 4.5B). Note that the grid spacing must be patient-specific to balance the number of gray and white cells, as a grid spacing that is too large will result in mostly gray cells, and a grid spacing that is too small will result in a large number of white cells. For time-dependent inflows, multiple injection bursts occur throughout the injection cycle at specified intervals, and a PRG can be generated for each injection burst (see Figure 4.5D for a selection of PRGs at four injection timings). Since the spatial grids are identical for each burst, PRG cell values can be compared across different injection timings, resulting in the CPRG cell value. For this study, the CPRGs were composed based on eight selected injection timings with a spacing of 0.1 s (1.6-2.3 s) to represent temporal variation during the full cardiac cycle. The value of the CPRG cells is defined as follows (Figure 4.5E): if most PRG cells of the selected timings (>75%) are "tumor" (green), the CPRG cell value is denoted as "tumor/constant" (green); if most PRG cells (>75%) are "healthy" (red), the CPRG cell value is denoted as "healthy/constant" (red); if most PRG cells (>75%) are "no exit" (black), the CPRG cell value is denoted as "no exit/constant" (black); if <75% but >50% of PRG cells throughout injection is "tumor", the cell value is denoted as "tumor/mostly" (yellow); if <75% but >50% of PRG cells is "healthy", the cell value is denoted as "healthy/mostly" (orange); if PRG cells are divided between "tumor", "healthy" and "no exit" without any of the above rules applying, then the resulting value is "temporally uncertain" (pink); however, if PRG cells are divided, but >37.5% of cells are "no value" (white), then the CPRG cell is denoted as "no value" (white); and similarly, if >37.5% of the cells are "spatially uncertain" (gray), the CPRG cell is denoted as "spatially uncertain" (grey), as well. As a result, merging multiple PRGs into a Composite Particle Release Grid (CPRG) combines spatial and temporal information on particle fate (Figure 4.5F).

4.3.3.2 Grid-Based Particle Distribution

For the planar injections, the PRGs for all injection timings throughout the injection cycle can be used to determine the grid-based particle distribution. For each outlet x, the "cell fraction" (or CF_x) can be determined, which is the number of grid cells associated with outlet x divided by the sum of the number of cells associated with one of the 48 outlets and the "no exit" outlets (Equation 4.17).

$$CF_x = \frac{\#cell_x}{\sum_{x=1}^{48} \#cell_x + \#cell_{noexit}} \tag{4.17}$$

For Geometries 2 and 3, the CF can only be calculated for the 38 and 17 outlets of those geometries, respectively. Therefore, to

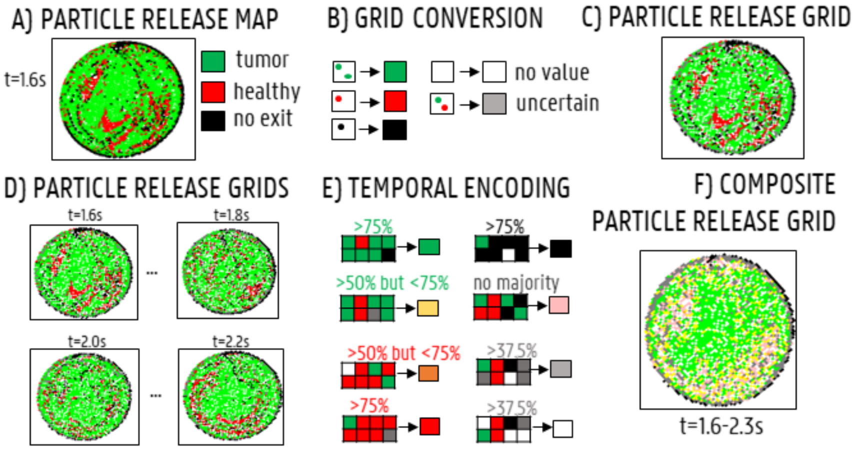

Figure 4.5: Generating Composite Particle Release Grids (CPRGs): (A) Particle Release Maps show the relation between injection location and particle fate (green: tumor, black: no exit, red: healthy, gray: spatially uncertain, white: no value). (B) By defining a reference grid and assigning each grid cell a color according to the particle fate of the injection positions within that cell, a Particle Release Grid (PRG) is obtained. (C) PRG for injection at the start of the cycle (1.6 s). (D) PRGs visualized for four injection timings (1.6 s, 1.8 s, 2.0 s, 2.2 s). (E) By comparing PRG cell values for different injection timings, a CPRG is generated (green: "tumor" for >75% of the timings, red: "healthy" for >75% of the timings, yellow: "tumor" >50%, orange: "healthy" >50%, black: >75% "no exit", pink: no majority fate found, gray: >37.5% "uncertain", white: >37.5% "no value"). (F) CPRG generated for the full cycle, based on 8 injection timings (1.6–2.3 s, with a spacing of 0.1 s).

determine the particle distribution at all 48 outlets of the original geometry, it is assumed that, beyond the truncated outlets of Geometry 2 and 3, particles distribute themselves proportional to the imposed flow distribution of Geometry 1. The resulting model is a hybrid particle-flow model, where particle distribution is modeled until the level of the truncated outlets, and the remainder of the particle distribution is modeled by the flow distribution. As a result, the CFs for Geometry 2 and 3 are not technically the same "cell fractions" as for Geometry 1; in these truncated geometries, they are named the "truncated cell fraction" (or TCF), and can be calculated as:

$$TCF_x = CF_{x*} \cdot FF_x \tag{4.18}$$

where FF_x is the flow fraction of outlet x (Q_x in Eq. 4.19), i.e., the outflow BC of outlet x in Geometry 1 divided by the outflow BC of the upstream, truncated outlet $x*$ in Geometry 2 or 3 (Q_{x*} in Equation 4.19). As a simple example, if a trifurcation of equal-flow branches (x_1-x_3) in Geometry 1 is simplified into a truncated single branch ($x*$) in Geometry 2, the outflow BC in the truncated single branch $x*$ will be three times the flow in any of the original trifurcation branches x_1-x_3; consequently, FF_x will be 1/3, and particles exiting outlet $x*$ in Geometry 2 will be assumed to distribute evenly among branches x_1-x_3). Hence, FF_x can simply be determined as:

$$FF_x = \frac{Q_x}{Q_{x*}} \tag{4.19}$$

4.3.3.3 Catheter Particle Distribution

For the catheter injections in Geometry 1, the particle distribution (also deemed the "exit fraction" (EF_x) in Equation 4.20) can simply be calculated as the fraction of the number of particles exiting through outlet x over the total number of particles which exit the catheter (Equation 4.20). Again, the truncated EFs (TEFs) are calculated by considering that the particles exiting the outlets in Geometry 2 and 3 distribute proportionally to the flow distribution (Equation 4.21), with FF_x defined as before.

$$EF_x = \frac{\#particles_x}{\#particles_{catheter-exit}} \tag{4.20}$$

$$TEF_x = \frac{EF_{x*}}{FF_x} \tag{4.21}$$

4.4 RESULTS

To determine the impact of geometry truncation on the particle distribution, the planar and catheter injections in each of the three geometries are compared. First, the CPRGs are compared in Section 4.4.2.1, both visually and quantitatively (based on the TD distribution for a number of randomly sampled catheter injection locations). Second, the grid-based particle distribution (i.e., (T)CFs) for the planar injections (Section 4.4.2.2) and the (T)EFs resulting from catheter injections (Section 4.4.3) are compared in each corresponding geometry.

4.4.1 Particle Progression in Domain

The cumulative particle exit fraction (relative to the total number of injected particles) is plotted in Figure 4.6. Generally, it can be seen that the particles started exiting from the fifth flow cycle onwards (see t = 3.2 s and arrows in Figure 4.6). For the planar injections (panel A in Figure 4.6, 12 flow cycles were needed for Geometry 1 (9 after the end of the particle injection cycle), 12 for Geometry 2, and 10 for Geometry 3. For the first catheter injection in Geometry 3 (panel B), only 10 cycles were run, compared to the 12 cycles necessary for Geometry 1 and 2. For the second catheter injection (panel C), 4 cycles less were needed for Geometry 3 than for Geometry 1 and 2 (10 compared to 14); for the third catheter injection (panels D), 2 cycles less were needed for Geometry 3 than for Geometry 1 (9 compared to 11), and 1 cycle less was needed for Geometry 2 compared to Geometry 1.

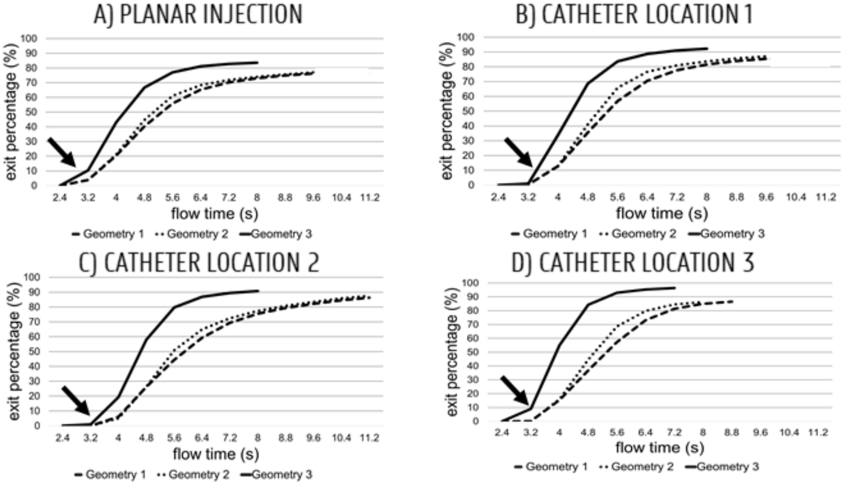

Figure 4.6: Cumulative particle exit fractions for Geometries 1–3 (Geometry 3 is the top curve, Geometry 1–2 are the dashed curves) plotted against flow time (plotted from the start of the fourth flow cycle onward; 2.4 s). (A) Planar injections. (B–C–D) catheter locations 1, 2 and 3, respectively. Globally, particles start exiting starting at the start of the 5th cycle (3.2 s—see arrow).

4.4.2 Planar Injections

4.4.2.1 Particle Grids

For the planar injections, the CPRGs of the axial injection plane of each geometry are displayed in Figure 4.7. Visually, there is some mismatch between the three CPRGs, although the major trends are similar for all geometries. At the center of the CPRG, there is a large green zone. Peripherally, a U-shaped zone of pink and yellow cells appears. The border is dominated by black or gray cells, while there are no large zones of orange or red cells.

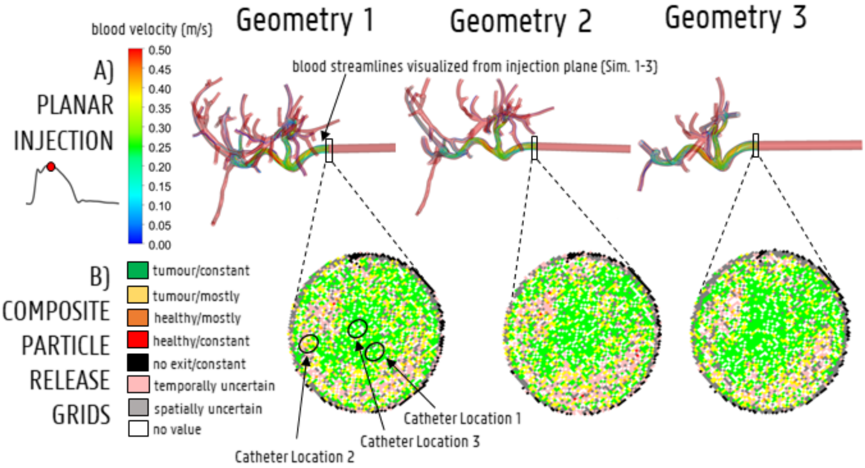

Figure 4.7: (A) Streamline visualization at peak systole for particle release at the injection plane for Geometry 1–3 (Sim. 1–3). (B) The CPRGs for the 3 geometries show that particles injected at the center of the cross-section (green zone) lead to >75% of tumor targeting throughout the cycle. Comparing CPRGs, consistency of the major visual trends across all geometries is visible, with only minor differences.

4.4.2.2 Grid-Based Particle Distribution

Computing the grid-based particle distribution for the planar injection (Figure 4.8A), the minima, maxima, median and interquartile ranges of the absolute (T)CF differences between the geometries are reported in Figure 4.8 (“Geometry 1 vs. 2”: comparing particle distribution between Geometry 1 and 2, “Geometry 1 vs. 3”: comparing particle distribution between Geometry 1 and 3, “flow vs. particle: comparing flow and particle distribution in Geometry 1). The median difference in outlet-specific (T)CF between Geometry 1 and 2 is 0.04% (with a reported maximum of 0.45% in outlet 48). The median difference in outlet-specific (T)CF between Geometry 1 and Geometry 3 is 0.21% (with a maximum of 0.70% reported in the truncated outlet 42). Comparing the flow distribution and the CF in Geometry 1, the median outlet-specific difference is 0.40% (maximum of 1.71% reported in outlet 36).

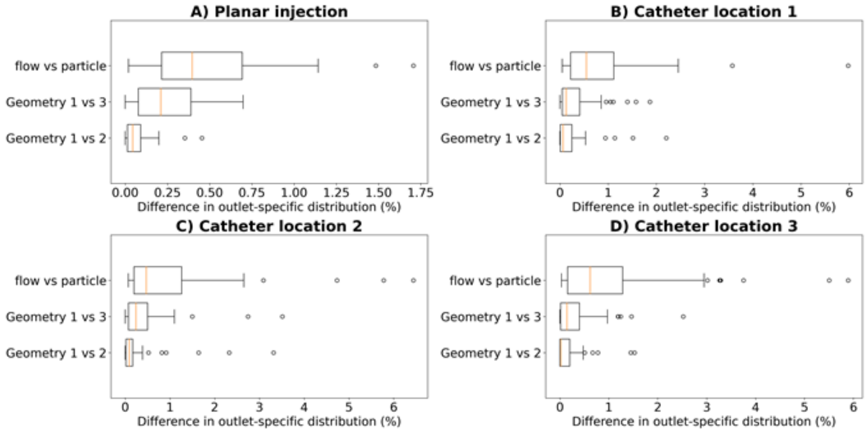

Figure 4.8: Boxplots comparing the differences in outlet particle distribution ((T)CF in panel A, (T)EF for panels (B–D) in Geometry 1 and 2 (“Geometry 1 vs. 2”), Geometry 1 and 3 (“Geometry 1 vs. 3”), and the differences in flow distribution and particle distribution in Geometry 1 (“flow vs. particle”). This is done for each of the 4 simulation sets: (A) the planar injection, and (B–C–D) catheter locations 1–3. For the planar injection, the error range is clearly much smaller than for the catheter injections (maximum of 1.75 vs. 6%).

4.4.3 Catheter Injections

To compare the particle (and flow) distribution after the catheter injections the three geometries, the median, maximum, interquartile ranges and outliers of the absolute (T)EF differences between the three geometries are displayed in Figures 4.8B-C-D. With regards to the (T)EF per outlet for the first catheter injection location (see Figure 4.3B), the median difference between Geometry 1 and 2 is 0.06% (maximum of 2.20% reported in outlet 28). The median difference between Geometry 1 and 3 is 0.13% (maximum of 1.86% reported in outlet 29). In Figure 4.9, the streamlines at peak systole during the particle injection cycle (cycle 3) are shown in several of these truncated outlets and compared to the hemodynamics in the original outlets, highlighting the impact of geometry on blood flow for both planar and catheter injections. The arrows in the panels for Geometry 2 and 3 indicate where outlets were truncated (and thus, where particle distribution was estimated based on solely flow modeling). For outlets 17–21 in Geometry 1, the EFs after catheter injection at Location 1 (Sim. 4) are compared to the TEFs of Geometry 2–3. The (T)EFs for the remaining outlets 22–27 were not compared visually in Figure 4.9B because the difference between geometries were negligible (<0.10% for each outlet). For the second injection location, the median difference in (T)EFs between Geometry 1 and 2 is 0.09% (maximum of 3.32% in outlet 17) and 0.24% between Geometry 1 and 3 (maximum of 3.51% in outlet 17). For the third injection location, the median difference in (T)EFs between Geometry 1 and 2 is 0.02% (maximum of 1.53% in outlet 42); the median difference between Geometry 1 and 3 is 0.14% (maximum of 2.52% in outlet 44). Next, the particle EF and flow distribution in Geometry 1 are compared. The median differences between outlet-specific EFs and outflows for the three catheter locations are 0.55, 0.24, and 0.62%, respectively. The maximal outlet-specific EF and outflow differences reported for these catheter injections are 5.97, 6.44, and 5.89%, respectively.

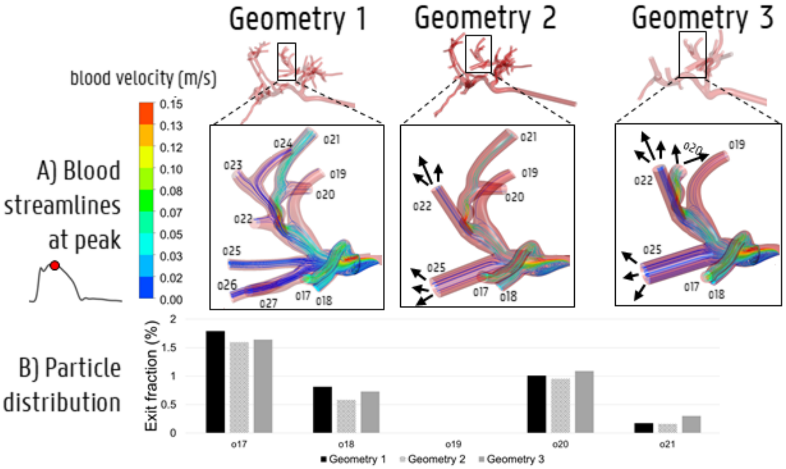

Figure 4.9: (A) The impact of simplifying the hepatic arterial geometry (Geometry 1–2–3) on the blood streamlines at peak systole. The arrows indicate where outlets were truncated with respect to Geometry 1, i.e., where the downstream flow distribution was used to model the particle distribution beyond the level of this truncated outlet. (B) The impact of truncation on particle distribution in outlets 17–21.

4.5 DISCUSSION

With regards to the computational strategy for determining the particle distribution in the patient-specific hepatic arterial geometry, four approaches can be outlined: i) modeling the full-complexity particle distribution in Geometry 1; ii) using the hybrid particle-flow model in the simplified Geometry 2, or iii) in the much more simplified Geometry 3; and, iv) assuming that the flow distribution is an appropriate estimator of the particle distribution. In approaches (i)-(iii), the microparticle behavior is explicitly modeled (until a certain level); while, in approach (iv), it is not. Importantly, each approach impacts the total computational complexity. Below, the accuracy of the obtained results of each approach are discussed (compared to the baseline particle distribution in Geometry 1, i.e., approach (i)).

4.5.1 Computational Cost

The plots of cumulative exit fraction with respect to flow time in Figures 4.6A,B show that the advantage of simplifying the hepatic arterial geometry from Geometry 1 to Geometry 3 with respect to computational cost and time is twofold. First, the mesh contains significantly less mesh elements, so overall computational cost decreases. Second, more particles also exit the truncated Geometry 3, and less flow cycles are needed to reach particle exit convergence. By truncating Geometry 1 to Geometry 2, these advantages are more limited: the decrease in mesh elements is not so significant (for Catheter Location 3 even non-existent), and the same number of flow cycles is needed to reach convergence (with the exception of Catheter Location 3). As an illustrative example of the impact of truncation on the computational time (determined here explicitly for Catheter Location 1), the average flow cycle time was 65 min for Geometry 1, 61.75 min for Geometry 2 and 57.25 min for Geometry 3 (run on a High-Performance Computing cluster with 384 cores and 250 GB RAM). Thus, by only considering the decrease in mesh elements, the computational cost of Geometry 3 is ∼12% lower than for Geometry 1. However, since only 10 flow cycles were needed for Geometry 3 to reach particle exit convergence, while 12 flow cycles were needed for Geometry 1, the total estimated computational time was 780 min for Geometry 1 and 572.5 min for Geometry 3. This indicates a ∼27% decrease in total computational cost by truncating Geometry 1 to Geometry 3 for the full simulation.

4.5.2 Planar Injections

The CPRGs of the three geometries (Figure 4.7) show similar global trends: particles which are injected at the periphery of the cross-section have more trouble exiting the domain (black cells); the center of the cross-section is the ideal injection location to target the main tumor feeders of this liver (green cells); near the east to north-west periphery, the uncertainty of tumor targeting increases (U-shaped zone with increasing number of yellow or pink cells). There appear to be only a few cells where injection leads to steering particles away from the main arterial feeders (red or orange cells). Conceptually, this means that the central green zone would be the preferred injection location over the more uncertain, U-shaped zone. Visually, these major trends seem consistent between geometries, although some minor differences between the CPRGs are apparent.

The grid-based particle distribution for the planar injections in Geometry 2–3 shows that the median differences in particle distribution with respect to Geometry 1 are very small (<0.25%) when truncating the geometry. As seen in Figure 4.8, the median difference increases slightly when truncating Geometry 2 to Geometry 3 (from 0.04 to 0.21%), illustrating the impact of truncation. Based on the limited median differences (<0.25%), the limited maximal differences (<0.70%) and the preservation of the major trends in the CPRGs, it can be said that the accuracy loss for a planar injection after truncating of Geometry 1 to Geometry 3 using the suggested pruning algorithm is limited for the patient-specific liver studied. When modeling only the flow distribution in the planar injection, the median and maximum differences between flow and particle distribution increase further (to 0.40 and 1.71%, respectively); indicating a decrease in accuracy that is caused by not modeling the particle distribution. However, due to limited maximum differences (<2%), it can be stated that, while modeling the particles has a clear advantage over modeling only the flow, the flow distribution is a decent estimator of the full-complexity particle distribution for the planar injection considered in this liver. If release maps similar to CPRGs need to be obtained, CFD simulations can be used to generate the flow pathlines after planar injection, as shown by Taebi et al. [130]. To estimate only the particle distribution, the CFD simulation would not even be needed, reducing the simulation time to 0 [112]. However, it should also be emphasized that the particles in this study are small, and that fluid-particle differences may increase for larger particles (i.e., for TACE).

4.5.3 Catheter Injections

With regards to the differences in microparticle behavior for the three catheter injections (“Geometry 1 vs. 2” and “Geometry 1 vs. 3” in Figures 4.8B-C-D), the median differences in the outlet-based EF between Geometry 1 and 2 (<0.10%) and Geometry 1 and 3 (<0.30%) are still very small for each catheter injection separately. However, for the maximal outlet-specific differences, some higher outliers (3.50%) are reported than for the planar injections. Also, the median and

75th percentile of the difference in particle distribution are always larger for Geometry 3 than for Geometry 2 (although the maxima are of a similar order of magnitude), illustrating the impact of truncation. However, these differences are still minor, indicating that the particle distribution in Geometry 1 can be reliably estimated by the hybrid-particle flow model using the truncated Geometry 3 (at least for this patient-specific case). It is also clear from Figure 4.8 that for the first and third catheter injection (panels B–D), the hybrid particle-flow model using Geometry 3 offers a significantly better estimation of the full-complexity particle distribution than using just the flow distribution, given the significantly smaller median and maximum differences for the truncated particle distribution. For the second catheter injection (panel C), this is still the case, but the discrepancy is less clear: the median difference in EF between Geometry 1 and 3 (0.24%) is still less than the median difference in flow and particle distribution (0.47%), but not as significantly as for the other injection locations. When using just the flow distribution, maximal outlet-specific differences of 6% are reported, which are significantly higher than the outliers for the catheter injections (3.50%) and for the planar injection (2%). Especially considering that numerous outlets have low outflows (30/48 outlets in Geometry 1 have <2% imposed outflows; maximum imposed outflow is 13.3%), absolute outlet-specific differences of 6% are relatively high. These results show that using the flow distribution as a surrogate for the particle distribution is considerably less accurate than using the hybrid model, indicating that flow modeling is preferably combined together with explicit particle modeling in the first generations of the tree (at least for catheter injections).

4.5.4 Summary

Summarizing the results of this study, the accuracy loss of the estimated particle distribution by truncating Geometry 1 to Geometry 3 is limited, but higher than truncating from Geometry 1 to 2, indicating the impact of truncation. However, truncating Geometry 1 to Geometry 2 does not offer much added value, since the decrease in computational time is very limited; in that sense, truncating Geometry 1 to 3 offers much more added value due to the limited accuracy loss and higher decrease in computational time. Meanwhile, the accuracy loss in each geometry is significantly higher when only the flow distribution is modeled (compared to also explicitly modeling the particle distribution). However, using the flow distribution as a surrogate for particle distribution is justified for the planar injection due to limited accuracy loss, but less so for the catheter injections. This indicates the importance of explicitly modeling the particle distribution for catheter injections, at least to the level of Geometry 3. These findings make sense because particles follow a select number of blood streamlines after catheter ejection, and will not mimic the flow distribution initially. However, for planar injections, particles are spread over the arterial cross-section, and tend to mimic the flow distribution more. Figure 4.10 shows that particles, after catheter injection in Geometry 3, have spread out over the entire arterial cross-section by the time they reach the outlets (albeit non-uniformly). This could partly explain why explicit particle modeling beyond the level of the truncated outlets of Geometry 3 is not strictly needed, and why hybrid particle-flow modeling may approximate the full-complexity particle distribution well enough (at least for this patient-specific geometry).

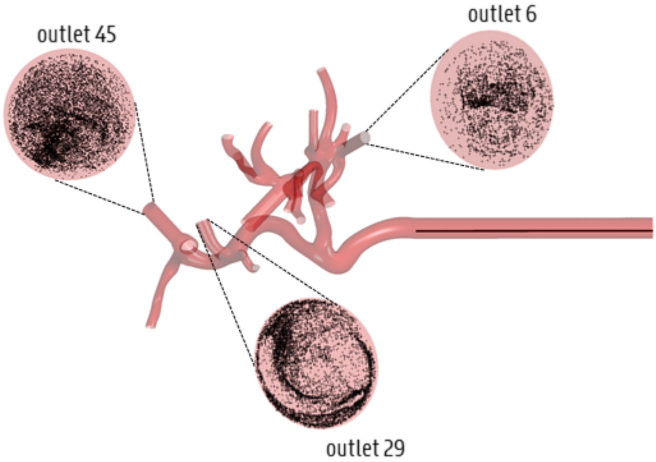

Figure 4.10: Illustration of the spread of particles across the cross-section by the time they reach the outlets of Geometry 3 (displayed here for Catheter Location 1).

4.5.5 Limitations and Future Work

This study puts forward an important approach to decrease computational complexity for current CFD simulations of transarterial radioembolization for HCC. We introduced a hybrid particle-flow model, as the results of this study stress the importance of modeling particle behavior in the first few generations of the hepatic arterial geometry (especially for catheter injections), but at the same time allowing to truncate the geometry further downstream according to the presented truncation algorithm. The additional novelty of this work lies in the consideration of a novel region growing method to determine outflow boundary conditions; modeling of outflow boundary conditions for outlets that perfuse both healthy and tumor tissue; and generating patient-specific CPRGs, which had never been done before (neither for CPRMs).

Importantly, this study also has several limitations. General limitations regarding the CFD modeling approach are discussed in Section 11.1, since the modeling approach was similar throughout the dissertation. We also note there that all findings reported should be interpreted with respect to this patient-specific case, and cannot simply be extrapolated to other patients as of this moment. Below, we discuss limitations regarding study approach.

First, only one particle type was modeled here, while many different particles types with distinct biophysical properties are commercially available (i.e., larger particles, which might decrease the accordance between flow and particle distribution and increase the importance of explicit particle modeling). Conversely, for smaller particles, particle inertia is lower, and the hybrid particle-flow model might be an even better fit. Second, only three catheter tip locations were investigated. While the three tip locations result in similar conclusions, we only modeled one axial location, and we assumed that results would be translatable to other tip and axial injection locations.

With regard to future work, the appropriate truncation level should be validated for more distal catheter injection locations, as it would likely take particles longer to spread over the arterial cross-section (see Figure 4.10) when injected at more downstream axial injection locations.

In summary, this work introduces a hybrid particle-flow model for truncated arterial trees and evaluates the suitability of this model for a patient-specific HCC case. This alternative approach to CFD modeling of radioembolization of liver tumors should allow to decrease the computational cost of future CFD simulations.

CHAPTER 5

The Hybrid Model for Selective Injection and Quantification of Particle Spread Phenomena

POSITIONING OF THE CHAPTER

To reduce the computational cost of patient-specific 3D CFD simulations of intra-arterial blood flow and drug transport, we showed in Chapter 4 that the size of the computational geometry can be reduced by truncating the outlets and assuming that microparticles follow the bloodstream downstream of the truncation points (hybrid particle-flow model). While we verified the hybrid particle-flow model for superficial injection, we will also verify this for selective injection in Chapter 5. Importantly, we also verify whether microparticles spread out across the cross-section as they travel downstream, which might increase the degree to which the particle and flow distribution agree, with novel space- and time-dependent spread measures. We will conclude Part II in Chapter 6 with the evaluation of additional simplification strategies aside from truncation.

This chapter is based on the publication *Spatiotemporal Analysis of Particle Spread To Assess The Hybrid Particle-Flow CFD Model of Radioembolization of HCC Tumors* (T. Bomberna et al, IEEE Transactions on Biomedical Engineering, 2023) [20].

5. THE HYBRID MODEL FOR SELECTIVE INJECTION AND QUANTIFICATION OF PARTICLE SPREAD PHENOMENA

5.1 INTRODUCTION

A popular strategy to reduce model complexity is reduction of the computational domain. Previously, Lertxundi et al. [124] introduced a segment-based truncation strategy of the hepatic arteries, which they illustrated in 3 patient-specific geometries with a fictional cancer scenario. However, this strategy does not offer any information on intrasegmental particle distribution. In contrast, we aimed to reduce the computational domain while still allowing an estimation of the particle distribution in the full arterial tree, including intrasegmental events. This greater level of detail has several advantages, including the possibility to reconstruct simulated patient-specific SPECT/CT scans based on CFD simulations for validation purposes [121]. Hence, we previously developed and illustrated a novel truncation strategy in a patient-specific geometry with a patient-specific cancer scenario. Our strategy consists of identifying the important arterial feeders of the tumor using region growing algorithms, and then performing truncation in different steps by grouping together healthy branches and grouping together tumor-feeding branches.

Importantly, for the truncated branches, it is assumed that particles distribute according to the flow distribution downstream of the point of truncation ('hybrid particle-flow model', illustrated for 3 outlets in Fig. 5.1A which are truncated to 1 outlet in Fig. 5.1B-C). Hence, even though we did not explicitly model microparticle behavior in these truncated downstream sections of the arterial tree, the hybrid modeling approach allows an (estimated) particle distribution in the full-complexity arterial tree, instead of only a number of segments (as was the case in [124]). The greatest downside to this truncation strategy is that it is more stringent: a similar particle distribution is not only wanted in truncated branches, but also in branches downstream of the truncated branches.

The accuracy of this hybrid surrogate model was validated for superficial microsphere injection in the PHA. Notably, the hybrid model performed well, and gave significantly better results than only modeling the flow distribution. We also hypothesized that a higher extent of particle spread across the lumen's cross-section could promote a more favorable match between flow and particle distribution. However, when the microcatheter tip is placed more downstream for more selective injections, two possible complications arise. First, the length between the catheter tip and the end-points of the (truncated) vessels decreases, possibly decreasing the extent to which particles spread across the lumen cross-section, and thereby also the match

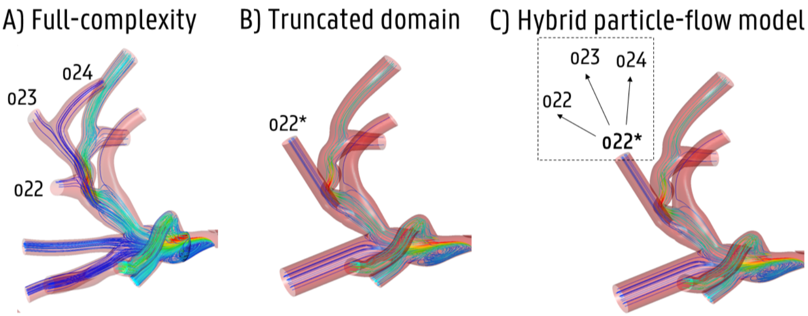

Figure 5.1: (a) Part of the full-complexity hepatic arterial tree with outlets 22-24 indicated. (b) Part of the truncated hepatic arterial tree with outlets 22-24 combined into outlet 22*. (c) In the hybrid model, the particle distribution at outlet 22* is determined with CFD, and then the particle distribution beyond outlet 22* is determined by the flow distribution going to o22-24.

between flow and particle distribution in the downstream vessels. Second, for selective injections, there is limited space for downstream truncation.

Hence, the goals of this study are threefold. First, the performance of the hybrid-particle flow model will be re-evaluated for two selective injection scenarios: in the RHA and LHA. Second, we will investigate how particle spread occurs across the lumen, and whether it decreases for selective injection. Third, we will evaluate whether upstream truncation is a reliable simplification strategy in addition to the hybrid model.

5.2 METHODS

In Section 5.2.1, an overview of the simulations used in this study is given. Details regarding the up- and downstream truncation algorithm, the meshing process and the particle spread measures are given in Sections 5.2.2-5.2.7. The mathematical details behind the multiphase model were previously given in Section 4.3.

5.2.1 Study design

One reference simulation is defined (Sim. 0) where microparticles are injected superficially in the PHA in the full arterial tree (Geometry 1). In Chapter 4, the downstream truncation algorithm of the full-complexity geometry (Geometry 1, 48 outlets) was presented in two steps, resulting in the moderately reduced Geometry 2 (38 outlets) and the severely reduced Geometry 3 (17 outlets) (see Fig. 5.2A). Here, the particle distributions for an RHA and an LHA selective injection scenario will be compared between the same three geometries, resulting in 6 simulations (Table 5.1, Sim. 1-6). For upstream truncation, three geometries with varying levels of reduction are defined as well (Fig. 5.2B-C; Table 5.1, Sim. 7-12).

Table 5.1: Study design

Simulation	Geometry	Outlets	Injection scenario
Sim. 0	Geometry 1	48	PHA (Superficial)
Sim. 1	Geometry 1	48	RHA (Selective)
Sim. 2	Geometry 2	38	RHA (Selective)
Sim. 3	Geometry 3	17	RHA (Selective)
Sim. 4	Geometry 1	48	LHA (Selective)
Sim. 5	Geometry 2	38	LHA (Selective)
Sim. 6	Geometry 3	17	LHA (Selective)
Sim. 7	Geometry RU1	6	RHA (Selective)
Sim. 8	Geometry RU2	6	RHA (Selective)
Sim. 9	Geometry RU3	6	RHA (Selective)
Sim. 10	Geometry LU1	13	LHA (Selective)
Sim. 11	Geometry LU2	13	LHA (Selective)
Sim. 12	Geometry LU3	13	LHA (Selective)

5.2.2 Truncation algorithm

The preparation of the patient-specific simulation geometry (based on conebeam CT-data, as approved by the Ethical Committee of University Hospitals Leuven) and the downstream truncation algorithm starting from Geometry 1 (48 outlets) was explained in detail in Chapter 4. In short, the geometry was truncated in two steps. In the first step, bifurcations which perfused <1% of the total tumor volume were deemed as 'healthy' and pruned; if higher tumor perfusion, they were deemed as 'tumor' and pruned (Geometry 2, 38 outlets, Fig. 5.2A). In the second step, bifurcations containing all 'healthy' branches or all 'tumor' branches were pruned until no more outlets perfusing the same tissue type could be grouped (Geometry 3, 17 outlets, Fig. 5.2A). If the lengths of the pruned outlets were too short, they were extruded artificially to allow proper flow development after bifurcations (avoiding unwanted disturbed flow behavior). For the upstream truncation, a three-step algorithm was used.

We only performed upstream truncation on Geometry 3 to keep the total number of simulations manageable; hereby, we assumed that the sensitivity of the particle distribution towards upstream truncation is similar for Geometries 1–2 compared to Geometry 3. First, the catheter-containing branch was truncated at a centerline length of 80 mm preceding the catheter tip (similar to the laminar entrance length). Every side branch branching off the catheter-containing branch upstream from the tip was kept intact for a length of 25 mm (we noted that shorter lengths can lead to flow reversal at the outlets). More specifically, if no other bifurcations were present on the side branch before the 25 mm-mark, the side branch was pruned at that mark; if other bifurcations arose off the side branch before the mark, the side branch was pruned before the bifurcation, and the branch was artificially extruded to 25 mm. For example, for the RHA injection, the bifurcation where the LHA splits off the PHA was kept intact, but the entire LHA was reduced to a single branch of 25 mm (Fig. 5.2B, Geometry RU1), reducing the total number of outlets from 17 to 6. For the LHA injection, the entire RHA branch was pruned, reducing the outlets from 17 to 13 (Fig. 5.2C, Geometry LU1). In the next two steps of the algorithm, the same procedure was repeated, but with a centerline length of 50 mm (Geometry RU2, LU2 in Fig. 5.2B-C) and 20 mm (Geometry RU3, LU3, Fig. 5.2B-C) before the catheter tip, respectively. This impacted the entrance length, but not the number of outlets.

5.2.3 Geometry and mesh details

The same meshing strategy was employed as in Chapter 4. In total, 6 geometries were developed for each of the 2 injection scenarios, leading to 12 different meshes. Mesh sensitivity analyses for both sizing of the catheter and arterial body were run. Target sizes of $7 \cdot 10^{-5}$ m and $3 \cdot 10^{-4}$ m were specified for the lumen of the catheter and the arteries, respectively. Parameters of interest were the wall shear stress and pressure fields, and cross-sectional velocity profiles at the first bifurcation (threshold of <5% difference in average and 95-percentile values between successive meshes) and the particle distribution at the outlets (<1% difference). Both bodies were meshed using tetrahedral elements; three prism boundary layers were enabled near the walls. The target size at the catheter inlet was $3 \cdot 10^{-5}$ m.

For the RHA models (Sim. 1–3, 7–9), the resulting meshes of Geometry 1–3 contained $11.2 \cdot 10^6$ elements (48 outlets), $10.6 \cdot 10^6$ elements (38 outlets) and $7.92 \cdot 10^6$ elements (17 outlets), respectively. The meshes generated by upstream truncation (Geometry RU1, RU2 and RU3; 6 outlets) contained $4.48 \cdot 10^6$ elements, $3.43 \cdot 10^6$ elements and $2.19 \cdot 10^6$ elements, respectively. For the LHA models, (Sim. 4-6,

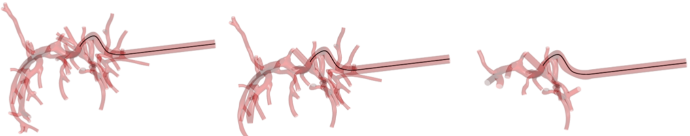

Geometry 1 Geometry 2 Geometry 3

(a) Downstream truncation

Geometry RU1 Geometry RU2 Geometry RU3

(b) Upstream truncation - RHA

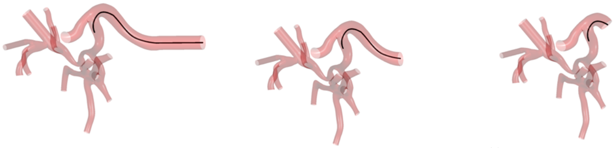

Geometry LU1 Geometry LU2 Geometry LU3

(c) Upstream truncation - LHA

Figure 5.2: (a) Geometry 1 (baseline geometry), Geometry 2–3 generated by the first and second step of downstream truncation, respectively. (b) Geometry RU1-RU3 generated by upstream truncation of Geometry 3; branches upstream of the catheter tip in the RHA are pruned. (c) Geometry LU1-LU3 generated by upstream truncation of Geometry 3; branches upstream of the catheter tip in the LHA are pruned.

10-12), the meshes of Geometry 1–3 contained 11.1 · 106 elements (48 outlets), $10.5 \cdot 10^6$ elements (38 outlets) and $7.85 \cdot 10^6$ elements (17 outlets), respectively. For Geometries LU1-LU3, the meshes contained $4.86 \cdot 10^6$ elements, $3.70 \cdot 10^6$ elements and $2.60 \cdot 10^6$ elements (13 outlets), respectively.

5.2.4 Numerical approach

Using CFD (Fluent, Ansys, USA) to calculate microparticle trajectories and distributions in the bloodstream entails a multiphysics approach: the continuous phase (blood flow) is solved using the conservation of mass and momentum, while the discrete phase (microparticles) is solved using Newton's second law. Blood is modeled as an incompressible, laminar, non-Newtonian fluid according to the simplified Quemada model; these equations were explained more in detail in Chapter 4.

For the boundary conditions, a time-dependent flow rate waveform with a period of 0.8 s was imposed at the inlet; the minimum-maximum volumetric flow rate was 88.1–566 ml/min (see Chapter 4 for the waveform shape). The volumetric catheter flow rate was set at 2.77 ml/min, so that the catheter flow velocity roughly corresponded with the mean velocity of the pulsatile blood flow signal at the inlet ($\sim$0.12 m/s).

At the outlets, outflow fractions were determined according to the volume and type of tissue perfused by each outlet. For cancerous tissue, the perfusion volume of each arterial outlet of Geometry 1 was determined through region growing. For healthy tissue, the perfusion volume of each hepatic segment (as described in [128]) was scaled to the patient-specific parenchymal volume, and the segmental volumes were then distributed across all outlets perfusing the same liver segment (assuming the flow split across an intrasegmental bifurcation is symmetric). Both the inlet and outlet boundary condition methodology were explained more in detail previously. Transient simulations were run for multiple cardiac cycles, and the simulation was stopped when $<$1.5% of the total number of injected particles exited in the latest cycle. The number of flow cycles necessary for each simulation is noted in Section 5.3.1. The time step size varied between 0.5-1 ms. For each time step, absolutely scaled residuals of at least 10^{-5} were reached. Solver settings were identical as before.

5.2.5 Post-processing of particle distributions

The particle distribution of all 48 outlets of Geometry 1 was calculated as the number of particles exiting through each outlet, divided over the total number of exiting particles for Geometry 1. However, for Geometry 2–3, the hybrid particle-flow model was used, leading to the following assumption: if outlets x, y and z of Geometry 1 are truncated and represented by outlet x* of Geometry 2 or 3, then the particle distribution at outlet x* can be multiplied with the flow percentage to outlets x, y and z, respectively, to give the (estimated) particle distribution at outlets x, y and z, even if the truncated domain does not physically contain outlets x, y and z (Fig. 5.1). This method allowed us to compare the full particle distribution at all 48 outlets for all geometries.

When reporting on differences in particle distributions between geometries, we reported absolute percentual differences (i.e. if 5% of particles exit through outlet x in Geometry 1, and 6% exit through the same outlet in Geometry 2, then the difference is 1%). Importantly, for comparison we only considered the outlets through which particles flowed (i.e. for LHA injection we dismissed the RHA outlets through which 0% of particles flow, and vice versa). Hence, for

RHA injection, we calculated the absolute percentual differences for 21 outlets in total, and reported on the median and maximum differences; while for LHA injection, we reported on the median and maximum differences of 27 outlets.

5.2.6 Global spread indices

The maximum spatial spread of microparticles across the vessel cross-section after injection was quantified using the Index of Particle Spread (IPS (%), Eq. 5.1). A square reference grid with a uniform cell length of 0.1 mm was defined for each vessel cross-section under study (see Fig. 5.3). The total number of grid cells within the cross-sectional plane of the arterial lumen ('plane grid cells') is given by N_{plane}. The total number of grid cells through which at least one particle passed ('particle grid cells') is given by N_{particle}. The IPS is then given as:

$$\text{IPS}(\%) = \frac{N_{\text{particle}}}{N_{\text{plane}}} \cdot 100 \tag{5.1}$$

Essentially, a low IPS means particles are confined to a small portion of the plane, while an IPS of ∼100% indicates that particles have spread (almost) over the entire plane. We only apply IPS in arteries and outlets with significant flow (>1% of total outflow). The particle spread is visualized in spread maps (see Fig. 5.3, Fig. 5.5) where the plane grid cells where no particles pass through are shown in grey and the particle grid cells are displayed in a color varying between white and red, depending on the number of particles that passed through the cell. Hence, the larger the grey region, the smaller the IPS.

To determine whether particles have spread out across the cross-section in a uniform manner or not, the number of particles passing through each grid cell was counted and computed as a percentage of the total number of particles passing through the cross-sectional grid (p_{ij}, being the percentage of particles passing through a grid cell in the ith row and jth column of the grid). Then, this particle distribution across the particle grid was compared against a hypothetical, uniform particle distribution U for each particle grid cell, where $U = \frac{100}{N_{\text{particle}}}$ represents that 100% of the particles are uniformly distributed over all particle grid cells. For each grid, the sum of the absolute percentual differences between pij and U gives the dissimilarity between the actual particle distribution and the hypothetical uniform particle distribution (numerator in Eq. 5.2).

For example, if all particles pass through one grid cell, and none pass through the remainder of the grid, the dissimilarity between the actual and uniform particle distribution is $(N_{\text{particle}} - 1)U + (100 - U)$, or, alternatively, $(N_{\text{particle}} - 2)U + 100$. Since the case where all particles pass through one grid cell is considered the most non-uniform distribution, this dissimilarity is also considered the maximal dissimilarity. By normalizing the actual dissimilarity over the maximal dissimilarity (denominator in Eq. 5.2), the Uniformity Index of Particle Spread of Eq. 2, or UIPS (%), gives a relative indication of the maximum uniformity of spread (0-100%).

$$\text{UIPS}(\%) = 100 - \frac{|\sum_i \sum_j p_{ij} - U|}{(N_{\text{particle}} - 2)U + 100} \cdot 100 \tag{5.2}$$

For a UIPS of 0%, all particles pass through one grid cell; for a UIPS of 100%, the particle distribution is perfectly uniform. Importantly, since the UIPS is a measure of spread uniformity, we only applied it when the IPS is significantly high (>33%). The UIPS is illustrated in Fig. 5.3, where particle grid cells are assigned a color based on pij on a linear color scale between white (0%) and red ($\geq$2%) (see Fig. 5.3). Hence, the more uniform the color, the more uniform the spread.

5.2.7 Temporal spread indices

To quantify whether spread is a time-dependent phenomenon, we calculated the temporal IPS (tIPS (%), 5.3) for specific injection 'bursts' of 0.2 s; here, (Eq. 5.1) still holds, but only particles which pass through the plane during a specific time interval of 0.2 s are considered for N_{particle}, given by N_{burst}. (The sensitivity of tIPS towards the choice of the interval length was also investigated; see Section 5.3.5). High fluctuations in tIPS indicate a high time-dependency of spread. Spread maps were made for a selection of time intervals, as seen in Fig. 5.5.

$$\text{tIPS}(\%) = \frac{N_{\text{burst}}}{N_{\text{plane}}} \cdot 100 \tag{5.3}$$

By summarizing the tIPS of each burst b weighed with the absolute number of particles in that burst (P_b), we get the weighted-averaged IPS (WIPS):

$$\text{WIPS}(\%) = \frac{\sum_b \text{tIPS}_b \cdot \text{P}_b}{\sum_b \text{P}_b} \tag{5.4}$$

It is crucial to give the bursts with higher P_b higher weight, since these bursts will be more important for the particle distribution. Here, high WIPS indicates high spread for a high number of particles; low WIPS indicates mostly low spread for a high number of particles (and possibly high spread for a lower number of particles).

5.3 RESULTS

In Section 5.3.1, an overview of the cycles needed for convergence of the particle distribution is given for each simulation. Next, the suitability of down- and upstream truncation for selective RHA and LHA injection is discussed in Sections 5.3.2 and 5.3.3, respectively. In Sections 5.3.4 and 5.3.5, the global (IPS, UIPS) and temporal spread indices (tIPS, WIPS) are evaluated for PHA, RHA and LHA injection.

5.3.1 Particle progression

For injection in the RHA, 8 flow cycles (since the start of the simulation) were needed to reach particle exit convergence for Geometry 3, while 10 cycles were needed for Geometries 1 and 2, with the particle exit percentages stabilized at 92%-95%. For Geometries RU1 and RU3, 7 flow cycles were needed, while for Geometry RU2 8 flow cycles were needed. The particle exit percentage stabilized at ~94%. For LHA injection, 10 flow cycles were needed for the truncated Geometry 3, while 14 cycles were needed for Geometry 1–2. In both cases, the particle exit percentage stabilized close to 80%. For Geometries LU1-LU2, 9 flow cycles were needed to reach a stable particle exit percentage around 80-85%; 13 flow cycles were needed for Geometry LU3 to reach a stable particle exit percentage of 95%.

5.3.2 Downstream truncation

For injection in the RHA (Sim. 1–3), the 5th percentile, median and 95th percentile outlet-specific differences in microparticle distribution between Geometry 1 and the truncated Geometry 2 were 0%, 0.27% and 1.4%, respectively, with a maximum difference of 1.7%. The 5th percentile, median and 95th percentiles differences between Geometry 1 and Geometry 3 were 0.012%, 0.32% and 3.7%, respectively (maximum: 11%). Comparing Geometry 1 to the pre-imposed flow distribution yielded the following differences: 0.11% (5th-percentile), 1.5% (median), 13% (95th-percentile) and 26% (maximum). For injection in the LHA (Sim. 4-6), the 5th percentile, median and 95th percentile differences in microparticle distribution between Geometry 1 and

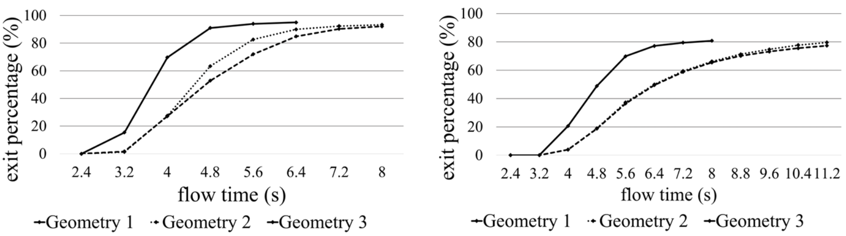

(a) RHA: downstream truncation (b) LHA: downstream truncation

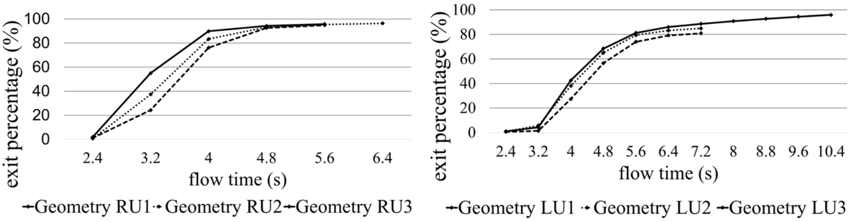

(c) RHA: upstream truncation (d) LHA: upstream truncation

Figure 5.3: Particle progression in domain.

2 were 0%, 0.19% and 0.60%, respectively (maximum: 1.0%). The 5th percentile, median and 95th percentiles differences between Geometry 1 and the heavily truncated Geometry 3 were 0.0046%, 0.40% and 3.0%, respectively (maximum: 4.2%). Comparing Geometry 1 to the pre-imposed flow distribution yielded the following differences: 0.34% (5th-percentile), 0.87% (median), 7.6% (95th-percentile) and 24% (maximum).

5.3.3 Upstream truncation

Inspecting the particle distributions, the median differences between Geometry 3 and the upstream truncated geometries were 0.090%, 0.18% and 0.77% for Geometries RU1, RU2 and RU3, respectively. The maximum differences were 0.35%, 0.78% and 7.7%, respectively. For LHA injection, the median differences with Geometry 3 were 0.26%, 0.22% and 0.50% for Geometries LU1, LU2 and LU3, respectively. The maximum differences were 1.57%, 1.94% and 9.0%. Fig. 5.4 shows the impact of upstream truncation on the near-tip hemodynamics after RHA and LHA injection, respectively. Contour plots of velocity magnitude at peak systole are shown for an arterial cross-section close to the catheter tip (‘plane’) in Geometries RU1–3. Additionally, a line profile of velocity magnitude at peak systole is shown and compared between the four geometries. From Fig. 5.4, it is clear that near-tip hemodynamics are very similar for Geometries U1–U2 but significant differences occur for U3.

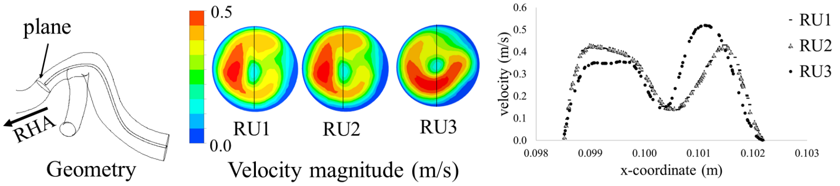

(a) Upstream truncation - RHA

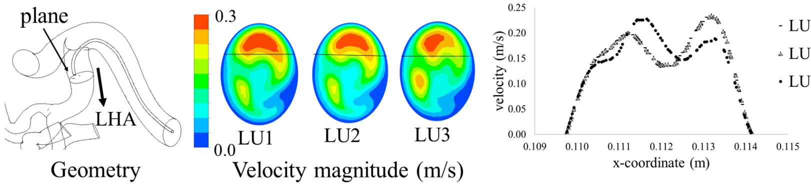

(b) Upstream truncation - LHA

Figure 5.4: Near-tip hemodynamics for (a) RHA (centered tip) and (b) LHA (off-center tip) injection at peak systole. Geometry shows the evaluation plane where section plots were made to illustrate the differences between Geometry U1-U2 and Geometry U3; the section plots show where the line profiles were taken.

5.3.4 Global particle spread

For both injection scenarios, the IPS, UIPS, spread maps and spread uniformity maps are shown in Fig. 5.5. For PHA injection (Fig. 5.5A), the IPS increased from 2.5% to 88% from the plane right after the catheter tip to Plane 3, and then remained more or less stable (84-88%) for Planes 4–6. For RHA injection (Fig. 5.5B), the IPS was again very small after catheter ejection (≈2%, Plane 1), but increased to 25% at Plane 2 and plateaued at ≈ 80% for Planes 3-6. For LHA injection (Fig. 5.5C), the IPS was lowest right after catheter ejection (23%, Plane 1), increased to 59% for Plane 2 and 91% for Plane 3, before dropping slightly for Plane 4–5 (81%, 89%). For PHA injection (Fig. 5.5A), the UIPS increased from 39% to 73% from Plane 1 to 4, and remained at 73%-74% for Planes 5–6. For RHA injection (Fig. 5.5B), the UIPS was 46% for Plane 3 and increased to 66% for Plane 4, plateauing at 62% and 65% for Plane 5–6, respectively. For LHA injection (Fig. 5.5C), the UIPS was 54%-58% for Planes 2–3 and 60-63% for Planes 4–5, showing a slight increase.

5.3.5 Temporal particle spread

For PHA and RHA injection, the IPS maps for 4 specific time intervals of interest (i.e. around the highest peak) in Planes 3 and 6, and the tIPS evolution in function of time for Planes 3 and 6 (with the

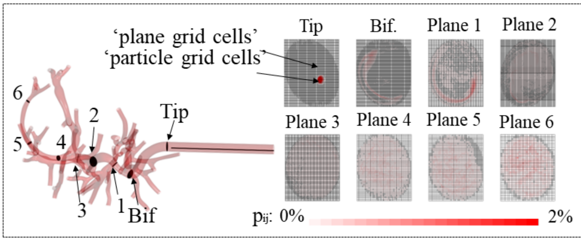

Plane	IPS (%)	UIPS (%)	WIPS (%)
Tip	2.5	-	1.5
Bif	19	-	7.5
1	54	39	13
2	70	50	34
3	88	67	39
4	88	73	43
5	84	73	30
6	88	74	34

(a) PHA injection

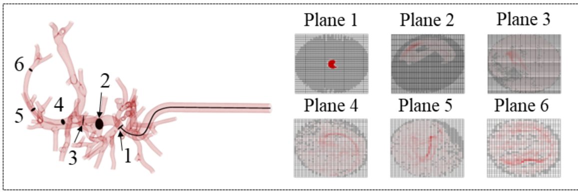

Plane	IPS (%)	UIPS (%)	WIPS (%)
1	2.4	-	1.7
2	25	-	9.6
3	83	46	37
4	81	66	27
5	79	62	19
6	81	65	24

(b) RHA injection

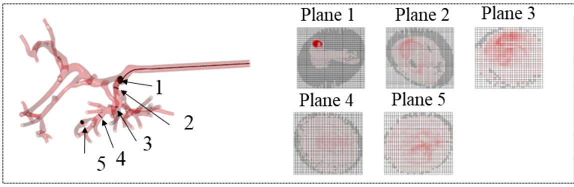

Plane	IPS (%)	UIPS (%)	WIPS (%)
1	23	-	7.1
2	59	58	25
3	91	54	57
4	81	60	33
5	89	63	37

(c) LHA injection

Figure 5.5: Particle spread maps and particle spread indices (IPS, UIPS, WIPS) for a selection of planes (indicated on the left) for Geometry 1 in case of (a) PHA injection, (b) LHA injection and (c) RHA injection. Both IPS and UIPS clearly increase from the catheter tip onward; after which the reported values evolve towards a plateau value for the most distal planes (3–6). The WIPS drops distally after reaching the maximum around Plane 3.

indicated dots corresponding to the middle of each time interval) are shown in Fig. 5.6. For both planes, the tIPS shows 3-4 high peaks before dropping. For PHA injection (Fig. 5.6A), the maximum peak tIPS is 58% at the 3.4–3.6 s interval (Plane 3) and 59% at 5.0-5.2 s (Plane 6). For RHA injection (Fig. 5.6B), the maximum peak is 49% (3.2–3.4 s, Plane 3) and 40% (5.0–5.2 s, Plane 6). For LHA injection (Fig. 5.6C), maximum peaks occur of 80% (3.2–3.4 s, Plane 3) and 60% (5.0–5.2 s, Plane 6). Inspecting WIPS for PHA injection (Fig. 5.5A), WIPS peaks at Plane 4 (43%) and decreases more distally, to 30–34%. For RHA injection (Fig. 5.5B), the WIPS peaks at Plane 3 (37%), then decreases to 19–24%. For LHA injection (Fig. 5.5C), WIPS peaks at Plane 3 (57%), decreasing to 33-37% more distally. The interval length (0.2 s) was chosen to be smaller than the cycle length (0.8 s); otherwise, cyclical events disappear. For smaller lengths (0.1 s, 0.05 s), it was noted the temporal values can increase (more particles are included in the bursts), but qualitative trends remain: 3-4 high peaks appear in time, and the values drop distally after the peak.

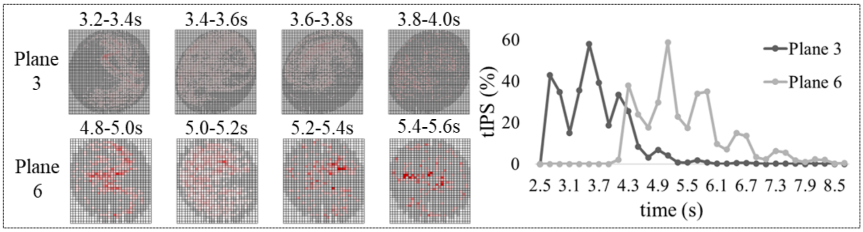

(a) PHA injection

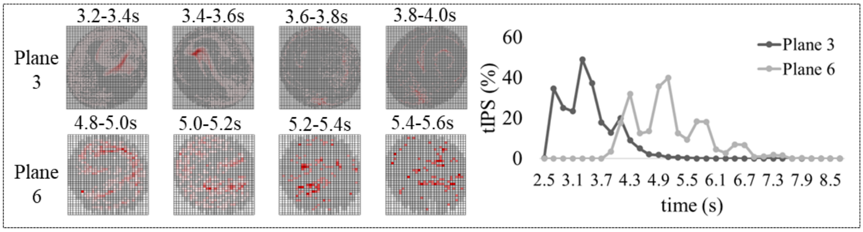

(b) RHA injection

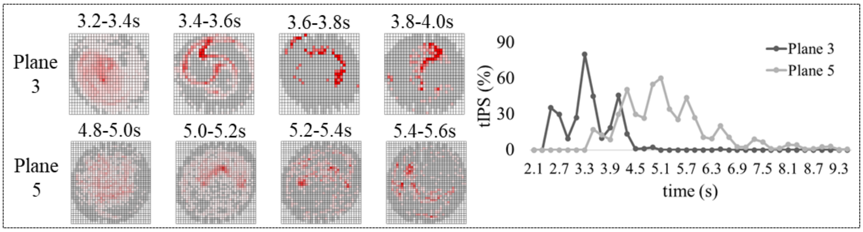

(c) LHA injection

Figure 5.6: Particle spread maps for four time intervals of interest and plots of temporal spread index (tIPS) in function of flow time for two planes for Geometry 1 in case of (a) PHA injection, (b) LHA injection, and (c) RHA injection. tIPS clearly varies in time, with maximum peaks around 3.3-3.5 s (Plane 3) and 5.1 s (Plane 5, 6).

5.4 Discussion

In Section 5.4.1, we discuss how effectively computational cost can be decreased by down- and upstream truncation. Next, the suitability of down- and upstream truncation for selective RHA and LHA injection is evaluated in Sections 5.4.2 and 5.4.3. In Sections 5.4.4 and 5.4.5, we overview trends regarding global and temporal spread. Finally, in Section 5.4.6, we discuss the novelties and limitations of the work and future steps that can be undertaken to further improve the work.

5.4.1 Simplicity gain

For severe downstream truncation, the reduction in geometry size for both RHA and LHA injections resulted in less flow cycles necessary to reach convergence of the particle distributions, and hence, a shorter simulation time. However, for upstream truncation, this trend was not consistently noticeable since Geometry LU3 needed 4 flow cycles more to reach convergence than Geometries LU1-LU2. This is explained by the fact that the particle distribution in Geometry LU3 differs significantly from the particle distributions in Geometry LU1-LU2 (see Section 5.3.3); in LU3, particles were pushed towards outlets with very low flows (<1%). These low-flow outlets lead to slower convergence (as these particles simply need more time to reach these outlets). This observation is notable, because it shows that, while geometry reduction is usually favorable for faster convergence, the current particle exit convergence criterion also depends on the particle distribution itself (i.e. which outlets receive particles), which makes the relationship between geometry size and convergence time more complicated.

Hence, the gain in computational simplicity with model truncation lies in (1) the reduced number of flow cycles necessary for particle exit convergence, here mostly observed for severe downstream truncation, (2) the reduction in mesh size, observed for all truncated models, and (3) the reduction in outlets, requiring less manual work during geometry construction, as observed for all truncated models.

5.4.2 Downstream truncation

For RHA injection, the median differences in particle distributions compared to Geometry 1 were similar for Geometry 2–3 (~0.30%) but the maximal differences were much higher for Geometry 3 (3.7% and 11%, respectively) than for Geometry 2 (1.7%). For LHA injection, the same trend was reported: between Geometry 1–2 and 1–3, the median difference was acceptable (0.19% and 0.40%, respectively) but the maximal difference was significantly larger for Geometry 1–3 (4.2%) than 1–2 (1.0%).

While the severely truncated Geometry 3 is still a considerable improvement over just the flow distribution (there, very high maximal differences of ~25% are reported in both RHA and LHA scenarios), the maximum differences are still considerable (>4%), indicating a decrease in surrogate model fidelity. Hence, medium truncation (Geometry 2) is more reliable than severe truncation (Geometry 3).

5.4.3 Upstream truncation

While the median differences for upstream truncation were very limited (<1%) for the highest degree of upstream truncation for both RHA and LHA injection, the maximum differences with Geometry 3 were significantly high (~8%). This shows that the highest degree of truncation is not a suitable simplification strategy. However, the first two degrees of upstream truncation only presented with a maximum difference of ~0.4% for RHA injection and ~1.9% for LHA injection, respectively, while in both cases median differences were always significantly smaller than 1% (~0.2%). This suggests that upstream truncation can be performed reliably if an entrance length of ~50 mm is preserved; a length of ~20 mm is too short. Interestingly, Lertxundi et al. [124] investigated upstream truncation lengths of 10 and 30 mm, confirming our results that the smallest entrance lengths (~10 mm) can lead to substantial errors, but that larger entrance lengths (~30 mm) are more reliable.

5.4.4 Global particle spread

Previously, we hypothesized that particle spread across the cross-sectional favorably impacts alignment of the particle distribution with the flow distribution, and hence, the accuracy of the hybrid model. In other work, Aramburu et al. [11] studied particle spread as a function of cross-sectional area, with particles spreading to maximally ~30% of the cross-sectional area in the ~20 mm after the catheter tip. Here, we elaborated upon this analysis by (1) not only quantifying particle spread, but also uniformity of spread, and time-dependency of spread, (2) investigating this particle behavior throughout the full tree, (3) and comparing between superficial and selective injections.

First, we investigated how the spread (IPS) evolved after ejection. For all three injections, the IPS rose significantly between Planes 1–3, before stabilizing at a high plateau value (~80-90%) from Plane 3 onward. Logically, smallest maximum spread appears closest to the catheter tip, and values increase further away from the tip. Comparing injections, the highest maximum IPS was reached for PHA and LHA injections (88%-89%, compared to 81% for RHA injection). This shows that while IPS increases with distance from the catheter tip, the plateau value is not specifically higher for more superficial injections, and likely still depends on other factors. We also investigated the uniformity of particle spread across the cross-section throughout the arterial tree. For each injection separately (PHA, RHA and LHA), the UIPS increased (37%–73%, 46%–63%, 58%–63%, respectively) from the most proximal to most distal plane, although not always as significantly. Again, this shows the impact of distance from the catheter tip on the UIPS. The plateau value reached was similar for RHA and LHA injection (65% and 63%, respectively) and slightly higher for PHA injection (74%). Generally, UIPS seems to stabilize more distally than IPS.

Interestingly, the maximum difference of 4.2% between Geometry 1–3 for LHA injection was found for outlet 20* in Geometry 3, which was the result of truncating outlets 20-21 from Geometry 1–2 (2 outlets after Plane 5, see Fig. 5.5C). Importantly, this point of truncation was situated after Plane 5, by which IPS and UIPS had already reached their maximal or plateau value. This shows that while a lack of particle spread can cause an important mismatch between particle and flow distribution proximal to the catheter tip, distal mismatch between flow and particle distribution can still arise independent of high and uniform IPS and UIPS, and cause errors in the hybrid model after truncation.

5.4.5 Temporal particle spread

While IPS and UIPS give a global view on the spread that is achieved over time, tIPS clearly shows that particle spread can also vary in time, with 3 to 4 high peaks before dropping to 0. The reported rises and drops of the temporal spread indices appear to be cyclical, repeating every ~0.8 s. Additionally, inspecting WIPS, we see an initial increase after the catheter tip, a peak around Plane 3, and then again a distal drop. This is a significant difference from IPS and UIPS, which reached a distal plateau. This underlines that total IPS in the downstream vessels can be high and more or less constant, but temporal IPS can be lower and still varying, both in space and time. Since lower spread can be indicative of a misalignment between particle and flow distribution, this stresses the importance of modeling microparticle behavior, and truncating only moderately downstream.

Comparing the most distal WIPS to the maximum WIPS, we see drops of 9% for PHA injection, 13% for RHA injection, and 20% for LHA injection. This is also clear visually from Fig. 5.6, where the tIPS peaks drop more from Plane 3 to Plane 5–6 for RHA and LHA injection than for PHA injection. Possibly, higher distal drops in particle-weighted spread for the selective injections could explain why the hybrid model (assuming that the particle flow follows the blood flow distribution downstream from the outlets onward) performs less accurately in these cases, but this effect is severely under-studied, and we need much more simulated data to find actual correlations.

5.4.6 Novelties, limitations and future work

In this study, we showed that moderate upstream and downstream truncation can be applied to reduce the simulation geometry, while the hybrid modeling approach still allows to estimate the full-tree particle distribution with high fidelity. The strengths of the hybrid particle-flow model were already explained before. Aside from studying the hybrid-particle flow model for realistic injection scenarios and the impact of upstream truncation, the other novelties of this work lie in the invention of novel spread measures and their application to investigate particle spread over the arterial tree. We showed that differences between flow and particle distribution can still arise distally, even if the spread and spread uniformity of all injected particles is high. However, spread can also drop to low values at specific time points, indicating that spread is a very time-dependent phenomenon and not constantly high far away from the catheter tip. Importantly, this particle behavior in the downstream vessels cannot be captured by flow modeling, and might induce differences between the hybrid and full-particle approach. To further simplify the modeling approach, we can also explore the impact of modeling blood as a Newtonian (instead of non-Newtonian) fluid in these larger truncated vessels.

Overall limitations of the CFD modeling approach are discussed in Section 11.1. Importantly, the results presented here cannot be generalized yet to other patients. Regarding study design, sensitivity of the spread measures towards the exact location and orientation of the plane should be studied, as it is a non-trivial task to replicate the same plane in different computational geometries. Additionally, a strong link between (particle-weighted) spread and particle flow-alignment has not been shown yet, as the sample size was much too small to make strong conclusions. To do that, spread measures should be compared between truncated versions of geometries where the hybrid model is valid (particle-flow alignment is high), and truncated geometries where it is not. We did show that mismatch between flow and particle distribution can still arise despite relatively high non-weighted spread values, showing that is not an ideal indicator of alignment. Whether higher particle-weighted spread values lead to higher particle-flow alignment, or if there are other important contributors to particle-flow alignment that were not considered here, is currently still unclear (and non-trivial).

5.5 CONCLUSION

The goal of this work was to determine whether we can simplify CFD models of selective injection of radioactive microparticles to become less computationally costly. We applied the hybrid particle-flow model in four truncated geometries (moderate and severe up- and downstream truncation) for two selective injection scenarios and evaluated whether they are suitable surrogate models for the particle distribution in the full hepatic arterial tree. We showed that severe truncation in both downstream and upstream scenarios introduced significant errors and can only be applied for superficial injection. However, we also showed that, for selective injection, both moderate upstream and downstream truncation can still be applied with limit risks, and with the added merit of reducing the mesh size from $\sim$11 million to $\sim$5 million elements. Hence, by combining the hybrid particle-flow model with upstream truncation, we have shown that we can reduce simulation complexity significantly while maintaining information on intrasegmental particle distributions, paving the way towards sensitivity analyses and surgical planning for TARE.

Chapter 6

Advanced Simplification Strategies for Particle Distribution and Tumor Dose Predictions

Positioning of the chapter

In Chapters 4, and 5, we showed that reduction of the physical geometry is an appropriate simplification strategy for complex 3D CFD simulations of blood flow and drug transport, albeit that severe truncation is only applicable to superficial injection (and selective injection should be limited to moderate truncation). In this chapter, we aim to explore other simplification strategies (and more broadly, strategies to reduce computational time) to predict tumor doses under patient-specific conditions.

This chapter is based on the publication *Simplification strategies for patient-specific CFD models of drug transport during liver radioembolization* (T. Bomberna et al, Computers in Biology and Medicine, 2024) [21].

6.1 Introduction

In clinical practice, 3D CFD simulations could enable personalized preoperative planning and better tumor targeting. However, the high computational cost of these 3D CFD models is still limiting, and does not allow point-of-care advice or global sensitivity analyses (yet). Recently, the use of deep learning or surrogate model-based approaches to cheaply replace complex CFD simulations has become more important. Aside from general advances in computing power, GPU-based computation can also accelerate flow simulations considerably [131]. However, currently, there still exists an important trade-off between computational complexity and computational time. Hence, result acceleration can also occur through model simplification, which has only been studied to a very limited degree for 3D CFD simulations of transarterial particle delivery.

Regarding model simplification, Lertxundi et al. [124] introduced a pruning approach, in which the hepatic arterial vessels were truncated both up- and downstream of the catheter tip, removing all intrasegmental vessels. They showed that reliable predictions of segmental radioactivity can still be made after truncation (based on 3 patient-specific geometries). Alternatively, we suggested that intrasegmental activity can still be predicted with a different truncation algorithm, by assuming that particles follow the blood flow distribution downstream of the truncated outlets (see Chapter 4). This hybrid particle-flow model was verified in both superficial (i.e. before the first intrahepatic bifurcation) and selective (i.e. before the second intrahepatic bifurcation) injection scenarios. For superficial selection, it was shown that both moderate and severe truncation for the hybrid particle-flow model could produce reliable predictions of the intrasegmental particle distribution. However, for selective injection, only moderate truncation proved to be reliable. Notably, these findings were only verified in 1 patient-specific geometry, and should be replicated for more patient-specific geometries in the future. Additionally, other simplification strategies than domain truncation were not yet tested, which leaves ample room to explore more diverse strategies. We also theorize that there might be a difference between sensitivity analysis and accurate tumor dose prediction. Hence, we suggest that more drastic CFD simplification strategies might be possible if the goal is to perform a reliable sensitivity analysis of injection parameters, rather than an accurate prediction of tumor dose, as was the case before.

Within this study, we quantify the trade-off between computational time and accuracy for 3D CFD simulations of transarterial particle delivery. We identify five alternative simplification strategies: (i) severe downstream truncation, (ii) steady flow instead of time-dependent flow, (iii) coarsening the grid, and (iv) running less flow cycles, and evaluate whether they can be used for (G1) accurately predicting the particle distribution and tumor dose (accuracy), and (G2) quantifying sensitivity of injection parameters towards particle distribution and tumor dose. We report on which simplification strategies we advise for goals (G1) and (G2) going forward, whether simulations can be simplified more drastically if we focus only on sensitivity, and whether there is significant difference in the advised simplification strategy when focusing on tumor dose as output parameter instead of the full downstream particle distribution. Third, we also note on how much computational times can be decreased by model simplification. Additionally, we evaluate how much computational times can be decreased by GPU-based computation.

Notably, this is the first study in which a broad range of simplification strategies are directly compared for these 3D CFD simulations of intrahepatic blood flow and particle transport, and where their impact on computational time is investigated. As long as the trade-off between computational time and complexity exists, model simplification will remain crucial to decrease computational cost, accelerate analysis, and make clinical transfer more likely.

6.2 METHODS

In Section 6.2.1, the study design is explained. In Section 6.2.2, we explain how we use CFD to convert medical images into a prediction of patient-specific particle distribution and tumor dose. Then, in Section 6.2.3, we define the evaluation metrics that are used to compare the particle distributions and tumor doses between different simplified models and the baseline model. Successively, in Section 6.2.4, we define the evaluation metrics that are used to assess whether the simplified models are similarly sensitivity to injection parameters as the original, baseline model.

6.2.1 Study Design

This study aims to evaluate the suitability of different simplification strategies for two goals: (G1) accurate prediction of tumor dose and downstream microparticle distribution, and (G2) sensitivity of the tumor dose and microparticle distribution towards specific injection parameters. To evaluate (G2), we will perform a local sensitivity analysis towards one representative injection parameter, namely injection flow rate, the time-dependent catheter injection mass flow rate (kg/s), varying from $2.04 \cdot 10^{-5}$ kg/s to $1.92 \cdot 10^{-4}$ kg/s ($\sim$0.019 cc/s to $\sim$0.1810 cc/s; these values were chosen to mimic a range of clinically realistic injection flow rates, as identified by clinicians as between ~0.05 cc/s and ~0.2 cc/s). In Chapters 4, and 5, moderate up- and downstream truncation was identified as a suitable simplification strategy for accuracy purposes (G1). For both the original-complexity CFD model and each of the 5 simplification strategies, we run 8 CFD simulations as a 'simulation batch' (Table 6.1). In each batch simulation, the injection mass flow rate of the catheter fluid is set at one of 8 equidistant points between (and including) the minimum and maximum mass flow rate ($2.04 \cdot 10^{-5}$ kg/s, $4.49 \cdot 10^{-5}$ kg/s, $6.93 \cdot 10^{-5}$ kg/s, $9.38 \cdot 10^{-5}$ kg/s, $1.18 \cdot 10^{-4}$ kg/s, $1.43 \cdot 10^{-4}$ kg/s, $1.67 \cdot 10^{-4}$ kg/s, $1.92 \cdot 10^{-4}$ kg/s).

First, we run the simulations with varying injection mass flow rate for the original CFD model; this batch serves as the baseline batch (labeled 'B' in Table 6.1) for comparison. The simplification strategies are: (i) severe downstream truncation (simulation batch labeled as 'T' in Table 6.1), (ii) steady inflow ('S' in Table 6.1), (iii) using a more coarse grid ('C' in Table 6.1), (iv) using an extra coarse grid ('XC' label in Table 6.1), and (v) combining the coarse grid with a reduced number of simulated cardiac cycles ('Cm' label in Table 6.1). Hence, in total, we run 48 simulations (6 batches of 8 simulations). Except for the S-batch, all simulations were time-dependent.

Table 6.1: Overview of the simplification strategies (S, T, C, Cm and XC) and the baseline batch (B). In total, 48 simulations were run (6 batches of 8).

Simulation batch	**Simplification strategy**
B01-B08	(Baseline)
S01-S08	Steady flow
T01-T08	Severe truncation
C01-C08	Coarse grid
Cm01-Cm08	Coarse grid with less flow cycles
XCO1-XC08	Extra coarse grid

6.2.2 Computational Fluid Dynamics

6.2.2.1 Pre-processing

Conebeam CT images of a HCC patient treated by TARE were collected from UZ Leuven (as approved by the Ethical Committee of University Hospitals Leuven) and segmented based on contrast difference between arteries and the surrounding tissue using Mimics (Materialise, Belgium). This initial geometry is shown in Figure 6.1A.

A microcatheter with an internal diameter of 0.7 mm was embedded in the RHA using SpaceClaim (Ansys, USA). As shown before, the hepatic arterial geometry can be moderately truncated up- and downstream for selective injection, truncating the 27 original outlets of the LHA into 1 LHA outlet, and 21 original outlets of the RHA into 15 RHA outlets. In total, the number of physical outlets of the reduced geometry is 16. The newly truncated geometry can be seen in the second panel of Figure 6.1A. For the severe truncation simplification strategy explained in Chapter 4, the number of RHA outlets was further reduced to 5, bringing the total number of physical outlets to 6 (this geometry can be found in Chapter 5).

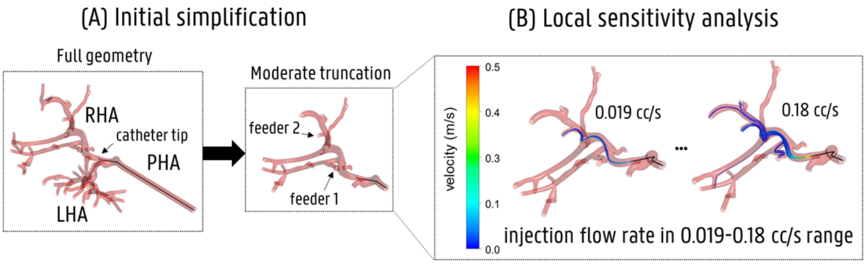

Figure 6.1: (A) As previously shown, geometries can be reliably simplified by moderately truncating outlets up- and downstream of the catheter tip, reducing the number of outlets from 48 to 16. (B) A local sensitivity analysis of injection flow rate (varying between 0.02-0.2 ml/s) is carried out to evaluate the suitability of the various simplification methods.

The mesh sensitivity study of the catheter-containing geometries focused on optimizing the sizing of the volume elements of the arterial and catheter lumen, in that order. The criterion was assuring convergence of specific hemodynamic-related parameters, such as wall shear stress, pressure over the entire volume, and cross-sectional velocity profiles at the first bifurcation (threshold of <5% difference in average and 95-percentile values between successive meshes) and the particle distribution at the outlets (<1% difference between successive meshes). Both bodies were meshed using tetrahedral elements for the bulk of the volume; three prism boundary layers were enabled near the walls. The target mesh size for the arterial and catheter bodies were $3 \cdot 10^{-4}$ and $7 \cdot 10^{-5}$ m, respectively. The target size at the catheter inlet was $3 \cdot 10^{-5}$ m. The final mesh contained $4.96 \cdot 10^{6}$ elements; this mesh was used for the baseline (B) and steady (S) models. Using the same meshing parameters, this resulted in $3.37 \cdot 10^{6}$ elements for the truncated (T) model. For the coarse mesh (C), the volume sizings were set at $6.00 \cdot 10^{-4}$ m for the arterial body and

$1.40 \cdot 10^{-4}$ m for the catheter body, resulting in $2.43 \cdot 10^6$ elements. This mesh was used for the coarse model and coarse model with less flow cycles (Cm). For the extra coarse mesh (XC), the volume sizings were set at $1.00 \cdot 10^{-2}$ and $5.00 \cdot 10^{-3}$ m for the arterial and catheter bodies, respectively, resulting in $1.36 \cdot 10^6$ elements.

6.2.2.2 Multiphysics model

For the CFD model in Fluent (Ansys, USA), blood flow was modeled as laminar fluid flow, with a density of 1060 kg/m^3 and modeling the shear-thinning viscosity behavior with a simplified Quemada model (see Chapter 4 for mathematical details of the fluid flow implementation). Using the Discrete Phase Model, microsphere trajectories were calculated using Newton's second law (see Chapter 4 for details on the forces acting on the particles). At the proper hepatic artery inlet, a time-dependent flow rate waveform with a period of 0.8 s was imposed (minimum-maximum: 88.1-566 ml/min, see Chapter 4 for the waveform shape derived from a 1D model of the arterial circulation [127]). The catheter mass flow rate was varied between $2.04 \cdot 10^{-5}$ kg/s to $1.92 \cdot 10^{-4}$ kg/s, as specified above. At the outlets, outflow fractions were applied using an algorithm that determined the flow percentage in each outlet according to the volume and type of tissue perfused by each outlet. To do so, three types of arteries were considered: tumor-feeding arteries, arteries which feed only the healthy tissue, and arteries located at the periphery of the tumor mass feeding both healthy and tumor tissue. To determine the tumor flow contribution, a region growing algorithm was used to calculate which fraction of the tumor mass was fed by each artery, using the arterial outlets as seed points (details on the algorithm specified in [125]). To calculate the healthy flow contribution, outlets were attributed to one of the eight hepatic segments based on the CT scan, and the total segmental flow (proportional to the segmental volume) was distributed across the different intrasegmental arteries, with blood flow splitting evenly across bifurcations. Both the inlet and outlet boundary condition methodology are explained more in detail in Chapter 4.

Time-dependent simulations were run for a priori unknown number of flow cycles, where the simulation was stopped when $<1.5\%$ of the total number of injected particles exited in the latest flow cycle. An alternative criterion ($<10\%$) was used for the simulation strategy with the reduced number of flow cycles (Cm). The time step size was alternated between 0.5 and 1 ms. For each time step, either absolutely scaled residuals of at least 10^{-5} or relative drops of at least 3 orders of magnitude were reached. Solver settings were identical as in Chapter 4.

6.2.2.3 Post-processing

The particle exit percentage for outlet i (PEP_i, Eq. 6.1) can be calculated as the fraction of particles exiting through outlet i (N_i) over the total number of exiting particles (N_{exit}).

$$PEP_i(\%) = \frac{N_i}{N_{exit}} \tag{6.1}$$

Importantly, this can only be done for the physical outlets contained in the domain; not for the outlets which were removed during (moderate or severe) truncation. For these outlets $i*$ outside of the physical domain, the hybrid particle-flow is used (see Chapter 4): since particles are assumed to distribute downstream of the truncated outlet i according to the flow distribution, PEP_{i*} is multiplied with the flow percentage flowing from the outlet i to the removed outlet i* (FP_{i*}). This value is known a priori because the flow distribution is imposed as an outlet boundary condition, and equals just 1 for the outlets contained within the geometry (i=i*). Hence, the particle exit percentage for outlet i* outside of the geometry (PEP_{i*}, Eq. 6.2) was calculated as:

$$PEP_{i*}(\%) = \frac{N_i}{N_{exit}} \cdot FP_{i*} \tag{6.2}$$

The tumor dose (TD (%), Eq. 6.3) can be simply calculated by an extension of the hybrid model: downstream of all outlets i*, a specific percentage of the flow flows to the tumor (TF_{i*}, 100% for tumor-feeding arteries, 0% for the arteries feeding the healthy tissue), which was previously determined through the region growing algorithm for each outlet. Hence, by multiplying the TF_{i*} with the PEP_{i*} and summarizing over all outlets, we obtain the total tumor dose (%).

$$TD(\%) = \sum_{i*} PEP_{i*} \cdot TF_{i*} \tag{6.3}$$

6.2.3 Accuracy measures

While CFD simulations of intrahepatic blood flow and particle transport are complex and produce many possible output parameters, we choose to focus here on two relevant output parameters to steer clinical decision-making: the particle distribution in each of the downstream vessels, and the tumor dose. As mentioned, we study both the accuracy of and sensitivity to the particle distribution and tumor dose to determine the optimal simplification strategy, which results in four different metrics by which the simplification strategies will be evaluated and compared.

6.2.3.1 Accuracy of the particle distribution

For each outlet i, we calculated the absolute difference ($D_{b,i}$ (%), Eq. 6.4) between the particle exit percentage for a simulation of the baseline batch B ($PEP_{B,i}$) and the corresponding simulation of the simplification batch b ($PEP_{b,i}$) (i.e. simulation with the same injection mass flow rate) as:

$$D_{b,i}(\%) = \left| PEP_{B,i} - PEP_{b,i} \right| \tag{6.4}$$

The larger the difference $D_{b,i}$, the higher the drop in accuracy for outlet i. We calculated the average difference, D_{ave}, and the maximum difference in accuracy, D_{max}, over the 21 RHA outlets. We calculated these values for each batch b and for each injection mass flow rate, resulting in 8 values for D_{ave} and 8 values for D_{max} for each of the 5 batches (40 values in total).

6.2.3.2 Accuracy of the tumor dose

We also compared the absolute difference (D_{dose} (%), Eq. 6.5) between a simulation of the baseline batch B (TD_B) and the simulation of batch b with the same injection mass flow rate (TD_b):

$$D_{dose}(\%) = |TD_B - TD_b| \tag{6.5}$$

The larger D_{dose} (%), the higher the drop in accuracy. We did this comparison between batches for each injection mass flow rate, resulting in 8 values for D_{dose} for each of the 5 batch comparisons (40 values in total).

6.2.4 Sensitivity measures

6.2.4.1 Sensitivity of the particle distribution

The minimum-maximum range in particle exit percentage for a specific outlet i in simulation batch b ($\Delta PEP_{b,i}$ (%), Eq. 6.6) as a consequence of varying injection mass flow rate was reported in absolute percentage (%):

$$\Delta PEP_{b,i}(\%) = max(PEP_{b,i}) - min(PEP_{b,i}) \tag{6.6}$$

$\Delta PEP_{b,i}$ is interpreted as an indication of sensitivity to injection mass flow rate; with a high range indicating a significant impact of injection mass flow rate (high-impact parameter), while a low range indicates a low-impact parameter. Comparing different simulation batches (and, hence, different simplification strategies), similar values of $\Delta PEP_{b,i}$ indicate similar sensitivities to injection mass flow rate. Hence, for each outlet i, we compared the sensitivity of the baseline batch B ($\Delta PEP_{B,i}$) and the sensitivity of the simplification batch b with the same injection flow rate ($\Delta PEP_{b,i}$), giving the similarity in sensitivities for outlet i ($\Delta\Delta PEP_{b,i}$ (%), Eq. 6.7) in absolute percentage (%):

$$\Delta\Delta PEP_i(\%) = \left|\Delta PEP_{B,i} - \Delta PEP_{b,i}\right| \tag{6.7}$$

A low value of $\Delta\Delta PEP_i$ indicates a similar sensitivity as the baseline batch, and hence, a reliable simplification strategy. Here, we compute the average and maximal $\Delta\Delta PEP_i$ ($\Delta\Delta PEP_{ave}, \Delta\Delta PEP_{max}$) over all outlets as an indication of the similarity in sensitivity, giving 1 value for $\Delta\Delta PEP_{ave}$ and $\Delta\Delta PEP_{max}$ for each batch comparison (5 in total).

6.2.4.2 Sensitivity of the tumor dose

Similarly as above, the minimum-maximum range in tumor dose (ΔTD_b (%), Eq. 6.8) was calculated as the difference between the maximum tumor dose attained in one simulation batch and the minimum attained in the same batch, indicating the sensitivity of the tumor dose to injection mass flow rate:

$$\Delta TD_b(\%) = max(TD_b) - min(TD_b) \tag{6.8}$$

We compared the sensitivity to the tumor dose of the baseline batch (ΔTD_B) and the simulation of the simplification batch (ΔTD_b) to compute the similarity of sensitivities ($\Delta\Delta TD$ (%), Eq. 6.9) in absolute percentage (%). Hence, a low value of $\Delta\Delta TD$ indicates a similar sensitivity and hence, a reliable simplification strategy. In total, we obtain 5 values, 1 for each batch comparison.

$$\Delta\Delta TD(\%) = |\Delta TD_B - \Delta TD_b| \tag{6.9}$$

6.2.5 Sensitivity of the tumor dose

Due to the importance of computational cost in the study, we will note on both the computational times for the baseline simulation and the speedup factor offered by the viable simplification strategies identified in this study. The speedup factor is defined as the computational time needed for the baseline simulation divided by the computational time needed for the simplified simulation, both computed on a AMD EPYC HPC cluster with 94 CPU cores.

Additionally, we aimed to quantify the possible speedup offered by GPU-based computation. Since GPU-based computation for Ansys Fluent (Ansys, USA) is still in development, we used a simplified reference simulation to evaluate the GPU solver available in Fluent 2023 R1. For the reference simulation, the following assumptions were made: (1) the same geometry was used, without a catheter, (2) blood was modeled as a Newtonian fluid with a density of 1060 kg/m^3 and a viscosity of 0.00309 $kg/m \cdot s$, (3) no microparticles were injected, (4) a constant steady inflow of 0.12 m/s was defined. The same simulation was run on a HPC cluster with 24 and 96 AMD EPYC CPU cores, and 1 and 2 NVIDIA Volta GPU cores. The speedup factor was defined with respect to the 96 CPU cores.

6.3 RESULTS

In Section 6.3.1, an overview is given of how many flow cycles are needed to reach particle distribution convergence for each simplification strategy. Next, in Section 6.3.2, we evaluate the simplification strategies for (G1) accuracy and (G2) sensitivity of the particle distribution and the tumor dose.

6.3.1 Particle progression

As a result of the particle distribution convergence criterion, for the baseline batch, 10 cardiac cycles were run for the lowest injection mass flow rate (B01), and 9 cardiac cycles for the higher velocities (B02—B08). In Figure 6.2, the fraction of exiting particles over the total number of injected particles (exit percentage, %) was plotted for the baseline, truncated, coarse and extra coarse batches. As is clear from Figure 6.2, the exit percentages increased from 69% to 87% from lowest to highest injection flow rate. For the truncated batch, 8 flow cycles were run for the 2 lowest injection flow rates (T01, T02) and 7 for the higher flow rates. There was a clear increase in exit percentage from lowest to highest flow rate (72%-91%). For the coarse batch, 9 flow cycles were run for each flow rate. Exit percentages increased from lowest to third-to-last highest flow rate (68%-84%), with the two highest flow rates dropping slightly around 82%. For the extra coarse batch, 10 flow cycles were run for the lowest flow rate, and 9 cycles for the higher flow rates. The exit percentages increased from 70% to 86% from the lowest to fourth-to-last highest flow rate, then dropping slightly for the three highest flow rates (82%-84%).

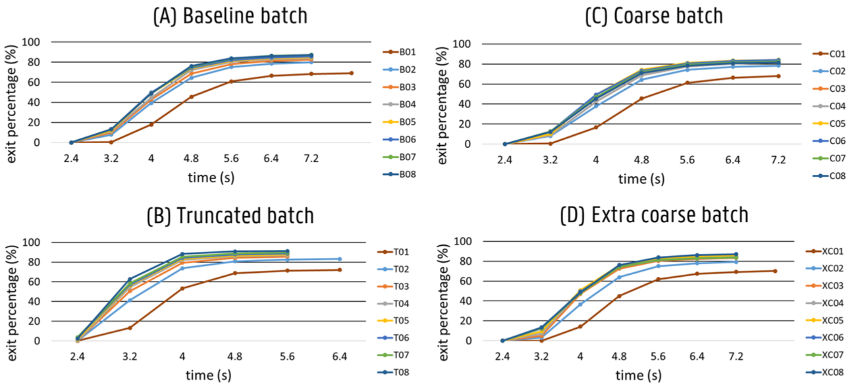

Figure 6.2: Particle progression in domain for (A) the baseline batch, (B) the truncated batch, (C) the coarse batch, and (D) the extra coarse batch. Clearly, lower injection flow rates result in lower exit percentages, and a longer flow time necessary to reach a stable particle exit distribution (see red line in A-D). Truncating the geometry also needs to a lower necessary flow time.

6.3.2 Evaluation of the simplification strategies

6.3.2.1 Accuracy of the particle distribution

In Table 6.2, we report the minimum-maximum ranges in the average and maximum differences in particle distribution of the 8 simulations when comparing corresponding injection flow rates between the baseline batch and the chosen simplification strategy (D_{ave}, D_{max}, computed over 21 outlets). For the sake of brevity, we only discuss the maximum values of D_{ave} and D_{max} in the section below. The highest average and maximal differences (D_{ave}, D_{max}) calculated over all outlets are 5.66% and 59.4% for the steady model, 1.04% and 9.27% for the truncated model, 0.579% and 3.02% for the coarse model, 0.622% and 4.38% for the coarse model with less flow cycles, and 1.599% and 14.9% for the extra coarse model.

6.3.2.2 Accuracy of the tumor dose

Using the tumor dose as the output parameter of interest instead of the full particle distribution, D_{dose} gives the difference range for

Table 6.2: Comparing accuracy (G1) between the simplification strategies (S: steady, T: truncated, C: coarse, XC: extra coarse, Cm: coarse with less flow cycles) and the baseline for both the particle distribution and the tumor dose. The minimum and maximum values of the average difference in particle distribution over the outlets (D_{ave}), maximal difference in particle distribution over the outlets (D_{max}), and tumor dose are given.

Batch	D_{ave} (%)	D_{max} (%)	D_{dose} (%)
S	3.61-5.66	28.4-59.4	5.59-19.8
T	0.346-1.04	2.11-9.27	0.269-3.65
C	0.322-0.579	1.23-3.02	0.0544-1.40
Cm	0.308-0.622	1.30-4.38	0.227-0.834
XC	0.505-1.599	2.58-14.9	0.534-5.00

each of the 8 simulations when comparing corresponding simulations between the baseline batch and a specific simplification strategy. Again, the full ranges can be found in Table 6.2, while we limit ourselves to the discussion of the maximum values here. For the steady model, the maximum difference between the steady and baseline tumor dose was 19.8%; for the truncated model, this difference was 3.65%; for the coarse model, 1.40%; for the coarse model with less flow cycles, 0.834%; for the extra coarse model, 5.00%. Hence, D_{dose} is the smallest for the coarse model and coarse model with less flow cycles (<1.5%).

6.3.2.3 Sensitivity of the particle distribution

First, we zoom in on the two main arterial feeders of the tumor (mentioned as feeder 1 and 2 below, and as indicated in Figure 6.1), contributing 11% and 20% of the total tumor perfusion (determined via region growing, as explained more in detail in Chapter 4) respectively. In the baseline model, the fraction of exiting particles flowing to feeder 1 varied between 0.143%-4.32% for the 8 injection flow rates (ΔPEP: 4.08%, see light blue curve in Figure 6.3A) and the fraction flowing to feeder 2 varied between 29.6%-44.3% (ΔPEP: 14.7%, see light blue curve in Figure 6.3B). Visually, it is already clear from both Figure 6.3A-B that the steady flow model is not an appropriate simplification strategy, since the total range of variation over injection flow rate (ΔPEP) is very dissimilar to both the baseline batch and other simplification strategies (0% for feeder 1, much larger range of 33.4% for feeder 2). Considering all simplification strategies, ΔPEP for feeder 1 was 0%, 3.10%, 1.69%, 2.04% and 1.75% for the steady, truncated, coarse, extra coarse and coarse with less flow cycles batches, respectively (see Figure 6.3A). Hence,

$\Delta\Delta PEP$ for feeder 1 was lowest (0.99%) for the truncated batch and highest (4.08%) for the steady batch. Additionally, ΔPEP for feeder 2 was 33.4%, 3.68%, 11.7%, 12.4% and 12.8% for the steady, truncated, coarse, extra coarse and coarse with less flow cycles batches, respectively (see Figure 6.3B). Here, $\Delta\Delta PEP$ for feeder 2 was lowest (1.82%) for the coarse model with less flow cycles and highest (18.75%) for the steady model.

Table 6.3: Comparing sensitivity (G2) between the simplification strategies (S: steady, T: truncated, C: coarse, XC: extra coarse, Cm: coarse with less flow cycles) and the baseline for both the particle distribution and the tumor dose. The average ($\Delta\Delta PEP_{ave}$) and maximal ($\Delta\Delta PEP_{max}$ (%)) differences in sensitivity towards the particle distribution are given, as well as the difference in sensitivity towards the tumor dose $\Delta\Delta TD$ (%).

Batch	$\Delta\Delta PEP_{ave}$ **(%)**	$\Delta\Delta PEP_{max}$ **(%)**	$\Delta\Delta TD$ **(%)**
S	2.68	26.2	10.1
T	1.08	11.0	3.33
C	0.597	2.98	0.68
Cm	0.576	2.53	1.63
XC	1.33	11.8	1.95

Considering all outlets instead of only the main tumor feeders, we report average and maximal values of ΔPEP and $\Delta\Delta PEP$ below and in Table 6.3. The average and maximal $\Delta\Delta PEP$ calculated over all outlets are 2.68% and 26.2% for the steady model, 1.08% and 11.0% for the truncated model, 0.597% and 2.98% for the coarse model, 1.33% and 11.8% for the extra coarse model, and 0.576% and 2.53% for the coarse model with less flow cycles.

6.3.2.4 Sensitivity of the tumor dose

In the baseline model, the tumor dose decreases from 55% to 51% from low to high injection velocity, respectively (ΔTD: 4.2%). As is clear from Figure 6.4, ΔTD is 14.4%, 0.892%, 4.91%, 2.27% and 5.86% for the steady, truncated, coarse, extra coarse and coarse with less flow cycles batches, respectively. Hence, when comparing to the baseline batch sensitivity, $\Delta\Delta TD$ is smallest for the coarse batch (0.68%) and largest for the steady batch (10.1%).

6.3.3 Computational times

Using 96 AMD EPYC cores, the baseline simulation took roughly 1487 minutes to run. For the optimal simplification strategies, we noted a decrease to 820 minutes (speedup factor of 1.81) for the

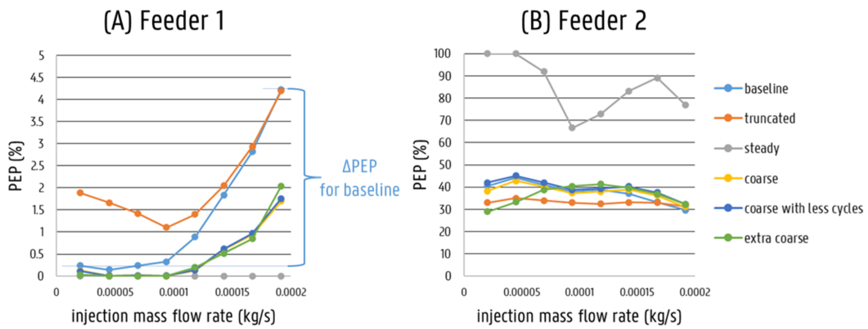

Figure 6.3: Plotting particle exit percentages (PEP, %) for the 8 injection flow rates of each simulation batch (baseline, truncated, steady, coarse, extra coarse and coarse with less flow cycles) for the two main tumor feeders, (A) outlet 36, and (B) outlet 40. The total range in variation gives the sensitivity, ΔPEP. Note that the range of the Y-axis is much smaller for outlet 36 (A) than for outlet 40 (B).

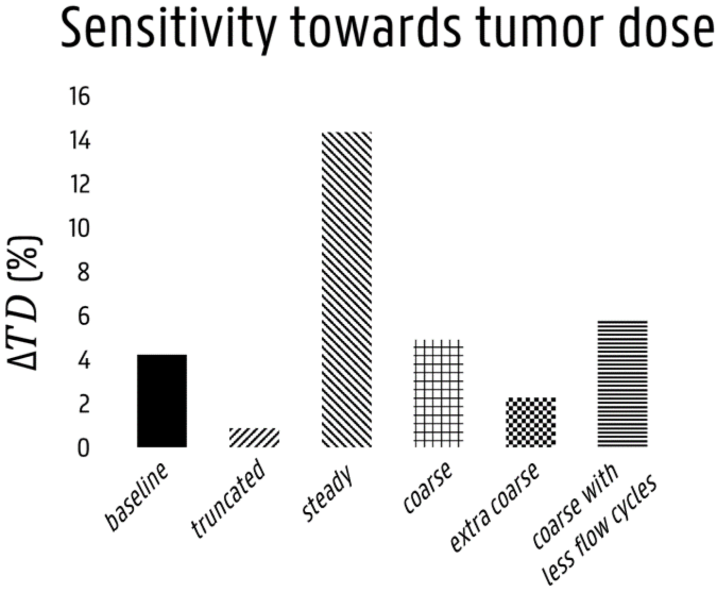

Figure 6.4: Comparing the sensitivity of injection flow rate towards the tumor dose for the different simulation strategies. Both the coarse and coarse model with less flow cycles approximate the baseline sensitivity the best; the steady and truncated models perform the worst.

coarse strategy, and a further drop to 580 minutes (total speedup factor of 2.56) for the coarse with reduced flow cycles strategy.

Additionally, we explored the impact of hard- and software improvements on the computational time, most notably the use of the Native GPU solver for Ansys Fluent. As shown in Figure 6.5, for 24 and 96 CPU cores (AMD EPYC) on the HPC cluster, a simulation wall clock time of 671.9 s and 257.4 s was noted. A slightly higher computational time of 304.3 s was noted for the single GPU core (NVIDIA Volta V100), but a significant drop was noted for the 2 GPU cores, with a time of 119.6 s (speedup factor of 2.15 compared to the 96 CPU cores).

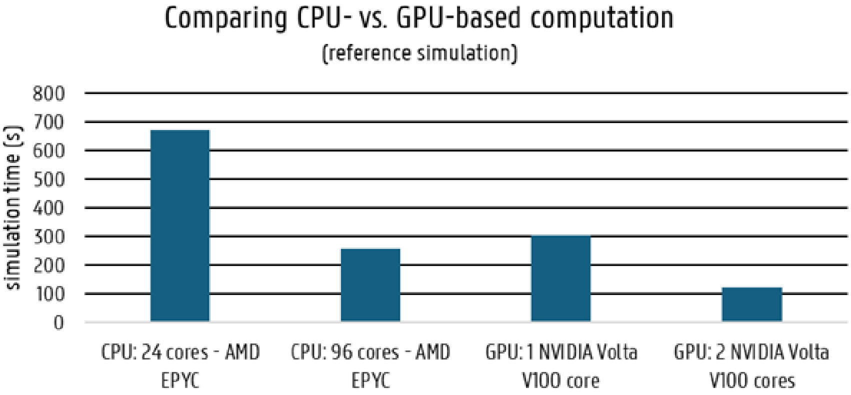

Figure 6.5: Comparing CPU-based computation with 24 and 96 AMD EPYC cores on a HPC cluster with GPU-based computation with 1 and 2 NVIDIA Volta V100 cores.

6.4 DISCUSSION

In Section 6.4.1, we discuss the impact of injection flow rate and the chosen simplification strategy on the number of flow cycles needed for particle distribution convergence. As we conclude Chapter 6 and the discussion on simplification strategies in the entirety of Part II, we discuss the optimal simplification strategies for accuracy and sensitivity in Section 6.4.2 and overview limitations and future steps in Section 6.4.4.

6.4.1 Particle progression

Figure 6.1 clearly shows that lower injection flow rates are correlated with lower exit percentages for the current particle distribution convergence criterion, although the difference is maximally 1 cycle (e.g. B01 compared to B02–B08). This effect was noted in both the baseline, truncated and extra coarse batch. Additionally, truncation of the physical domain also cut down the number of cardiac cycles necessary to meet the convergence criterion, resulting in a maximum flow time of 5.6–6.4 s, while it was 7.2–8.0 s for the baseline, coarse and extra coarse batches.

6.4.2 Selection of the optimal strategy

Based on accuracy, the coarse model and coarse model with less cardiac cycles performs best. As shown in Table 6.2, the average difference in particle distribution is small for both simulation strategies (maximum value considerably smaller than 1%). Studying the tumor dose, the coarse model with less cardiac cycles performs slightly better than the coarse model (maximum difference of 0.834% compared to 1.40%). However, studying the maximum difference in particle distribution, the coarse model performs slightly better (maximum value of 3.02% compared to 4.38%). For all other strategies, the average and maximum differences in particle distribution increase significantly (maximum values larger than 1% and 5%, respectively), and the accuracy in tumor dose decreases (maximum difference larger than 2%). It should be noted that a maximum difference in particle distribution of 3.02% in one of the outlets (as is the case of our coarse model) is larger than the maximum difference we allowed for our mesh sensitivity study (1%) and explains why our mesh sensitivity study led to a higher mesh density than the coarse model considered here. Hence, coarsening the mesh is possible, but it is associated with a considerable decrease in accuracy for the particle distribution. At the same time, a tumor dose accuracy less than 1.5% difference with the baseline value should be acceptable. Importantly, this shows that judging the suitability of the simplification strategy is dependent on the specific output parameter(s) considered (particle distribution versus tumor dose). Additionally, the stringency on accuracy (i.e. whether or not a maximum difference in particle distribution of 3.02% is acceptable or not) will likely depend on both the eventual application and the persons designing and using the application. Summarizing the above, the coarse model performs best, but there is a drop-off in accuracy, as was already evident from our original mesh sensitivity study.

Based on sensitivity, the coarse model performs best (see Table 6.3), as it is the only strategy with both very similar sensitivities to tumor dose (<1% difference) and very similar sensitivity to the particle distribution (average difference over all outlets <1%, maximum difference <3%). The next best alternative is the coarse model with less cardiac cycles, which performs slightly worse for the sensitivity to tumor dose (difference of 1.63% with the baseline, see Figure 6.4). For all other strategies, the maximum difference over all outlets is always at least 10%. The extra coarse batch is the only strategy which still has acceptable sensitivity to tumor dose (1.95% difference with the baseline, see Figure 6.4); for the other strategies, it is already significantly higher (3.33% and 10.1% difference with the baseline for the truncated and steady strategies, respectively). Clearly, the steady strategy performs the worst overall. From the above, we conclude coarsening the mesh is the optimal strategy for sensitivity purposes.

Notably, when focusing on specific arterial feeders, different conclusions can be made on the suitability of simplification strategies. For example, as was shown in Figure 6.3 for feeder 1 and 2, the truncated and extra coarse batch were identified as the most suitable strategies, respectively. Again, this shows that the output parameter considered has a significant impact on the choice of the simplification strategy of interest. However, focusing on only one arterial feeders would be too narrow (feeder 2 itself only still contributes 20% of the total tumor perfusion). Hence, we choose to focus on the global picture (tumor dose and full particle distribution) when deciding on the best simplification strategy. We advise not to focus only on tumor dose but also to consider particle distribution, since tumor dose (as considered here) is essentially a weighted average of the particle distribution, and the particle distribution is the underlying physical parameter informing the tumor dose.

There is not a very distinct difference in performance when evaluating these simplification strategies for accuracy or sensitivity. For example, the maximal difference in particle distribution for one outlet with the coarse model was reported as 3.02% (accuracy), and the maximal difference in sensitivity in one outlet for the coarse model was reported as 2.98% (sensitivity) (see Table 2). However, by design, accuracy is a more stringent goal than sensitivity, since the goal of the latter is typically to either rank parameters from high to low impact, which is typically a tool for model diagnosis, while the first aims to give a reliable prediction of the output parameter of interest. Additionally, much more simulations are also needed for extended, global sensitivity analyses, increasing the need for shorter computational times more than for accuracy purposes. Crucially, we tracked the computational cost for the simulations with the highest injection mass flow rate (run on separate days on a High Performance Computing system using 94 cores of an AMD EPYC 7552 2.2 GHz processor with RHEL 8 operating system). Here, we noted a 45% decrease in computational time for the full simulation for the coarse model (compared to the baseline) and a 60% decrease for the coarse model with less cardiac cycles. Combining the arguments above (sensitivity studies require much more simulations, and are less stringent than accuracy studies), we advise to use mesh coarsening (and reducing the number of cardiac cycles) for sensitivity analysis first and foremost, and for accuracy only when strictly necessary.

6.4.3 Computational time vs complexity

Importantly, computational complexity and computational time are not the same thing; for a given complexity, the computational time depends highly on the hardware used, which (non-trivially) depends on the resources available to the user. Here, we mainly opted for a High Performance Computing system and noted computational times could be decreased with a speedup factor of 2.56 by using a coarsened mesh with a reduced number of flow cycles. Additionally, we also explored GPU-based computing using the Native GPU Fluent solver (available in Fluent 2023 R1). With 2 GPU cores, we noted a speed increase with a factor of 2.15 compared to 96 CPU cores, indicating the high potential of GPU-based computation. The improvement for using 2 GPU cores instead of 1 was of a factor of 2.54, showing good parallelization and indicating that using a higher number of cores could decrease computational times even further. Other work confirms that for similar biomedical cases, such as air flow in the airways, GPU-based computational offers significant acceleration [131]. Importantly, these computational times are only valid for the reference, steady-flow simulation, which we showed in this study is not an accurate predictor of the time-dependent tumor dose or microsphere distribution. Therefore, as shown in this study, model simplification cannot make a bridge towards GPU-based computation yet, since significant steps still need to be made to run more complex models via GPU-based computation. Currently the trade-off between computational time and computational complexity still exists for our 3D CFD simulations, and model simplification is still an important, valid strategy to decrease computational cost.

6.4.4 Limitations and future work

From the modeling point of view, several limitations arise, which are explained more in detail in Section 11.1. Specifically, for the purpose of this study, there are other notable limitations. This computational study was done in only 1 patient-specific geometry. Although the injection scenario was realistic (selective injection in the RHA), more injection scenarios, patient-specific geometries and cancer scenarios should be investigated before generalizing the conclusions made here. Additionally, we judged the suitability of specific simplification scenarios by studying sensitivity towards one specific parameter, i.e. injection mass flow rate. Ideally, it should be investigated whether the conclusions regarding suitability of the coarse mesh model for sensitivity are translatable to other varying parameters. If so, we can use these significantly simplified models for sensitivity studies. These sensitivity studies are crucial to determine the most influential clinical and numerical model input parameters (e.g. boundary conditions). Importantly, the evaluation of the current strategies only applies for the chosen two output parameters (tumor dose and particle distribution); if other parameters are deemed relevant by other users to inform clinical decision-making, the conclusions should be re-evaluated. Of course, other strategies still exist which might drive down computational time even further while still allowing reliability. Recently, data-driven surrogate modeling has become popular, although sufficient high-fidelity training samples are still needed to train the model, whose computational cost is far from trivial. While we used a ‘brute-force’ grid coarsening approach here, adaptive mesh refinement in certain sensitive regions (i.e. near the catheter tip) might allow to decrease the total number of mesh elements. Since the study emphasized the added value of GPU-based computation with regards to computational times, other numerical techniques (e.g. Lattice Boltzmann) might offer additional acceleration, although their performance was not considered in the current study.

Once validated, these patient-specific models and sensitivity analyses of influencing injection parameters can play an important role in preoperative planning. They can help to improve tumor targeting and reduce the need for invasive pre-treatment. Specifically, simplified models which are not computationally too complex are more likely to be successfully translated to clinical practice.

6.5 CONCLUSIONS

In Chapters 4 and 5, we already showed that moderate up- and downstream truncation is possible while still allowing sufficient accuracy. In Chapter 6, we showed that coarsening the mesh (and possibly reducing the number of flow cycles) are the most suitable simplification strategies, especially for sensitivity (accuracy only if we are less strict, which depends on the application and the preferences of the user). Throughout the dissertation so far, we named the high computational cost of 3D CFD models of intrahepatic drug transport the main reason why global sensitivity analyses (which require many model evaluations) are not feasible. While the current simplification strategies (i.e. coarse model with less flow cycles) can cut down the computational cost by roughly 60%, these simplified models are from simplified enough to run hundreds or thousands simulations within a reasonable time frame. Hence, we will use these simplified models as a starting point, and explore other strategies, such as data-driven surrogate modeling, to further drive down computational time.

III

Uncertainty Quantification of Clinical and Numerical Parameters

CHAPTERS

What a frightening thing is the human,
a mass of gauges and dials and registers,
and we can only read a few
and those perhaps not accurately.

J. Steinbeck

Chapter 7

Uncertainty Quantification With Uncertain Injection Position

Positioning of the chapter

In Part II, we focused mainly on identifying reliable simplification strategies of patient-specific 3D CFD simulations. In this part, we will use simplified CFD models as a starting point to perform uncertainty quantification and sensitivity analysis. For our application of drug transport during TARE, uncertainty quantification and sensitivity analysis are especially relevant because we consider two types of uncertain parameters. First, specific clinical injection parameters introduce uncertainty because they are uncontrollable (e.g. cross-sectional injection position) or difficult to quantify or keep constant (e.g. injection flow rate). Second, uncertain numerical input parameters (e.g. boundary conditions) also introduce uncertainty. Here, we will illustrate uncertainty quantification of both clinical and numerical parameter types. In Chapter 7, we will quantify uncertainty in the tumor dose caused by an uncertain, uncontrollable in vivo cross-sectional position of the catheter tip using a low fidelity CFD model. In Chapter 8, we will explore surrogate models to perform sensitivity analysis of the inlet waveform. By the end of Chapter 8, the goal is to have shown feasible methods of performing uncertainty quantification and sensitivity analysis for a wide range of uncertain clinical and numerical parameters, despite the initial complexity of our 3D CFD simulations.

This chapter is based on the publication *A Hybrid Particle-Flow CFD Modeling Approach in Truncated Hepatic Arterial Trees for Liver Radioembolization: A Patient-Specific Case Study* (T. Bomberna et al, Frontiers in Bioengineering and Biotechnology, 2022) [19].

7.1 Introduction

In previous work, the microsphere distribution was typically calculated deterministically, with fixed clinical parameters serving as input for the CFD model [10, 15]. Similary, in Chapters 4 and 5, the particle distributions were calculated for a fixed catheter tip position, axial injection location, catheter flow rate, etc. Additionally, in Chapter 6, the tumor dose resulting from this particle distribution was calculated, again deterministically.

However, Chapter 6 also introduced the notion of tumor dose range, where an input parameter (injection flow rate) was varied across a realistic range, and the resulting spread in tumor dose values was quantified. This notion is similar to Monte Carlo approaches, because it treats a parameter as stochastic (that was in other work considered deterministically) [132]. As a result, a large spread in the tumor dose output indicates a high sensitivity towards this varying parameter, a low spread indicates a low sensitivity. Specifically, in Chapter 6, the spread (for the baseline model, B) was between 50.8 % and 55.0% (from high to low injection flow rate). Hence, the total tumor dose range was 4.22%.

Importantly, the more controllable parameters are, and the more they are fixed at or near a specific value, the smaller this tumor dose range becomes. At the start of injection, injection flow rate is typically easy to set, while it might become more difficult during the procedure as the downstream vascular resistance increases. Other clinical parameters can be even more difficult to control, such as the catheter tip position. Hence, in this chapter, we will quantify uncertainty in the tumor dose caused by an uncertain, uncontrollable cross-sectional position of the catheter tip.

We will vary the tip position across a specific axial injection plane, and calculate the resulting tumor dose ranges. However, because the forward CFD model is costly, and repeatedly calculating the tumor dose resulting from many different catheter tip positions will be very expensive, we introduce a simplifying approach to generate the tumor dose ranges much more cheaply. We will also compare the tumor dose ranges generated from the moderately and severely truncated geometries from Chapter 4 to inspect the impact of truncation.

7.2 METHODS

In Section 7.2.1, we discuss the study design of this chapter. Next, in Section 7.2.2, we introduced a simplified CFD model which can cheaply compute tumor doses resulting from a varying catheter tip position. We refer to this approach as a low fidelity CFD model since it requires strong simplification of the forward CFD model for cheap computation.

7.2.1 Study Design

For this study, we re-use Simulations 1–3 (see Table 4.1) from Chapter 4. In summary, this study considers the same planar injections as in Chapter 4 (i.e. with the axial location superficially before the first bifurcation) for the full-complexity hepatic arterial geometry (Geometry 1) and two arterial geometries with different levels of truncation (Geometry 2 & 3; see Section 4.2.2.2). However, as discussed below, we post-process the results differently.

7.2.2 Low Fidelity-based Tumor Dose Range

The meshing, blood flow and particle physics, in- and outflow boundary condition methodology and solver settings were all identical to the settings explained in Chapter 4. Additionally, in Section 4.3.3.2, it was explained how the grid-based particle distribution could be computed with the planar injections, resulting in the CFs (cell fractions) of Geometry 1 or the TCFs (truncated cell fractions) for the truncated Geometries 2-3. Since we use the hybrid-particle flow model to assume particles distribute proportionally to the flow distribution downstream of the truncated outlets, both CFs and TCFs result in 48 values, one for each outlet of the original Geometry 1. With this method, CFs and TCFs can be easily compared.

However, the goal is to mimic catheter injection using our planar injections. To do this, the $(T)CF_x$ is not calculated for the full cross-section (as in Chapter 4), but also for a small section of the grid that would coincide with the catheter tip exit location for a catheter injection. This catheter-associated $(T)CF_x$ offers an estimation of the particle distribution after catheter injection for a hypothetical catheter injection location.

The tumor dose (TD in Equation 7.1) can then be estimated by multiplying the $(T)CF_x$ with the fraction of particles flowing to the tumor for outlet x (calculated as the ratio of the tumor flow contribution, $Q_{t,x}$, as defined in Equation 4.15, over the total flow in the outlet, $Q_{t,x} + Q_{h,x}$) and adding together these contributions for all 48 outlets. This gives a measure of the total number of particles flowing to the tumor (i.e., total "tumor dose"):

$$TD = \sum_{x=1}^{48} (T)CF_x \cdot \frac{Q_{t,x}}{Q_{t,x} + Q_{h,x}} \tag{7.1}$$

When the small, catheter-associated grid section is shifted randomly across the injection plane to represent randomly sampled catheter injection locations (see Figure 7.1A), the tumor dose distribution shows how much the tumor dose changes for random injection locations within the injection plane. Essentially, this tumor dose distribution can offer a direct quantification of the differences between the different (C)PRGs obtained for the simulations as listed in Table 4.1, since similar (C)PRGs should lead to similar tumor dose distributions. Accordingly, the tumor dose distribution is also a direct indicator of the impact of cross-sectional catheter tip position: if the impact of this varying tip location would be small, the resulting tumor dose distribution should be limited in range; if the impact is large, the dose distribution should be significantly larger in range.

Here, the sampling over the plane was done in Matlab (MathWorks, United States), with a uniform distribution for all grid cells included in the sampling set. However, grid cells that were located too close to the periphery (i.e., when catheter tip placement was not possible) were not deemed "appropriate" and excluded from the sampling set. Essentially, these were grid cells where a 7×7-square (i.e., with sides of $7 \cdot 10^{-4}$ m) could not be placed around the central cell.

7.3 RESULTS

Studying the tumor dose ranges (minimum-maximum) based on the low fidelity modeling approach, the sampled grid cells (the same for all three geometries) are given in Figure 7.1A. The tumor dose distribution for these 50 randomly sampled catheter injections in each geometry are given in a violin plot in Figure 7.1B, with the colored area surrounding the boxplot representing the sample density. The median tumor doses are 43.1, 44.0, and 44.6%, respectively. The ranges in tumor dose are 31.9%–47.9% for Geometry 1, 34.6%–48.4% for Geometry 2, and 37.5%–49.9% for Geometry 3. Hence, the sensitivity to the varying parameter, ΔTD (as defined in Chapter 6), for Geometry 1 is 16.0%.

Comparing the impact of truncation, we see that the sensitivity similarity parameter $\Delta\Delta TD$ (as defined in Chapter 6) for Geometry 2 is 2.2% compared to the baseline Geometry 1, and $\Delta\Delta TD$ for Geometry 3 is 3.6%. In general, the tumor dose distribution is slightly more concentrated for Geometry 3, while the bell-like distribution shapes for Geometry 1 and 2 are more similar to each other.

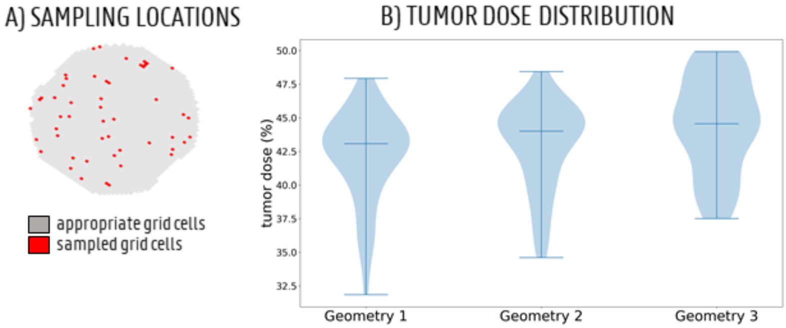

Figure 7.1: (A) The full sampling set of appropriate grid cells (grey) and 50 sampled grid cells (red) to simulate particle injection from these catheter tip locations. (B) Low Fidelity-based distribution of tumor dose (TD) for 50 randomly sampled catheter injection locations in each geometry. The 3 bars denote the minimum, median and maximum, respectively. The violin plot for Geometry 3 looks slightly different than for Geometries 1 and 2, but the medians are very similar.

7.4 DISCUSSION

First, we discuss the most important results regarding the tumor dose distributions: the impact of cross-sectional tip position on the tumor dose in Section 7.4.1, and the impact of truncation on the sensitivity in Section 7.4.2. Afterwards, the limitations of this low fidelity CFD modeling approach are discussed, showing the clear need for a more broadly applicable simplifying framework for uncertainty quantification in Section 7.4.3.

7.4.1 Expected dose and sensitivity

Judging the tumor dose distribution for the baseline Geometry 1, the median dose is 43.1%. This can be interpreted as an indication of the expected dose, if we are not able to control the catheter tip position within the plane. Additionally, the tumor dose range resulting from this varying catheter tip position is 16%. In comparison, the tumor dose range resulting from the varying injection flow rate in Chapter 6 was 4.22%. These results indicate that, under these patient-specific conditions, the tumor dose is considerably more sensitive to catheter tip position than it is to injection flow rate.

7.4.2 Impact of truncation on sensitivity

As is clear from Figure 7.1B, the overall tumor dose range is highest for Geometry 1 (16.1% instead of 13.8% for Geometry 2 and 12.4% for Geometry 3). This discrepancy for Geometry 3 is most likely due to the increased truncation level. Importantly, this means that the predicted sensitivity of the tumor dose to catheter tip location is slightly larger for Geometries 1 and 2 (i.e. Geometry 1–2 have a larger ΔTD). In comparison, the computed $\Delta\Delta TD$ for Geometry 2-3 was 2.2–3.6% (with Geometry 1 as the baseline), which is of a similar order of magnitude as the $\Delta\Delta TD$ of 3.33% for the severely truncated model when we considered injection flow rate as the varying input parameter in see Chapter 6. Importantly, these values for $\Delta\Delta TD$ are also still considerably larger than the $\Delta\Delta TD$ for the coarsened model in Chapter 6. This seems to confirm our results form Chapter 6, where we already noticed that truncation has a clear impact on sensitivity, and we preferred coarsening the mesh as the optimal strategy instead.

However, the impact on the medians of the distribution is limited (43.1% for Geometry 1, 44% for Geometry 2, and 44.6% for Geometry 3). Also, even given small variations because of truncation, the tumor dose ranges for the truncated geometries when varying cross-sectional tip position are still significantly larger than when varying injection flow rate, as in Chapter 6. That means, even though truncation induces differences in sensitivity, we still would have made the correct conclusions regarding which of the two is the highest-impact clinical parameter. Hence, truncation might also be an appropriate third-choice simplification strategy for sensitivity. However, we still need to be careful in generalizing this, as it is likely that we will encounter clinical parameters in the future which might not differ so much in sensitivity as the two parameters compared here.

7.4.3 Limitations and future work

With catheter tip position as the only varying clinical parameter, the low fidelity-based tumor dose range approach based on 1 planar injection is a cheap uncertainty propagation method. Importantly, the validity of the low fidelity CFD modeling approach was verified for several catheter tip locations, but not for the entire range of locations considered here. Hence, instead of 1 planar injection and 50 samples processed after the simulation, 50 different catheter locations (i.e. 50 different geometries and meshes) and 50 different simulations would have to be run to verify whether explicitly modeling 50 different catheter tip locations or using 50 samples of the planar injection results in a similar tumor dose distribution. However, both the manual work and computational time would explode significantly. While this simplifying approach might be a likely assumption for standard microcatheters, this might differ significantly for other catheter types which significantly alter the near-tip hemodynamics. Since Kleinstreuer et al. [9] already emphasized the importance of catheter presence, we cannot underestimate the importance of explicitly modeling the catheter, which is not done here. Additionally, this simplifying approach only works well when the varying parameter of interest is the catheter tip position, and would not work when we want to vary other clinical parameters. Hence, we conclude from the above that to have an uncertainty quantification framework that generalizes well, a new approach will be needed.

7.5 CONCLUSIONS

In Chapter 6, we already quantified the sensitivity of the tumor dose towards varying injection flow rate, and introduced the notion of tumor dose ranges because of uncertainties in clinical input parameters. Here, we quantified the tumor dose range or sensitivity for varying catheter tip location, using a simplified low fidelity CFD modeling approach. Importantly, the tumor dose range was of the order of 16%, which indicates a clinical parameter of high importance. This is crucial, since it is currently technically unfeasible to accurately control the catheter tip location in vivo, and determining the tumor dose distribution or expected dose for a given axial plane may help to quantify the uncertainty regarding catheter tip location for that plane. However, since the approach used here had strong limitations, we will explore more broadly applicable uncertainty quantification approaches (such as surrogate modeling) in the next chapter.

CHAPTER 8

Sensitivity Analysis of the Inflow Waveform Shape

POSITIONING OF THE CHAPTER

In Chapter 7, we introduced a simplifying modeling framework to quantify the uncertainty in the tumor caused by an unknown cross-sectional catheter tip position. However, there are many more clinical parameters, and additional numerical model-based input parameters, whose uncertainty cannot be quantified using planar injections. Additionally, we do not only want to perform uncertainty quantification, but also global sensitivity analysis, where multiple parameters are varied at once (as in clinical practice) and the most impactful parameters can be identified. Hence, in this chapter, we rely on surrogate models to introduce a broad framework for sensitivity analysis of all types of input parameters, while still considering the high computational complexity of our 3D CFD multiphase simulations.

This chapter is based on the publication *Adaptive Design of Experiments to Fit Surrogate Gaussian Process Regression Models Allows Fast Sensitivity Analysis of the Input Waveform for Patient-Specific 3D CFD Models of Liver Radioembolization* (T. Bomberna et al, Computer Programs and Methods in Biomedicine, 2024) [22].

8.1 INTRODUCTION

CFD studies have shown that many different injection parameters which vary in clinical practice, such as infusion flow rate [12, 15, 92], size and density of the microspheres [14], microcatheter type [10, 90, 133], microcatheter axial tip location [130], microcatheter tip location within in the arterial cross-section [113, 116], etc. significantly impact the downstream microsphere distribution. Since treatment success also wildly varies for TARE [100], the impact of these many clinical parameters on the treatment outcome is preferably studied on a patient-specific basis.

Preliminary evidence shows that these clinical injection parameters strongly interact, making sensitivity analysis (SA) more complex. For example, Taebi et al. [130] showed that the sensitivity of the particle distribution towards the cross-sectional injection position was much higher for an injection plane close to a bifurcation than far away from it. This underlines that local SA does not suffice to capture these interaction effects. Importantly, next to clinical parameters, many model-related numerical input parameters, such as boundary conditions, are also uncertain because they are often estimated through imperfect measurements or mathematical modeling, which can introduce extra uncertainty in model outcomes [118]. For example, Taebi et al. [134] investigated the impact of outlet boundary conditions on hemodynamics and blood flow distribution, varying two parameters of the 3-element Windkessel models applied at the outlets: the summation of the distal and proximal resistance (total resistance), and the ratio between the distal and proximal resistance. They noted that mainly the choice of the total resistance impacted model outcomes. Hence, we should use global SA to determine the most impactful clinical and numerical input parameters.

For SA, forward uncertainty propagation techniques are used to estimate the effect of uncertainties in model inputs on the outputs [135]. However, repeatedly running 3D CFD simulations for uncertainty propagation is costly. To reduce computational cost for global SA, both the CFD model and the uncertainty propagation technique can be simplified. Regarding CFD models, we previously identified three strategies for reliable simplification: truncation of the downstream vessels, coarsening the mesh significantly and running a reduced number of flow cycles (see Chapter 6). However, the computational cost of a single CFD simulation remains high, and low-fidelity approaches are not always applicable (see Chapter 7). Luckily, several other techniques exist to further reduce the computational cost of uncertainty propagation techniques, such as the use of surrogate models [136]. Currently, examples of surrogate models are severely lacking for our application of 3D CFD models of intrahepatic drug transport. As an only example, Yuan et al. [137] developed a convolutional neural network (CNN) to predict the drug distribution field in a 2D branching geometry with 1 inlet and 5 outlets, which allowed them to speed up the prediction time by a factor of 132,935 compared to the numerical simulation. However, it should be noted here that that training samples for the CNN are still relatively cheap to compute for 2D simulations. For complex 3D arterial geometries, generating surrogate models becomes even more of a challenge, because the high computational cost limits the number of available training samples.

Hence, in this study, we illustrate the feasibility of designing a surrogate model specifically for SA of complex 3D CFD simulations with a limited number of samples. As an illustrative but relevant case, we will perform SA of the tumor dose output towards three shape parameters of the inlet mass flow waveform boundary condition: the peak systolic height, the ratio between the duration of systole and diastole, and the heart rate. To the authors' knowledge, uncertainty quantification towards inlet boundary conditions is very limited in this domain. If successful, these methods can be translated to other SA problems, such as quantifying the sensitivity of the tumor dose towards more clinical and numerical parameters.

8.2 METHODS

In Section 8.2.1, we explain the goal of this chapter and the study design. In Section 8.2.2, a brief overview is given of how we use patient-specific CFD modeling to convert medical images into tumor dose predictions. Next, in Section 8.2.3, we explain how a surrogate model can be used to fit a relationship between CFD inputs and outputs. We illustrate the suitability of using this surrogate model to reliably obtain sensitivity indices for the example Ishigami function in Section 8.2.4. Finally, in Section 8.2.5, we apply these techniques to our waveform sensitivity problem.

8.2.1 Study Design

Previously, we used patient-specific 3D CFD simulations of blood flow and drug transport to predict the tumor dose after drug infusion. In this study, we want to perform a global SA of the tumor dose towards three specific shape parameters of the input mass flow rate waveform:

the peak systolic mass flow rate, the ratio between the duration of systole and diastole, and the heart rate. We aim to do this using a computationally cheap surrogate model (a Gaussian process regression model, GPR), which is fit on a (limited) number of complex 3D CFD model evaluations. We optimize the GPR to perform SA reliably by a novel adaptive design of experiments (ADOE) algorithm, which adds additional model evaluations to the initial design of experiments (DOE) if the GPR is not sufficiently sensitive yet. The study consists of several parts:

- First, a multiphase CFD model "M" is defined, which calculates the tumor dose from patient-specific imaging data.
- Second, we introduce the novel ADOE algorithm to appropriately fit the surrogate GPR for our purpose of SA. We will illustrate and optimize the design of our ADOE algorithm using the example Ishigami function [138], and use this function to optimize several ADOE hyperparameters.
- Third, we apply the ADOE to our waveform problem and fit our surrogate GPR, $\mathcal{M}$.
- Finally, we use $\mathcal{M}$ to determine the sensitivity of the tumor dose towards the three shape parameters using the Sobol variance-based method [139].

More details on each part are given below.

8.2.2 Physics-based Tumor Dose Model

Below, the CFD approach to convert patient-specific images into a tumor dose prediction is briefly described (more details on the approach can be found in Chapter 4). A patient-specific hepatic arterial tree with a microcatheter tip position in the right hepatic artery was reconstructed based on a conebeam CT dataset from UZ Leuven (Leuven, Belgium) (see Figure 8.1A). The mesh consisted of $2.43 \cdot 10^6$ volume elements, with tetrahedral elements in the bulk of the domain and three prism layers enabled near the boundaries (the optimal mesh density was determined in Chapter 6). We used a multiphase approach in Fluent (Ansys, USA) to model the continuous intra-arterial blood flow and discrete microsphere behavior. Blood was modeled as a shear-thinning fluid with a density of 1060 kg/m^3. The microspheres were modeled as inert spheres (diameter of

40 µm, density of 1600 kg/m^3). With regards to boundary conditions, a time-dependent mass flow rate was applied at the inlet (specified later) and a flow distribution was applied at the outlets as constant flow fractions. Each time-dependent simulation was run for 9 flow cycles, with a time step size of 0.1 ms. Convergence (either absolutely scaled residuals of at least 10^{-5} or relative drops of at least 10^{-3}) was reached in each time step.

To convert the particle distribution into a tumor dose, the particle exit fraction at each arterial outlet was multiplied with the fraction of the outlet flow flowing to the tumor (100% for internal tumor-feeding arteries, 0% for the arteries feeding healthy tissue; assuming that microspheres downstream of the computational domain follow the flow distribution). By summing the microsphere fractions flowing to the tumor for each arterial outlet, we obtain the tumor dose, as explained more in detail in Chapter 4.

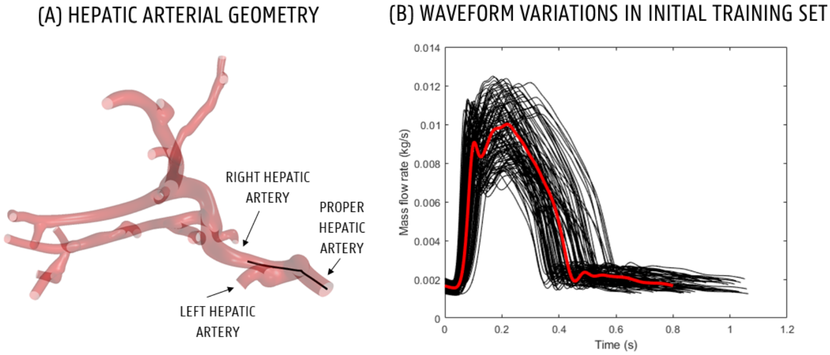

Figure 8.1: (A) Hepatic arterial geometry with 16 outlets, with the inlet 50 mm away from the catheter tip, and the catheter tip embedded in the right hepatic artery. The left hepatic artery is reduced to 1 outlet. (B) Original waveform (red) and 100 additional waveforms generated by Latin hypercube sampling of three shape parameters ($x_1 - x_3$) within 75%-125% of their original (red) values.

8.2.3 Fitting of the surrogate model

Below, we explain how we fit a surrogate GPR, $\mathcal{M}$, compute a cheaper relationship between inputs and outputs of the complex model, M.

8.2.3.1 Gaussian Process Regression Model

A GPR is a probability distribution over possible functions that fit the observed (training) data. As input, the GPR uses the inputs and outputs of the complex model, M, and a specific covariance function (kernel k, Eq. 8.1). As output, it reports the mean function of the outputs as well as the probability ranges of the predicted outputs; we use these probabilities in the ADOE. Our kernel was a radial basis function (RBF) which took the form:

$$k(x_i, x_j) = \sigma^2 exp(-\frac{1}{2l} \left| x_i - x_j \right|^2) \tag{8.1}$$

In Eq. 8.1, x_i and x_j are points in input space, l is the length-scale, and σ is the variance. Hyperparameters of the GPR such as the length-scale l and variance σ are learned from the data during the training process. The GPR model was implemented in Python (Python Software Foundation, USA) using the sklearn package (https://scikit-learn.org/stable/)

8.2.3.2 Sobol Sensitivity Method

After fitting the GPR, $\mathcal{M}$, we use $\mathcal{M}$ to predict the tumor dose output for 8.192 Saltelli sampled inputs [139], based on which we compute Sobol's sensitivity indices. In short, Sobol's variance-based sensitivity method decomposes the variance of the model output into contributions from individual input parameters and their interactions, which allows us to understand which input parameters have the most significant impact on the model output [139]. The first-order indices (S1) quantify the total impact of each input parameter individually (Eq. 8.2). Here, V[Y] denotes the total variance of the output (Y, tumor dose), and $V[E[Y|X_i]]$ the variance in the expected value of the output, given that one parameter, X_i, is known. If $V[E[Y|X_i]]$ is large, the variance reduction made possible by knowing X_i is large, and, hence, X_i, is an influential parameter with a large sensitivity index, S_i.

$$S_i = \frac{V[E[Y|X_i]]}{V[Y]} \tag{8.2}$$

Higher-order Sobol indices include interaction effects between different parameters. Since the sum of all Sobol indices for X_i (including interactions with other parameters) equals 1 by construction, the total effect of X_i, including interactions with other parameters, can be quantified with the total-order index, ST_i (Eq. 8.3). Here, $V[E[Y|X_{\neg i}]]$ is the variance in the output caused by variations in all uncertain parameters except X_i. Notably, the sum of the total-order indices of all parameters is larger than 1 for non-additive models. Again, a high ST_i indicates a high influence of parameter X_i. The

Sobol indices were calculated in Python using the SALib package (https://salib.readthedocs.io/en/latest/).

$$ST_i = 1 - \frac{V[E[Y|X_{\neg i}]]}{V[Y]} \tag{8.3}$$

8.2.3.3 Design of the ADOE algorithm

Since it is a priori unknown how many model evaluations are needed to appropriately fit the GPR and because of the high computational cost of every single CFD model evaluation, our ADOE actively tries minimize the number of necessary CFD model evaluations while still reliably performing SA. To fit $\mathcal{M}$, we need to sample the input parameters across input space (design of experiments, DOE) and compute the true outputs using M for the full set of samples. As shown in Figure 8.2, the ADOE works as follows:

- First, we define an initial design of experiments (DOE) of N_{init} samples for 3 input parameters using Latin Hypercube sampling (LHS). This generates a N_{init}-by-3 matrix.
- Second, we evaluate the complex model, M, for each point of the DOE, and then use these in- and output pairs to fit our GPR.
- Third, we use LHS to generate 10.000 new samples in the 3D input parameter space (10.000-by-3 matrix). We use the surrogate GPR, $\mathcal{M}$, to predict both the output and the uncertainty on the output for each of the 10.000 samples. Then, we divide each input parameter axis of the 3D input parameter space into B bins, and determine the most uncertain predictions in each bin (resulting in B^3 bins, see Figure 8.2), and determine the most uncertain prediction in each bin (B^3 points out of the 10.000 candidate points).
- Fourth, we use the complex model, M, to calculate the true output for the B^3 uncertain predictions from the previous step, and add these in- and output pairs (‘batch’) to the DOE. We re-fit the GPR, including the extra batch of input-output pairs. After one extra batch, the DOE has a size of ($N_{init} + B^3$)-by-3.
- Fifth, we use the Sobol method to calculate the 3 first-order sensitivity indices and calculate the absolute change (Δ) in the indices with respect to the previous iteration. We continue

adding batches of B^3 points to the DOE until the sensitivity indices have converged ($\Delta<0.02$).

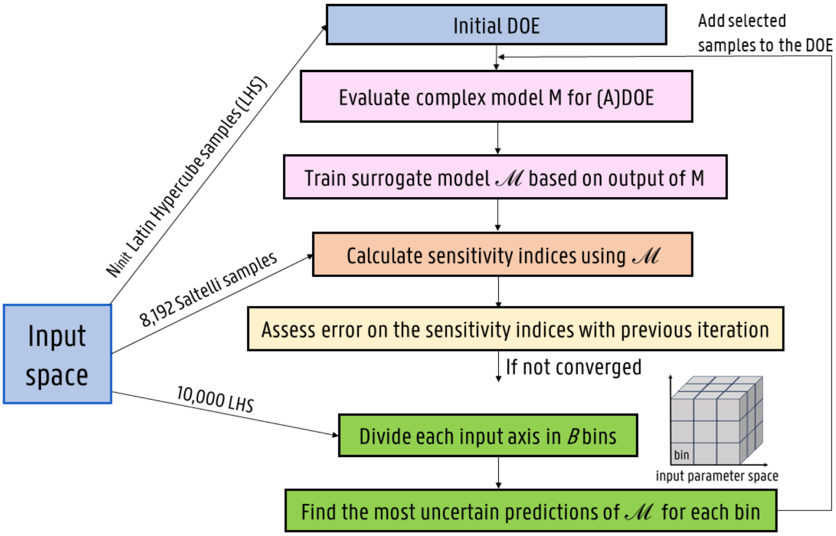

Figure 8.2: The initial design contains N_{init} points. Using N_{init} complex model evaluations, we fit a surrogate Gaussian process regression model, which we use to compute the sensitivity indices using the Sobol method. We strategically add points to the DOE in batches of B^3 points until the sensitivity indices have converged.

It should be noted that both the 8.192 Saltelli input space samples generated to calculate the sensitivity indices with $\mathcal{M}$, and the 10.000 LHS input space samples generated to calculate the most uncertain predictions, are hyperparameters of the ADOE that can be adapted easily by the user. Since these samples are only evaluated with $\mathcal{M}$, their computational cost is negligible.

8.2.4 Testing ADOE with Ishigami

To test the suitability of the ADOE, we use it on the Ishigami function (Eq. 8.4) [138], which contains three inputs (x_1,x_2,x_3, varying between -π and π; a and b are constants, typically taken as 7 and 0.1):

$$f(x) = sin(x_1) + a \cdot sin^2(x_2) + b \cdot {x_3}^4 \cdot sin(x_1) \tag{8.4}$$

The Ishigami function (SALib Python package) is a useful test case because the sensitivity indices are known a priori (S_{x1}=0.31, S_{x2}=0.44, S_{x3}=0.00, as in salib.readthedocs.io), and the cost of a single model evaluation is very low.

8.2.4.1 Sensitivity

For different sizes of N_{init} (50, 100, 150, 200), we compared the performance of the 2-bin and 3-bin ADOE (resulting in 8 bins and 27 bins in total, respectively) to a rigid DOE (RDOE) algorithm, where only the N_{init} total model evaluations were used to define the DOE. Note that the eventual number of model evaluations for the ADOE will be higher than N_{init} depending on how many batches are added to reach convergence; for the 2-bin ADOE, the batch size is 8 simulations, while for the 3-bin ADOE, the batch size is 27. To assess the suitability of the 2-bin ADOE, 3-bin ADOE and RDOE, we run 20 repeats of both ADOEs and RDOE, report the absolute error on S_{x1} and S_{x2} (since S_{x3}=0.00, absolute errors on the sensitivity indices are too low to be considered a relevant evaluation criterion). We evaluate the ADOE mainly to reach an absolute maximum error <0.1, but also for a performance largely independent of N_{init}. The latter is specifically useful for SAs of costly novel problems (such as ours), for which the number of model evaluations necessary to compute reliable sensitivity indices is a priori unknown.

8.2.4.2 Accuracy

We also tested the suitability of our ADOE-based GPR to accurately predict the output of the Ishigami function and the CFD model. This is non-trivial since the ADOE is an optimization algorithm for predicting sensitivity (not accuracy). We did this by using the ADOE-based GPR to predict the output of $\mathcal{M}$(Y) for 10 previously unseen test samples (randomly sampled in input space) and comparing with the true output of M(Y). We normalized the output vector, $\left|\hat{Y} - Y\right|$, by taking the mean and dividing by the mean of $|Y|$, and reporting the relative error e in % (Eq. 8.5).

$$e(\%) = \frac{\sum_{10} \left|\hat{Y} - Y\right|}{\sum_{10} |Y|} \tag{8.5}$$

8.2.5 Sensitivity analysis of the input waveform

Finally, we apply the ADOE to our waveform sensitivity problem. Therefore, we determined nominal values of three shape parameters, x_{1-3}, from the input waveform, which we extracted from a one-dimensional model of the arterial circulation [127], as explained in Chapter 4:

- x_1: peak systolic mass flow rate (kg/s): 0.01 kg/s

- x_2: heart rate (bpm): 75 beats/minute
- x_3: ratio between the time needed to reach the systolic peak and the full cycle period [%]: 27.375%

For each input shape parameter x, we sampled values, x_{sample}, within a lower limit of 75% of the nominal value and an upper limit of 125% of the nominal value, $x_{nominal}$(given above). This is done by generating normalized LHS samples between 0 and 1, LHS_{sample}, which define the spread between the lower and upper limit:

$$x_{sample} = (0.75 + 0.5 \cdot LHS_{sample}) \cdot x_{nominal} \tag{8.6}$$

As a result, x_1 varied between 0.075–0.125 kg/s, x_2 varied between 56.25–93.75 bpm (leading to periods between 0.64-1.07s), and x_3 varied between 20.53–34.22%. For the initial set of 100 simulations used in the ADOE, 100 parameter combinations resulted in the 100 different waveforms visualized in Figure 8.1B. We computed the tumor dose using M for each unique waveform. Then, after using the ADOE to fit our surrogate GPR, we compute the Sobol indices.

8.3 RESULTS

In Section 8.3.1, the suitability of the ADOE to compute reliable Sobol indices is illustrated with the example Ishigami function. Next, in Section 8.3.2, we use the ADOE to determine the Sobol indices of the three waveform shape parameters in our current patient-specific model.

8.3.1 ADOE performance using Ishigami

8.3.1.1 Sensitivity

For different sizes of N_{init} (50, 100, 150, 200), we quantified the error on the sensitivity indices of the Ishigami function for 20 repeats of the 2-bin and 3-bin ADOE. We compared this error range to the RDOE with N_{init} total model evaluations (50-200). The maximum errors are 0.178, 0.0537, 0.0511, 0.0186 for S_{x1} and 0.309, 0.136, 0.0637, 0.0251 for S_{x2} for 50, 100, 150, 200 evaluations, respectively (Figure 8.3A). For the 20 repeats of the 2-bin ADOE , the maximum errors are 0.173, 0.050, 0.316 and 0.0114 for S_{x1}, and 0.364, 0.0846, 0.442 and 0.0249 for S_{x2} (Figure 8.3B). The median number of 2-bin ADOE model evaluations necessary for each N_{init} was 82 ($N_{init} = 50$), 108

(N_{init} = 100), 158 (N_{init} = 150) and 208 (N_{init} = 200). The errors of the 3-bin ADOE were much lower, even for a small N_{init} (Figure 8.3C): the maximum errors were 0.0838, 0.0533, 0.0278 and 0.010 for S_{x1}, and 0.142, 0.0792, 0.0259 and 0.0222 for S_{x2}, respectively. The median number of model evaluations for the 3-bin ADOE were 185 (N_{init} = 50), 154 (N_{init} = 100), 177 (N_{init} = 150), and 227 (N_{init} = 200).

Notably, lower N_{init} does not necessarily correspond with lower number of final model evaluations. For the final number of model evaluations for the 3-bin ADOE, the initial DOE was either large enough or already too large (i.e. only one extra batch was added) for 0/20 cases with N_{init} = 50 and 100, 12/20 cases for N_{init} = 150, and 19/20 cases for N_{init} = 200. Hence, preferably, N_{init} is chosen small enough to avoid as much unnecessary model evaluations as possible. Because of its superior performance, we set the number of bins at 3 for the remainder of the study.

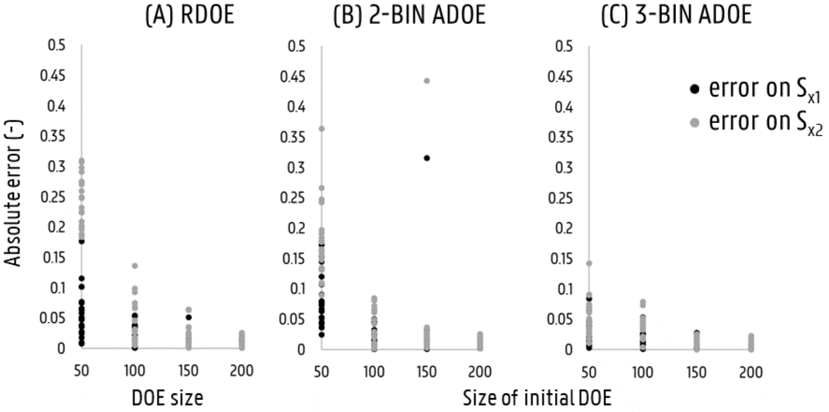

Figure 8.3: For both the RDOE and 2-bin ADOE, the absolute error on the sensitivity indices still depends on the size of the initial set. This dependency becomes much smaller for the 3-bin ADOE, with much smaller maximum errors already reported for an initial set of 50 model evaluations.

8.3.1.2 Accuracy

Since the ADOE optimizes the surrogate GPR for sensitivity analysis and not a true output prediction, it is paramount to distinguish between performance on sensitivity and accuracy. For the Ishigami function, we compared the predicted output ($\mathcal{M}$) with the true output of the Ishigami function (M) by constructing the relative error e (in %). For a specific GPR based on the 3-bin ADOE (initial size of 100, final size of 154), the maximum reported error on 10 unseen samples was 13% (meanwhile, all first-order sensitivity indices were predicted with an absolute error well below 0.1).

8.3.2 Sensitivity analysis of the input waveform

Applying the ADOE to our waveform sensitivity problem, we set N_{init} at 100 and the number of bins at 3. The final number of model evaluations necessary to reach convergence was 181. In these 181 simulations, the tumor dose varied between 49.2%-60.0%. Judging the evolution of S_{x1-x3} during ADOE: after N_{init} (100) simulations, S_{x1-x3} are 0.045, 0.041, 0.30, respectively; after 121 simulations, S_{x1-x3} are 0.076, 0.058 and 0.38; after 154 simulations, S_{x1-x3} are 0.058, 0.023, 0.41. Finally, S_{x1-x3} are 0.055, 0.019 and 0.41, respectively. Considering also interaction effects, ST_{x1-x3} are 0.41, 0.44 and 0.73, respectively. In Figure 8.4, the final S_{x1-x3} and ST_{x1-x3} are shown.

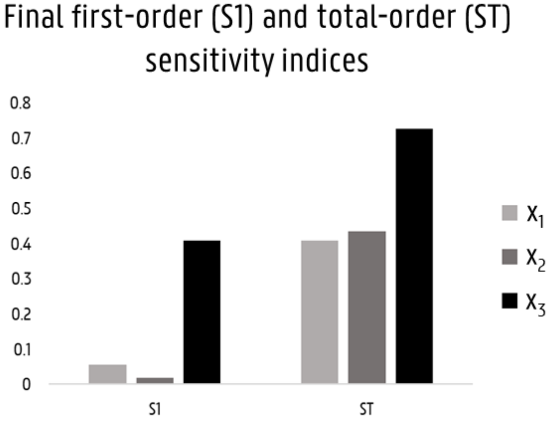

Figure 8.4: The final first-order and total-order indices show the high impact of x_3 (systolic duration).

For the waveform sensitivity problem, for a separate GPR fit with all 181 samples computed previously via the 3-bin ADOE, the maximum reported error on 10 unseen samples was 5.44%.

8.4 DISCUSSION

As above, we first evaluate ADOE performance for the Ishigami function in Section 8.4.1, and then apply the ADOE to our waveform sensitivity problem in Section 8.4.2. Finally, we discuss the limitations and future work of the current chapter in Section 8.4.3.

8.4.1 ADOE performance for Ishigami function

In Figure 8.3A, for the RDOE, we clearly see that both median and maximum error for S_{x1} and S_{x2} decrease with increasing DOE size (50 to 200). Acceptable maximum errors for both indices (<0.1) are reported only for 150 model evaluations onward. For the 2-bin ADOE, the median errors for S_{x1} and S_{x2} also clearly decrease with increasing N_{init}, but the maximum errors do not, showing no clear improvement over the RDOE.

However, as seen in Figure 8.3C, the 3-bin ADOE is clearly superior to both the RDOE and the 2-bin ADOE. First, the maximum errors are much lower for low N_{init} (0.142 for S_x2 compared to 0.364 and 0.309 for the 2-bin ADOE and RDOE, respectively). Second, the maximum errors are smaller than 0.1 for both S_x1 and S_x2 from $N_{init} = 100$ onward, which was not the case for the 2-bin ADOE and RDOE. Note that the high maximum errors for the 2-bin ADOE seem to indicate the importance of distributing new DOE points across input space, which is enforced by increasing the number of bins.

Of course, the important trade-off is that of computational cost: for example, the maximum error for N_{init} of 50 might be lower for the 3-bin ADOE, but the median number of simulations necessary to reach this low error is considerably higher than for the 2-bin ADOE and RDOE. Importantly, we cannot ignore the impact of the number of considered model evaluations. Looking at $N_{init} = 100$ for the 3-bin ADOE, we see that the maximum error for S_x2 is 0.0792, for a median number of 154 model evaluations. Instead of comparing to the RDOE with 100 final model evaluations, as we did before and in Figure 3 (where the maximum error is 0.136, and hence, significantly higher), it is more fair to compare to the RDOE with 150 final model evaluations. Here, the maximum error is 0.0637, which is slightly better than the ADOE. This makes clear that the ADOE is not specifically more accurate when compared to an RDOE with a similar number of final model evaluations. However, for RDOE, it is difficult to know its optimal size a priori.

Hence, the crucial advantage of the 3-bin ADOE is in its much lower dependency on N_{init}, with reliable performance even for the lowest N_{init}, which was definitely not the case for the 2-bin ADOE and RDOE. Hence, for novel problems, where the optimal size of the DOE is unknown, the 3-bin ADOE algorithm can be expected to produce reliable sensitivity indices, even if a random DOE size is chosen.

With regards to accuracy, the 3-bin ADOE for the Ishigami function resulted in a DOE size of 154 simulations, with still a relatively large error of 13% on the unseen output. First, this shows that the ADOE can predict sensitivity indices beneath our error limit (<0.1) while not performing optimally on accuracy. Hence, we advise to differentiate between goals of sensitivity and accuracy, and only to use the current ADOE for sensitivity analysis problems where model evaluations are costly.

8.4.2 Sensitivity analysis of the input waveform

From Figure 8.4, S_{x1} and S_{x2} are low (0.0550 and 0.0191, respectively), indicating a low impact of peak systolic flow rate and heart rate. However, S_{x3} is much higher (0.407), indicating that the systolic duration ratio is by far the most impactful parameter to quantify individually. Interestingly, the much higher impact of the duration ratio compared to the heart rate and peak height is already clearly noticeable from the first iteration of the ADOE, indicating that a rougher, more qualitative sensitivity analysis might already be possible at even lower computational cost. Notably, this is only possible because the difference between low- and high-impact parameters was so outspoken for this illustrative case; for other cases, where sensitivity indices are closer together, this might not be possible.

In addition, the total-order indices, ST_{x1-x3}, are significantly higher than the first-order indices, indicating high interaction effects. Especially due to the high first- and total-order sensitivity indices of the systolic duration parameter, the interaction effects between the peak flow rate and heart rate with the duration parameter are likely to be considerable. For the sake of completeness, it should also be noted that these indices are only valid for the considered 75%-125% parameter variation range; in higher or lower ranges, sensitivities might vary.

8.4.3 Limitations and future work

Limitations on the CFD modeling approach are explained in Section 11.1. We used the Ishigami function to verify our ADOE performance, which is especially relevant in our case because it is also a strongly non-linear function with three input variables, similar to our waveform sensitivity problem. Regarding the definition of our waveform sensitivity problem, we introduced shape variations in our waveform somewhat artificially by varying the three shape parameters within 75%-125% of their nominal values. In the future, we can use the 1D arterial circulation model [127] to generate more physiologically realistic waveform shape ranges by varying patient statistics such as age and weight, and perform statistical shape analysis to extract the most relevant shape parameters (which were assumed here).

Nonetheless, several important limitations regarding the ADOE arise. The maximum error threshold of 0.1 by which we compared RDOE and ADOE, can be chosen by the user, depending on the accuracies that need to obtained (here, we prioritized fast, rough SA). Since the convergence criterion for the ADOE ($\Delta<0.02$) was absolute, it is likely that the estimation of the sensitivity indices is slightly more reliable for the larger sensitivity indices. Currently, only the stability of the first-order indices is considered as a convergence criterion; this could be easily expanded to include also the total-order indices. Clearly, the ADOE can be further improved upon; for example, for the 3-bin ADOE, computational cost could be reduced by not including all 27 bins in the DOE update, but prioritizing the most uncertain bins. Regarding the surrogate modeling approach, a Gaussian Process Regression model was opted, but other surrogate model types might be suitable as well. An ensemble approach could be tried, where multiple surrogate model types are fitted on subsets of the DOE using bootstrapping. Additionally, we choose here to use Sobol's variance-based method to compute the sensitivity indices, while in future work, we can also explore computationally less expensive methods, such as Morris sensitivity measures, for our analysis [140].

Although we focused here on three key waveform shape parameters, many other clinical and numerical model parameters can influence the CFD prediction of tumor dose. Likely, both outflow boundary conditions (Taebi et al. [134] previously studied this), the hepatic arterial network (by parametrizing the geometry such as in [141]), and tumor size and location are critical parameters, next to the inflow waveform parameters studied here. As more of these parameters are studied in global SAs, the number of input space dimensions grows significantly. This will make the ADOE more useful, since DOE size becomes both more difficult to predict and more critical to optimize (with regards to computational efficiency) for these large-dimensional problems. While applicable to a broad range of problems, global SA supported by ADOE is specifically useful for CFD modeling of radioembolization, where large-dimensional sensitivity analysis is a necessary for model validation, and differentiating between high- and low-impact injection parameters will be crucial for peri-operative treatment optimization.

8.5 Conclusion

In Chapters 4, 5 and 6, we have tested the feasibility of physics-based reduction measures (domain truncation, mesh coarsening, reducing the number of flow cycles) to reduce computational time for expensive sensitivity analysis. Sensitivity analysis and parameter ranking is a crucial aspect of model diagnosis.

In this chapter, we illustrated how to use surrogate modeling to perform fast sensitivity analysis of complex models with (1) a limited number of complex model evaluations, and (2) a priori unknown optimal size of the design of experiments. We used an illustrative case where we quantified the sensitivity of the tumor dose towards three characteristic shape parameters of our input waveform: peak systolic mass flow rate, heart rate, systolic to total cycle duration ratio. Using a Gaussian process regression model fit on 181 CFD model evaluations, we found that the systolic duration ratio was by far the most influential parameter. We tested this workflow on the Ishigami test function, allowing us to predict Sobol's sensitivity indices with a maximum error below 0.1. (For the interested reader, more investigation into the impact of systolic duration is done in Appendix A).

In future work, these methods can be translated to other SA problems, quantifying the sensitivity of the tumor dose towards clinical and more numerical parameters. While there are likely to still be small errors on the sensitivity indices, they are reliable enough to fulfill their goal of model diagnosis (i.e. identifying the most impactful numerical input parameters) and clinical optimization (i.e. identifying the most impactful clinical parameters). The current study was an illustrative case where we only varied waveform shape, while many other parameters (e.g. injection location) that likely strongly interact with the waveform shape parameters were still kept constant. Including even more varying parameters is an added level of complexity we did not consider here, although the ADOE paves the way for this.

IV

Validation

Chapters

CHAPTER 9

Patient-Specific Validation

POSITIONING OF THE CHAPTER

As Part III focused on uncertainty quantification and sensitivity analysis, this part will focus on the third crucial aspect of the VVUQ principles, validation. Specifically, we will illustrate how current in vitro validation techniques can be replicated in complex 3D patient-specific hepatic arterial geometries.

This chapter is based on the publication *Transarterial Drug Delivery for Liver Cancer: Numerical Simulations and Experimental Validation of Particle Distribution in Patient-Specific Livers* (T. Bomberna et al, Expert Opinion on Drug Delivery, 2020) [18].

9.1 INTRODUCTION

In the context of investigating transarterial therapies such as TARE and TACE, experimental in vitro studies can be carried out to (1) perform parameter analyses experimentally, or (2) validate CFD findings. An overview of experimental parameter analyses (1) was given in Section 2.4.1. Conversely, experimental work to (2) validate CFD findings has been very limited. As explained in Section 2.4.1, Richards et al. [84] showed the high impact of cross-sectional injection position with their experimental set-up, and compared these results with CFD findings. Although there were significant discrepancies between both CFD and in vitro results, a large number of injection zones still agreed between the two. In a different study, Aramburu et al. compared outcomes of their 0D-model with an experimental set-up of a balloon-occluding microcatheter [83]. Additionally, these experimental analyses have been carried out in planar, simplified hepatic arterial geometries. Therefore, we aimed to perform the first experimental study of transarterial drug delivery in a patient-specific hepatic arterial geometry, based on patient-specific imaging, to compare the numerical and experimental particle distribution.

9.2 METHODS

The goal of this study is to compare CFD with experimental results. First, it is explained in Section 9.2.1 how we obtained micro-CT images of a cirrhotic liver discarded for transplantation. Next, more details of the CFD approach are given in Section 9.2.2, while the experimental set-up is explained in 9.2.3.

9.2.1 Data generation

A patient-specific hepatic arterial geometry of a cirrhotic liver was used. As originally approved by the Ethical Committee of the University Hospitals Leuven (Belgium) and by the Belgian Liver and Intestine Committee, these datasets were previously generated by Debbaut et al. [142] and Peeters et al. [143] using a two-step process. First, a vascular corrosion cast of the livers was made resulting in a polymer vascular replica. Secondly, micro-CT scanning resulted in detailed images of the liver casts with a resolution of 110-128 µm. More detailed information on these methodologies can be found in [142, 143]. The hepatic arteries of the cirrhotic liver geometry were segmented in Mimics software (Materialise, Leuven, Belgium). Only arteries up to the 4th generation were considered for computational purposes. The 3D reconstructions of the arterial trees were further processed (i.e. smoothing, truncating the outlets etc.) in Mimics and 3-matic (Materialise, Leuven, Belgium) resulting in the 3D simulation geometries of Fig. 9.1.

9.2.2 Computational fluid dynamics

9.2.2.1 Pre-processing

For the cirrhotic liver geometry, a good quality surface mesh was generated in 3-matic. ICEM CFD (Ansys Inc., Canonsburg, USA) was used to generate volume meshes using the Octree method. The bulk of the volume elements were unstructured tetrahedral elements,

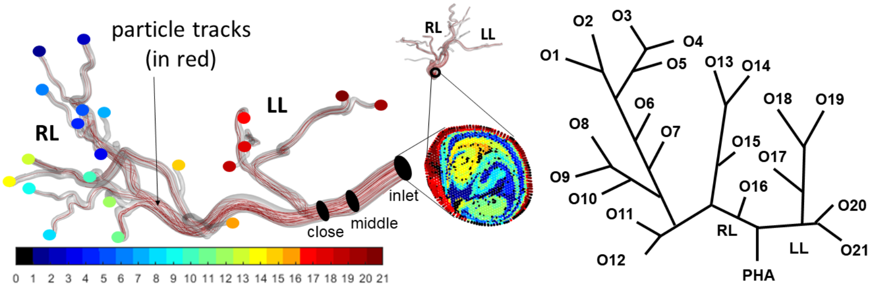

Figure 9.1: Illustrations of the simulation geometries. 3D models of the arterial network of the cirrhotic liver. The particle release map (PRM) of the baseline model is also shown with respect to the model orientation. The colored sections of the PRM show through which branches the particles exit if they are injected in that specific section (see color bar). Particles that do not exit the domain are denoted in black. Schematic 2D representation of the branching topology of the cirrhotic liver with 21 outlets is shown.

complemented by three prism layers at the boundaries to ensure a smooth transition between the walls and the fluid domain. Mesh densities were increased at the bifurcations to locally capture more complex flow patterns. Mesh sensitivity analyses were performed to determine the most optimal mesh density for the CFD simulations, leading to meshes of $9.1 \cdot 10^6$ volume elements. Minimum and maximum volume of the elements were $2.7 \cdot 10^{-16}$ m^3 and $4.9 \cdot 10^{-12}$ m^3.

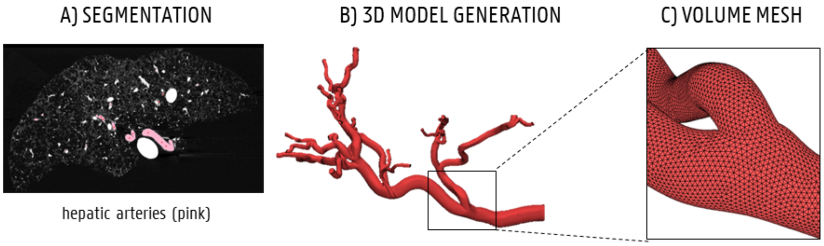

Figure 9.2: (A) Indication of the hepatic arteries (in pink) on the CT scan. (B) Reconstructed arterial geometry (C) Indication of the surface mesh at the first bifurcation.

9.2.2.2 Simulation details

The Discrete Phase Model (DPM) in ANSYS Fluent (Ansys Inc., Canonsburg, USA) was used to model the mass transport of the discrete phase (microparticles) dispersed in the continuous phase (blood flow) following a Euler-Lagrangian approach. The DPM was chosen because the particle-fluid mixture can be considered as a dilute suspension. Here, we used water in the experimental set-up instead of blood. Water flow was modeled as laminar flow using the Navier-Stokes equations. Mathematical details were previously explained in Chapter 4.

Particles were modeled as SIR-Spheres (Sirtex Medical, Australia), which are typical treatment particles for TARE. A representative particle diameter (40 µm) and density (1600 kg/m^3) was chosen. The trajectories of the discrete particles are calculated by integrating the force balance of the particles (see Chapter 4). Here, the gravitational force, drag force and pressure gradient force were enabled. One-way coupling between the discrete and fluid phase was enabled. Particle collisions at the walls were modeled as elastic with zero slip at the walls. Particles were injected over the entire inlet plane with a uniform velocity profile approximately equal (<0.5% difference) to the inlet blood flow velocity.

The outlet BCs were set according to the arterial perfusion model developed by Aramburu et al. [128]. Knowing the tumor and healthy volume in each segment, the arterial perfusion of each segment can be calculated as the sum of arterial perfusion contributions for the healthy and cancerous tissue, as previously explained in Chapter 4. Here, we specifically set the tumor size to 0 ml (we used a cirrhotic liver, not a cancerous one) and only considered the healthy flow contributions. By identifying which branches perfuse which segment and assuming that flow splits occur symmetrically along bifurcations perfusing the same segment, the arterial perfusion of each branch in the domain can be computed and imposed as an outlet flow fraction. The branching characteristics of the cirrhotic liver are given in Fig. 9.1b, and the flow split resulting from this is given in Table 9.1.

The inlet boundary condition (BC) was set to a constant flat velocity profile. From the total sum of outflows, we determined the inflow (principle of mass conservation), which we translated into a velocity (we considered a circular cross-section and an inlet plane diameter of 0.00737 m). This method resulted in a steady inlet velocity of 0.0977 m/s.

Regarding solver settings, the SIMPLE scheme was chosen for pressure-velocity coupling. The spatial discretization schemes used were Least Squares Cell Based for gradient, Standard for pressure and Second Order Upwind for momentum. An automated particle tracking scheme was chosen which switches automatically between

Table 9.1: Overview of the outlets and flow fractions.

Outlet	Flow fraction (%)
1	0.86
2	0.86
3	0.43
4	0.43
5	0.86
6	3.46
7	6.91
8	6.46
9	6.63
10	6.63
11	8.54
12	8.03
13	13.26
14	8.54
15	4.07
16	6.40
17	4.02
18	2.41
19	2.41
20	4.83
21	4.02

the high order trapezoidal scheme and the low order implicit scheme. For all simulations, absolute globally scaled residuals of at least $2 \cdot 10^{-6}$ were reached.

9.2.2.3 Post-processing

Specific measures were analyzed to quantify the particle distribution. The particle exit fraction (PEF) denotes the percentage of particles that exit the domain through a specific outlet or larger vascular zone (e.g. outlets draining the right or left lobe). The particle non-exit fraction (PNEF) is the fraction of particles that do not exit the domain.

9.2.3 In vitro experiments

An in vitro set-up was built to validate the CFD modeling approach by means of an experimental flow circuit using a 3D print. One scenario for the cirrhotic liver was tested in the in vitro set-up in order to study its feasibility and potential for future, more elaborate validation studies.

9.2.3.1 3D print

The 3D simulation geometry of the cirrhotic arterial tree was imported into Magics (Materialise, Leuven, Belgium) to prepare it for 3D printing. First, an offset thickness of 1.5 mm was added to the outer walls of the domain (only containing the lumen of the arteries) and the geometry was hollowed out. Second, extensions (10-15 mm) were added to the outlets; their outer diameters were adjusted to facilitate attachment to the downstream tubing. Stereolithography was chosen to manufacture the 3D print using TuskXC2700T material (Materialise, Leuven, Belgium), which is a transparent material that is recommended for use in flow analysis experiments.

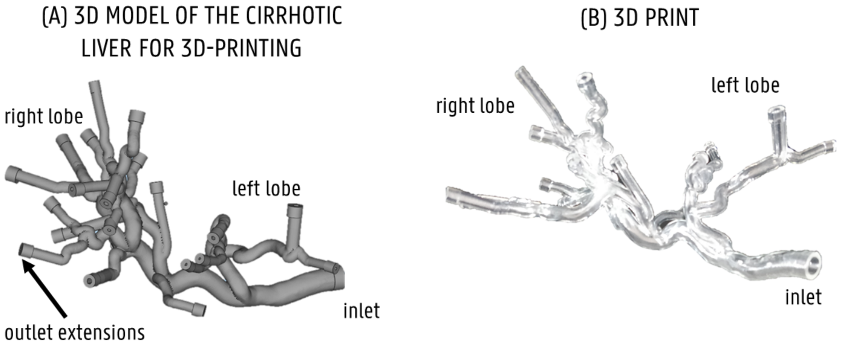

Figure 9.3: (A) 3D model of the cirrhotic liver arteries that was optimized for 3D printing, adding outlet extensions which fit the PVC tubing. (B) 3D print of the cirrhotic liver arteries. The resemblance with the 3D model is a bit more difficult to see due to light reflections on the physical print.

9.2.3.2 Experimental set-up

The resulting 3D print (Fig. 9.3B) was subsequently mounted in the experimental setup (Fig. 9.4). The water in the main reservoir (1) was transferred with a DC circular pump (VERDER, The Netherlands) (2) to an elevated reservoir (3). The elevated reservoir was set at a fixed height to mimic the inlet pressure at the PHA (approx. 100 mmHg). When the clamp (4) was released, water flowed down from the reservoir through the 3D-printed geometry (5). The orientation of the 3D print was set with the outlets oriented downwards, so that gravity would facilitate fluid flow. Polyvinyl chloride (PVC) connecting tubes (6) with tunable resistances (7) were attached to the outlets leading into 10 collecting reservoirs (8). Before releasing particles into the set-up, the boundary conditions were set manually by iteratively adapting the resistances at the PVC tubes until all outflows matched the computational boundary conditions (< 5% error margin, see Table 9.1).

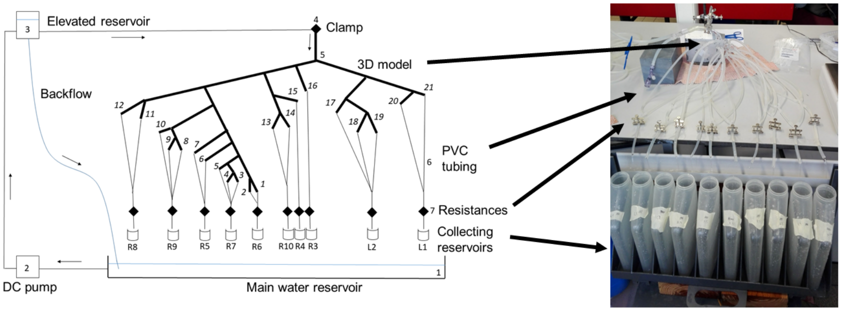

Figure 9.4: Experimental in vitro set-up and results. (A) schematic representation of the set-up. 1: main reservoir. 2: DC pump. 3: Elevated water reservoir. 4: Clamp. 5: 3D printed liver geometry (cirrhotic). 6: PVC connecting tubes. 7: Collecting reservoirs. (B) Overview of the set-up, showing the 3D model, the PVC tubing attached to the outlets, the resistances used to tune the flow distribution and the collection reservoirs. (C) Experimental set-up in the lab, showing the 3D model of the liver vasculature, the elevated reservoir and the collecting reservoirs at the outlets.

9.2.3.3 Experiments

Non-radioactive SIR-Spheres (typically used for training purposes, Sirtex Medical, Australia) were mixed with water in the main reservoir for the first experiment. During the second experiment, particles were manually injected with a syringe via side-branch of the inlet branch leading to the PHA and then flushed with water. The 21 outlets were combined in 10 collecting reservoirs (see Fig. 9.4) and the resulting particle-water mixture was collected in these reservoirs for a total duration of 1 minute starting from the moment of injection. Whatman paper of grade 2 and 3 (pore size 8 and 6 µm, respectively) was used to filter the particles from the collected particle-water mixtures. After drying, the filters were weighed to determine the added weight of the particles, and hence, the particle distribution among the collecting reservoirs. The PNEF could not be considered in these experiments (the sum of all PEFs at the outlets was assumed to be 100% of the particles).

9.3 RESULTS

In Fig. 9.5, the flow distribution and particle fraction for each reservoir (reservoir exit fraction, or REF) was compared for the 2 experiments and the corresponding numerical simulation. The high similarity between experimental and theoretical flow distribution (0.407% difference per reservoir on average) shows that the implementation of the outlet BCs through tuning of the resistances was successful. However, after particle injection, the average difference per reservoir between experimental particle and flow (PD, FD) distribution was 2.45% (min: 0.0784% – max: 5.44%) and 2.14% (min: 0.902% – max: 4.03%) for experiment 1 and 2, respectively. Moreover, the average difference for a reservoir between numerical and experimental particle distribution was 2.73% (min: 0.394% – max: 6.47%) and 2.97% (min: 1.21% – max: 6.17%) for experiment 1 and 2, respectively.

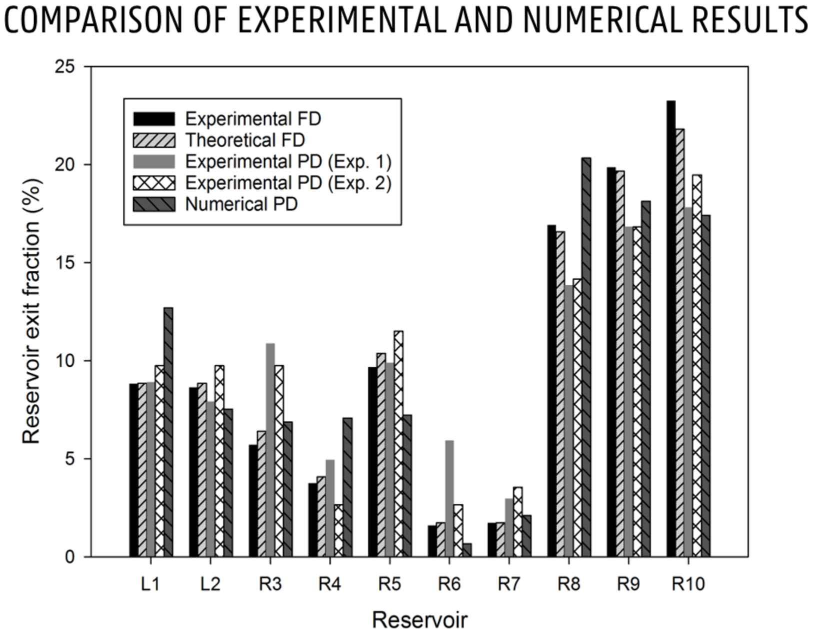

Figure 9.5: Experimental in vitro results. Results of the validation study. The experimental and theoretical flow distribution (FD) are compared with the particle distributions (PD) for Experiment 1 and 2, and the numerical simulation.

9.4 Discussion

Since Simoncini et al. [121] and Roncali et al. [123] reasoned that particle distribution is linearly proportional with the flow distribution, the similarity between flow-particle distribution is useful to consider. In the validation study and numerical results, it was shown that flow distribution is not a perfect surrogate for particle distribution, at least not for the complex patient-specific livers studied (Figure 9.5). Note that flow distribution also does not consider the non-exiting particles, which may be relevant because these can contribute to offsite toxicity. Hence, we conclude from this experimental study that particle distribution should preferably be studied instead of only flow distribution. It should also be noted that particles were added to the set-up either via a syringe or via mixing in the main water reservoir, but not through a microcatheter, which might even increase the discrepancy between particle and flow distribution (as discussed in Chapter 4). In general, the conclusion to study particle transport and distribution agrees with the findings from Chapter 4.

Regarding the feasibility of patient-specific validation, we showed that generating patient-specific geometries for in vitro validation using 3D-printing is feasible. This is a completely novel step and significantly adds to the state-of-the-art. In the future, we can obtain hepatic arterial geometries from medical images instead of via vascular corrosion casting. Aside from the fact that these geometries better represent the patient population, geometries generated from vascular corrosion casting can be slightly expanded compared to in vivo conditions, but that shrinkage of the resin can also occur [144]. An important step for improvement is also to integrate pulsatile flow, which is more realistic that the steady flow circuit used here.

Regarding the success of patient-specific validation, we showed that there are still significant differences between the computational and in vitro particle distribution (Figure 9.5), emphasizing the need for further validation and finetuning of methods. Several steps can be taken to improve the current in vitro set-up. First, we used training vials of microspheres from Sirtex Medical (Sirtex, USA). Although these microspheres have the advantage of being non-radioactive, they also do not go through the same quality control as the microspheres used for treatment of patients. Hence, we should verify particle dimensions to ensure that we are using the proper particle dimensions in our CFD model. Second, the current method of measuring the particle distribution (i.e. through measuring the added weight on the filter paper) is very sensitive to noise (e.g. dust can easily gather in the set-up, and influence the weight of the filter paper). Multiple injections should be done to get an idea of the variations in the results under constant injection conditions. Third, the method of injection should be more accurately reproduced between simulation and experiment. Now, a planar injection was used in the simulation, while in the experiments, particles were mixed in the main reservoir (experiment 1) or injected through a syringe (experiment 2). In the future, we should prioritize experimentally modeling realistic microcatheter injection conditions. Illustratively, with the computational study in Chapter 4, we showed that important differences can arise between flow and particle distribution for catheter-based injections. This underlines the importance of performing experiments under realistic injection conditions.

9.5 CONCLUSION

In conclusion, the scope of the experimental study was currently limited to a proof-of-concept for patient-specific in vitro validation (which we regard successful). The experimental quantification of microsphere distribution in a 3D-print of a patient-specific hepatic arterial geometry was completely novel. In the future, such a set-up could be improved upon and used to investigate the sensitivity of the experimental particle distributions towards varying injection conditions (e.g. catheter tip position, injection flow rate, varying inflow waveforms, etc.). For example, in Chapter 7, we quantified the computational tumor dose range resulting from an uncertain, uncontrollable catheter tip position. This tumor dose range could be validated experimentally by quantifying the microparticle distribution after multiple injections at multiple cross-sectional tip locations. For the interested reader, an example of a simplified experimental study investigating the impact of cross-sectional tip position is illustrated in Appendix B.

V

Valorization

Chapters

All models are wrong
but some are useful

G. Box

Chapter 10

Development of a Pre-Treatment Planning Framework using 3D Personalized CFD

POSITIONING OF THE CHAPTER

As Part III focused on uncertainty quantification, and Part IV focused on validation, which are two crucial aspects of good simulation practice, this dissertation also aims to give a view of how these CFD models could be used in clinical practice. We showed in Part III that CFD can give an idea of the tumor dose range. However, other patient-specific aspects, such as vascular accessibility, must be considered as well in a patient-specific pretreatment workflow.

Previously, we stressed the computational complexity of these CFD simulations. In Chapters 4, 5 and 6 and proposed multiple CFD simplification strategies. However, if the proposed pre-operative framework only works for hundreds or thousands of CFD simulations, it is likely that high computational times will still limit clinical integration (even with the current simplification strategies). Therefore, it is paramount to define how the use of CFD fits strategically within a broader pre-operative optimization framework. Hence, Part V exceeds the domain of CFD, and reframes these aspects within a possibly valorizable, pre-operative optimization framework.

This chapter is based on a patent application (filing number EP 23177284.9) prepared together with UGent TechTransfer Office.

10.1 Introduction

Efficient resource allocation in cancer care should prioritize improving treatment outcomes and reducing intervention-related variations impacting post-operative outcome [145]. Relevantly, transarterial therapies such as TARE lack standardization, and a large discrepancy in treatment response currently exists between patients, raising the question of whether execution-related variations can be reduced [146]. For example, computational fluid dynamics (CFD) studies have shown catheter in-plane tip location to be an impactful interventional parameter, but its inability to be controlled in vivo is a source of uncertainty [9, 113, 116], as we also showed in Chapter 7. Additionally, the axial catheter injection site has been shown to be very impactful as well, and is easier to control [15, 112]. At the end of Chapter 7, we noted that both the expected tumor dose and tumor dose ranges can be compared for both proximal and distal injection locations to determine which injection location would be more likely to be clinically successful.

However, tumor dose is not the only parameter to consider. For example, while the expected tumor dose might be higher when injecting in the tumor-feeding arteries, selective or super-selective injection of microparticles in the tumor-feeding arteries is often restricted by limited vascular access of these arteries [147]. Hence, a likely trade-off exists between vascular accessibility and tumor dose, which has not been quantified or considered before.

Hence, the goal of this work is to introduce a computational pre-treatment planning framework to optimize the axial injection location, considering the trade-off between target specificity and vascular accessibility, and the uncertainty introduced by the catheter in-plane tip location. Currently, no such framework exists according to the authors' best knowledge. (In Chapter 3, other frameworks such as CFDose [123] were explained, although these lack consideration of this important trade-off.)

10.2 Materials and Methods

First, we describe how we obtained patient data for the patient-specific case study in this chapter in Section 10.2.1. Second, we explain the study design and the different injection locations considered in this study for comparison in Section 10.2.2. Finally, in Sections 10.2.3-10.2.5, the calculation of tumor coverage, vascular cost and tumor dose range is explained in detail.

10.2.1 Segmentation and tumor perfusion

A patient-specific conebeam CT-dataset of the hepatic arteries of a patient diagnosed with HCC was previously segmented and converted into a 3D-model by us, as described in Chapter 4. The resulting hepatic arterial model contained 1 inlet at the level of the PHA and 48 outlets. A region growing algorithm was used with each of the outlets as seed points to assign all voxels of the tumorous tissue to its perfusing artery. Voxels were added in the six orthogonal directions iteratively to the centerline of the arteries generated in Mimics (Materialise, Belgium). As a result, the volume percentage of tumor tissue perfused by each computational outlet (tumor perfusion percentage, TPP) was known. Based on the TPPs and visual inspection of the 3D-reconstruction (Figure 10.1A.), it was determined that 2 outlets fed only the tumor tissue (internal feeders), 17 outlets fed only the healthy tissue, while the remaining 29 outlets fed both the tumor and healthy tissue (peripheral tumor feeders) (see Fig. 1A for indicative examples of the healthy and peripheral feeders, and indication of the two internal feeders).

10.2.2 Study design

We identified four relevant injection locations: superficially (in the PHA), selectively in the RHA and LHA, and super-selectively in the RHA, which perfuses most of the tumor tissue (see Section 10.3.1). These injection locations are indicated in Figure 10.1B.

For each injection location, four parameters were considered as crucial for clinical decision-making: vascular accessibility (expressed as a vascular cost, C, which is preferably low), expected tumor dose (eTD, preferably high), in-plane tip uncertainty (ΔTD, preferably low), and tumor coverage (γ, preferably high).

10.2.3 Tumor coverage

The tumor coverage was determined as the maximally attainable tumor dose, if all injected microparticles flow from the injection site to the tumor (no off-site delivery). As determined with the region growing algorithm, each tumor-feeding artery was associated with a certain volume percentage of tumor tissue (TPP (%)). Hence, all outlets downstream of the considered injection location (denoted by

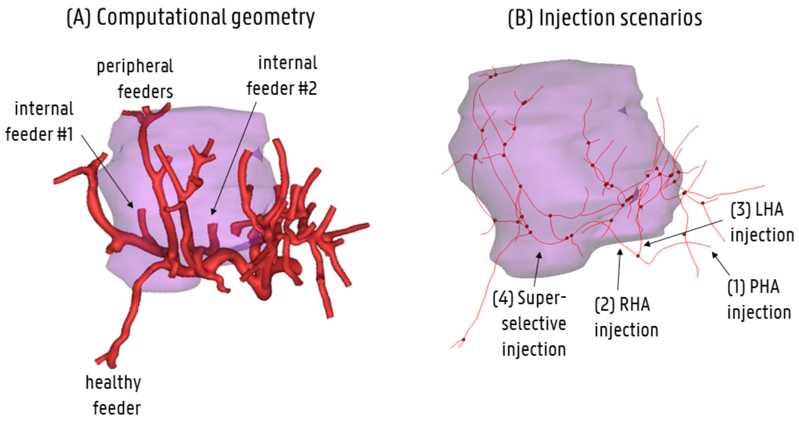

Figure 10.1: (A) Computational geometry of the hepatic arterial network (red). Tumor mass added in purple. (B) (1-4) Four clinically realistic injection scenarios at different axial injection locations.

index i in Equation 10.1) contributed to a total perfused volume between 0-100%, which is deemed as the 'tumor coverage':

$$\gamma = \sum_i TPP_i \tag{10.1}$$

10.2.4 Vascular accessibility

For each injection scenario, the relative vascular cost of the arterial path leading up to a particular injection location was calculated using information on size of the vessel (diameter), the curvature and tortuosity of the paths.

10.2.4.1 Cost parameters

The centerline of the hepatic arteries was generated using Mimics. The diameters along this path were extracted at each point and collected in D. The x-, y- and z- centerline coordinates of each point up until the injection location were collected in R. Next, tortuosity of the centerline (τ (-)) was calculated as the deviation of the centerline from a straight line (Equation 10.2):

$$\tau = \frac{L_{centerline}}{L_{rectilinear}} - 1 \tag{10.2}$$

Here, $L_{centerline}$ was the sum of the Euclidian distances between each successive point of R until the point of interest (i.e. the injection location under study), and $L_{rectilinear}$ was the Euclidian distance between the start of R and the point of interest. Hence, for a straight line, τ=0.

Additionally, the curvature ($\kappa[mm^{-1}]$) of the centerline was calculated for each point of R by computing the first and second derivatives of the centerline position (approximated here using central finite differences around the point of interest) (Equation 10.3):

$$\kappa = \frac{\left|\dot{R} \times \ddot{R}\right|}{\left|\dot{R}\right|^3} \tag{10.3}$$

These mathematical definitions of tortuosity and curvature are as expressed in [148].

10.2.4.2 Cost function

To calculate the (relative) vascular cost, C, the normalized costs of diameter, tortuosity and curvature were added together. To compute the normalized cost for tortuosity, the maximum tortuosity of the arterial path was compared to the maximum tortuosity of all paths (i.e. for all considered injection locations). For example, if the path leading to the injection location of Scenario x had a maximum tortuosity of 0.5, and the maximum tortuosity of the paths in all other scenarios was 1, the relative cost (with respect to tortuosity) for Scenario x would be 0.5. The same normalization could be done for other vascular parameters. By adding together the normalized costs of each parameter and dividing by the total number of considered parameters (3), we achieved a resulting cost for each scenario as a number between 0-1 indicating the relative vascular cost of each scenario compared to the other scenarios (Equation 10.4). For example, if we considered diameter, curvature and tortuosity as the relevant parameters (with equal weights of importance), the cost function C could be expressed as:

$$C = \frac{\frac{min(D)_{allpaths}}{min(D)_{path}} + \frac{max(\kappa)_{path}}{max(\kappa)_{allpaths}} + \frac{max(\tau)_{path}}{max(\tau)_{allpaths}}}{3} \tag{10.4}$$

Hence, a vascular cost of 1 was only reached if it is the least optimal for all parameters.

10.2.5 Computational model

The parameters of expected tumor dose and in-plane tip uncertainty were determined using computational fluid dynamics (CFD). A CFD simulation was run for each injection scenario, with all settings and parameters kept constant except the injection location and total simulation length (see below).

10.2.5.1 CFD details

After reconstruction in SpaceClaim (Ansys, USA), the hepatic arterial geometry was meshed in Fluent Meshing (Ansys, USA). Using tetrahedral elements for the bulk of the domain and three prism boundary near the walls, the optimal total number of elements was determined through a mesh sensitivity study as $6.68 \cdot 10^6$. Next, the mesh was imported into Fluent (Ansys, USA). A multiphase CFD approach was used to solve the conservation of mass and momentum equations for fluid flow, and the particle force balance to compute the microparticle trajectories from inlet to outlets. In the particle force balance, the virtual mass force and pressure gradient force were enabled additionally to the drag and gravitational forces. Mathematical details can be found in Chapter 4. One-way coupling between the two phases was enabled, meaning the fluid phase exerted impact on the discrete phase, but not vice versa.

With regards to boundary conditions, a time-dependent mass flow rate waveform was applied at the inlet (see Chapter 4). According to the methodology defined in Chapter 4, the outflow through each artery can be determined as a summation of the healthy flow and cancerous flow contributions. The healthy flow contribution was calculated by scaling literature-based segmental flows to the patient-specific liver mass, and by dividing the healthy flow to each segment equally across intrasegmental bifurcations. The tumor flow contribution was determined based on the TPPs. The total feeder flow of the peripheral feeders was the summation of the healthy and tumoral flows terms, explained as above and derived mathematically in Chapter 4. When outlets perfused only one type of tissue (i.e. healthy or tumor), the other contribution was set at zero. These flow terms were transformed into flow fractions and applied as outflow boundary conditions in Fluent. Furthermore, a no-slip condition and normal and tangential restitution coefficients of 1 were applied at the wall.

Simulations were run for each injection for 13 flow cycles, 14 cycles, 11 cycles and 10 cycles, for PHA, LHA, RHA and super-selective injection, respectively, until <1.5% of the microparticles exiting the domain in the final cycle in each case. Microparticles were injected over the entire cross-section (see Figure 10.1) with a particle time step of 10 ms throughout the 3rd cardiac cycle; the fluid time step alternated between 0.5 and 1 ms. Convergence was attained in each time step; globally scaled residuals dropped at least below $1 \cdot 10^{-5}$. More details on the computational approach can be found in Chapter 4.

10.2.5.2 Tumor dose calculations

In theory, the tumor dose (TD (%)) for one in-plane catheter tip location could simply be calculated by modeling microsphere release from a catheter embedded in the hepatic arterial geometry, and then dividing the fraction of microspheres reaching the tumor (n_{tumor}) by the total number of ejected microspheres (n_{total}) (full model, M_f) (Equation 10.5):

$$TD(\%) = \frac{n_{tumor}}{n_{total}} \cdot 100 \tag{10.5}$$

However, to assess the impact of N in-plane catheter tip locations (and hence, the uncertainty associated with catheter tip position), M_f is too computationally heavy to run N times. Therefore, in Chapter 7, a simplified low-fidelity framework was proposed, M_s, where the catheter is not embedded in the geometry, but microparticles are released over the entire arterial cross-section, and clusters of particle injection are sampled afterwards in the cross-section (each cluster representing a ‘catheter tip location’) to generate a range of tumor doses, rather than a single, deterministic value. This framework reduced the number of CFD simulations from N to 1, resulting in tumor dose range of N_c samples (where N_c can be freely chosen after the simulation), but disregarding the physical presence of the catheter. Specifically, the cluster of particle injection locations was determined by considering all injected particles within a radius of 0.3 mm of a certain central location (i.e. mimicking a catheter with an internal diameter of 0.6mm). N_c was set at 100; these central locations were randomly sampled within the cross-section. This concept is illustrated in Figure 10.2. The larger the tumor dose range for the evaluated samples, the larger the catheter tip uncertainty. The mean of the tumor dose range is referred to as the ‘expected tumor dose’. The lower the (expected) tumor dose, the more embolic material flows to the healthy tissue.

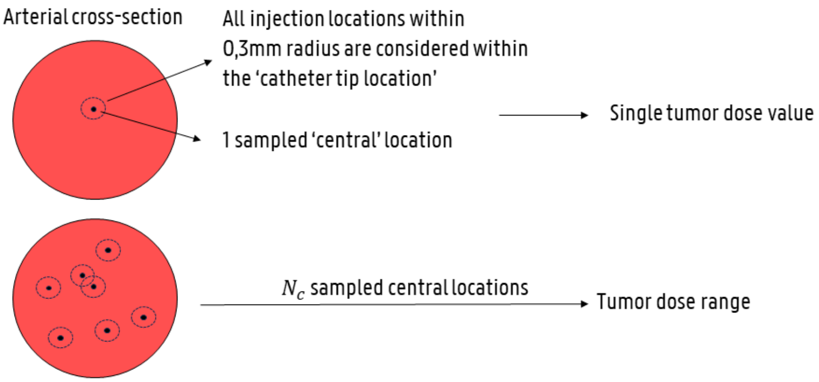

Figure 10.2: Low-fidelity model from Chapter 7 to compute tumor dose ranges: 100 central injection locations are sampled in the cross-section, and the tumor dose is calculated for all points within <0.3 mm of the central location, representing a catheter with an internal diameter of 0.6mm.

10.3 RESULTS

In Sections 10.3.1-10.3.3, the results regarding tumor coverage, vascular cost and tumor dose range are discussed, respectively, for each of the injection scenarios.

10.3.1 Tumor coverage

The first parameter to compare between the four injection scenarios was the tumor coverage. As seen in Figure 10.3, injection done superficially in the PHA resulted in a tumor coverage of 100% (purple mass in Figure 10.3A); advancing the catheter to RHA decreased the total tumor coverage to 69.6% (green mass in Figure 10.3B); further advancing the catheter to inject super-selectively in the RHA decreased the tumor coverage even further to 52% (blue mass in Figure 10.3C). Alternatively, injection in the LHA lead to a tumor coverage of 30.4% (orange mass in Figure 10.3D).

10.3.2 Vascular accessibility

The second parameter to compare was vascular accessibility. In Figure 10.4A, the centerline of the hepatic arterial geometry is shown. For the four injection locations considered in this study, the two most distal injection locations were reached for super-selective injection in the RHA and selective injection in the LHA. In Figure 10.4B-D, we zoom in on the region of interest of the centerline, and color this region according to diameter, curvature and tortuosity, respectively.

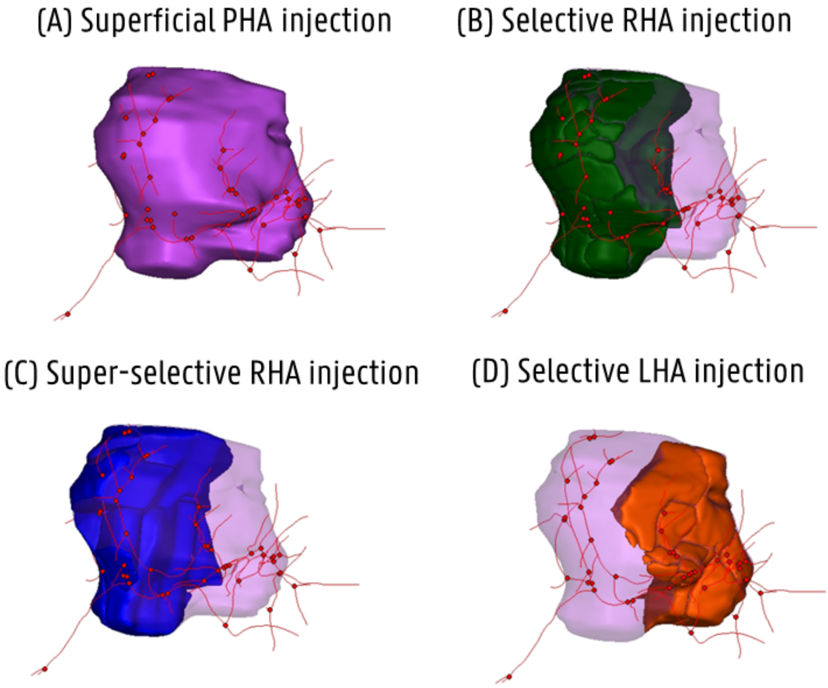

Figure 10.3: Fractions of the tumor mass perfused by the arteries downstream of each of the four injection locations: (A) PHA, (B) RHA, (C) LHA, and (D) super-selective RHA.

As shown before, the exact injection locations can be found in Figure 10.1B.

Even for the most distal injection locations (selective LHA injection and super-selective RHA injection), the diameter was still >4 mm (Figure 10.4B). Hence, these locations are considered easily accessible, and diameter was not considered as a relevant parameter in the cost function. As seen in Figure 10.4C, tortuosity steadily increased from the PHA over the first bifurcation and along the RHA, and made a significant jump in the LHA. From Figure 10.4D, we see that curvature has a high local value at the first bifurcation into the LHA, but is otherwise generally low. The resulting maximal values for curvature and tortuosity for each of the four scenarios are given in Table 10.1. The relative cost (C) is also given in Table 10.1. As can be seen, the relative cost of PHA injection was 0, since this injection location was located at the inlet of the hepatic arterial tree. Selective

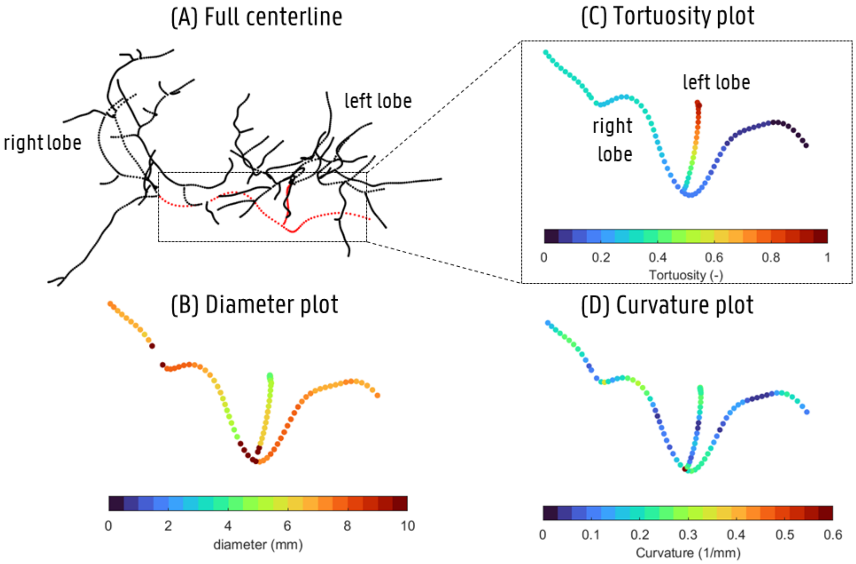

Figure 10.4: (A) Centerline of the hepatic arteries, region of interest colored by (B) diameter, (C) tortuosity, (D) curvature

injection in the LHA had a relative cost of 1, due to maximal tortuosity and curvature values. Both selective and super-selective RHA scenarios ranked in between.

Table 10.1: Maximum curvature and tortuosity values leading to calculation of the relative cost of each of the four injection scenarios.

Scenario	$max(\kappa)$ **(mm^{-1})**	$max(\tau)$ **(-)**	**C (-)**
Superficial	0	0	0
Selective (LHA)	1.0	0.49	1
Selective (RHA)	0.27	0.21	0.35
Super-selective (RHA)	0.34	0.33	0.5

10.3.3 Tumor dose and tip uncertainty

The two final parameters to consider were the expected tumor dose and the in-plane catheter tip uncertainty. The expected tumor doses were 42.9%, 48.7% and 50.8% for PHA, RHA and super-selective RHA injection, respectively. For LHA injection, the expected tumor dose is 41.7%.

In Figure 10.5, the tumor dose ranges are visualized. For PHA injection, the tumor dose range varied between 30.2% and 50.5%; for

RHA injection, the dose varied between 38.6% and 57.5%; for super-selective RHA injection, the dose varied between 30.1% and 81.9%; and between 25.7% and 64.1% for selective LHA injection.

Inspecting the super-selective scenario with the largest range more closely, the in-plane tip location corresponding to the highest tumor dose in the range (81.9%) occurred because 70.8% of particles flowed to one of the two internal feeders of the tumor. In the most non-optimal case (30.1%), only 7.11% flowed to the internal feeders; the rest flowed to the peripheral feeders which also partly perfuse the healthy parenchyma, explaining the large range.

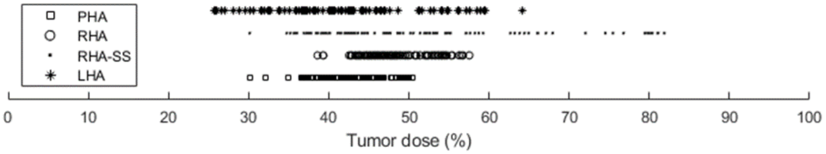

Figure 10.5: Tumor dose ranges generated for 100 randomly sampled input locations, for PHA injection, RHA injection, super-selective RHA injection (RHA-SS), and selective LHA injection.

10.4 Discussion

In Section 10.4.1, the different injection scenarios are compared based on the data generated above, and the optimal injection scenario is chosen. Additionally, in Section 10.4.2, the limitations of the current approach are discussed.

10.4.1 Scenario comparison

Regarding tumor coverage, the full tumor can only be targeted if two successive injections are performed in the RHA and LHA, or if the injection is done superficially in the PHA.

Regarding tumor dose, the expected doses all vary between 41.7%-50.8%. However, much larger differences are found for the dose ranges. For all scenarios, the minima are relatively constant (i.e. within the range 25.7%-38.6%), but the maxima vary significantly between 50.5%-81.9%. The highest maximum (81.9%) is reached for super-selective RHA injection, but a total uncertainty of 51.8% is also associated with this scenario, meaning the risk-reward trade-off is high. Additionally, the lowest uncertainty is reported for RHA injection (18.9%), with a maximum dose of 57.5%, making it a relatively safe injection scenario. Single LHA injection is associated with the lowest expected dose (41.7%) and high uncertainty (38.4%), making it a generally unfavorable scenario.

Regarding vascular accessibility, the LHA location is least accessible due to the curvature of the first bifurcation, while the superficial PHA injection location was most accessible. As expected, super-selective RHA injection is less accessible than selective RHA injection (since the latter is performed more upstream), but the difference is only slight.

Overall, combining all decision criteria, selective RHA injection seems most optimal, with high tumor coverage (69.6%), low uncertainty (18.9%), a similar expected dose compared to other scenarios (48.7%) and relatively high accessibility (0.35). Importantly, superficial PHA injection has maximal tumor coverage (100%), but since the expected dose is 42.9%, more than half of the injected material flows to healthy parenchyma, which is (in this case) the full liver. Additionally, it should be noted that, even though LHA injection is far from optimal (high uncertainty; low accessibility), we can only reach full tumor coverage by selective injection if we inject in the RHA and LHA. Finally, there seems little advantage of super-selective RHA injection over selective RHA injection at the current locations, due to slightly worse accessibility (0.5), a similar expected dose (50.8%), and much more uncertainty (51.4%).

These results of the multi-parameter-framework show that neither super-selective RHA or selective LHA injection are more optimal than RHA injection; the latter was performed in the clinic. Importantly, these results show why the current injection locations are suboptimal, and how this can inspire the search for alternative injection locations and scenarios. For example, successive selective injections in the LHA and the RHA can be done to obtain a combined tumor coverage of 100%. However, as stated above, LHA injection suffers from high uncertainty and high cost. Therefore, using a flexible catheter to enter the LHA would make the region of high curvature more accessible, and decrease the cost. To decrease uncertainty, super-selective injection in the LHA can also be considered instead.

10.4.2 Limitations and future work

This example shows how our patient-specific framework can 1) compare different injection scenarios based on multiple criteria, such as vascular accessibility, tumor coverage, expected dose and tip uncertainty; 2) propose new injection scenarios and illustrate which improvements they might offer over the more ‘conventional’ injection scenarios (e.g. the combined RHA + super-selective LHA scenario proposed here based on the current results); and 3) highlight important catheter properties for each patient-specific case (e.g. flexibility for LHA injection), which should inspire the catheter choice on a patient-specific bases. The consideration of all three parameters in a full multi-parameter optimization problem is novel compared to the state-of-the-art.

Verification, validation and uncertainty quantification (VVUQ) are considered the core principles for the implementation of any simulation technology in clinical practice, and their importance cannot be understated here [120]. First, verification was performed in-house, including grid convergence analysis, residual monitoring to assess solution history convergence, testing the sampling approach for catheter tip position for other injection locations, testing the region growing algorithm in other hepatic arterial and renal arterial geometries, visual checks of the morphological measurements, among others. Second, this chapter posits an uncertainty quantification framework for inplane catheter tip location, but uncertainty quantification of other CFD-related model parameters (boundary conditions, etc.) will need to be performed as well to understand the accuracy of the tool. Since we suggested a very specific model design for pre-operative optimization, this design offers more clarity on which inputs would be used, which mathematical model would be used, and which outputs would be predicted. Hence, we can apply uncertainty quantification (and validation) to this specific model design instead of a broader CFD problem. Third, validation efforts are ongoing, both in vitro and ex vivo, and are part of future work. Importantly, we only considered one patient-specific case here, which means that these findings cannot be generalized or transferred to other patients. Validation of the predicted tumor dose ranges and testing the current framework in more patients, are currently needed before considering the transfer of this technology to clinical practice. Hence, the current framework can only be considered as proof-of-concept. For validation, the model credibility level should also be clarified, and it is currently unclear which credibility level is needed (and achievable) to appropriately assist clinicians during decision-making.

10.5 Conclusions

As stated in Chapter 3, there is a large gap between using computational models for investigative purposes (such as discussed in Section

3.3) and using computational models in clinical tools for preoperative optimization (which was broadly discussed by Kleinstreuer et al. [9] as the Computational Medical Management Program). Here, we decreased that gap considerably, and suggested a very specific model design, which is a necessary stop to perform specific uncertainty quantification and validation. Importantly, when used in the clinic, this decision analysis tool should not be used as a sole source of information, but an additional source next to the clinician's own view and insights.

VI

Conclusions

CHAPTERS

CHAPTER 11

Conclusions and Perspectives

While the idea of using computer simulation in healthcare has been around for longer, Kleinstreuer et al. [9] suggested the Computational Medical Management program as a clinical workflow integrating computer simulations for the optimization of drug delivery of both microspheres in the hepatic arteries and aerosols in the lungs. Since then, multiple modeling studies (mostly CFD) have shown the non-negligible impact of injection parameters on the tumor dose for transarterial therapies. Although these findings open a window for patient-specific pre-operative optimization of injection parameters, this will remain complex due to several practical complications. These complications include, but are not limited to, high computational times, uncertain model input parameters, and limiting factors not considered with CFD. Hence, despite the initial roadmap provided by Kleinstreuer et al. [9], many obstacles remain. In this dissertation, we aimed to make significant strides towards a holistic pre-operative optimization workflow which integrates, but is not limited to, CFD. This was done throughout Parts II, III, IV and V.

In this final chapter of the dissertation, we will discuss global limitations of the CFD modeling approach. Of course, these limitations already inspire future work. Next, we summarize the key results and findings obtained throughout this PhD dissertation, and we compare them with similar results from literature where relevant. We also discuss which future work can help to verify these results, and build upon them. Additionally, we overview the most significant future steps that will be needed to realize our pre-operative workflow and integrate it in the clinic. Finally, we discuss whether this dissertation has made significant strides in answering the clinical questions first posited in Chapter 2, and to which insights it has led.

11.1 LIMITATIONS OF THE MODELING APPROACH

First, we want to discuss global limitations of the current CFD modeling approach, which apply to Chapters 4-10. More detailed limitations regarding study design etc. were given at the end of each individual chapter.

Importantly, the CFD model we introduced has significant limitations. First, the catheter was modeled as thin-walled and massless, and the fluid inside the catheter was modelled as blood. The same approach is used throughout literature [10–12, 15, 106]. While we estimate that the influencing of adding a wall thickness is likely to be small, the properties of the carrier fluid inside the catheter might not be negligible. In clinical practice, the fluid inside the catheter is an aqueous solution, such as saline, with distinctly different properties than blood. Hence, the interactions between blood and the catheter fluid will likely play an important role, and these differences are currently underestimated with our single fluid phase approach. To mitigate this, a third phase (i.e. second fluid phase) can be introduced in the current multiphase set-up (e.g. using the Eulerian-Eulerian volume of fluid model, as in [149]). Initially, we chose to limit ourselves to a dual-phase approach for the sake of simplicity. However, recent in vitro validation experiments conducted in collaboration with the University of Twente have suggested an non-negligible effect of the second catheter fluid phase. Should future model validation confirm this potential epistemic error, then appropriately modeling the catheter fluid properties and its interaction with the blood phase should be a priority.

Second, for a given cross-sectional tip position, typically only one microcatheter direction was considered. As shown in [15], the catheter direction can play a role in downstream microsphere distribution. In a future study, we could use CFD simulations to show whether the tumor dose ranges resulting from unknown catheter tip position as computed in Chapter 7 are significantly impacted by considering different catheter directions or not. When explicitly modeling catheter presence, investigating the sensitivity of the reported outputs towards varying microcatheter directions would make the modeling approach more robust.

Third, blood was modeled as a single fluid with the Quemada viscosity model [126], which captures the hematrocrit-dependent shear-thinning behavior of blood. The particulates which partly make up the composition of blood (mainly red blood cells) were not considered at the individual level. This might be a relevant point of study later on as the size of red blood cells ($\sim 8\mu m$) is not that much smaller than the smallest microspheres used for TARE (diameter of $\sim 20-40\mu m$) and might interact. Again, this would make the modeling approach more complex, adding a third phase (e.g. a second discrete phase) to the current multi-phase approach (e.g using a Eulerian-Lagrange model as in [150]).

Fourth, microspheres were modeled as inert spheres, with one-way coupling enabled between the fluid and discrete phase, and no interactions between the particles. Additionally, microsphere concentration was not specifically set realistically in this simulation, as the microsphere distribution was always calculated as a relative fraction with respect to the injected dose. Interestingly, in a patient-specific computational study, Lertxundi et al. [151] noted that, with increasing microsphere concentration in the vial, the peak microsphere concentration in the blood also increased, possibly increasing the chances of clogging [151]. Hence, microsphere concentration might be a parameter of interest under conditions where clogging events are more likely. While not case for the current set-up, when smaller vessels and larger microspheres are considered, setting a realistic concentration and modeling particle-particle interaction effects will become much more important.

Fifth, several key assumptions were made regarding boundary conditions. While realistic injection flow rates were set for the catheter, they were set constant in time. However, as the vascular downstream resistance increases, it might become more difficult to inject, hence reducing the flow rate. Additionally, when manual injection is performed (i.e. not through the use of a syringe pump), injection flow rate can be more subject to variations. Similarly, the outflows imposed at each outlet were constant in time, but with progressive embolization, the flow distribution (and hence, outflow fractions at the outlets) will likely change over time as well. Of course, the boundary condition methodology to calculate the tumor flow contributions in each outlet is based on an in-house developed region growing model, as was first introduced in Chapter 4 [125]. This region growing model is currently being validated for predicting renal perfusion zones. Preferably, it should also be validated for use in the liver. The boundary condition methodology to calculate the healthy flow contributions (as explained in Chapter 4) was based on the approach by Aramburu et al. [128]. Preliminary in vivo validation for a small number of patients has already shown that these boundary conditions can work [16].

With regards to the inflow boundary conditions, a realistic albeit not patient-specific waveform was applied. Based on [128], the total inflow was calculated a posteriori from the outflow distribution, and the waveform shape (which we extracted from [127]) was scaled to this inflow. Hence, as explained mathematically in Chapter 4, this made that the total inflow was very dependent on the volume of liver parenchyma and tumor mass(es), which were computed patient-specifically, and the healthy and cancerous perfusion constants, which were generalized values [128]. Consequentially, it should be concluded that both our in- and outflow boundary conditions should be considered patient-inspired rather than patient-specific. However, they are currently our best solution in the absence of reliable patient-specific measurements. More studies like the waveform shape sensitivity study such as in Chapter 8 are needed to determine the exact impact of the boundary conditions, and the parameters from which the boundary conditions are computed, on the tumor dose output.

Finally, regarding the used geometries and segmentation approach, the inlet was artificially extruded in a straight manner to obtain a fully developed flow profile (which was symmetric by design). In reality, it is possible that the inlet flow profile is more skewed, due to bends in the hepatic arterial geometry preceding the computational inlet, which might impact the (C)PRGs and downstream particle distribution. This is a limitation of the current segmentation approach, where high-quality contrast differences between the arteries and the surrounding parenchyma are often not available upstream of the catheter tip. Additionally, the walls of the hepatic arterial vasculature were modelled as rigid, which is, of course, not the case in the human body. An example of a fluid-structure interaction approach, and how this relates to CFD results in this specific domain of drug delivery in the hepatic arteries, was already discussed in Chapters 3 [113] .

Importantly, while the emphasis of this PhD dissertation was on patient-specific modeling, only 2 patient-specific geometries were considered (1 cancerous liver in Chapters 4-8 and Chapter 10 and 1 cirrhotic liver in Chapter 9). Hence, all results (as overviewed below and in the individual chapters) should be interpreted as difficult to generalize (at this moment). The results should be verified in more patient-specific geometries before generalizing the conclusions made here.

11.2 KEY RESULTS AND FUTURE WORK

The research results of this PhD dissertation were divided in four parts: (1) Simplification of complex 3D CFD simulations of intra-arterial blood flow and drug transport, (2) Uncertainty quantification of the tumor dose, and sensitivity analysis of model input parameters, (3) Feasibility study of patient-specific in vitro validation, and (4) Integration of CFD in a valorizable, pre-treatment planning framework for treatment optimization.

Below, we will discuss the most relevant results for each part, and how they relate to the state-of-the-art. Additionally, we discuss future work and perspectives: how our results may be replicated and verified, and to which crucial insights or concrete tools they can lead.

11.2.1 The hybrid particle-flow model and particle spread

In Chapter 4, we introduced the hybrid particle-flow model, which used a novel truncation algorithm that was more strict than the truncation algorithm developed by Lertxundi et al. [124] because it still aimed to accurately predict intrasegmental events. In Chapters 4 and 5, we showed that severe truncation (i.e. more distal) was applicable to superficial injections, but only moderate truncation (i.e. less distal) was appropriate when the injection was done more downstream. The most important future work regarding the hybrid model is the verification in more patient-specific geometries.

In Chapter 5, we introduced novel particle spread measures, including two time-dependent spread measures, which also included one particle-weighted spread measure. We introduced spread measures to assess the underlying assumption of the hybrid particle-flow model, i.e. that particles mix with the blood as they travel downstream, and spread over the cross-sectional area. Previously, Aramburu et al. [11] quantified global particle spread very proximal to the catheter tip (no bifurcations were encountered) and noted that spread also depends on injection velocity. While we did not study the dependency on injection velocity, we studied both the time-dependency and uniformity of spread, and investigated this throughout the tree (encountering many bifurcations). Importantly, we showed that the maximum degree to which particles spread increases more distally, but that spread is very time-dependent, leading to parts of the cycle where microspheres are still very localized within the arterial cross-section. We showed this in one patient-specific geometry, but for multiple (superficial and selective) injection scenarios.

Regarding future work, these spread measures may be used as evaluation metrics for novel catheter types. Specific designs, such as the microslit catheter design, are designed to promote particle spread and alignment with the blood flow, which can now be verified using our novel spread measures. If these novel designs are successful and are confirmed by our spread indices to increase flow-particle alignment, these and other novel catheter types can help to decrease the impact of injection parameters (such as injection position and injection velocity) and steer microspheres towards regions with higher flow (ideally, tumors).

11.2.2 Simplification

Aside from the truncation suggested by Lertxundi et al. [124], no specific simplification strategies had been forwarded in the context of TARE modeling. Hence, in Chapter 6, we forwarded grid coarsening and reducing the number of flow cycles as the first and second best simplification strategies for sensitivity studies. The same conclusions hold when simplifying with a focus on accuracy, but this depends highly on the accuracy required or preferred by the user. For a moderately truncated, coarsened mesh, we ended up with $\sim 2.4 \cdot 10^6$ elements (much lower than our original mesh sensitivity study allowed).

11.2.3 Uncertainty quantification

Uncertainty quantification and sensitivity analysis are crucial elements of VVUQ, and play an important role in model diagnosis. However, to make this type of analysis feasible for complex models, we need to reduce the computational times necessary for forward uncertainty propagation. This can be done by simplifying the forward model itself, and by using surrogate models. These ideas are not novel and are well reported in literature (e.g. in [152–154]).

However, we suggested that these techniques are not only useful to apply to numerical input parameters, but also to clinical parameters which can impact the outcome of TARE. For example, in Chapter 7, we quantified the uncertainty on the tumor dose ($\sim$16%) because of an uncertain catheter tip location using a low-fidelity modeling approach. In Chapter 6, we quantified the uncertainty on the tumor dose because of uncertain injection flow rate as much lower (~4.2%). Additionally, in Chapter 8, we showed that specific surrogate models can help reduce computational complexity of performing sensitivity analysis. Although we applied the ADOE on the sensitivity analysis of input waveform shape, we can easily extend the input parameter range to wider ranges of clinical and numerical parameter sources. To make our conclusions more robust, we should also consider more patient-specific geometries (and more cancer scenarios).

11.2.4 Validation

The discussion of validation, another tenet of VVUQ, was limited in this dissertation to Chapter 9. Specifically, we focused on the application of in vitro validation in patient-specific geometries, and used this set-up to highlight important differences between flow and particle distribution under the current conditions. Improvements over the state-of-the-art include building a patient-specific 3D-printed model of the hepatic arterial network, and tuning outlet boundary conditions in the in vitro set-up to a predetermined flow distribution. While we also attempted to compare both the numerical and experimental particle distribution, the current set-up was not finetuned enough to allow a highly quantitative comparison. For example, the microspheres used were training spheres (Sirtex, Australia), which are not tightly controlled for size and density (which are important CFD input parameters). Additionally, follow-up research showed that the current quantification method of the particle distribution (i.e. through weighing filter paper) is sensitive to dust, which can collect in the circulating fluid [155]. We have explored other alternatives than high-precision weighing (e.g. Coulter counter) which should be more investigated in further research [156].

However, we did show the feasibility of performing patient-specific in vitro experiments of hepatic arterial drug delivery. While this method is far from trivial to carry out, and improvements are still necessary (see above), we could use this set-up to test novel catheter types [156], or specific injection parameters, and evaluate their impact. For example, the in vitro validation set-up could be used to verify whether specific injection parameters (e.g. cross-sectional tip position, injection flow rate) result in a similar *size* of tumor dose range when compared with the simulation. In vitro validation is also very useful for bench testing of novel catheter designs [156]. Before and in Chapter 3, we studied particle spread to assess where differences between particles and flow could arise, and suggested they could be used to assess whether specific catheter types promote particle-flow alignment. Given that particle distribution measurements can be performed more reliably for the in vitro set-up, our in vitro experiments could also be used to investigate the impact of catheter type on particle-flow alignment (as also studied computationally by Ortega et al. [133]). However, since boundary conditions are fixed a priori in the in vitro set-up through the tuning of resistances to reach a specific outflow distribution, the in vitro set-up is not fit for to judge whether the CFD model can accurately predict the tumor dose (range) in actual patients.

To assess the validity of CFD to accurately predict the tumor dose (range), in vivo validation techniques are likely to be more appropriate. The particle distribution itself is an artificial parameter, because it is a CFD result, but not a health outcome in patients. Hence, using the CFD-based particle distribute to estimate where microspheres will lodge in the smaller downstream vessels and how radioactivity will spread from these sources will be a crucial step of in vivo validation. The importance of simulating to health outcomes is discussed more in detail below.

To conclude, we propose using specific validation techniques for specific purposes: (1) in vitro validation for investigating the impact of injection parameters and bench testing novel catheter designs, and (2) in vivo validation for comparing patient-specific health outcomes to model outcomes and testing the validity of the model.

11.2.5 Valorization

Treatment planning for TARE is a multi-objective optimization process. If we were to compute the optimal treatment conditions based on CFD outcomes alone, a likely conclusion would be to inject as close as possible to the tumor, selectively in each tumor-feeding artery. However, other problems stand in the way. The axial injection position can be controlled, but depends highly on vascular accessibility. Additionally, even if we can determine the exact impact one injection parameter has on the treatment outcome, some parameters remain largely uncontrollable. Think of the cross-sectional injection position, or the injection flow rate (which is largely impacted by the downstream vascular resistance). Our pre-operative workflow aims to consider governing uncertainties (due to uncontrollable parameters) and barriers to optimization (such as vascular access). This has transformed TARE planning from a single-objective optimization process (maximizing tumor dose) to a multi-objective optimization process (maximizing tumor dose under specific constraints).

Notably, the current framework of Chapter 10 likely only works for standard microcatheter types and microsphere injection velocities similar to blood flow velocities. This is because the employed CFD model was not a catheter-based injection, but a planar injection. Planar injections do not account for presence of the catheter, which is likely only to be negligible for standard microcatheters (for example, balloon-occluding microcatheters have a great impact on the near-tip blood flow velocity and pressure drop). Similarly, planar injections do not account for the velocity or properties (viscosity, density) of the injectate fluid, which have been shown to be relevant [92]. Likely, two-way coupling between the microspheres and the blood flow may help solve the velocity problem, as the inertia of the microspheres will be taken into account. Whether the impact of a different density and viscosity of the injectate is low enough to warrant the use of planar injections, will need to be shown in future work.

The development of a valorization framework is important because model diagnosis and validation is much more relevant to carry out when the relevant output parameters are known. Given computational and time restraints, performing uncertainty quantification and validation towards hemodynamic parameters that would not be considered during therapy planning, seems like a waste. Hence, the CFD output parameter of interest of the current pre-operative framework is the CFD tumor dose range resulting from a planar injection. Hence, regarding future work, we quantified the impact of waveform shape on the tumor dose in Chapter 8 for a catheter-based injection, but it would be relevant to investigate the uncertainty introduced by waveform shape on the planar-based tumor dose range as well. While the impact on the catheter-based tumor dose was significant, the impact on the planar-based tumor dose range might be different, and can show whether waveform shape is an important parameter to finetune and quantify for the current pre-operative framework. If the increase in tumor dose range due to varying waveform shape is limited compared to the uncertainty due to unknown cross-sectional tip position, more generic waveforms might be applied at the inlet. If it is shown that waveform shape cannot be quantified, or other clinical parameters prove to be completely uncontrollable, they can be included in the tumor dose uncertainty range currently considered during optimization. However, the more parameters that can be quantified or fixed, the smaller this uncertainty range (and the more certain our prediction) can become, which stresses the need for uncertainty mitigation.

11.3 Future Steps for Our Pre-operative Workflow

Above, we already discussed our key findings for each part of this PhD dissertation, and the future work inspired by these findings (further simplification, more extensive uncertainty quantification and sensitivity analysis of a wider range of parameters, using our spread measures to evaluate novel catheter designs, etc.). However, we have not yet provided a roadmap for the future, which would allow to make the bridge between the current state of our work, and the eventual goal of integrating our pre-operative workflow in clinical practice. Here, we give a global overview of future steps we deem necessary to bridge that gap.

11.3.1 Simulating to health end-points

Notably, simulating to a health end-point that is measurable in the clinic (such as a spatial radioactivity distribution) instead of a somewhat artificial particle distribution (as is done now) allows proper in vivo validation based on SPECT- and PET-CT scans. The artificiality of the current particle distribution arises from the fact that the outlets of the computational geometry through which the microspheres exit, do not physiologically represent their final fate. Specifically, in the body, the microspheres will travel further downstream and lodge in the smaller, more downstream vessels of the hepatic arterial network, where they will release high-intensity β-radiation through radioactive decay of the radiotracer. To mitigate this problem, Simoncini et al. [121] showed that smaller generations of the hepatic arteries (beyond what current medical images allow us to visualize and segment) can be generated using vascular tree models. Hence, to more accurately determine the location of the microsphere sources using the current methodology, the hybrid particle-flow model should be complemented with additional steps: after using CFD to calculate the particle distribution in the truncated geometry, (1) the vascular tree model can be used to estimate the spatial distribution of the downstream vessels, (2) and then the particle distribution at the geometry outlets can be distributed over the newly generated downstream vessels (assuming that particles follow the bloodstream).

To convert the current particle distribution (i.e. microsphere sources) into a radioactivity distribution over tissue and simulate to health end-points, Roncali et al. [123] showed how radioactivity originating from microsphere sources in water medium can be modeled using Monte Carlo simulation. In [157, 158], this modeling approach was improved upon by modeling radioactive emission from microsphere sources in realistic, heterogeneous tissue. Attempts were already made in [157, 158] to validate the spatial radioactivity distribution in the liver with PET-CT scans, albeit in only 2 patients.

An alternative health end-point that is measured in the clinic is the total tumor dose over the dose delivered to healthy tissue, e.g. the T/N ratio. This was also calculated and compared with in vivo data in [158]. Although this gave promising results, this validation was only done for 1 patient, and uncertainty quantification was not yet done. Of course, when calculating only global parameters (such as the T/N ratio) instead of spatially heterogeneous parameters (such as the spatial radioactivity distribution), the added value of using Monte Carlo simulation and generating downstream arterial bifurcations should be investigated. The disadvantage of using global parameters as health end-points is that they offer a much less detailed analysis (it depends on clinicians which level of detail they prefer to support their decision-making); the possible advantage is that the modeling approach might necessitate less complexity, as illustrated above.

In short, the totality of simulating to health outcomes (e.g. T/N ratio, radioactivity distribution) and validation of these health outcomes based on clinical in vivo data represents a crucial step to increase model reliability, which is currently lacking.

11.3.2 Inter-subject variability

This dissertation used patient-specific hepatic arterial geometries for both the computer modeling and in vitro experimental studies. While we have noted that it is difficult to generalize our findings because of their likely patient-specific nature, the exact inter-subject variability is unknown. Importantly, there exists an important diversity in not only the anatomy of the hepatic arterial geometries (which vary commonly among humans), but also the tumor size(s) and location(s). In the future, a much wider range of patient-specific anatomies and cancer scenarios should be considered to replicate our findings and truly grasp the inter-subject variability with regards to impact of clinical parameters, downstream particle-flow alignment, etc. This is especially relevant because it could show under which conditions inter-subject variability might decrease. For example, Feng et al.

[159] showed that, for small particles between 500 nm and 2 μm, inter-subject variability to predict the total deposition of particles within the lungs was negligible, meaning that one upper airway model could be used to represent an entire subpopulation of patients. If the conditions under which inter-subject variability is low are significant in scope, this means not all results should be computed patient-specifically (such as the identification of low- and high-impact parameters), which would be helpful to reduce computational times in the clinic.

11.3.3 Towards real-time prediction

While the main focus of Part II was to simplify complex 3D CFD simulations, current computational times might allow sensitivity analysis, but they are far from allowing real-time (or near real-time) prediction of treatment outcomes, which would be desirable in the clinic. Real-time prediction for drug distribution fields was done by Yuan et al. [137], but only for 1 simple pre-trained 2D geometry. Currently, the main method to achieve real-time prediction would be through the use of deep learning and reduced-order modeling, by pre-training a library of drug distribution and tumor doses with specific input features, such as hepatic arterial anatomies, cancer scenarios and high-impact clinical parameters, and then computing patient-specific results using this deep learning framework in a matter of seconds. Importantly, this cannot only be done for real-time tumor dose prediction in complex hepatic arterial anatomies, but the same framework was suggested by Feng et al. [160] to be used to predict aerosol distribution in patient-specific airways.

11.4 CLINICAL IMPLICATIONS

In Chapter 2, this PhD dissertation and its goals were framed around two crucial clinical questions regarding the possible improvement of treatment outcomes of transarterial therapies. Of course, as we discussed above, this dissertation provided key results in specific subdomains, but was not able to answer these clinical questions in their completeness. To that end, more future work is needed. However, the key results from this dissertation do provide us with more insight into how we might (and should) answer these questions in the future, and how these questions might have changed after the dissertation.

11.4.1 1st Clinical Question

The first clinical question as outlined in Chapter 2 was:

- **Question 1**: Can we reliably predict the tumor dose before the procedure, and, use this prediction to adapt treatment parameters where necessary?

Of course, the underlying assumption is that we need a reliable prediction of tumor dose to optimize the treatment. Apart from our approach, other efforts regarding optimization might focus on perioperative optimization, such as image guidance. Roosen et al. [161] have focused on using Holmium-microspheres that are visualizable with MRI during the treatment to assess whether microspheres are flowing to their downstream target. While image guidance is extremely valuable, this technique is still invasive and physical, and we previously made the point that non-invasive, virtual finetuning of injection conditions before the procedure has considerable merit (and lower cost). Ideally, both methods (pre-procedural finetuning and intra-procedural image-guided feedback) can continue to be developed in parallel and supplement each other in the clinic in the future.

Regarding the reliability of prediction, we made several advancements in this dissertation. Specifically, we suggested computing tumor dose *ranges* instead of specific tumor dose values. These ranges arise because of uncontrollable parameters such as the cross-sectional catheter tip position, or because of uncertain numerical input parameters. For these numerical parameters, identification is key. Low-impact parameters can be set at generalized values (parameter fixation), while for high-impact parameters, either more efforts should be done to measure these parameters (e.g. for the systolic duration parameter, 4D-flow MRI can be an option) or their uncertainty should be included in the tumor dose range prediction. While quantifying these uncertainties might decrease certainty on the prediction, this also increases its reliability. Of course, we already stated the importance of in vivo validation to confirm the ability of the CFD model to predict tumor dose ranges.

Regarding the optimization of clinical parameters, identification by sensitivity analysis is again of crucial importance. Low-impact clinical parameters should not be considered in the pre-operative workflow because they only increase the computational time. High-impact parameters should be considered in the pre-operative workflow if they are controllable; if they are not, their uncertainty should be included in tumor dose range, as discussed above.

Knowing these results, we should probably re-frame Question 1 as follows: Can we reliably predict the tumor dose **range** before the procedure, and, use this prediction to adapt **high-impact, controllable** treatment parameters where necessary?

11.4.2 2nd Clinical Question

The second clinical question as outlined in Chapter 2 was:

- **Question 2**: Can we decrease variable outcomes in TARE and TACE by optimizing the clinical injection parameters preoperatively, given a reliable prediction of treatment outcome?

Even with the advancements made by this PhD dissertation, Question 2 remains largely uncertain, mainly because future prospective clinical studies would be needed to fully answer this question. However, it is important to consider what Question 2 implies, and that it might not be the only route towards better health outcomes.

Relevantly, the CMMP as forwarded by Kleinstreuer et al. [9] considers that treatment parameters are highly controllable, and fixing them at their optimal values will lead to better health outcomes. The most remarkable example of this is their suggestion of the Smart Microcatheter [9], which fixes the cross-sectional catheter tip position at its most optimal location, as identified by computer simulations. This (undeveloped) invention considers the the cross-sectional catheter tip position as a *controllable* parameter, while currently, clinical practice proves otherwise. The Smart Microcatheter might solve this problem, but it will have to be able to stabilize the microcatheter tip in a dynamic environment such as the blood flow, with expanding and contracting walls, making it far from a trivial technological task. At this point, the question of controllability becomes almost a philosophical one, imbued with one's view on scientific progress, on what will be possible in the future, and what might remain impossible (despite our most valiant efforts). This school of thought, which considers that all parameters will eventually be controllable and optimizable in clinical practice, is further referred to as the *school of control*. This *school of control* is shown as the blue zone in Figure 11.1.

Of course, the Smart Microcatheter as conceptualized by Kleinstreuer et al. [9] is not the only example of the school of control. In fact, most CFD studies in this domain, which fix parameters such as catheter direction and injection velocities, at fixed, deterministic values and compute tumor dose as single values resulting from these fixed set of input conditions fit within this train of thought. Additionally, other, ongoing research also fits within this philosophy. For example, Michaud et al. [162] demonstrated the feasibility of magnetic resonance navigation to steer magnetized microspheres towards specific arterial branches, with the aim of achieving selective embolization. This clear example of the school of control was shown in a simple bifurcation phantom. Importantly, a balloon-occluding microcatheter was used to decrease the magnitude and pulsatility of the circulating fluid.

Interestingly, a different route towards optimization than the school of control can be considered as well. Instead of firmly fixing the injection conditions at their optimized values (given a reliable prediction by computer simulations), efforts can also be made to decrease the impact of these injection conditions. For example, high mixing of the microspheres with the blood flow could decrease the impact of cross-sectional position, and increase the agreement between flow and particle distribution. In case of tumors which have a high blood flow demand, this might be near an optimal scenario, as particles following the blood flow distribution are already preferentially led towards the tumor. Several novel catheter designs, such as the microslit or sidehole catheter [133, 163, 164], aim to increase mixing, and may decrease the impact of certain injection parameters. Perhaps, it is possible that we decrease the variability in outcomes, not by gaining a deeper understanding of the impact of injection parameters, but by decreasing their impact on the final particle distribution. This antithetical school of thought, of increased mixing and decreased control, is referred to as the *school of mixing*. This *school of mixing* is shown as the pink zone in Figure 11.1.

To be inclusive, Question 2 is probably best reframed as: Can we decrease variable outcomes in TARE and TACE by optimizing the clinical injection parameters pre-operatively, given a reliable prediction of treatment outcome by computer simulations, **or by decreasing the impact of clinical injection parameters, using specifically developed tools**?

11.5 FINAL THOUGHTS

In the past decade, generalized CFD approaches have been applied to the domain of transarterial therapies and provided insights that were

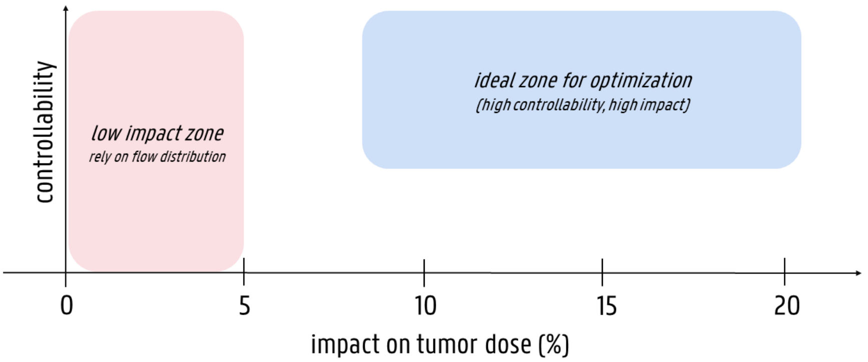

Figure 11.1: The blue zone represents the school of control, where all injection parameters are controllable. The pink zone represents the school of mixing, where the impact of all injection parameters is decreased to ensure microparticles follow the flow distribution.

more difficult to quantify experimentally or in vivo. These important foundations were laid by several people and their research teams, including (but definitely not limited to): Clement Kleinstreuer, Yu Feng, Emily Childress, Christoper A. Basciano, Andrew Kennedy, Jorge Aramburu, Raul Antón, Emilie Roncali and Amirtahà Taebi. Perhaps, the research field has matured enough at this point to develop more specific modeling strategies, finetuned to the precise clinical questions that we outlined earlier in this dissertation, and the precise problems that undermine outcome optimization in transarterial therapy planning. As George Box eloquently (or cynically) put it: *All models are wrong, but some are useful.* Such a specific transarterial modeling strategy, such as our own valorization framework, might not even belong to the *school of mixing* or the *school of control*, as considered above, but sits firmly between the two.

In context, this PhD dissertation walks a fine line between the *school of mixing* and the *school of control*. Since it is currently not clear which philosophy is more realistic to lead to optimal outcomes in transarterial therapy planning, it makes sense that these lines intersect regularly in research works such as these. Our pre-operative workflow considers uncontrollable clinical parameters and the uncertainty that arises from these parameters, which is already a much looser interpretation of the *school of control* than Kleinstreuer et al. [9] posited before. Since exact control of all influencing injection parameters might not be possible, the consideration of uncertain tumor dose ranges might be the most relevant development in this work.

With this in mind, we return to John Steinbeck, the great American novelist who once wrote: *What a frightening thing is the human, a mass of gauges and dials and registers, and we can only read a few and those perhaps not accurately.* Although mechanistic views on the human body pre-date Steinbeck (Descartes said that everything in nature occurs mathematically), Steinbeck's suggestion that the complexity of man partly originates from our inability to read all inputs into the system properly, resonates hard with those of us who engage in computer modeling of biological systems. For example, as shown in Figure 11.2, the waveform shape is an impactful input parameter which cannot be controlled (because it is inherent to the patient). Hence, because we do not know the exact shape, the uncertainty this introduced on the output must be considered in the final tumor dose prediction, as we quantified previously.

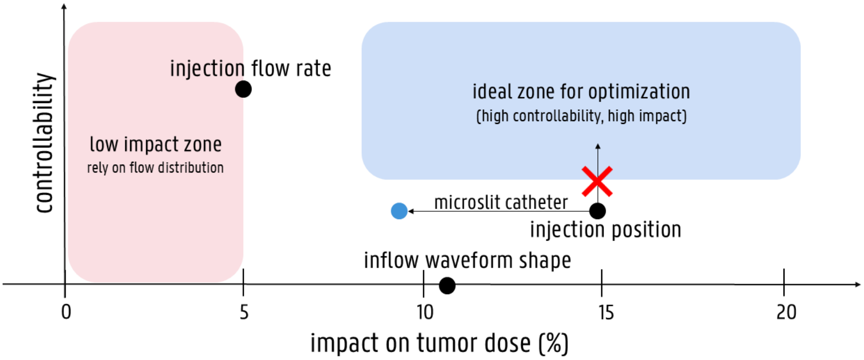

Figure 11.2: The clinical parameters of injection flow rate and injection position and the numerical parameter of inflow waveform shape can both be plotted on the controllability-impact grid. If the controllability cannot be increased, such as for injection position, perhaps novel catheters can help decrease the impact on the tumor dose, and minimize negative outcomes. For parameters which remain high-impact but uncontrollable, which is the case mainly for the injection position and waveform shape, the uncertainty they introduce on the tumor dose output should be included in the simulation results.

As shown throughout this dissertation, the inability to control all clinical parameters perfectly, or to accurately determine all numerical input parameters, introduces uncertainty. However, uncertainty ranges that are too large can make our simulations unusable in practice, and undermines the *school of control.* Hence, we also introduced spread measures to quantify mixing of microspheres with the blood, and suggested them as possible evaluation metrics for future novel catheter designs (such as the microslit catheter suggested by Ortega et al. [133]) to increase particle-flow alignment. If successful, mixing could help decrease the impact of injection conditions, especially for uncontrollable parameters, reducing the uncertainty ranges on the tumor dose prediction. This is shown in Figure 11.2. It was stated previously that it is difficult to enhance the controllability of high-impact parameter of injection position. Hence, reducing its impact might be necessary to minimize possible negative outcomes of an uncontrollable injection position. This might help to reduce the uncertainty that is introduced by an unknown, uncontrollable injection position, as seen in Figure 11.2. To summarize these considerations, limited controllability or predictability might induce uncertainty, but uncertainty might be mitigated by mixing (or other clever solutions).

As is clear, both strategies of the *school of mixing* and the *school of control* have considerable merit, but it might be more interesting to combine them rather than to choose between them. Going forward, we might call this dual approach the school of *uncertainty quantification and uncertainty minimization.* Our pre-operative workflow to optimize axial injection location under governing uncertainties (such as the range introduced by an uncertain catheter tip position) might present a first step in this specific direction. These final thoughts make this dissertation both a culmination of the work that came before it, a re-contextualization of ideas that have circulated in this field for over a decade, as well as - if we are lucky - a stepping stone for future modeling efforts to optimize health outcomes in liver cancer.

and the end of all our exploring
will be to arrive where we started
and know the place for the first time.

T.S. Eliot

VII

Appendices for the Interested Reader

Chapters

APPENDIX A

The Impact of Systolic Duration on Microsphere Distribution

POSITIONING

The Appendices as presented here are solely meant as supplementary material for the interested reader. They are typically not peer-reviewed, are smaller in scope, and contain larger methodological gaps than the main body of the dissertation. Hence, they should be seen more as exploratory and preliminary results. Because of this reason, it was chosen not to add them to main body, as their more obvious limitations would distract from the overall narrative. However, they are added here as appendices because they do supplement results from the main body, present interesting (if not incremental) findings on their own, and give an idea of other ongoing and future work.

In Chapter 8, the duration of systole was identified as an impactful inflow waveform shape parameter. In Appendix A, the near-tip hemodynamics and microsphere distribution for three waveforms which vary only in systolic duration are investigated, zooming in in more detail on how high differences in downstream microsphere distribution might arise from varying durations. This work was presented at the 7th International Conference on Computational and Mathematical Biomedical Engineering (27-29 June, 2022, Milan, Italy).

A.1 INTRODUCTION

The aim of this appendix is to further investigate the impact of systolic duration on the microsphere distribution, which was shown in Chapter 8 to be a very impactful parameter.

A.2 METHODOLOGY

The same patient was used as before (Geometry 3 in Chapter 4, see Fig. A.1). At the inlet, a spatially uniform and time-varying velocity profile was imposed (same profile as in Chapter 4.) The original profile was derived from a 1D model of the arterial circulation [127]. Two alternate profiles were developed by prolonging the systolic sections of the cardiac waveform by scaling factors of 1.5 and 2, respectively, keeping total cycle length constant at 0.8 s (waveform 1–3 in Fig. A.2A).

Two different geometries, one with a microcatheter and one without (to generate a planar injection), were generates. To study the impact of systolic duration, four CFD simulations were run. For the model with the catheter, three different simulations were run, with either waveform 1, 2 or 3 imposed at the inlet. For the model without the catheter, waveform 1 was imposed at the inlet, and particles were released over the entire cross-section (i.e. at the same axial plane where the catheter tip was located in the other simulations).

The mathematical implementation was the same as in Chapter 4. Using the Discrete Phase Model in Fluent (Ansys, USA), the transport problem of a discrete phase (i.e. radioactive microparticles) dispersed in a continuous phase (i.e. blood) was solved. Here, microparticles were modeled as inert spheres with a diameter of $40 \cdot 10^{-6}$ m and a density of 1600 kg/m^3. Blood was modeled with a density of 1060 kg/m^3 and a viscosity according to a simplified, shear thinning Quemada model with a minimum dynamic viscosity of $3.04 \cdot 10^{-3}$ kg/(ms). At the outlets, a flow fraction was imposed, which was either a healthy flow contribution for the non-tumor outlets or the sum of a healthy and cancerous flow contribution for the tumor outlets. Mathematical details behind the multiphase approach as it was implemented here can be found in Chapter 4.

Microparticles were injected with injection bursts every 0.01 s throughout the third cardiac cycle with an injection velocity of 0.12 m/s. For the models with the catheter, the catheter fluid (modeled here as blood) was also injected at a constant velocity of 0.12 m/s. One-way coupling was enabled between blood and microparticle flow. Simulations were run on a cycle to cycle basis: when <1.5% of the injected particles exited the geometry during the latest cycle, the simulation was halted. The time step size was varied between $0.5 \cdot 10^{-3}$ and $1.0 \cdot 10^{-3}$ s during each simulation. Absolutely globally scaled residuals lower than $1 \cdot 10^{-5}$ were attained during every time step.

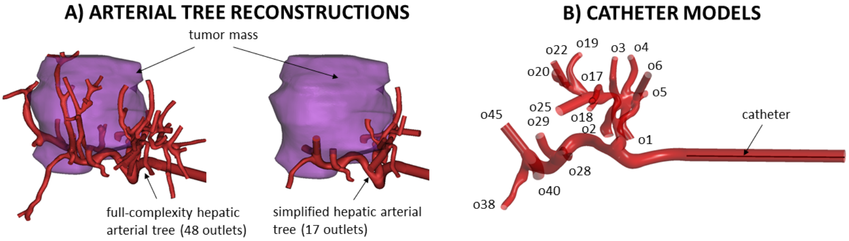

Figure A.1: (A) 3D-reconstructions of the full-complexity and simplified hepatic arterial tree and tumor mass, B) Solid model of the simplified tree with microcatheter

To study the microparticle behavior in the catheter models, the particle distribution was calculated by dividing the number of microspheres exiting through outlet x of the geometry by the total number of particles released into the bloodstream via the catheter tip (deemed as the exit fraction or EF for outlet x). The EF can be calculated globally (i.e. for the entire duration of injection) or for specific injection bursts at specific injection timings. Additionally, the EF was also calculated on a lobe-specific level, giving the right lobe and left lobe EFs. Consequently, by dividing the right lobe EF by the left lobe EF, the right-over-left lobe fraction ratio (RLF) was attained. For the model without the catheter, Particle Release Maps (PRMs) were generated for each injection burst to visualize the impact of in-plane injection location on particle fate (Fig. A.2C).

A.3 RESULTS

Inspecting the global particle distribution after the first bifurcation (i.e. towards the right or left lobe) in Fig. A.2D, the left lobe global EF increased from 27.8% to 33.0% and 37.9% when the systolic section was prolonged by a factor of 1.5 and 2, respectively. At the same time, the global RLF dropped from 2.32 to 1.77 and 1.42, respectively. The right lobe blood flow divided by the left lobe blood flow (imposed by the outlet BC, and thus the same for each waveform) is 2.02, which shows that the particle and flow distribution do not entirely agree in these patient-specific CFD simulations. Inspecting the particle distribution on an outlet-specific basis, the changes in EFs between the different waveforms were limited for most outlets (<2.5%), but largest for outlets 6, 38, 40 and 45 (see Fig. A.2D). Notably, from waveform 1 to 3, the EF for outlet 6 increased from 3.72% to 13.61% and the EF for outlet 40 decreased from 27.12% to 20.24%.

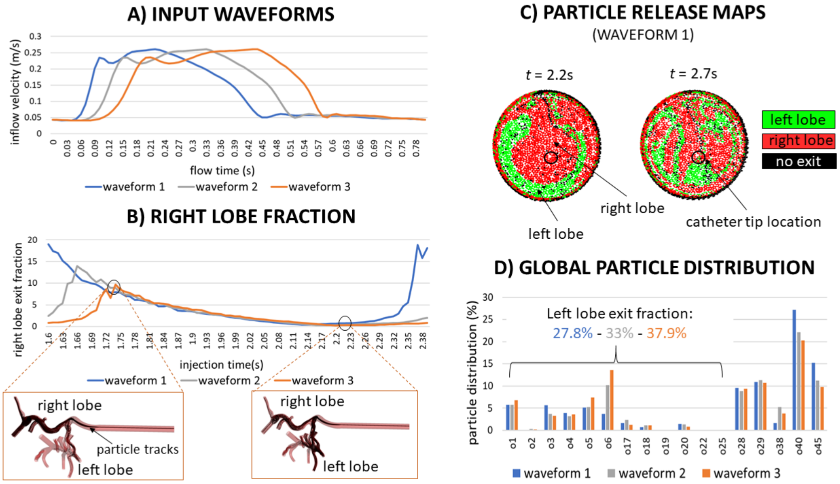

Figure A.2: (A) Three input waveforms. B) Right lobe fraction (RLF) for the three different waveforms. C) Particle Release Grids generated for the median exit time of particle injections at 1.74 and 2.22s. D) Global particle distribution for three different waveforms.

Investigating the particle distribution for specific injection timings, the RLF is plotted for each injection burst occurring throughout the third cycle in Fig. A.2B. Clearly, the RLF did not remain constant throughout the injection cycle. Inspecting the differences between the three waveforms, the minimum RLF was 0.387, 0.291 and 0.244 for waveforms 1, 2 and 3, respectively, while the maximum RLF was 19.0, 14.0 and 9.68 for waveforms 1–3. The change in RLF for the 3rd waveform is also shown clearly by plotting the particle tracks for the particles released at 1.74 s and 2.24 s, showing preferential flow towards the right lobe (i.e. higher RLF) for the particles released at 1.74 s, and a much more balanced outflow for the particles released at 2.24s. These findings indicate that both waveform shape and injection timing have a considerable impact on the particle distribution.

Looking at the results for waveform 1 (blue curve in Fig. A.2A), the median catheter ejection timings (i.e. the median time when particles exit the catheter) for the two injection bursts at 1.74 s and 2.22 s were calculated as 2.19 s and 2.67 s, respectively. Then, PRMs were generated at 2.2 s and 2.7 s to show the distribution of injection zones at the axial injection plane around the median ejection time. These PRMs confirm the findings above: for the particle front released at 1.74 s (and ejection time ∼2.2 s), the catheter tip is located well within the right lobe targeting region (red zone), leading to a high RLF (see blue RLF curve at 1.74s in Fig. A.2B). However, it should be noted that this only reflects the PRM generated at the median ejection time, meaning that a considerable number of particles exit the catheter before and after this timing. This explains why, for a catheter tip clearly located within the right lobe region at 2.2 s, some particles injected at 1.74 s still exit the left lobe. Conversely, for the particle front released at 2.22 s (with median ejection time ∼22.7 s), the catheter tip is located in an unclear transition region, with particles traveling to both the right and left lobe (red and green zone), leading to an RLF more reflecting of the flow distribution (see blue RLF curve at 2.22 s in Fig. A.2B).

A.4 DISCUSSION

From the results above, it is clear that there are two competing phenomena determining particle fate: the blood flow distribution, and the catheter tip location. When injection velocity is high (relatively compared to blood velocity, i.e. during diastole), the inertial effects of the injected particle stream temporarily dominate over the inertial effects of the bloodstream, leading to high peaks in RLF. On the other hand, when injection velocity is low (relatively compared to blood velocity, i.e. during systole), the inertial effects of the bloodstream dominate, and the RLF approaches the level imposed by the blood flow distribution (∼2.2). This is reflected by the RLF curves in Fig. A.2B: for the waveforms with delayed systolic peaks (i.e. longer periods of relatively low particle injection velocity during systole), the RLF maxima are lower. After the RLF maxima, the RLF curves in Fig. A.2B tend to coincide (1.75s-2.2s), indicating that the impact of input waveform is not as great for all injection timings. However, it is difficult to directly relate the input waveform with the RLF curve, as particles tend to arrive at the catheter exit at different timings.

Remaining challenges with the study set-up are that only a limited range of waveforms were tested, that blood was modelled as the catheter fluid, and that the impact of waveform shape was only evaluated with regards to particle distribution and not a more relevant clinical parameter such as tumor dose. Future work should focus on tackling these challenges and validating these findings in a wider range of waveforms and more patient-specific geometries.

A.5 CONCLUSIONS

In conclusion, injection timing, input waveform, catheter tip location, and injection velocity all impact the particle distribution, but are best understood in accordance with each other. The catheter tip location will determine the direction of the injected particle stream, but the relative difference between injection velocity and the surrounding blood velocity will determine which inertial effects are most impactful at each timepoint. These results generate additional insight into the results of Chapter 8, and why the parameter of systolic duration is so important. They also emphasize the importance of carrying out global sensitivity analyses of a wide range of parameters: once the highest-impact parameters have been identified, their impact can be investigated and verified in more focuses parameter analyses where only the most important parameter is varied, such as this study.

APPENDIX B

Qualitative In Vitro Experimental Study of the Impact of Cross-Sectional Injection Position

In Chapter 9, the possibility of using in vitro validation techniques to perform experimental parameter analyses in a patient-specific set-up was discussed. Here, the patient-specific in vitro experimental set-up is used to investigate the impact of cross-sectional injection position. This work was developed by Heather Boudry, Laura Burgelman, Marthe De Smet and Matthias Pex, who were at the time Bachelor students in Biomedical Engineering, during the course Cross-Disciplinary Project.

B.1 INTRODUCTION

In the current study, color dye experiments are executed to visualize the flow from the catheter tip through a patient-specific 3D-print of the hepatic arteries and collected in downstream reservoirs. The goal is to assess the impact of two different cross-sectional tip locations (top, bottom) visually. This is the first time such an experimental parameter study was conducted in a patient-specific geometry, albeit with injection of color dye instead of microspheres. Below, the methodology of this proof-of-concept study is explained, and the preliminary results are visualized and discussed.

B.2 METHODOLOGY

First, the same 3D-print of the patient-specific hepatic arterial geometry was used as in Chapter 9; the process to generate the 3D-print based on imaging data was also previously explained there. Second, two different 3D-printed designs were created in SpaceClaim (Ansys, USA) to fix the catheter tip position: one with a central fixation position, and one with a fixation position at the periphery (which could be rotated to fix at different top and bottom positions, etc., see Fig. B.1A). Regarding design parameters, axial thickness of the design is 6 mm (lower thickness led to tilting of the design due to the flow), wall thicknesses of 0.35 mm (lower thicknesses were not feasible for printing). The outer diameter of the model (6 mm) was designed to roughly correspond with the inner diameter of the hepatic artery 3D-print before the first bifurcation.

During the experiments, the 3D design was inserted first, after which the pump was turned on. A pulsatile flow was generated using a ViVitro Superpump (ViVitro Labs, Canada). Next, the microcatheter was inserted. During each injection, a dye-water mix was injected through the fixed microcatheter. Each mix consisted of 10 ml of distilled water and two drops of color food dye (blue). The 21 outlets of the hepatic artery print were combined with PVC tubing into 9 collecting reservoirs. The contrast difference between the reservoirs is used to give a (qualitative) indication of dye distribution. The contrast is only comparable if all reservoirs contain roughly the same volume of water, so the resistances at the PVC tubing were adapted to allow equal outflow to all reservoirs.

B.3 RESULTS

Here, two cross-sectional tip positions are compared: one at the bottom of the cross-section (see Fig. B.1C for the orientation) and one at the opposite, top side. In Fig. B.1D, we focus mainly on container C2, which is connected to the left hepatic artery outlets. It is clear that, for the bottom position, there is significantly less color dye in container C2 than for the top position. Judging B.1C, this seems realistic: for the bottom position, the color dye visually only flows through one side of the bifurcation, avoiding the outlets which lead to container C2 (that side of the bifurcation is oriented upwards).

For the top position (which is closer to the point where the left hepatic artery branches off upwards), the opposite is true, and color dye flows through both sides of the bifurcation, also leading to color dye deposition in C2.

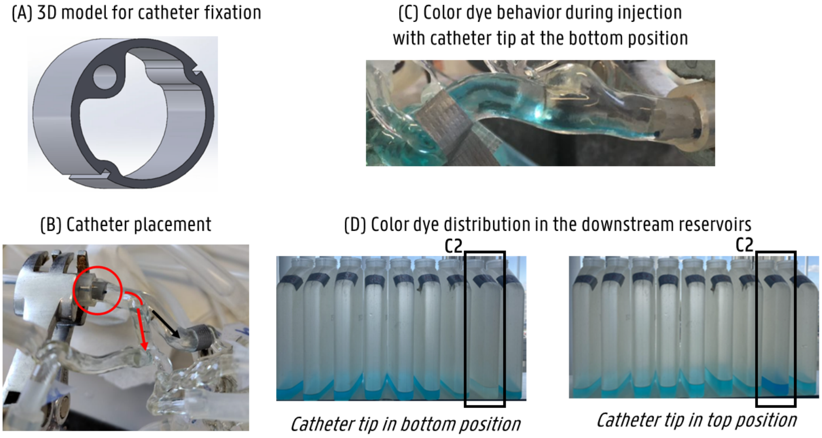

Figure B.1: (A) 3D design developed for 3D-printing which fits the hepatic artery 3D-print and allows catheter tip fixation. (B) In vitro placement of the catheter tip using a 3D design to fix the tip at the center before the first bifurcation (red circle). The red arrow indicates how the left hepatic artery branches off from the top, leading to container C2. (C) Streamline visualization of the color dye during injection at the top position. Clearly, the color dye only flows through one side of the first bifurcation. (D) Downstream color dye distribution in the reservoirs show a high contrast difference in container C2 for the bottom vs top position.

B.4 DISCUSSION

It is clear that the study above is only qualitative. However, despite the obvious limitations, this study does show that it is possible to stabilize the catheter tip position in vitro, and to inspect resulting differences in color dye contrast in downstream reservoirs. The impact of catheter tip position can be mostly explained by the direction of the arteries after the first bifurcation; further, more detailed analysis was not conducted.

Several important limitations limit this study. First, the exact flow characteristics of the pump (i.e. the exact inflow waveform shape) were not measured, and are unknown. This is not trivial, because if the flow would be unrealistically high, turbulence could cause higher color dye dispersion than under more physiological circumstances (i.e. laminar flow). Second, color dye was injected instead of microspheres, which have significantly different biophysical properties. Third, it is difficult to replicate the exact same axial injection position between different experiments, as the 3D design is removed and added from the set-up for each experiment. Of course, another limitation of the current set-up is that the fixation device can disturb the flow, which might introduce a discrepancy between in vitro and in vivo flow conditions. he added value of color dye is that streamlines following catheter ejection can be easily visualized, which is much less the case for microspheres. In the future, a combined approach of injecting microsphers embedded in color dye can be of interest. Future work could focus on using a spectrophotometer to quantify the contrast differences.

B.5 CONCLUSIONS

This proof-of-concept study invented a novel in vitro fixation device, which could be used to stabilize the catheter tip position in vitro, albeit with some slight flow disturbances near the device. A bench test evaluating a bottom and top catheter tip position showed differences in the downstream distribution that were deemed logical by inspecting the flow behavior near the first bifurcation. In the futre, more locations should be tried, the downstream distribution should be quantified, and the repeatability of the results should be verified at measured, physiological flow conditions.

Acknowledgements

If I'd have to compare doing a PhD to anything, I'd say it was eerily similar to a revolving door – a manual one, where you have to push the door ahead yourself. The moment you step in that door, the people who entered before you are already in the process of their own revolution. They might become a good friend, a mentor. The further you progress, the closer those people come to exiting the door – such is the nature of starting a project that is finite by nature. At the same time, new people start entering behind you. They might become your friend, you might become something resembling a mentor for them. As a result, doing a PhD feels like a constant symphony of goodbyes and welcomes. And as time goes on, you find everyone who is caught in the door together with you doing the same thing: doubting, wondering, trying, thinking, failing, repeating. And, most importantly: gently turning, in that door, pushing ahead.

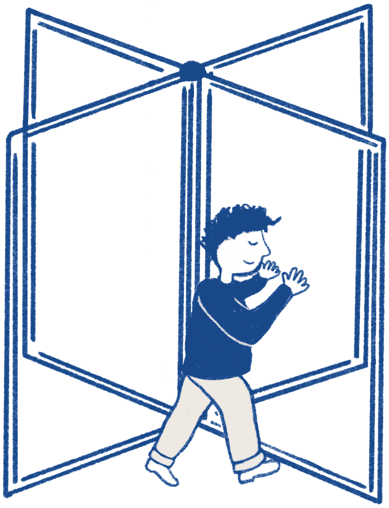

Late September 2019, Patrick welcomed me at Blok B for the very first day of my research career. My first office constellation (in the now derogatorily used ‘old building’) consisted of Annette, Federico and Matthias (give or take a couple of Cubans who were really into Bohemian Rhapsody). **Federico**, I remember your Italian-ness and your kindness most of all, making sure to explicitly invite me to lunch on my first day (the new kids wouldn’t understand this, but back then there was no crazy person yelling ‘LUNCH!’ in the hallway to gather everyone). You also gave crucial information from ‘ground zero’ (Italy in March 2020), correctly predicting that we would all be working from home ‘soon’. It’s a shame the panini hit us around that time, because you’re one of the people I feel like I didn’t get to spend enough time with during our short period together. **Matthias**, my big bear, you would continue to sit with me in that office for years to come, my stable beacon in the most turbulent times. I remember the thing we bonded over initially was The National at my Starter’s Party. While it took both of us some time to let each other in, I see you now as one of my dearest friends. I’m very happy that, even after you left the office, we remained neighbors (more or less) and can still share the occasional espresso martino. Hope we can talk more soon about your school and that I can give you many, many more dilemma’s to overthink. **Annette** (emphasizing the final ‘e’ here in text, because I never remember to do it in real life, for which I can only apologize), with time you would become my go-to mentor, and I’m incredibly grateful for all the times you let me pop in to your office for some ‘quick advice’ (which typically turned into at least 1-hour conversations). I know you were always incredibly busy, but I’ve cherished your advice like holy scripture throughout the years. Notably, you’re also just a very nice person to hang out with, a strong leadership figure and an incredible scientist! (I know this, not only from my own judgement, but from the way the people who work with you talk about you!)

In those early days, I remember being intimidated by quite a lot of people, especially the people who were in the office before me (even only by a couple of weeks). One of those people was **Amith**. You dazzled me with Fluent knowledge, always ready to give your advice; the definition of an academic older-brother-figure. We bonded over Liverpool/Arsenal and Indiana Jones, while also teaching quite a lot together. Next to being just a straight-up great guy, I honestly don’t think the lab would have functioned at all without you: both me and Sarah desperately needed you at times, and without your wits my PhD would've gone a lot less smooth. We did not have many postdocs at the lab, but you were a true 'postdoc' in spirit. **Lise**, I also look up to/was intimidated by you, as you were always extremely well-prepared and insightful, and displayed a level of professionalism I strived to for years (but never quite reached). I thoroughly enjoyed our lunch BBB sessions (after they were done) and watching you speed by in the swimming pool. Undoubtedly, my favorite moments were with you and Sarah during Ingenieursproject. Every company or school to hire you will be lucky to have an exemplary figure as yourself among their ranks. I also sincerely want to thank **Ghazal**, my OG thesis supervisor, for helping me with the transition of student to PhD. All three of you were important role models for me during those early moments, and I would not be where I am today without your guidance.

Next to these role models, there were also a lot of Starters starting their own trajectories alongside of me. **Sarah**, I wholeheartedly apologize for 'putting you on the rooster' every lunch. It was a pleasure hosting Ingenieursproject and heart dissections with you. You are an intelligent person with your heart in the right place, both attributes that you will get you very far during your adventure abroad. I wish you all the best for what lies ahead! **Jens**, fellow Starter, I also apologize to you, mainly for all the hugs you were involved in that you probably didn't want to be involved in. You were always someone who I felt connection to because our journeys were so similar with respect to timing and future prospects, and I'm really grateful to have shared that with you. You're a very nice and kind person and I'm very happy for you that you have a great imaging team to work with at Medisip! **Gert**, I'm glad that, while I'm writing this, I can congratulate you with your PhD and the work that you did - it really is impressive. We didn't see you that often but it was always a pleasure having you around. **Ashkan**, another fellow Starter, I'm not sure whether we can actually be considered colleagues because I still don't know why you were actually located on our floor, but you're probably the most hard-working, driven person that I know, and the trajectory you've been on with Exoligamentz is truly inspiring. In addition to that, the bond you have with your family is beautiful, and you never forgot to pass by my office when you were around, which I really appreciated. Bro, I hope that we keep running into, and fist bumping, each other for the foreseeable future.

Milan, **Gerlinde**, **Charlotte T.**, **Mariele**, **Emma C.**, you are all people who were at the lab way before me, and just as I said with

Federico, I would've liked to spend more time together, but I feel like we didn't get to do that because of the panini. You made feel very comfortable during those early-day lunch conversations, for which I am very grateful! Other OGs, **Mohammad** (the first colleague I went to a conference with) and **Hooman**, I feel like we would've seen even less of you if you wouldn't have come to steal our water once every day, but it was always nice to talk to you and I really appreciated the discussion we had about future plans. Next to being nice guys you also give solid career advice! **Mathias**, prof. Peirlinck, it was an honor to inherit your seat in Blok B; I sincerely want to thank you for the help that you offered regarding the first draft of 'De Medische Revolutie' and my FWO application. I am also sure that you didn't actually need my help for your PhD Cup write-up but I'm very grateful that I could still give you some pointers, because that was definitely a confidence booster!

As hinted above, we only spent a couple of months together before a Chinese bat started to wreak havoc. It was March 2020 and I had just handed in my FWO application when we received the news that we would have to work from home for 'a couple of weeks'. This marked the end of the first phase of my PhD life, and brought us into an entirely new era.

We would spend the next year-and-a-half mostly indoors, holding virtual coffee breaks and experiencing the highs and (mostly) lows of Microsoft Teams. I consider the Covid period until early 2023 the second phase of my PhD because I formed some key friendships there, even if they were stalled a bit by the circumstances. It was during the panini that I first started to go on walks with **Jolan**. Despite your small hands, I consider you one of my best friends (top 4?), and the partnership we formed during lunch conversations was absolutely horrifying for everyone but us. Those walks were also around the time you bought a canoe, which is not super relevant here, but I just think it's funny you bought a canoe. Your YOLO sunk-cost attitude to finances would become a theme in the next years, and my favorite most unnecessary expense of yours is definitely that Christmas troll (the second XL Christmas tree being a close second). Next to being incredibly caring, you're one of the smartest persons that I know (even though you will never admit that, you silly goose!). Of course, another topic that (regrettably) came up often during walks and talks was your turbulent love life, which seamlessly brings me to my next point.

In the second part of 2020, **Saar** joined the lab. We taught quite some courses together, including Ingenieursproject and CBFM (to a lot of future colleagues), which gave rise to some all-time quotes (‘sebietjes’, ‘ke me vant weekend eki gesmeten ip die pomp’). The first of many races we ran together was the Blaarmeersen Trail Run in late 2021; in the next years, many Exploots, a 10 Miles and a 20 km van Brussel, and of course many, many training sessions, would follow. In you, I found a partner in crime, and having you around was a life-saver for my mental health. Maybe not even my mental health alone, since you apparently diagnose long-term illnesses better than most doctors. That being said, you would also throw me in front of rabid dogs to save yourself if you had the chance so I guess that more or less evens out. Regrettably, a topic that also came up often during our many runs was also your love life, which peaked from the Starters Party 2023 onwards. Highlights for the three of us definitely include the Dune tri-costume cosplay at Saar’s Starters Party and the after-running Kantien sessions.

Not so long after Saar, **Emma** also joined the lab. Emma, the words-per-minute ratio increased significantly after you joined our lives; your office (or oven) would become a crucial office-hang-out spot; and I look back very fondly to our Christmas raclettes and brunches. You are one of the most resilient persons that I know, and I hope that you can find some rest in the years to come. From Bordeaux, London to Sicily, the four of us made quite some unforgettable trips together. Other highlights I have to include is our White Lotus binge and Big Lebowlski team-up at the Personeelskampioenschap Bowlen.

Another lab legend **Simeon**, who also joined the Ingenieursproject team (who didn’t actually?). I can only thank you sincerely, Simeon, for your additions to the office lore. From FMK Office to top-3s (or top 10 arrows?) to ‘least woke moment of the weekend’, from Draakklaps to Bourgondiëklaps, you were the heart and soul of many, many social events. You’re the kind of guy who’s always got a weekend story in store, a fact to share or a joke to tell - if I could take anyone to my next office, it would definitely be you. When you are done building walls, I hope you and those carotid signals finally work it out, because I think what you can have together is beautiful. Ar-te-ry!

The panini was not without its academic highlights (my first publication, receiving funding for four years by the FWO), but I was more than eager to return to the office whenever we were given the chance.

The string of office parties and Baracita Fridays that followed the end of the panini (or was it?) was undoubtedly the one of the wildest office life streaks we had. By that time, the office had changed quite a bit, with Federico graduating, Annette moving offices, and Bhawna and Yousof moving in. **Bhawna**, your taste in music is great and I still listen to our shared playlist now and then! I look back very fondly on the fun times we had together (Baracita especially!). **Yousof**, since I don't have peripheral vision, it was extra scary sharing an office with you for so many years because I never knew where you were standing exactly. That being said, you brought an energy and enthusiasm to the office that was unmatched, and office life would have looked entirely different without you. Another legend to spice up office life was **Samaneh**; while it took some time for you to warm up to our ways (and the other way around), I'm so glad you were part of our lab because it was so much fun going out with you (the policeman is a core memory). Additionally, **Wouter**, your Morty impressions will haunt me until the day I die, and your Word of the Day scheme enriched my life to the point that I am now aware of the importance of carcinization.

Over the years, we also welcomed a lot of interns to the office. **Melissa**, you broke the mold of what an intern could be; it still amazes me to this day how you charmed everyone and formed such great bonds over such a short period. From the moment you left, I knew you were destined to join us again, and I'm very happy that we could be colleagues for all those extra years. I also want to shout out **Vlada**, broad-shouldered **Nino**, Parisian chef **Solene** who prepared a four-course meal on her goodbye party, Swiss **Paula** who made an unexpected but very welcome return, Portugal 1 and 2 **David** and **Maria**, the kindest OG Portugal **Goncalo**, and Master student **Robin**. During your periods, you formed an integral part of lunch conversations, afterworks and the social tapestry of office life.

The third and final phase started halfway 2023, with a tumultuous move out of Blok B and many ex-students joining the lab as colleagues. **Jessie**, it was already clear when I was teaching CBFM to you, but now that we're colleagues I'm 100% sure you're one of the smartest people I know. Together with Ashkan, I would also consider you the most driven person that I know and you've also very fun to hang around and sit on a Flibco bus with (even if your social battery is running low). However, your navigation skills are questionable, and I just hope you never get the death penalty because your final meal would be the most saddening final meal ever. I promise I will make you chili con carne once and you will like it! **Jellis**, I can only say it's been an extreme honor being colleagues with someone who will either become the first president of Belgium or go to jail for a failed secession - whatever it will be, best of luck! And even though we have a different vibe politically, we agreed on many other things, such as the amount of alcohol that should be consumed in-flight during a professional trip. **Ariana**, honestly, when I look at you (academically), I see much of my younger self. That being said, you also have a lot of good qualities: you're very smart, motivated, sportive and very nice to talk to! I see in you a natural successor to our top-3 shenanigans, but you will have some competition for the leader role (see below). In you, I found a great swimming partner; I will miss our weekly outings! **Beatrice**, grawzie millee for showing us around Taormina and giving us the full Sicilian-American experience, you're one of the most fun persons I have ever met! I'm glad that we could overcome our initial teacher-student relationship and I hope you never have to ignore me on a plane to Milan again. Cala cala cala! For all four of you, I'm absolutely sure your PhD stories will be a success, but next to that, I also hope you enjoy and relax during your time here.

Of course, there were also some additional new faces who I never taught. **Elias**, Bambino, Pilsken, even though you're a bit scared of me, I thoroughly enjoyed having you around (and sharing a bed with you of course); you have a great career ahead of you and I'm sure you will make Flemish Charleroi proud. If you would spend a little bit less time scrolling through Instagram Reels and a little bit more time taking over the lunch conversations, you would already be a group leader! **Nicole**, not everyone was always sure who you were during meetings, and it was only in Edinburgh that I really got to know you as well, but our discussions about the top 5 pop girlies and your IAESTE stories were definitely the highlight of that conference. **Sina**, I have no idea what you're actually working on, but you're a very nice guy and you gave us an all-time scientific bio moment when you taught us how to uncook an egg! It was probably the only time we discussed something during an scientific bio that was useful in practice.

At long last, an important shout-out to my Corelleagues, **Sarah**, **Rosalie**, **Winter** and **Simon** (among others). Leaving Blok B for The Core was one of the best work-related changes that happened during the PhD, and the many kitchen conversations and Corefterworks were true highlights. Coref wiedersehen?

Of course, a huge shout-out my colleagues from Medisip. **Zoé**, I hope you stay strong and never succumb to peer pressure! I'm already looking forward to some new klaps that we can do. **Rabia**, the 8 minutes I had to lie down in your scanner when you were doing tests were the only 8 peaceful minutes of my PhD; I am forever indebted to you for that. **Maya**, I enjoyed looking forward to and then critically analysing the Taylor Swift Eras Tour with you. I hope you never get over your chips addiction because chips are awesome. Mr. **Amir**, you truly are a ray of sunshine that lit up our office, please never change. And say hi to your daughter from me! But enough breaks now, let's get to work, OK? To Jolan and Amir! **Boris**, your Norwegian cheesecake is life-altering, and it's because of that that I forgive you for always eavesdropping every time we talk about you. It's just not very polite! You're also my secret style king, always wearing something that makes me want to copy your fits. **Florence**, Romance, I am still waiting for the invite to your Restarters Party! Why do you keep going to the US and coming back? Don't you like us? **Meysam**, I will never forget the look of instant regret on your face when you were joking that I was late one morning and I replied that I just came back from my psychologist. It's OK, king! I will miss your kind spirit!

From the end of 2023 onwards, I stopped most of my analyses and start working on writing this little book here. I completed the first version in March 2024 and saved the acknowledgments for the end, as a little treat for myself. I knew that I would enjoy looking back on all these memories and people throughout the years. You were not only colleagues but companions, in easy and hard times; all of us working toward similar goals, wondering, trying, thinking, failing, starting over. All of you were instrumental in making my time here a core memory.

Of course, I also want to thank all of my friends and family for their unwavering support. Your enthusiastic response to things I told you about my PhD often helped me to see my own project again through different, often less analytic eyes, which can really help if you've been stuck in the grind. I've made a non-exhaustive list here: **Katrien, Marc, Silke, Frieda, Daniël, Liesbet, Steven, Jasper, Hannelore, Willy, Leen, Dina, Fien, Eline, Céline**. Additionally, I want to thank the many students I encountered (also the ones I didn't name in the preface) because teaching you was by far my favorite part of the job. A special thank you also has to go out to Eline Van Herreweghen for providing me with these beautiful illustrations. Finally, I want to thank the team at AZ Maria Middelares for taking care of me and always being available.

My other main thank you can only go out to my constant companion, **Nele**. I'd like to think I'm good with words, but still then it's difficult to express in words the impact you have had on my life (the few words I do have for that I'm saving for a different occasion, so I'm not wasting them here). You have been so intertwined with this process from its very beginning: In the summer of 2019, we were discussing whether I should pursue a PhD or not while walking along the cliffs in sunny Spain. In the winter of 2022, when we came back from celebrating Christmas, we were discussing everything that I think was going wrong in my PhD. We celebrated the highs and dealt with the lows and now we'll be celebrating this milestone together for many times, I'm sure! In the six-and-counting years that we have been together, you've helped me grow as a person, and the book I put down here is a result of that. From the moment this book is printed, the lines I've written on all of these pages will belong to everyone, but everything that's between the lines will belong to us, and us alone.

And so, you might ask, after all this: How does someone think back on a PhD? For me, it's mainly all of the people I've listed here. This book is a product of its circumstances, and it would be impossible to think about my PhD without thinking about all of you. And yes, sometimes it was hard. There were times that I had to push the door, push hard, to keep things moving. On the one hand, you want to keep things moving for yourself, because you really want to finish that paper, that presentation, that class. On the other hand, sometimes you push when you feel there's lots of work to do around you, so others don't have to push as hard. Because when you push, you can make space for others to get in behind you. And that's where the magic kicks in - keep things moving long enough, and you'll find that those revolving doors might not even need you that much. Years fly by; and after a while, with enough critical mass inside, you can start to let your grip off the handle, softly at first. You notice that the door keeps turning, one person after another, one generation after another, everyone pushing at their own rhythm and writing their own stories, and you feel that you can finally let go. And the beauty of that? It goes on turning, round and round again.

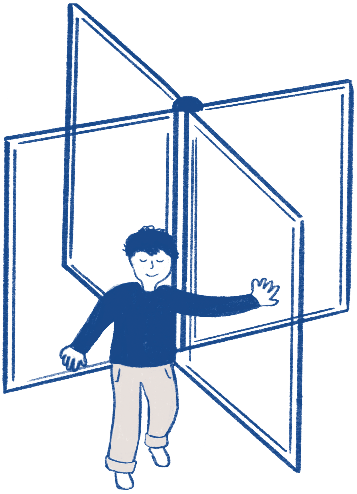

Bibliography

[1] A. Tang, O. Hallouch, V. Chernyak, A. Kamaya and C. Sirlin, ‘Epidemiology of hepatocellular carcinoma: Target population for surveillance and diagnosis’, *Abdominal Radiology*, vol. 43, no. 1, pp. 13–25, 2018.

[2] H. El-Serag and K. Rudolph, ‘Hepatocellular carcinoma: Epidemiology and molecular carcinogenesis’, *Gastroenterology*, vol. 132, no. 07, pp. 2557–76, 2007.

[3] H. El-Serag, ‘Hepatocellular carcinoma’, *New England Journal of Medicine*, vol. 365, no. 12, pp. 1118–1127, 2011.

[4] R. Salem and R. J. Lewandowski, ‘Chemoembolization and radioembolization for hepatocellular carcinoma’, *Clinical Gastroenterology and Hepatology*, vol. 11, no. 6, pp. 604–11, 2013.

[5] H. Ahmadzadehfar, C. Pieper, S. Ezziddin, H.-J. Biersack and C. Meyer, ‘Radioembolization with y-90 resin microspheres for hcc patients with extensive tumor thrombosis into the extrahepatic vessels’, *Clinical Nuclear Medicine*, vol. 39, no. 3, pp. 305–7, 2014.

[6] A. Teyateeti *et al.*, ‘Survival outcomes for yttrium-90 transarterial radioembolization with and without sorafenib for unresectable hepatocellular carcinoma patients’, *Journal of hepatocellular carcinoma*, vol. 7, pp. 117–131, 2020.

[7] C. Sposito and V. Mazzaferro, ‘The sirvenib and sarah trials, radioembolization vs. sorafenib in advanced hcc patients: Reasons for a failure, and perspectives for the future’, *HepatoBiliary Surgery and Nutrition*, vol. 7, no. 6, pp. 487–489, 2018.

[8] M. Jiang, A. Fischman and F. Nowakowski, ‘Segmental perfusion differences on paired tc-99m macroaggregated albumin (maa) hepatic perfusion imaging and yttrium-90 (y-90) bremsstrahlung imaging studies in sir-sphere radioembolization: Associations with angiography’, *Journal of Nuclear Medicine & Radiation Therapy*, vol. 03, no. 1, 2012.

[9] C. Kleinstreuer, Y. Feng and E. Childress, ‘Drug-targeting methodologies with applications: A review’, *World journal of clinical cases*, vol. 2, pp. 742–56, 2014.

[10] J. Aramburu, R. Antón, A. Rivas, J. C. Ramos, B. Sangro and J. I. Bilbao, ‘Computational assessment of the effects of the catheter type on particle–hemodynamics during liver radioembolization’, *Journal of Biomechanics*, vol. 49, no. 15, pp. 3705–3713, 2016.

[11] J. Aramburu, R. Antón, A. Rivas, J. Ramos, B. Sangro and J. Bilbao, ‘The role of angled-tip microcatheter and microsphere injection velocity in liver radioembolization: A computational particle-hemodynamics study’, *International Journal for Numerical Methods in Biomedical Engineering*, vol. 33, no. 12, 2017.

[12] C. Kleinstreuer, C. Basciano, E. Childress and A. Kennedy, ‘A new catheter for tumor targeting with radioactive microspheres in representative hepatic artery systems. part i: Impact of catheter presence on local blood flow and microsphere delivery’, *Journal of biomechanical engineering*, vol. 134, no. 5, p. 051 004, 2012.

[13] A. Kennedy, C. Kleinstreuer, C. Basciano and W. Dezarn, ‘Computer modeling of yttrium-90–microsphere transport in the hepatic arterial tree to improve clinical outcomes’, *International journal of radiation oncology, biology, physics*, vol. 76, no. 2, pp. 631–7, 2009.

[14] C. Basciano, C. Kleinstreuer, A. Kennedy, W. Dezarn and E. Childress, ‘Computer modeling of controlled microsphere release and targeting in a representative hepatic artery system’, *Annals of biomedical engineering*, vol. 38, no. 5, pp. 1862–79, 2010.

[15] J. Aramburu, R. Antón, A. Rivas, J. Ramos, B. Sangro and J. Bilbao, ‘Numerical investigation of liver radioembolization via computational particle–hemodynamics: The role of the microcatheter distal direction and microsphere injection point and velocity’, *Journal of Biomechanics*, vol. 49, no. 15, pp. 3714–21, 2016.

[16] R. Antón *et al.*, ‘A proof-of-concept study of the in-vivo validation of a computational fluid dynamics model of personalized radioembolization’, *Scientific Reports*, vol. 11, no. 3895, 2021.

[17] A. Van den Hoven, M. Lam, S. Jernigan, M. Bosch and G. Buckner, ‘Innovation in catheter design for intra-arterial liver cancer treatments results in favorable particle-fluid dynamics’, *Journal of experimental & clinical cancer research*, vol. 34, no. 74, 2015.

[18] T. Bomberna, G. Adeli, C. Claerebout, C. Verslype, G. Maleux and C. Debbaut, ‘Transarterial drug delivery for liver cancer: Numerical simulations and experimental validation of particle distribution in patient-specific livers’, *Expert Opinion on Drug Delivery*, vol. 18, no. 3, pp. 409–422, 2021.

[19] T. Bomberna *et al.*, ‘A hybrid particle-flow cfd modeling approach in truncated hepatic arterial trees for liver radioembolization: A patient-specific case study’, *Frontiers in Bioengineering and Biotechnology*, vol. 10, no. 914979, 2022.

[20] T. Bomberna, S. Vermijs, L. Bonne, C. Verslype, G. Maleux and C. Debbaut, ‘Spatiotemporal analysis of particle spread to assess the hybrid particle-flow cfd model of radioembolization of hcc tumors’, *IEEE transactions on bio-medical engineering*, vol. 71, no. 4, pp. 1219–1227, 2023.

[21] T. Bomberna, G. Maleux and C. Debbaut, ‘Simplification strategies for patient-specific cfd models of drug transport during liver radioembolization’, *Submitted to Computers in Biology and Medicine*, 2024.

[22] T. Bomberna, G. Maleux and C. Debbaut, ‘Adaptive design of experiments to fit surrogate gaussian process regression models allows fast sensitivity analysis of the input waveform for patient-specific 3d cfd models of liver radioembolization’, *Submitted to Computer Methods and Programs in Biomedicine*, 2024.

[23] C. Debbaut and T. Bomberna, ‘Numerical modeling in support of locoregional drug delivery during transarterial therapies for liver cancer’, in 2022.

[24] I. Dimov *et al.*, ‘Assessment of hepatic arterial hemodynamics with 4d flow mri: In vitro analysis of motion and spatial resolution related error and in vivo feasibility study in 20 volunteers’, *European radiology*, vol. 32, no. 12, pp. 8639–48, 2022.

[25] T. Bomberna, ‘Targeted drug delivery for liver cancer: Modelling the impact of cancer burden on the particle distribution in a patient-specific cirrhotic liver’, M.S. thesis, Ghent University, 2019.

[26] S. Abdel-Misih and M. Bloomston, ‘Liver anatomy’, *The Surgical clinics of North America*, vol. 90, pp. 643–53, 2010.

[27] C. Berasain, M. Arechederra, J. Argemi, M. Fernandez-Barrena and M. Avila, ‘Loss of liver function in chronic liver disease: An identity crisis’, *Journal of Hepatology*, vol. 78, no. 2, pp. 401–414, 2022.

[28] C. Eipel, K. Abshagen and B. Vollmar, ‘Regulation of hepatic blood flow: The hepatic arterial buffer response revisited’, *World journal of gastroenterology : WJG*, vol. 16, no. 48, pp. 6046–57, 2010.

[29] R. P. Mathew and S. Venkatesh, ‘Liver vascular anatomy: A refresher’, *Abdominal Radiology*, vol. 43, no. 8, pp. 1886–95, 2018.

[30] H. Wynne, L. Cope, E. Mutch, M. Rawlins, K. Woodhouse and O. James, ‘The effect of age upon liver volume and apparent liver blood flow in healthy man’, *Hepatology*, vol. 9, no. 02, pp. 297–301, 1989.

[31] U. Dandekar, K. Dandekar and S. Chavan, ‘Right hepatic artery: A cadaver investigation and its clinical significance’, *Anatomy Research International*, vol. 2015, pp. 1–6, 2015.

[32] Y. Iwakiri, ‘Pathophysiology of portal hypertension’, *Clinics in liver disease*, vol. 18, pp. 281–291, 2014.

[33] H. Ho, K. Sorrell, A. Bartlett and P. Hunter, ‘Modeling the hepatic arterial buffer response in the liver’, *Medical Engineering & Physics*, vol. 35, no. 8, pp. 1053–8, 2012.

[34] B. Sureka, N. Sharma, P. Khera, P. Kumar Garg and T. Yadav, ‘Hepatic vein variations in 500 patients: Surgical and radiological significance’, *The British Journal of Radiology*, vol. 92, no. 1102, p. 20 190 487, 2019.

[35] J. Cazejust, B. Bessoud, N. Colignon, C. Garcia-Alba, O. Planché and Y. Menu, ‘Hepatocellular carcinoma vascularization: From the most common to the lesser known arteries’, *Diagnostic and Interventional Imaging*, vol. 95, no. 1, pp. 27–36, 2014.

[36] J. Gong, W. Tu, J. Liu and D. Tian, ‘Hepatocytes: A key role in liver inflammation’, *Frontiers in Immunology*, vol. 13, p. 1 083 780, 2023.

[37] D. Kang *et al.*, ‘Bioprinting of multiscaled hepatic lobules within a highly vascularized construct’, *Small*, vol. 16, no. 13, p. 1 905 505, 2020.

[38] E. Trefts, M. Gannon and D. Wasserman, ‘The liver’, *Current Biology*, vol. 27, R1147–R1151, 2017.

[39] F. Bévalot, N. Cartiser, B. Charline, J. Guitton and L. Fanton, ‘State of the art in bile analysis in forensic toxicology’, *Forensic science international*, vol. 259, pp. 133–154, 2016.

[40] E. Abdalla, J.-N. Vauthey and C. Couinaud, ‘The caudate lobe of the liver: Implications of embryology and anatomy for surgery’, *Surgical oncology clinics of North America*, vol. 11, no. 4, pp. 835–48, 2002.

[41] C. Couinaud, ‘The Liver: Anatomical and Surgical Investigations’. Masson, 1957.

[42] L. Uliel, H. Royal, M. Darcy, D. Zuckerman, A. Sharma and N. Saad, ‘From the angio suite to the -camera: Vascular mapping and 99mtc-maa hepatic perfusion imaging before liver radioembolization–a comprehensive pictorial review’, *Journal of nuclear medicine : official publication, Society of Nuclear Medicine*, vol. 53, pp. 1736–47, 2012.

[43] H. Bismuth, ‘Surgical anatomy and anatomical surgery of the liver’, *World journal of surgery*, vol. 6, no. 1, pp. 3–9, 1982.

[44] H. Bismuth, ‘A new look on liver anatomy: Needs and means to go beyond the couinaud scheme’, *Journal of hepatology*, vol. 60, no. 3, pp. 480–1, 2013.

[45] A. Cervone, A. Sardi and G. Conaway, ‘Intraoperative ultrasound (ious) is essential in the management of metastatic colorectal liver lesions’, *The American surgeon*, vol. 66, no. 7, pp. 611–5, 2000.

[46] J. Fasel, P. Majno and H.-O. Peitgen, ‘Liver segments: An anatomical rationale for explaining inconsistencies with couinaud’s eight-segment concept’, *Surgical and radiologic anatomy: SRA*, vol. 32, no. 8, pp. 761–5, 2010.

[47] W. Platzer and H. Maurer, ‘Zur segmenteinteilung der leber’, *Cells Tissues Organs*, vol. 63, pp. 8–31, 1966.

[48] N. Michels, ‘Newer anatomy of the liver and its variant blood supply and collateral circulation’, *American Journal of Surgery*, vol. 112, no. 3, pp. 337–47, 1966.

[49] S. Favelier *et al.*, ‘Anatomy of liver arteries for interventional radiology’, *Diagnostic and Interventional Imaging*, vol. 96, no. 6, pp. 537–46, 2014.

[50] G. Noussios, I. Dimitriou, I. Chatzis and A. Katsourakis, ‘The main anatomic variations of the hepatic artery and their importance in surgical practice: Review of the literature’, *Journal of Clinical Medical Research*, vol. 9, no. 04, pp. 248–252, 2017.

[51] J. Chung, H.-C. Kim, M. Lee, J. Choi, H. J. Jae and S. Hur, ‘Anatomic variations of the hepatic artery in 5625 patients’, *Radiology: Cardiothoracic Imaging*, vol. 3, no. 4, e210007, 2021.

[52] G. Prager *et al.*, ‘Global cancer control: Responding to the growing burden, rising costs and inequalities in access’, *ESMO Open*, vol. 3, no. 02, e000285, 2018.

[53] K. McGlynn, J. Petrick and H. El-Serag, ‘Epidemiology of hepatocellular carcinoma’, *Hepatology*, vol. 73, no. 1, pp. 4–13, 2020.

[54] A. Vogel, T. Meyer, G. Sapisochin, R. Salem and A. Saborowski, ‘Hepatocellular carcinoma’, *The Lancet*, vol. 400, no. 10360, pp. 1345–62, 2022.

[55] Y. Ghouri, I. Mian and J. Rowe, ‘Review of hepatocellular carcinoma: Epidemiology, etiology, and carcinogenesis’, *Journal of Carcinogenesis*, vol. 16, no. 1, 2017.

[56] J. Balogh *et al.*, ‘Hepatocellular carcinoma: A review’, *Journal of Hepatocellular Carcinoma*, vol. 3, pp. 41–53, 2016.

[57] B. Rushing and M. Selim, ‘Aflatoxin b1: A review on metabolism, toxicity, occurrence in food, occupational exposure, and detoxification methods’, *Food and Chemical Toxicology*, vol. 124, pp. 81–100, 2018.

[58] R. Simonetti, C. Cammà, F. Fiorello, F. Politi, G. D'Amico and L. Pagliaro, 'Hepatocellular carcinoma. a worldwide problem and the major risk factors', *Digestive diseases and sciences*, vol. 36, no. 7, pp. 962–72, 1991.

[59] J.-H. Kao, 'Hepatitis b vaccination and prevention of hepatocellular carcinoma', *Best Practice & Research Clinical Gastroenterology*, vol. 29, no. 6, pp. 907–17, 2015.

[60] K. Schütte, F. Balbisi and P. Malfertheiner, 'Prevention of hepatocellular carcinoma', *Gastrointestinal Tumors*, vol. 3, no. 1, pp. 37–43, 2016.

[61] K. Schütte *et al.*, 'Delayed diagnosis of hcc with chronic alcoholic liver disease', *Liver cancer*, vol. 1, no. 3, pp. 257–66, 2012.

[62] V. Sun and L. Sarna, 'Symptom management in hepatocellular carcinoma', *Clinical journal of oncology nursing*, vol. 12, no. 5, pp. 759–66, 2008.

[63] A. Waghray, 'Hepatocellular carcinoma: From diagnosis to treatment', *World Journal of Hepatology*, vol. 7, no. 8, pp. 1020–9, 2015.

[64] L. Charach, L. Zusmanovitch and G. Charach, 'Hepatocellular carcinoma. part ii: Clinical presentation and diagnosis', *European Medical Journal*, vol. 5, pp. 81–88, 2017.

[65] P. Galle *et al.*, 'Easl clinical practice guidelines: Management of hepatocellular carcinoma', *Journal of Hepatology*, vol. 69, no. 1, pp. 182–236, 2018.

[66] J. Trojan, S. Zangos and A. Schnitzbauer, 'Diagnostics and treatment of hepatocellular carcinoma in 2016: Standards and developments', *Visceral medicine*, vol. 32, no. 2, pp. 116–20, 2016.

[67] A. Villanueva, 'Hepatocellular carcinoma', *New England Journal of Medicine*, vol. 380, no. 15, pp. 1450–1462, 2019.

[68] J. Namur *et al.*, 'Embolization of hepatocellular carcinoma with drug-eluting beads: Doxorubicin tissue concentration and distribution in patient liver explants', *Journal of hepatology*, vol. 55, no. 6, pp. 1332–8, 2011.

[69] R. Lencioni, P. Petruzzi and L. Crocetti, 'Chemoembolization of hepatocellular carcinoma', *Seminars in interventional radiology*, vol. 30, no. 1, pp. 3–11, 2013.

[70] S. Shin, ‘The current practice of transarterial chemoembolization for the treatment of hepatocellular carcinoma’, *Korean journal of radiology: Official journal of the Korean Radiological Society*, vol. 10, no. 5, pp. 425–34, 2009.

[71] J. Song and D.-Y. Kim, ‘Conventional vs drug-eluting beads transarterial chemoembolization for hepatocellular carcinoma’, *World Journal of Hepatology*, vol. 9, no. 18, pp. 808–814, 2017.

[72] H. Y. Woo and J. Heo, ‘Transarterial chemoembolization using drug eluting beads for the treatment of hepatocellular carcinoma: Now and future.’ *Clinical and molecular hepatology*, vol. 21, no. 4, pp. 3–11, 2015.

[73] C. Mosconi, A. Cappelli, C. Pettinato and R. Golfieri, ‘Radioembolization with yttrium-90 microspheres in hepatocellular carcinoma: Role and perspectives’, *World journal of hepatology*, vol. 7, no. 5, pp. 738–752, 2015.

[74] H.-C. Kim, ‘Radioembolization for the treatment of hepatocellular carcinoma’, *Clinical and Molecular Hepatology*, vol. 23, no. 2, pp. 109–14, 2017.

[75] M. E. Hamami *et al.*, ‘Spect/ct with 99mtc-maa in radioembolization with 90y microspheres in patients with hepatocellular cancer’, *Journal of Nuclear Medicine*, vol. 50, no. 05, pp. 688–92, 2009.

[76] H. N. Lee and D. Hyun, ‘Complications related to transarterial treatment of hepatocellular carcinoma: A comprehensive review’, *Korean Journal of Radiology*, vol. 24, no. 3, 2023.

[77] M. Reincke *et al.*, ‘Hepatic decompensation after transarterial radioembolization: A retrospective analysis of risk factors and outcome in patients with hepatocellular carcinoma’, *Hepatology Communications*, vol. 6, no. 11, pp. 3223–33, 2022.

[78] A. Facciorusso, G. Serviddio and N. Muscatiello, ‘Transarterial radioembolization vs chemoembolization for hepatocarcinoma patients: A systematic review and meta-analysis’, *World Journal of Hepatology*, vol. 8, no. 18, p. 770, 2016.

[79] H. Ahmadzadehfar, H.-J. Biersack and S. Ezziddin, ‘Radioembolization of liver tumors with yttrium-90 microspheres’, *Seminars in Nuclear Medicine*, vol. 40, no. 2, pp. 105–21, 2010.

[80] A. Brown *et al.*, ‘Tace versus tare for patients with hepatocellular carcinoma: Overall and individual patient level meta analysis’, *Cancer Medicine*, vol. 12, no. 3, pp. 2590–99, 2022.

[81] A. Casadei Gardini, E. Tamburini, M. Iñarrairaegui, G. L. Frassineti and B. Sangro, 'Radioembolization versus chemoembolization for unresectable hepatocellular carcinoma: A meta-analysis of randomized trials', *OncoTargets and Therapy*, vol. 11, pp. 7315–21, 2018.

[82] E. Dhondt *et al.*, 'Yttrium-90 radioembolization versus drug-eluting beads chemoembolization for unresectable hepatocellular carcinoma: Results from the trace phase 2 randomized controlled trial', *Journal of Hepatology*, vol. 303, no. 3, pp. 699–710, 2022.

[83] J. Aramburu *et al.*, 'In vitro model for simulating drug delivery during balloon-occluded transarterial chemoembolization', *Biology*, vol. 10, p. 1341, 2021.

[84] A. Richards, C. Kleinstreuer, A. Kennedy, E. Childress and G. Buckner, 'Experimental microsphere targeting in a representative hepatic artery system', *IEEE transactions on bio-medical engineering*, vol. 59, no. 1, pp. 198–204, 2011.

[85] Terumo, *Devices for interventional radiology*, `https://www.terumo-europe.com/en-emea/medical-field/interventional-oncology`, Accessed: 2024-03-21.

[86] Guerbet, *Drakon standard microcatheter*, `https://www.guerbet.com/products-solutions/interventional-radiology/drakon-microcatheters`, Accessed: 2024-03-21.

[87] B. Scientific, *Direxion torqueable microcatheter*, `https://www.bostonscientific.com/en-US/products/embolization/Direxion_and_Direxion_HI-FLO_Microcatheters.html`, Accessed: 2024-03-21.

[88] S. Rose, K. Narsinh, A. Isaacson, A. Fischman and J. Golzarian, 'The beauty and bane of pressure-directed embolotherapy: Hemodynamic principles and preliminary clinical evidence', *American Journal of Roentgenology*, vol. 212, pp. 1–10, 2018.

[89] T. L. Sciences, *Pressure-enabled drug delivery approach with trinav infusion system*, `https://trinavinfusion.com/pedd/`, Accessed: 2024-02-18.

[90] S. Rose, S. Kikolski and J. Chomas, 'Downstream hepatic arterial blood pressure changes caused by deployment of the surefire antireflux expandable tip', *Cardiovascular and interventional radiology*, vol. 36, no. 5, pp. 1262–9, 2012.

[91] Embolx, *Sniper balloon microcatheter*, `https://embolx.com/products/`, Accessed: 2024-01-17.

[92] M. Caine *et al.*, 'Impact of yttrium-90 microsphere density, flow dynamics, and administration technique on spatial distribution: Analysis using an in vitro model', *Journal of Vascular and Interventional Radiology*, vol. 28, no. 2, pp. 260–268, 2016.

[93] M. Medical, *Hepasphere*, `https://www.merit.com/product/hepasphere-microspheres/`, Accessed: 2024-03-21.

[94] Y. Nouri, J. Kim, H. Yoon, H. Ko, J. Shin and D. I. Gwon, 'Update on transarterial chemoembolization with drug-eluting microspheres for hepatocellular carcinoma', *Korean Journal of Radiology*, vol. 20, p. 34, 2019.

[95] J. Zhang, G.-a. Feng, Y. Li and W. Wang, 'Drug-eluting bead transarterial chemoembolization with medium-sized versus small-sized callispheres microspheres in unresectable primary liver cancer', *Asia-Pacific Journal of Clinical Oncology*, vol. 18, no. 4, pp. 388–393, 2021.

[96] S. Medical, *Sir-sphere*, `https://www.sirtex.com/eu/patients/sir-spheres-y-90-resin-microspheres/about-sir-spheres/`, Accessed: 2024-03-21.

[97] B. Scientific, *Therasphere*, `https://www.bostonscientific.com/en-US/medical-specialties/interventional-radiology/interventional-oncology/therasphere.html`, Accessed: 2024-03-21.

[98] M. T. Reinders, M. L. Smits, C. van Roekel and A. J. Braat, 'Holmium-166 microsphere radioembolization of hepatic malignancies', *Seminars in Nuclear Medicine*, vol. 49, no. 3, pp. 237–243, 2019.

[99] J. Roosen *et al.*, 'Development of an mri-guided approach to selective internal radiation therapy using holmium-166 microspheres', *Cancers*, vol. 13, no. 21, p. 5462, 2021.

[100] J.-L. Raoul *et al.*, 'Evolving strategies for the management of intermediate-stage hepatocellular carcinoma: Available evidence and expert opinion on the use of transarterial chemoembolization', *Cancer Treatment Reviews*, vol. 37, no. 3, pp. 212–220, 2011.

[101] A.-L. Hermann *et al.*, ‘Relationship of tumor radiation–absorbed dose to survival and response in hepatocellular carcinoma treated with transarterial radioembolization with 90 y in the sarah study’, *Radiology*, vol. 296, no. 3, pp. 673–684, 2020.

[102] M. Guerrero *et al.*, ‘Validation of a commercial software dose calculation for y-90 microspheres’, *Brachytherapy*, vol. 21, no. 4, pp. 561–66, 2022.

[103] G. Chen, Z. Lu, H. Jiang, K.-H. Lin and G. Mok, ‘Voxel-s-value based 3d treatment planning methods for y-90 microspheres radioembolization based on tc-99m-macroaggregated albumin spect/ct’, *Scientific Reports*, vol. 13, no. 1, 2023.

[104] A. Dieudonné *et al.*, ‘Clinical feasibility of fast 3-dimensional dosimetry of the liver for treatment planning of hepatocellular carcinoma with y-90-microspheres’, *Journal of nuclear medicine : official publication, Society of Nuclear Medicine*, vol. 52, no. 12, pp. 1930–7, 2011.

[105] S. Medical, *Sureplan liver y90*, `https://www.sirtex.com/us/products/sir-spheres/insyte-with-sureplan-liver-y90/`, Accessed: 2024-02-18.

[106] J. Aramburu, R. Antón, A. Rivas, J. Ramos, B. Sangro and J. Bilbao, ‘Computational particle-hemodynamics analysis of liver radioembolization pretreatment as an actual treatment surrogate’, *International Journal for Numerical Methods in Biomedical Engineering*, vol. 33, no. 2, 2016.

[107] S. Healthineers, *Syngo embolization guidance*, `https://www.siemens-healthineers.com/nl/angio/options-and-upgrades/clinical-software-applications/syngo-embolization-guidance`, Accessed: 2024-03-21.

[108] E. Leen *et al.*, ‘Detection of hepatic metastases using duplex/color doppler sonography’, *Annals of surgery*, vol. 214, no. 5, pp. 599–604, 1991.

[109] M. Andreucci, R. Solomon and A. Tasanarong, ‘Side effects of radiographic contrast media: Pathogenesis, risk factors, and prevention’, *BioMed research international*, vol. 2014, p. 741 018, 2014.

[110] R. Colquitt, D. Colquhoun and R. Thiele, ‘In silico modeling of physiologic systems’, *Best practice & research. Clinical anaesthesiology*, vol. 25, no. 4, pp. 499–510, 2011.

[111] R. Sacco *et al.*, ‘Transarterial chemoembolization for the treatment of hepatocellular carcinoma: A review’, *Journal of Hepatocellular Carcinoma*, vol. 4, pp. 105–110, 2017.

[112] J. Aramburu, R. Antón, A. Rivas, J. Ramos, B. Sangro and J. Bilbao, ‘Liver radioembolization: An analysis of parameters that influence the catheter-based particle-delivery via cfd’, *Current Medicinal Chemistry*, vol. 27, no. 10, pp. 1600–15, 2018.

[113] E. Childress and C. Kleinstreuer, ‘Impact of fluid–structure interaction on direct tumor-targeting in a representative hepatic artery system’, *Annals of biomedical engineering*, vol. 42, no. 3, pp. 461–74, 2013.

[114] C. Debbaut *et al.*, ‘From vascular corrosion cast to electrical analog model for the study of human liver hemodynamics and perfusion’, *IEEE transactions on bio-medical engineering*, vol. 58, no. 01, pp. 25–35, 2011.

[115] J. Aramburu *et al.*, ‘Numerical zero-dimensional hepatic artery hemodynamics model for balloon-occluded transarterial chemoembolization’, *International Journal for Numerical Methods in Biomedical Engineering*, vol. 34, no. 7, e2983, 2018.

[116] E. Childress, C. Kleinstreuer and A. Kennedy, ‘A new catheter for tumor-targeting with radioactive microspheres in representative hepatic artery systems-part ii: Solid tumor-targeting in a patient-inspired hepatic artery system’, *Journal of biomechanical engineering*, vol. 134, no. 05, p. 051 005, 2012.

[117] J. Aramburu *et al.*, ‘A methodology for numerically analysing the hepatic artery haemodynamics during b-tace: A proof of concept’, *Computer Methods in Biomechanics and Biomedical Engineering*, vol. 22, no. 5, pp. 518–532, 2019.

[118] D. Groen *et al.*, ‘Vecmatk: A scalable verification, validation and uncertainty quantification toolkit for scientific simulations’, *Philosophical Transactions of the Royal Society A: Mathematical, Physical and Engineering Sciences*, vol. 379, no. 2197, p. 20 200 221, 2021.

[119] C. Roy and W. Oberkampf, ‘A complete framework for verification, validation, and uncertainty quantification in scientific computing (invited)’, *Computer Methods in Applied Mechanics and Engineering*, vol. 200, no. 25, pp. 2131–2144, 2011.

[120] M. Viceconti *et al.*, 'Theoretical foundations of good simulation practice', in 2024, pp. 9–23.

[121] C. Simoncini *et al.*, 'Towards a patient-specific hepatic arterial modeling for microspheres distribution optimization in sirt protocol', *Medical & Biological Engineering & Computing*, vol. 56, pp. 1–15, 2017.

[122] A. Kulesza *et al.*, 'Model development', in 2024, pp. 25–42.

[123] E. Roncali, A. Taebi, C. Foster and C. Vu, 'Personalized dosimetry for liver cancer y-90 radioembolization using computational fluid dynamics and monte carlo simulation', *Annals of Biomedical Engineering*, vol. 48, no. 5, pp. 1499–1510, 2020.

[124] U. Lertxundi *et al.*, 'Cfd simulations of radioembolization: A proof-of-concept study on the impact of the hepatic artery tree truncation', *Mathematics*, vol. 9, no. 8, p. 839, 2021.

[125] S. Vermijs *et al.*, 'A novel three-dimensional planning tool for selective clamping during partial nephrectomy: Validation of a perfusion zone algorithm', *European Urology*, vol. 83, no. 5, pp. 413–421, 2023.

[126] J. Buchanan, C. Kleinstreuer and K. Comer, 'Rheological effects on pulsatile hemodynamics in a stenosed tube', *Computers & Fluids*, vol. 29, no. 6, pp. 695–724, 2000.

[127] P. Reymond, F. Merenda, F. Perren, D. Rüfenacht and N. Stergiopulos, 'Validation of a one-dimensional model of the systemic arterial tree', *American journal of physiology. Heart and circulatory physiology*, vol. 297, no. 1, H208–22, 2009.

[128] J. Aramburu, R. Antón, A. Rivas, J. Ramos, B. Sangro and J. Bilbao, 'Liver cancer arterial perfusion modelling and cfd boundary conditions methodology: A case study of the haemodynamics of a patient-specific hepatic artery in literature-based healthy and tumour-bearing liver scenarios', *International Journal for Numerical Methods in Biomedical Engineering*, vol. 32, no. 11, 2016.

[129] C. Kleinstreuer and E. Childress, 'Computationally efficient particle release map determination for direct tumor-targeting in a representative hepatic artery system', *Journal of Biomechanical Engineering*, vol. 136, no. 1, p. 011 012, 2013.

[130] A. Taebi, N. Janibek, R. Goldman, R. Pillai, C. Vu and E. Roncali, ‘The impact of injection distance to bifurcations on yttrium-90 distribution in liver cancer radioembolization’, *Journal of Vascular and Interventional Radiology*, vol. 33, no. 6, pp. 668–677, 2022.

[131] Z. Cooper-Baldock, B. Vara Almirall and K. Inthavong, ‘Speed, power and cost implications for gpu acceleration of computational fluid dynamics on hpc systems’, *Supercomputing Asia*, vol. 1, 2024.

[132] A. Johansen, ‘Monte carlo methods’, in 2010, pp. 296–303.

[133] J. Ortega *et al.*, ‘Computational study of a novel catheter for liver radioembolization’, *International Journal for Numerical Methods in Biomedical Engineering*, vol. 38, no. 4, e3577, 2022.

[134] A. Taebi, R. Pillai, B. Roudsari, C. Vu and E. Roncali, ‘Computational modeling of the liver arterial blood flow for microsphere therapy: Effect of boundary conditions’, *Bioengineering*, vol. 7, no. 3, p. 64, 2020.

[135] J. Helton and F. Davis, ‘Latin hypercube sampling and the propagation of uncertainty in analyses of complex systems’, *Reliability Engineering & System Safety*, vol. 81, pp. 23–69, 2002.

[136] M. Askarian, R. Zarghami, F. Jalali Farahani and N. Mostoufi, ‘Uncertainty propagation in condensate stabilization column’, vol. 31, 2012, pp. 115–9.

[137] X.-Y. Yuan *et al.*, ‘Real-time prediction of transarterial drug delivery based on a deep convolutional neural network’, *Applied Sciences*, vol. 12, no. 20, p. 10 554, 2022.

[138] T. Ishigami and T. Homma, ‘An importance quantification technique in uncertainty analysis for computer models’, in *Proceedings of ISUMA 1990. First International Symposium on Uncertainty Modeling and Analysis*, 1990, pp. 398–403.

[139] A. Saltelli, ‘Making best use of model evaluations to compute sensitivity indices’, *Computer Physics Communications*, vol. 145, no. 2, pp. 280–297, 2002.

[140] M. D. Morris, ‘Factorial sampling plans for preliminary computational experiments’, *Quality Engineering*, vol. 33, no. 2, pp. 307–310, 1991.

[141] G. García Isla *et al.*, ‘Sensitivity analysis of geometrical parameters to study haemodynamics and thrombus formation in the left atrial appendage: Virtual haemodynamics and thrombus formation study in laa’, *International Journal for Numerical Methods in Biomedical Engineering*, vol. 34, 2018.

[142] C. Debbaut *et al.*, ‘Analyzing the human liver vascular architecture by combining vascular corrosion casting and micro-ct scanning: A feasibility study’, *Journal of anatomy*, vol. 224, no. 4, pp. 509–17, 2014.

[143] G. Peeters *et al.*, ‘A multilevel modeling framework to study hepatic perfusion characteristics in case of liver cirrhosis’, *Journal of biomechanical engineering*, vol. 137, no. 5, p. 051 007, 2014.

[144] R. Kratky and M. Roach, ‘Shrinkage of batson’s and its relevance to vascular casting’, *Atherosclerosis*, vol. 51, no. 2-3, pp. 339–41, 1984.

[145] S. Wait *et al.*, ‘Towards sustainable cancer care: Reducing inefficiencies, improving outcomes. a policy report from the all.can initiative’, *Journal of Cancer Policy*, vol. 13, pp. 47–64, 2017.

[146] A. Facciorusso, R. Licinio, N. Muscatiello, A. Di Leo and M. Barone, ‘Transarterial chemoembolization: Evidences from the literature and applications in hepatocellular carcinoma patients’, *World Journal of Hepatology*, vol. 7, no. 16, pp. 2009–19, 2015.

[147] T. Clark, ‘Complications of hepatic chemoembolization’, *Seminars in interventional radiology*, vol. 23, no. 2, pp. 119–25, 2006.

[148] M. Piccinelli, A. Veneziani, D. Steinman, A. Remuzzi and L. Antiga, ‘A framework for geometric analysis of vascular structures: Application to cerebral aneurysms’, *IEEE transactions on medical imaging*, vol. 28, no. 8, pp. 1141–55, 2009.

[149] S. Sarker, Y. Chatzizisis and B. Terry, ‘Computational optimization of a novel atraumatic catheter for local drug delivery in coronary atherosclerotic plaques’, *Medical Engineering & Physics*, vol. 79, pp. 26–32, 2020.

[150] P. Longest, C. Kleinstreuer and J. Buchanan, ‘Efficient computation of micro-particle dynamics including wall effects’, *Computers & Fluids*, vol. 33, no. 4, pp. 577–601, 2004.

[151] U. Lertxundi, J. Aramburu, M. Rodriguez-Fraile, B. Sangro and R. Antón, 'Computational study of the microsphere concentration in blood during radioembolization', *Mathematics*, vol. 10, no. 22, p. 4280, 2022.

[152] S. S. Sajjadinia, B. Carpentieri, S. Duraisamy and G. Holzapfel, 'Multi-fidelity surrogate modeling through hybrid machine learning for biomechanical and finite element analysis of soft tissues', *Computers in Biology and Medicine*, vol. 148, p. 105 699, 2022.

[153] L. Gheysen, L. Maes, A. Caenen, P. Segers, M. Peirlinck and N. Famaey, 'Uncertainty quantification of the wall thickness and stiffness in an idealized dissected aorta', *Journal of the Mechanical Behavior of Biomedical Materials*, vol. 151, p. 106 370, 2024.

[154] M. Peirlinck, F. Costabal and E. Kuhl, 'Sex differences in drug-induced arrhythmogenesis', *Frontiers in Physiology*, vol. 12, 2021.

[155] A. De Backere and G. Meiresonne, 'Locoregional drug delivery for liver cancer: Experimental validation of drug carrier transport as part of a patient-specific optimization workflow', M.S. thesis, Ghent University, 2023.

[156] B. Azzi and L. Verhaeghe, 'Targeted therapy for hcc: Investigating catheter type influence on distribution within a patient-specific 3d liver vascular tree and evaluating particle measurement reliability', M.S. thesis, Ghent University, 2024.

[157] E. Woestenborghs, 'Patient-specific dosimetry for y-90 radioembolization of hepatocellular carcinoma based on cfd modeling', M.S. thesis, Ghent University, 2023.

[158] M. De Smet, 'Patient-specific in-vivo validation of computational fluid dynamics and monte carlo modelling for liver radioembolization', M.S. thesis, Ghent University, 2024.

[159] Y. Feng *et al.*, 'An in silico inter-subject variability study of extra-thoracic morphology effects on inhaled particle transport and deposition', *Journal of Aerosol Science*, vol. 123, no. 8, pp. 185–207, 2018.

[160] Y. Feng, 'Create the individualized digital twin for noninvasive precise pulmonary healthcare', *Significances of Bioengineering & Biosciences*, vol. 1, 2018.

[161] J. Roosen *et al.*, ‘Intraprocedural mri-based dosimetry during transarterial radioembolization of liver tumours with holmium-166 microspheres (emeritus-1): A phase i trial towards adaptive, image-controlled treatment delivery’, *European Journal of Nuclear Medicine and Molecular Imaging*, vol. 49, no. 13, pp. 4705–15, 2022.

[162] F. Michaud *et al.*, ‘Selective embolization with magnetized microbeads using magnetic resonance navigation in a controlled-flow liver model’, *Medical Physics*, vol. 46, no. 2, pp. 789–99, 2018.

[163] J. Zeebroek, ‘Using cfd for the evaluation of the impact of side-hole catheters and injection velocity on particle spread for transarterial liver cancer treatments: A patient-specific case study’, M.S. thesis, Ghent University, 2024.

[164] C. De Smet, ‘Computational fluid dynamics modelling of liver radioembolization: Comparison of side-hole versus end-hole catheters in a patient-specific geometry’, M.S. thesis, Ghent University, 2024.